

ADDRESS OF PUBLISHER
& EDITOR'S OFFICE:

GDAŃSK UNIVERSITY
OF TECHNOLOGY

Faculty of Ocean Engineering
& Ship Technology
G. Narutowicza 11/12
80-233 Gdańsk, POLAND

tel.: +48 58 347 13 66
fax: +48 58 341 13 66

EDITORIAL STAFF:

Jacek Rudnicki
| Editor in Chief
Rafał Szłapczyński
| Associate Editor
Jerzy Świrzydźczuk
| Associate Editor
Przemysław Wierzchowski
| Associate Editor
Aleksander Kniat
| Editor for international
relations

Price:
single issue: 25 PLN

Prices for abroad
single issue:
- in Europe EURO 15
- overseas USD 20

WEB:
pg.edu.pl/pmr

e-mail : pmr@post.pl

ISSN 1233-2585

CONTENS

- | | |
|----|--|
| 4 | Andrzej S. Lenart
<i>SPHERE – TO – SPHEROID COMPARISON – NUMERICAL ANALYSIS</i> |
| 10 | Marcin Życzkowski, Rafał Szłapczyński
<i>MULTI-OBJECTIVE WEATHER ROUTING OF SAILING VESSELS</i> |
| 18 | Alfonso López, Miguel Gutiérrez, Andrés Ortega, Cristina Puente, Alejandro Morales, Diego Gonzalez, Emma Díaz
<i>PERFORMANCE ANALYSIS OF A MEDIUM FREQUENCY OFFSHORE GRID FOR IDENTIFICATION OF VESSELS SAILING ON HIGH DENSITY MARITIME EUROPEAN ROUTES</i> |
| 27 | Teresa Abramowicz-Gerigk, Zbigniew Burciu, Jacek Jachowski
<i>AN INNOVATIVE STEERING SYSTEM FOR A RIVER PUSH BARGE OPERATED IN ENVIRONMENTALLY SENSITIVE AREAS</i> |
| 35 | Grażyna Grelowska, Eugeniusz Kozaczka, Wojciech Szymczak
<i>ACOUSTIC IMAGING OF SELECTED AREAS OF GDANSK BAY WITH THE AID OF PARAMETRIC ECHOSOUNDER AND SIDE-SCAN SONAR</i> |
| 42 | Aleksander Kniat
<i>VISUALIZATION OF A LIFEBOAT MOTION DURING LOWERING ALONG SHIP'S SIDE</i> |
| 47 | Ryszard Jasiński
<i>PROBLEMS OF THE STARTING AND OPERATING OF HYDRAULIC COMPONENTS AND SYSTEMS IN LOW AMBIENT TEMPERATURE (PART V)</i> |
| 57 | Jerzy Girtler
<i>FEATURES OF LOAD AND WEAR OF MAIN PROPULSION DEVICES ON SEA-GOING SHIPS WITH PISTON COMBUSTION ENGINES AND THEIR IMPACT ON CHANGES IN TECHNICAL STATES OF THE SYSTEMS</i> |
| 67 | Bogdan Landowski, Michał Pająk, Bogdan Żółtowski, Łukasz Muślewski
<i>METHOD OF BUILDING A MODEL OF OPERATIONAL CHANGES FOR THE MARINE COMBUSTION ENGINE DESCRIBING THE IMPACT OF THE DAMAGES OF THIS ENGINE ON THE CHARACTERISTICS OF ITS OPERATION PROCESS</i> |
| 77 | Wojciech Litwin, Wojciech Leśniewski, Jakub Kowalski
<i>ENERGY EFFICIENT AND ENVIRONMENTALLY FRIENDLY HYBRID CONVERSION OF INLAND PASSENGER VESSEL</i> |
| 85 | Marek Dzida, Jacek Frost
<i>OPERATION OF TWO-SHAFT GAS TURBINE IN THE RANGE OF OPEN ANTI-SURGE VALVE</i> |

**ADDRESS OF PUBLISHER
& EDITOR'S OFFICE:**

**GDAŃSK UNIVERSITY
OF TECHNOLOGY**

**Faculty of Ocean Engineering
& Ship Technology
G. Narutowicza 11/12
80-233 Gdańsk, POLAND**

tel.: +48 58 347 13 66

fax: +48 58 341 13 66

- 93 Andrzej Tomporowski, Józef Flizikowski, Marek Opielak, Robert Kasner, Weronika Kruszelnicka**
ASSESSMENT OF ENERGY USE AND ELIMINATION OF CO2 EMISSIONS IN THE LIFE CYCLE OF AN OFFSHORE WIND POWER PLANT FARM
- 102 Zbigniew Korczewski**
A METHOD TO ASSESS TRANSVERSE VIBRATION ENERGY OF SHIP PROPELLER SHAFT FOR DIAGNOSTIC PURPOSES
- 108 Łukasz Breńkacz, Grzegorz Żywica, Marta Drosińska-Komor**
THE EXPERIMENTAL IDENTIFICATION OF THE DYNAMIC COEFFICIENTS OF TWO HYDRODYNAMIC JOURNAL BEARINGS OPERATING AT CONSTANT ROTATIONAL SPEED AND UNDER NONLINEAR CONDITIONS
- 116 Dariusz Skibicki, Łukasz Pejkowski, Michał Stopel**
FINITE ELEMENT ANALYSIS OF VENTILATION SYSTEM FIRE DAMPER DYNAMIC TIME-HISTORY
- 124 Waldemar Magda**
COMPARISON OF SOIL MODELS IN THE THERMODYNAMIC ANALYSIS OF A SUBMARINE PIPELINE BURIED IN SEABED SEDIMENTS

Editorial

POLISH MARITIME RESEARCH is a scientific journal of worldwide circulation. The journal appears as a quarterly four times a year. The first issue of it was published in September 1994. Its main aim is to present original, innovative scientific ideas and Research & Development achievements in the field of :

Engineering, Computing & Technology, Mechanical Engineering,

which could find applications in the broad domain of maritime economy. Hence there are published papers which concern methods of the designing, manufacturing and operating processes of such technical objects and devices as : ships, port equipment, ocean engineering units, underwater vehicles and equipment as well as harbour facilities, with accounting for marine environment protection.

The Editors of POLISH MARITIME RESEARCH make also efforts to present problems dealing with education of engineers and scientific and teaching personnel. As a rule, the basic papers are supplemented by information on conferences , important scientific events as well as cooperation in carrying out international scientific research projects.

Scientific Board

Chairman : Prof. JERZY GIRTLEK - Gdańsk University of Technology, Poland

Vice-chairman : Prof. MIROSŁAW L. WYSZYŃSKI - University of Birmingham, United Kingdom

Dr POUL ANDERSEN
Technical University of Denmark
Denmark

Dr MEHMET ATLAR
University of Newcastle United
Kingdom

Prof. GÖRAN BARK
Chalmers University of Technology
Sweden

Prof. SERGEY BARSUKOV
Army Institute of Odessa Ukraine

Prof. MUSTAFA BAYHAN
Süleyman Demirel University
Turkey

Prof. VINCENZO CRUPI
University of Messina, Italy

Prof. MAREK DZIDA
Gdańsk University of Technology
Poland

Prof. ODD M. FALTINSEN
Norwegian University of Science
and Technology
Norway

Prof. PATRICK V. FARRELL
University of Wisconsin Madison,
WI
USA

Prof. HASSAN GHASSEMI
Amirkabir University of Technology
Iran

Prof. STANISŁAW GUCMA
Maritime University of Szczecin
Poland

Prof. ANTONI ISKRA
Poznań University of Technology
Poland

Prof. JAN KICIŃSKI
Institute of Fluid-Flow Machinery
of PASci
Poland

Prof. ZBIGNIEW KORCZEWSKI
Gdańsk University of Technology
Poland

Prof. JANUSZ KOZAK
Gdańsk University of Technology
Poland

Prof. JAN KULCZYK
Wrocław University of Technology
Poland

Prof. NICOS LADOMMATOS
University College London United
Kingdom

Prof. JÓZEF LISOWSKI
Gdynia Maritime University Poland

Prof. JERZY MATUSIAK
Helsinki University of Technology
Finland

Prof. JERZY MERKISZ
Poznań University of Technology
Poland

Prof. EUGEN NEGRUS
University of Bucharest Romania

Prof. YASUHIKO OHTA
Nagoya Institute of Technology
Japan

Dr YOSHIO SATO
National Traffic Safety and
Environment Laboratory
Japan

Prof. KLAUS SCHIER
University of Applied Sciences
Germany

Prof. FREDERICK STERN
University of Iowa, IA, USA

Prof. ILCEV DIMOV STOJCE
Durban University of Technology
South Africa

Prof. JÓZEF SZALA
Bydgoszcz University
of Technology and Agriculture
Poland

Prof. WITALIJ SZCZAGIN
State Technical University of
Kaliningrad, Russia

Prof. BORIS TIKHOMIROV
State Marine University of St.
Petersburg, Russia

Prof. DRACOS VASSALOS
University of Glasgow and
Strathclyde United Kingdom

SPHERE – TO – SPHEROID COMPARISON – NUMERICAL ANALYSIS

Andrzej S. Lenart
Gdynia Maritime University

ABSTRACT

Differences of orthodromic distances calculated on the sphere in comparison to the spheroid are numerically analyzed in the full range of departure point latitudes, courses over the ground and orthodromic distances for the global and limited range of latitudes. Optimum solutions for the radii of the sphere are provided.

Keywords: sphere in navigation; great circle distance; geodesics; direct and inverse geodesic solutions; numerical simulations

INTRODUCTION

In traditional navigation, to reduce the number of calculations, calculations are done with many simplifications, for example on a plane or a sphere instead of a spheroid. In modern navigation the spheroid such as WGS-84 ellipsoid is applied but in simpler navigation devices and in instructions for practical navigation a sphere is still used. The question arises what are differences between these two models of the earth.

In [1] comparison has been made between great circle distance on the navigation sphere and great ellipse on the spheroid and it has been concluded that this difference is near to 0.5%.

In [3] similar results have been obtained by simple comparison of extreme radiuses of curvature and an average substitute radius of the sphere.

In [4] the problem of differences for this radius have been partially numerically analysed for the global range of latitudes.

There are many global average radii defined such as mean, authalic, volumetric or rectifying. In [3] it has been proposed the radius of the sphere which gives minimum absolute

percentage value of differences given by the equation (for the global range of latitudes)

$$R_S = \frac{R_{M\max} + R_{M\min}}{2} \quad (1)$$

where

$$R_{M\min} = R_M(\varphi = 0^\circ) = \frac{b_0^2}{a_0} \quad (2)$$

$$R_{M\max} = R_M(\varphi = 90^\circ) = R_N(\varphi = 90^\circ) = \frac{a_0^2}{b_0} \quad (3)$$

and R_M , R_N are the radius of curvature in meridian and the radius of curvature in the prime vertical, respectively

$$R_M = \frac{a_0(1-e^2)}{\sqrt{(1-e^2 \sin^2 \varphi)^3}} \quad (4)$$

$$R_N = \frac{a_0}{\sqrt{1 - e^2 \sin^2 \varphi}} \quad (5)$$

For WGS-84

$$R_S = 6\,367\,516 \text{ m} \quad (6)$$

The set of procedures for calculating orthodromes (defined as the path of the shortest distance on any surface) by the application of solutions of the problems known in geodesy as the direct and the inverse geodetic problems, have been presented in [2,3].

In formal notations:

$$\varphi_2, \lambda_2 = \text{DGP}(\varphi_1, \lambda_1, S, C_{gs}) \quad (7)$$

$$S = \text{IGP}(\varphi_1, \lambda_1, \varphi_2, \lambda_2) \quad (8)$$

$$\varphi_{\max} = \text{FIMAX}(\varphi_1, \lambda_1, \varphi_2, \lambda_2) \quad (9)$$

where φ_1, λ_1 and φ_2, λ_2 are the departure point and the destination point, respectively, S is the orthodromic distance, C_{gs} is the Course Over the Ground (COG) at the departure point of the orthodrome, DGP is the procedure of solving the direct geodetic problem, IGP is the procedure of solving the inverse geodetic problem, FIMAX is the procedure of calculating maximum latitude.

In this paper these procedures, with results based on full accuracy Sodano's solutions [5,6,7] on WGS-84 reference ellipsoid (as in [2,3]), will be analysed in comparison to the great circle distance

$$S_S = R_S \cos^{-1}((\sin \varphi_1 \sin \varphi_2 + \cos \varphi_1 \cos \varphi_2 \cos(\lambda_2 - \lambda_1))) \quad (10)$$

for the full range of φ_1, C_{gs} and S and for the global and limited range of latitudes.

GLOBAL RANGE OF LATITUDES

For the departure latitude φ_1 taken from 0° to 90° in steps of 10° , $\lambda_1 = 0$, the departure course C_{gs} -from 0° to 180° in steps of 10° and the spheroidal orthodromic distance S - from 100 NM to 10000 NM the destination points φ_2, λ_2 are calculated with the use of the procedure (7) and for these points the great circle distance S_S is calculated by using Eq. (10). Tables for the given orthodromic distances S are generated from the differences

$$\Delta S = S_S - S \quad (11)$$

or percentage differences

$$\Delta S_{\%} = \frac{S_S - S}{S} \cdot 100\% \quad (12)$$

Such exemplary tables are: Tab. 1 ($\Delta S_{\%}$ for $S = 100$ NM) and Tab. 2 (ΔS for $S = 5400$ NM).

For each given distance S the maximum positive and negative differences $\Delta S_{\max\%+}$, $\Delta S_{\max\%-}$, $\Delta S_{\max+}$, $\Delta S_{\max-}$ can be found. These differences are presented in Tab. 3, Fig. 1 and 2.

Maximum differences have been found with the use of extremes finding tool (Microsoft Excel Solver) where values φ_1 and C_{gs} are not limited to values in Tables and therefore maximum differences in Tab. 2 are not the same as in Tab. 3 for $S = 5400$ NM.

It has been proved that R_S from Eq.(1) is the only one which gives symmetrical (and therefore minimum) absolute and percentage differences reaching up to $\pm 0.5\%$ and ± 17 NM, respectively. A small asymmetry is due to the fact that this equation gives exact symmetry for S near to zero distance.

Maximum positive differences appear for meridional orthodromes symmetrical to the equator and negative differences appear for meridional orthodromes symmetrical to the poles.

Maximum percentage differences appear for shorter orthodromes due to the bigger part of extreme difference between the radius of curvature in meridian and R_S at the equator and the poles in shorter orthodromes and the smaller part in longer orthodromes.

Maximum absolute differences of about ± 17 NM appear for $S = 5400$ NM for meridional orthodromes from 45° N to 45° S (and reversed) and from 45° N to 45° N or from 45° S to 45° S through the poles.

From $S = 7840$ NM the maximum negative differences of orthodromes change position from the poles to the equator where the percentage difference is constant and the absolute difference grows proportionally to the orthodromic distance.

LIMITED RANGE OF LATITUDES

LIMITED HIGHER LATITUDES

In marine navigation higher latitudes are not accessible. For this reason and for navigation in limited range of latitudes, orthodromic differences can be analysed for orthodromes for which

$$\varphi_{\max} \leq \varphi_{\text{lim}} \quad (14)$$

where φ_{\max} is from the procedure (9) and φ_{lim} is a limited latitude.

Differences in Tab. 1 and 2 are the functions

$$\Delta S = f(\varphi_1, C_{gs}, S, R_S) \quad (15)$$

which can be extended to

$$\Delta S_{lim} = f(\varphi_1, C_{gs}, S, R_s, \varphi_{lim}) \quad (16)$$

The tables can be generated for a given S and φ_{lim} with points

$$\Delta S_{lim} = f(\varphi_1, C_{gs}, S, R_s, \varphi_{max} > \varphi_{lim}) = 0 \quad (17)$$

and for each table

$$\Delta S_{limmax} = \max(|\Delta S_{lim}|) \quad (18)$$

is calculated and R_s is searched for which

$$\Delta S_{limmax} = \min \quad (19)$$

Therefore such R_s is optimum one to minimize maximum differences.

Since maximum percentage differences are for S = 100 NM (and are similar for all shorter orthodromes – Fig. 1) and maximum absolute differences are for S = 5400 NM therefore exemplary tables for $\varphi_{lim} = 60^\circ$ for the two distances are presented as Tab. 4 and 5.

Optimum R_s and ΔS_{limmax} in function of φ_{lim} are presented in Tab. 6, Fig. 3, Fig. 4 and Tab. 7, Fig. 5, Fig. 6.

Results for S = 5400 NM and lower φ_{lim} are rather of little importance because for these values tables of ΔS_{lim} have a few possible orthodromes only.

LIMITED LOWER LATITUDES

Nothing prevents from limiting also lower latitudes. In this case Eq. (17) can be extended to

$$\Delta S_{lim} = f(\varphi_1, C_{gs}, S, R_s, \varphi_1 < \varphi_{min}, \varphi_2 < \varphi_{min}, \varphi_{max} > \varphi_{lim}) = 0 \quad (20)$$

where φ_{min} is limited lower latitude.

Exemplary table for φ taken from 20° to 60° and for S = 100 NM is presented as Tab. 8.

CONCLUSIONS

The performed numerical analysis has proved that assessments of the sphere – to – spheroid differences in distances reaching $\pm 0.5\%$, which can be found in the referred to literature sources, are valid for short orthodromes only. For longer orthodromes the maximum of absolute differences of ± 17 NM exists for 5400 NM orthodrome. For global and limited ranges of latitudes the ready- to- use optimum radii of the sphere, which minimize maximum absolute and percentage differences, are provided in this paper.

BIBLIOGRAPHY

1. Earle M.A.: *Sphere to Spheroid Comparisons*. The Journal of Navigation, 59 (2006), pp. 491-496.
2. Lenart A.S.: *Solutions of Direct Geodetic Problem in Navigational Applications*. TransNav – The International Journal on Marine Navigation and Safety of Sea Transportation, 5(4) (2011), pp. 527-532.
3. Lenart A.S.: *Solutions of Inverse Geodetic Problem in Navigational Applications*. TransNav – The International Journal on Marine Navigation and Safety of Sea Transportation, 7(2) (2013), pp.253-257.
4. Nadrowski L.: *Analysis of errors of orthodromic distances on the sphere in comparison to the ellipsoid* (in Polish). Gdynia Maritime University, Faculty of Navigation – Engineer’s Thesis 2016.
5. Sodano E.M.: *A rigorous non-iterative procedure for rapid inverse solution of very long geodesics*. Bulletin Géodésique, 47/48 (1958), pp. 13-25.
6. Sodano E.M.: *General non-iterative solution of the inverse and direct geodetic problems*. Bulletin Géodésique, 75 (1965), pp. 69-89.
7. Sodano E.M.: *Supplement to inverse solution of long geodesics*. Bulletin Géodésique, 85 (1967), 233-236.

CONTACT WITH THE AUTHOR

Andrzej S. Lenart

e-mail: aslenart@am.gdynia.pl

Gdynia Maritime University

Al. Jana Pawła II 3

81-345 Gdynia

POLAND

Tab. 1. $\Delta S_{\%}$ [%] for $S = 100$ NM

ϕ_1 [°]	C_{gs} [°]																		
	0	10	20	30	40	50	60	70	80	90	100	110	120	130	140	150	160	170	180
90	-0.501	-0.501	-0.501	-0.501	-0.501	-0.501	-0.501	-0.501	-0.501	-0.501	-0.501	-0.501	-0.501	-0.501	-0.501	-0.501	-0.501	-0.501	-0.501
80	-0.476	-0.476	-0.478	-0.480	-0.483	-0.486	-0.488	-0.490	-0.491	-0.491	-0.489	-0.487	-0.483	-0.479	-0.475	-0.471	-0.468	-0.466	-0.466
70	-0.393	-0.395	-0.401	-0.411	-0.423	-0.435	-0.447	-0.456	-0.461	-0.462	-0.458	-0.449	-0.437	-0.423	-0.409	-0.395	-0.384	-0.376	-0.374
60	-0.262	-0.267	-0.281	-0.302	-0.328	-0.356	-0.382	-0.402	-0.414	-0.417	-0.410	-0.393	-0.369	-0.340	-0.309	-0.280	-0.257	-0.242	-0.237
50	-0.100	-0.108	-0.131	-0.167	-0.211	-0.257	-0.300	-0.335	-0.357	-0.363	-0.352	-0.325	-0.286	-0.239	-0.189	-0.142	-0.104	-0.079	-0.071
40	0.075	0.063	0.030	-0.021	-0.084	-0.151	-0.213	-0.263	-0.295	-0.305	-0.290	-0.253	-0.199	-0.132	-0.062	0.004	0.057	0.092	0.104
30	0.241	0.226	0.183	0.117	0.036	-0.050	-0.130	-0.195	-0.237	-0.250	-0.233	-0.187	-0.117	-0.033	0.056	0.139	0.207	0.251	0.267
20	0.379	0.361	0.310	0.232	0.136	0.034	-0.062	-0.139	-0.189	-0.206	-0.186	-0.133	-0.052	0.046	0.150	0.248	0.328	0.380	0.398
10	0.471	0.451	0.395	0.309	0.203	0.090	-0.016	-0.102	-0.158	-0.177	-0.156	-0.098	-0.011	0.097	0.211	0.317	0.404	0.461	0.481
0	0.506	0.486	0.428	0.338	0.229	0.112	0.002	-0.088	-0.146	-0.167	-0.146	-0.088	0.002	0.112	0.229	0.338	0.428	0.486	0.506

Tab. 2. ΔS [NM] for $S = 5400$ NM

ϕ_1 [°]	C_{gs} [°]																		
	0	10	20	30	40	50	60	70	80	90	100	110	120	130	140	150	160	170	180
90	0.05	0.05	0.05	0.05	0.05	0.05	0.05	0.05	0.05	0.05	0.05	0.05	0.05	0.05	0.05	0.05	0.05	0.05	0.05
80	-5.90	-5.82	-5.57	-5.17	-4.62	-3.93	-3.13	-2.22	-1.24	-0.22	0.83	1.85	2.83	3.72	4.50	5.14	5.62	5.91	6.01
70	-11.12	-10.98	-10.57	-9.89	-8.94	-7.75	-6.32	-4.70	-2.91	-1.00	0.98	2.95	4.86	6.62	8.18	9.47	10.43	11.03	11.23
60	-14.98	-14.82	-14.34	-13.53	-12.40	-10.94	-9.16	-7.08	-4.74	-2.20	0.49	3.22	5.89	8.41	10.65	12.52	13.93	14.80	15.09
50	-17.02	-16.87	-16.42	-15.67	-14.57	-13.11	-11.28	-9.08	-6.53	-3.67	-0.58	2.62	5.81	8.86	11.61	13.92	15.67	16.76	17.13
40	-16.98	-16.89	-16.58	-16.03	-15.20	-14.02	-12.45	-10.46	-8.05	-5.24	-2.11	1.23	4.63	7.93	10.94	13.51	15.46	16.68	17.10
30	-14.90	-14.88	-14.80	-14.60	-14.21	-13.55	-12.52	-11.06	-9.12	-6.72	-3.91	-0.79	2.48	5.72	8.74	11.34	13.33	14.59	15.02
20	-11.03	-11.10	-11.30	-11.55	-11.74	-11.77	-11.49	-10.80	-9.62	-7.93	-5.75	-3.18	-0.36	2.53	5.28	7.68	9.55	10.74	11.15
10	-5.84	-6.01	-6.51	-7.24	-8.08	-8.88	-9.47	-9.71	-9.48	-8.72	-7.42	-5.66	-3.56	-1.28	0.97	2.98	4.58	5.60	5.96
0	0.06	-0.21	-0.99	-2.20	-3.67	-5.24	-6.72	-7.93	-8.72	-8.99	-8.72	-7.93	-6.72	-5.24	-3.67	-2.20	-0.99	-0.21	0.06

Tab. 3. ΔS_{max} for different S

S	100	500	1000	2000	4000	5400	6000	7840	10000	NM
$\Delta S_{max\%}$	-0.501	-0.499	-0.494	-0.474	-0.396	-0.320	-0.283	-0.167	-0.167	%
$\Delta S_{max\%+}$	0.506	0.505	0.499	0.478	0.399	0.322	0.285	0.168	0.041	%
ΔS_{max}	-0.501	-2.497	-4.942	-9.472	-15.842	-17.263	-17.003	-13.083	-16.651	NM
ΔS_{max+}	0.506	2.523	4.992	9.561	15.964	17.377	17.113	13.199	4.095	NM

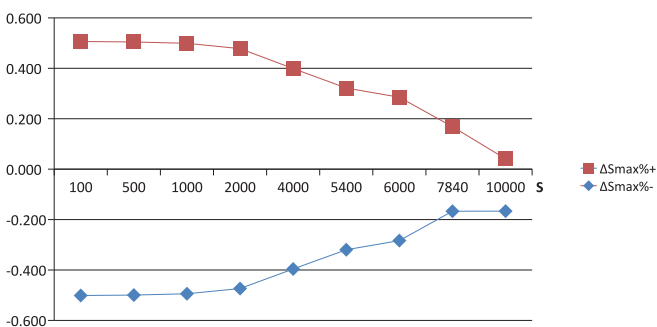


Fig. 1. $\Delta S_{max\%}$ [%] for different S [NM]

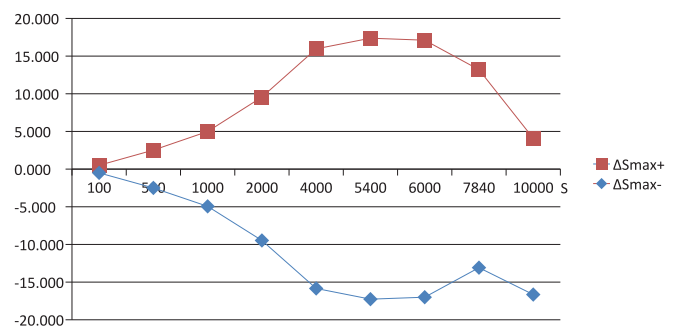


Fig. 2. ΔS_{max} [NM] for different S [NM]

Tab. 4. $|\Delta S_{lim}|[\%]$ for $S = 100$ NM, $\varphi_{lim} = 60^\circ$, $R_S = 6\,364\,691$ m

φ_1 [°]	C_{gs} [°]																		
	0	10	20	30	40	50	60	70	80	90	100	110	120	130	140	150	160	170	180
90	0.000	0.000	0.000	0.000	0.000	0.000	0.000	0.000	0.000	0.000	0.000	0.000	0.000	0.000	0.000	0.000	0.000	0.000	0.000
80	0.000	0.000	0.000	0.000	0.000	0.000	0.000	0.000	0.000	0.000	0.000	0.000	0.000	0.000	0.000	0.000	0.000	0.000	0.000
70	0.000	0.000	0.000	0.000	0.000	0.000	0.000	0.000	0.000	0.000	0.000	0.000	0.000	0.000	0.000	0.000	0.000	0.000	0.000
60	0.000	0.000	0.000	0.000	0.000	0.000	0.000	0.000	0.000	0.461	0.454	0.437	0.413	0.384	0.353	0.325	0.302	0.286	0.281
50	0.144	0.152	0.176	0.211	0.255	0.301	0.345	0.379	0.401	0.407	0.396	0.369	0.330	0.283	0.233	0.186	0.148	0.124	0.115
40	0.031	0.019	0.014	0.066	0.128	0.195	0.257	0.308	0.339	0.349	0.334	0.298	0.243	0.177	0.106	0.041	0.013	0.048	0.060
30	0.197	0.182	0.139	0.073	0.008	0.094	0.174	0.240	0.281	0.294	0.277	0.231	0.162	0.078	0.011	0.095	0.163	0.207	0.222
20	0.334	0.316	0.265	0.187	0.092	0.010	0.106	0.183	0.234	0.250	0.230	0.177	0.096	0.002	0.106	0.204	0.283	0.335	0.353
10	0.426	0.406	0.350	0.264	0.158	0.046	0.060	0.146	0.202	0.221	0.200	0.143	0.055	0.052	0.166	0.273	0.360	0.416	0.436
0	0.461	0.441	0.383	0.294	0.184	0.067	0.042	0.132	0.190	0.211	0.190	0.132	0.042	0.067	0.184	0.294	0.383	0.441	0.461

Tab. 5. $|\Delta S_{lim}|[NM]$ for $S = 5400$ NM, $\varphi_{lim} = 60^\circ$, $R_S = 6\,365\,799$ m

φ_1 [°]	C_{gs} [°]																		
	0	10	20	30	40	50	60	70	80	90	100	110	120	130	140	150	160	170	180
90	0.00	0.00	0.00	0.00	0.00	0.00	0.00	0.00	0.00	0.00	0.00	0.00	0.00	0.00	0.00	0.00	0.00	0.00	0.00
80	0.00	0.00	0.00	0.00	0.00	0.00	0.00	0.00	0.00	0.00	0.00	0.00	0.00	0.00	0.00	0.00	0.00	0.00	0.00
70	0.00	0.00	0.00	0.00	0.00	0.00	0.00	0.00	0.00	0.00	0.00	0.00	0.00	0.00	0.00	0.00	0.00	0.00	0.00
60	0.00	0.00	0.00	0.00	0.00	0.00	0.00	0.00	0.00	3.65	0.97	1.76	4.44	6.95	9.19	11.06	12.47	13.34	13.63
50	0.00	0.00	0.00	0.00	0.00	0.00	12.74	10.53	7.98	5.12	2.04	1.16	4.36	7.40	10.15	12.46	14.21	15.30	15.67
40	0.00	0.00	0.00	0.00	0.00	15.47	13.90	11.91	9.50	6.69	3.57	0.23	3.17	6.47	9.48	12.04	14.00	15.22	15.64
30	0.00	0.00	0.00	0.00	15.67	15.00	13.97	12.51	10.57	8.17	5.36	2.25	1.02	4.27	7.28	9.88	11.87	13.13	0.00
20	0.00	0.00	0.00	0.00	13.20	13.22	12.94	12.25	11.07	9.38	7.21	4.64	1.82	1.07	3.82	6.22	0.00	0.00	0.00
10	0.00	0.00	0.00	0.00	9.54	10.34	10.93	11.17	10.93	10.17	8.88	7.12	5.01	2.74	0.49	1.53	0.00	0.00	0.00
0	0.00	0.00	0.00	0.00	5.13	6.70	8.18	9.38	10.17	10.45	10.17	9.38	8.18	6.70	5.13	0.00	0.00	0.00	0.00

Tab. 6. $\Delta S_{limmax\%}$ and R_S for different φ_{lim} and $S = 100$ NM

φ_{lim}	10	20	30	40	50	60	70	80	90	°
$\Delta S_{limmax\%}$	0.341	0.355	0.378	0.405	0.434	0.461	0.484	0.498	0.503	%
R_S	6 357 045	6 357 965	6 359 376	6 361 109	6 362 954	6 364 691	6 366 108	6 367 033	6 367 355	m

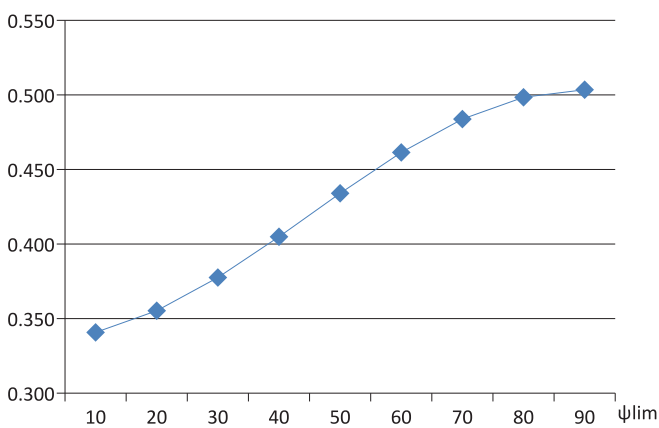


Fig. 3. $\Delta S_{limmax\%}$ for different φ_{lim} and $S = 100$ NM

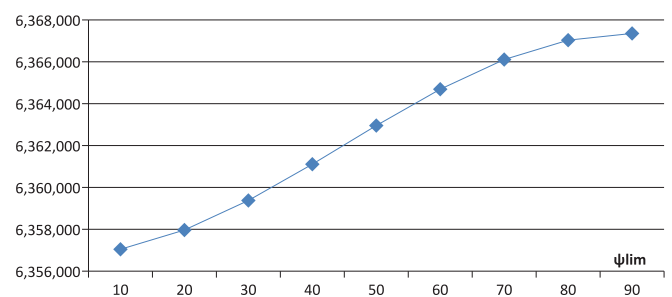


Fig. 4. R_S [m] for different φ_{lim} and $S = 100$ NM

Tab. 7. ΔS_{limmax} and R_s for different φ_{lim} and $S = 5400$ NM

φ_{lim}	10	20	30	40	50	60	70	80	90	°
ΔS_{limmax}	0.786	3.152	6.644	11.216	15.335	15.668	16.579	16.853	17.072	NM
R_s	6 377 209	6 374 991	6 372 423	6 367 838	6 365 408	6 365 799	6 366 871	6 367 193	6 367 450	m

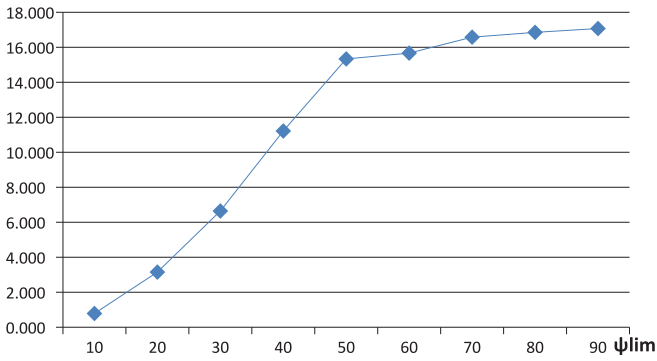


Fig. 5. ΔS_{limmax} for different φ_{lim} and $S = 5400$ NM

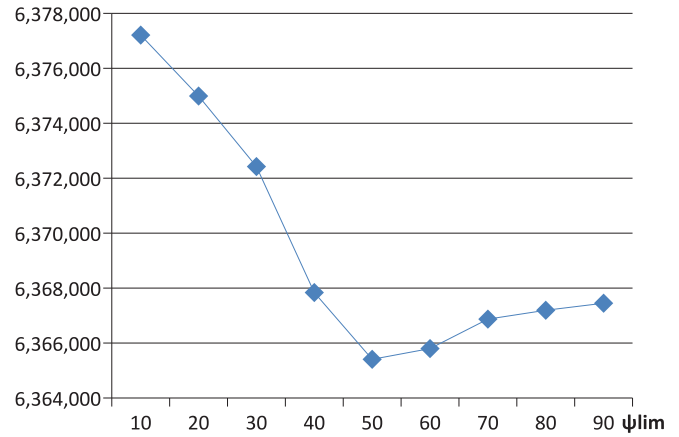


Fig. 6. R_s for different φ_{lim} and $S = 5400$ NM

Tab. 8. $|\Delta S_{lim}|$ [%] for $S = 100$ NM, $\varphi_{min} = 20^\circ$, $\varphi_{lim} = 60^\circ$, $R_s = 6\,368\,747$ m

φ_1 [°]	C_{gs} [°]																		
	0	10	20	30	40	50	60	70	80	90	100	110	120	130	140	150	160	170	180
90	0.000	0.000	0.000	0.000	0.000	0.000	0.000	0.000	0.000	0.000	0.000	0.000	0.000	0.000	0.000	0.000	0.000	0.000	0.000
80	0.000	0.000	0.000	0.000	0.000	0.000	0.000	0.000	0.000	0.000	0.000	0.000	0.000	0.000	0.000	0.000	0.000	0.000	0.000
70	0.000	0.000	0.000	0.000	0.000	0.000	0.000	0.000	0.000	0.000	0.000	0.000	0.000	0.000	0.000	0.000	0.000	0.000	0.000
60	0.000	0.000	0.000	0.000	0.000	0.000	0.000	0.000	0.000	0.398	0.391	0.374	0.350	0.321	0.290	0.261	0.238	0.223	0.218
50	0.080	0.089	0.112	0.148	0.192	0.238	0.281	0.316	0.338	0.343	0.333	0.306	0.267	0.219	0.169	0.123	0.085	0.060	0.052
40	0.094	0.083	0.049	0.002	0.065	0.132	0.194	0.244	0.276	0.285	0.271	0.234	0.179	0.113	0.043	0.023	0.076	0.111	0.123
30	0.261	0.246	0.203	0.137	0.056	0.030	0.111	0.176	0.218	0.231	0.213	0.167	0.098	0.014	0.075	0.159	0.226	0.271	0.286
20	0.398	0.380	0.329	0.251	0.155	0.053	0.042	0.120	0.170	0.000	0.000	0.000	0.000	0.000	0.000	0.000	0.000	0.000	0.000
10	0.000	0.000	0.000	0.000	0.000	0.000	0.000	0.000	0.000	0.000	0.000	0.000	0.000	0.000	0.000	0.000	0.000	0.000	0.000
0	0.000	0.000	0.000	0.000	0.000	0.000	0.000	0.000	0.000	0.000	0.000	0.000	0.000	0.000	0.000	0.000	0.000	0.000	0.000

MULTI-OBJECTIVE WEATHER ROUTING OF SAILING VESSELS

Marcin Życzkowski

Rafał Szłapczyński

Gdańsk University of Technology, Faculty of Ocean Engineering and Ship Technology, Poland

ABSTRACT

The paper presents a multi-objective deterministic method of weather routing for sailing vessels. Depending on a particular purpose of sailboat weather routing, the presented method makes it possible to customize the criteria and constraints so as to fit a particular user's needs. Apart from a typical shortest time criterion, safety and comfort can also be taken into account. Additionally, the method supports dynamic weather data: in its present version short-term, mid-term and long-term weather forecasts are used during optimization process. In the paper the multi-objective optimization problem is first defined and analysed. Following this, the proposed method solving this problem is described in detail. The method has been implemented as an online SailAssistance application. Some representative examples solutions are presented, emphasizing the effects of applying different criteria or different values of customized parameters.

Keywords: sailing vessels, weather routing, weather forecast, comfort, penalty

INTRODUCTION

Weather routing methods for sailing vessels has long been developed due to the great regattas such as America's Cup, Cowes Races, Mug Races and others related events. For obvious reasons regatta crews are interested in accurate minimal time routes, however route optimization is a more general problem, where multiple criteria may be applied. In this paper we present a method finding a route with the shortest journey time as a main objective, while also taking into account other aspects important for route planning. Shortest journey time is obviously essential for regatta crews; however, the situation is different for other users. For example, for recreational cruises comfort throughout voyage is equally important as it largely affects the passengers' overall satisfaction. Also, the safety-associated constraints are much stronger for recreational passenger cruises. In practice this means that route planning method eliminates routes, where strong winds, and high waves can constitute serious

discomfort or danger. The same concerns unexperienced sailors, who also do not need the fastest route with minimum time, but are interested in safe and comfortable sailing. On the other end of the problem, sailors looking for extreme experiences may specify maximum speed as their main objective, while lowering the level of safety restrictions.

The aim of this paper is to present a method of determining optimal sailing routes, which supports some greatly varying user requirements. All these requirements are modelled as configurable parameters of a goal function defined in the paper. Among others, this includes a newly introduced customized cost of a turn: low for experienced sailors, much higher for beginners or passenger cruises, so as to cover the inconvenience caused by a rapid change of direction. In practice applying various turn costs translates to sailing routes consisting of either multiple short tacks or just a few long ones.

Another new element of hereby presented version of the method is that it supports dynamic weather data: all available weather forecasts are analysed simultaneously by the optimization algorithm. In the current version of the method short-term, mid-term and long-term forecasts are taken into account during route determining, though it is possible to handle practically unlimited number of forecasts.

RELATED WORKS.

The theory of sailing has been described in detail in [12]. However, the problem of deterministic route planning for a sailing vessel has not been sufficiently documented in literature. Most available publications concern routing of unmanned sailing ships [18,19]. Other mostly focus on weather routing of motor-driven vessels. Only a few articles since the '60s to nowadays [9,15,3,13] present the development of research on the route planning of sailing vessels. Discretization of vessel's motion can be found in [23,24,11]. Advanced deterministic route planning algorithms are presented among others in [2,6,17]. The basic principles of navigation are outlined in the book [8], and the use of e-navigation in [22]. A method of graph Dijkstra-based [16] weather routing for motor-driven vessels have been presented in [4]. Dynamic weather forecasts have been discussed in [14], while other dynamic data have been applied in [16]. The issue of the comfort or discomfort perceived by the crew and passengers of the boat during different journeys have been documented in [1,7]. The cost of course changes has been applied in [21], while multicriteria route optimization has been researched in [20,5,10]. However, in general, up till now, there has been very little published research dedicated to a deterministic weather routing of sailing vessels, and the following paper aims to fill this gap.

MODEL OF THE PROBLEM

OPTIMISATION PROBLEM

The optimisation task is to minimize a multicriteria goal function, while fulfilling all of given constraints. The assumed goal function is as follows.

$$f_g = \sum_{i=1}^m [t_i \cdot c(\beta_i)] + \sum_{i=1}^{m-1} [t(\alpha_i) + p(\alpha_i)], \quad (1)$$

where:

m – a number of straight segments (tacks) of a route,
 i – a number of a successive straight segment of a route,
 t_i – a time of travelling i -th segment of a route
 $c(\beta_i)$ – a discomfort factor for i -th segment of a route, resulting from a significant heel (the factor is equal to 1 for a comfortable cruise when only minor heel values occur),
 $t(\alpha_i)$ – an actual time cost of changing course,

$p(\alpha_i)$ – an additional penalty for discomfort resulting from course changes.

The assumed optimisation constraints are as follows:

- a statically limited navigable zone (landmass, shallows and navigational obstacles)
- dynamically limited navigable zone (a vessel must avoid areas where true wind speed exceeds threshold values)
- vessel's maximal tilt should not exceed a threshold value

Below a discrete model of the abovementioned problem is developed. First, it is assumed that the considered sailing area is approximated by a grid, whose cells are navigable or not navigable, based on the sailing conditions in grid points.

GRID REPRESENTATION

The grid used here is a representation of Mercator's projection. Main elements of Mercator projection are: map scale s , initial and final latitude φ_1, φ_m and longitude λ_1, λ_n , and the structural latitude φ_c , which is an arithmetic average of φ_1 and φ_m .

Another element is the linear length of longitude in minutes, denoted as l and given below as:

$$l = \frac{1852000}{s} \cdot \cos \varphi_c \quad [\text{mm}] \quad (2)$$

Next element is expanded latitude V_i for φ_i , which is given by:

$$V_i = 7915,70447' \cdot \log \tan(45^\circ + \frac{\varphi_i}{2}) - a \cdot e^2 \sin \varphi_i - [a \cdot e^4 / 3] \cdot \sin \varphi_i^3 \quad (3)$$

where:

$i = 1, 2, \dots, m$

e – is the eclipse of the Bessel earth ellipsoid

a – is the value of the semi major axis of the Bessel Earth ellipsoid expressed in minutes

Using the above we can obtain spacing between latitudes and spacing between longitude on grid determined in millimetres.

$$\Delta\varphi_{mm} = \Delta V \cdot l \quad [\text{mm}]$$

$$\Delta\lambda_{mm} = \Delta\lambda \cdot l \quad [\text{mm}]$$

Grid points P_k are selected at regular intervals $\Delta\varphi$ and $\Delta\lambda$. P_k is determined by the latitude φ_i and longitude λ_j ,

$$P_k = P_{ij} = P(\varphi_i, \lambda_j) \quad i=1,2,\dots,m ; j=1,2,\dots,n \quad (4)$$

An example route in a grid, is shown in Fig. 1.

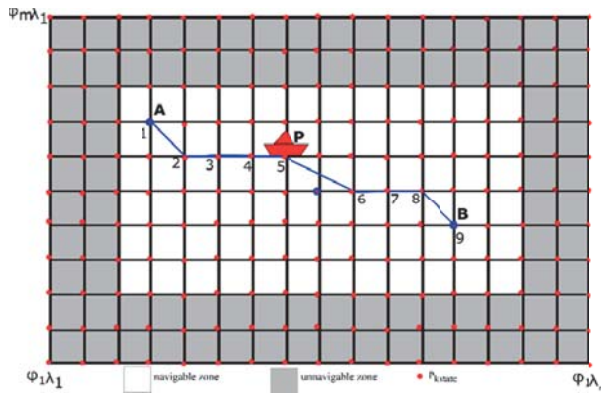


Fig. 1 The grid as navigational chart

Thus, a route can be presented as:

$$Route = \{P_1, P_2, \dots, P_z\} \quad (5)$$

where:

P_1 = A start point of a route

P_z = B end point of a route

z – the number of points in the route

Sailing vessel movement from P_k to another P_{k+1} is determined by sailing condition SC_k in point P_k , movement possibilities from P_k to P_{k+1} determined by the polar diagram of a specific sailing vessel.

Sailing conditions in each point P_k are determined by wind vector \vec{W}_k (3) and sea state data. In this article, only wind vector is considered:

$$\vec{W}_k = (w_k, \beta_k) \quad (6)$$

where:

\vec{W}_k – wind vector,

w_k – wind velocity,

β_k – true wind direction.

In the proposed model, we consider 32 possible directions of movement in a grid. They are all shown in Fig. 2.

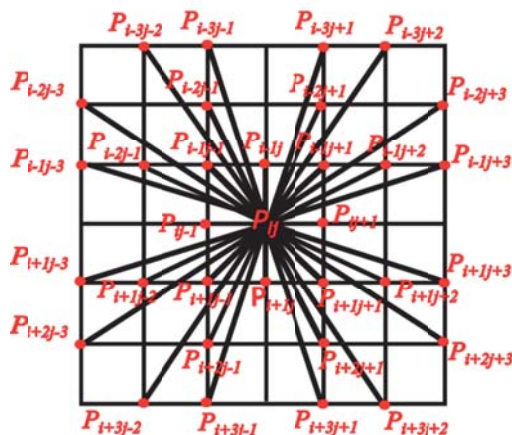


Fig. 2 Illustration of all vessel movement possibilities in a grid

A vessel's speed in each direction, depending on wind's direction and speed can be presented on a polar diagram, whose example is shown in Fig. 3.

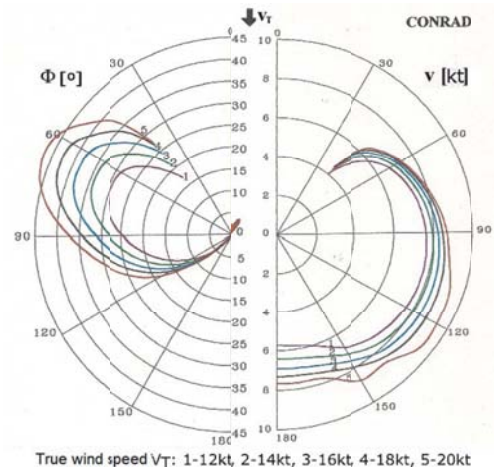


Fig. 3 Polar diagram of sailing vessel Conrad

In each point P_k there is a specific wind vector. Therefore, for a particular vessel polar diagram some of the movement directions may be eliminated due to wind's direction and speed.

Each of 32 possible movements from point P_k to P_{k+1} in Fig. 2, is associated with a number parameters including a distance and vessel's velocity. A distance is calculated according to formula (7), which is used for short distances only (less than 10 Nm):

$$distance(P_k, P_{k+1}) = \sqrt{(\varphi_k - \varphi_{k+1})^2 + (\lambda_k - \lambda_{k+1})^2 \cdot \cos((\varphi_k + \varphi_{k+1})/2)} \quad (7)$$

As for velocity between points P_k and P_{k+1} , formula (8) is used:

$$velocity(P_k, P_{k+1}) = \gamma(\vec{W}_k, \alpha_{k,k+1}) = \gamma(w_k, \beta_{k,k+1}) \quad (8)$$

where:

$\alpha_{k,k+1}$ – true course from P_k to P_{k+1} ,

$\beta_{k,k+1}$ – relative wind direction,

$\gamma(w_k, \beta_{k,k+1})$ – γ function, computing velocity value of sailing vessel based on polar diagram for wind speed w_k and direction $\beta_{k,k+1}$.

Next, we obtain the sailing time $t(P_k, P_{k+1})$ from P_k to P_{k+1} using formula (9)

$$t(P_k, P_{k+1}) = \frac{distance(P_k, P_{k+1})}{velocity(P_k, P_{k+1})} = \frac{\gamma(w_k, \beta_{k,k+1})}{\sqrt{(\varphi_k - \varphi_{k+1})^2 + (\lambda_k - \lambda_{k+1})^2 \cdot \cos((\varphi_k + \varphi_{k+1})/2)}} \quad (9)$$

Following this, we determine the discomfort factor c (from goal function (1)) for a segment between points P_k and P_{k+1} . It is done based on the following formula (10).

$$c(P_k, P_{k+1}) = 1 + \frac{(\text{heel}(P_k, P_{k+1}))^4}{10} \quad (10)$$

The predicted heel value is dependent on the specific wind vector and the chosen move direction from P_k to P_{k+1} (11):

$$\text{heel}(P_k, P_{k+1}) = \delta(\vec{W}_k, \alpha_{k,k+1}) = \delta(w_k, \beta_{k,k+1}) \quad (11)$$

where:

$\alpha_{k,k+1}$ – Course Over Ground from P_k to P_{k+1} ,
 $\beta_{k,k+1}$ – relative wind direction,

Function $\delta(w_k, \beta_{k,k+1})$ – determines the heel of the sailing vessel based on the polar diagram for the wind speed w_k and direction $\beta_{k,k+1}$.

True course of a vessel sailing from P_k to P_{k+1} is presented in Fig. 4 and is determined by formula (12):

$$\alpha_{k,k+1} = \angle(\vec{l}, \overrightarrow{P_k P_{k+1}}) \quad (12)$$

where:

\vec{l} – versor indicating north geographic,
 $\overrightarrow{P_k P_{k+1}}$ – vector created by points P_k and P_{k+1} .

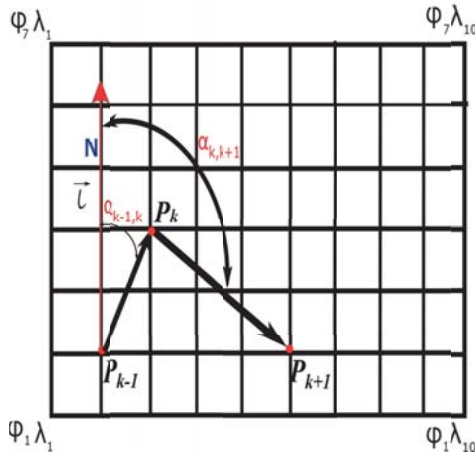


Fig. 4 Presentation of true course from P_k to P_{k+1}

A GRAPH-BASED SOLUTION OF THE PROBLEM

Once a grid representation is prepared and appropriate dependencies are derived, a transformation of a grid into a graph can be performed. A graph $G(V, E)$ is created (with V being the set of its vertices and E being the set of its edges) as follows. Each point grid point P_k becomes a graph vertex

and all possible movements between points in the navigable area constitute graph edges. In general, the graph takes into account multiple successive weather forecasts (three weather forecasts are used for the examples shown in this paper). As a result, the graph is a dynamic one, meaning that some of its parameters change in time due to predicted changes in the weather. The following parameters are associated with each of the graph's edges:

- P_k – a starting point of edge (P_k, P_{k+1});
- P_{k+1} – ending point of edge (P_k, P_{k+1});
- $\text{distance}(P_k, P_{k+1})$ – expressed in nautical miles from P_k to chosen point P_{k+1} ;
- q – a total number of available weather forecasts ($i = 1, 2, \dots, q$);
- $t(P_k, P_{k+1})$ – a table of travel times from P_k to P_{k+1} determined separately for each of q weather forecasts
- $\alpha_{k,k+1}$ – true course from P_k to P_{k+1} ;
- c – discomfort factor determined for moving from P_k to P_{k+1}

To obtain sailing time from P_k to P_{k+1} we assume that the current weather forecast is valid for both points. Then, for such weather data, sailing conditions are determined based on the polar diagram presented in . Successive weather forecasts are taken into account for successive validity periods. An illustration of applying three successive weather forecasts is shown in Fig. 5. Three route parts for which successive weather forecasts, are taken into account are shown in white, red and blue background respectively. As a result, each edge is associated with a table of travel times, each of them determined depending on a particular weather forecast, which is valid for a specific period.

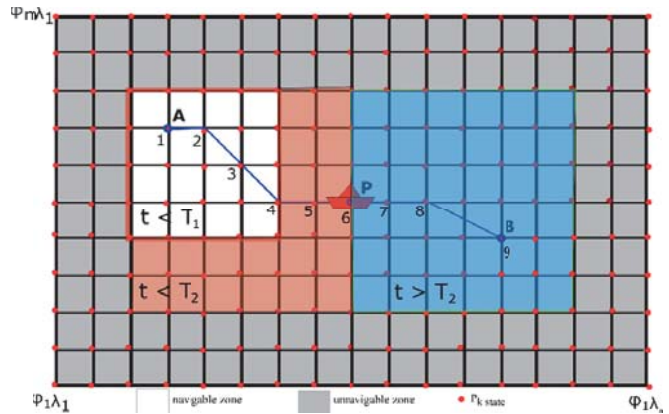


Fig. 5 Illustration of three different weather forecasts taken into account when determining a route

The total time of travelling a route is a sum of times determined for each straight segment and additional costs of changing direction. The latter is proportional to the size of course change and such a situation is shown in Fig. 6.

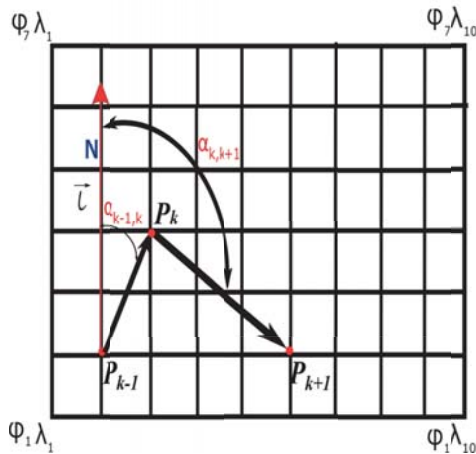


Fig. 6 A change of true course from $\alpha_{k-1,k}$ to $\alpha_{k,k+1}$ at point P_k

Once a dynamic graph is constructed, a customized version of a Dijkstra algorithm [16] is used to find the route, which minimizes the goal function (1). The algorithm that is used extends the classic Dijkstra algorithm by a number of elements, such as:

- dynamically computed weight of each edge (based on an exact time, when this edge is travelled), which takes into account sailing time and heel-dependant discomfort factor
- additional course alteration costs and penalties, which are added to the sum of weights

Since the sense of comfort is relative, the abovementioned discomfort factor is additionally dependant on a user-configured parameters reflecting the user type and routing's purpose (regatta sailing, recreational sailing, passengers cruise etc.). The estimation of discomfort factor used here is inspired by research on cruise comfort published in 7. The formula (8) from Section 3 has been calibrated to approximate discretised comfort estimation presented there.

SIMULATION EXPERIMENTS AND THEIR RESULTS

To investigate how the criterion of comfort and multiple weather forecasts affect the final route, we considered three variants of route optimisation. The first one, with discomfort factor set to 1, totally ignores comfort criterion. The second one applies heel-dependant discomfort factor and course alteration-based penalties, which stimulate longer tacks. The third one additionally applies three successive weather forecasts to compare static routing with a dynamic one.

The proposed method weather routing has been implemented as SailingAssistance application, already mentioned in 29. The polar diagram data of a sailing vessel Conrad (Fig. 3) has been used throughout the experiments. The vessel's parameters are gathered in Table 1.

Tab.1 Parameters of Conrad 1200 RT

Parameters	Value
Sail area [m ²]	80
Sail type	Bermuda rig
Length [m]	12.00
Beam [m]	4.04
Draught [m]	2
Free board [m]	1.08
Waterplane [m ²]	32.889
Lwl/Bwl [-]	3.161
Bwl/T [-]	4.844

Seven examples of determined routes are shown in Figures 7 to 13. Red arrows in each figure inform on wind direction from first weather forecast, one yellow arrow indicates the wind direction from the second weather forecast.

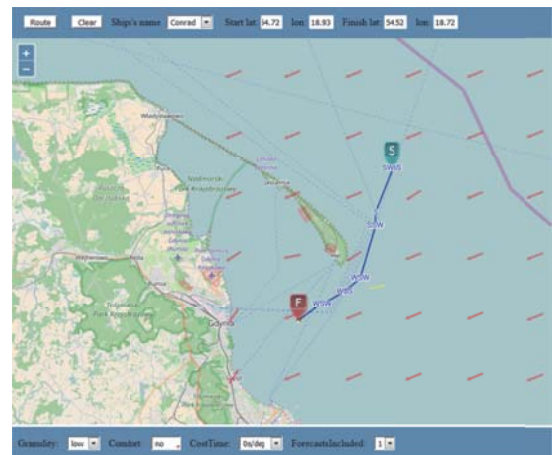


Fig. 7 Route 1, determined for the following settings: comfort criterion ignored, costs of course changes set to 0, only one weather forecast taken into account

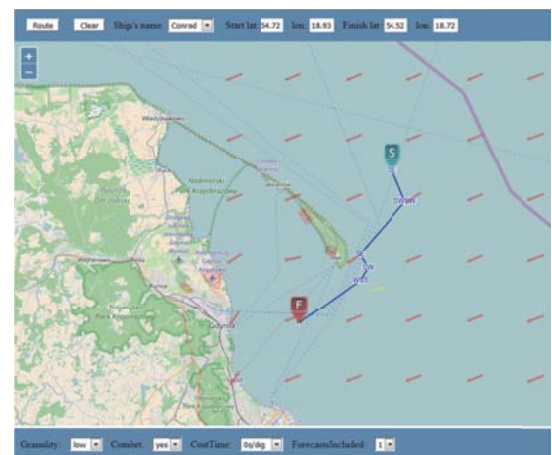


Fig. 8 Route 2, determined for the following settings: comfort criterion taken into account, costs of course changes set to 0, only one weather forecast taken into account

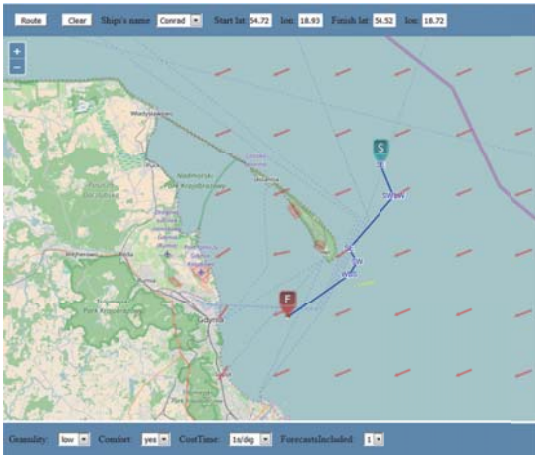


Fig. 9 Route 3, determined for the following settings: comfort criterion taken into account, costs of course changes set to 1 second per degree, only one weather forecast taken into account

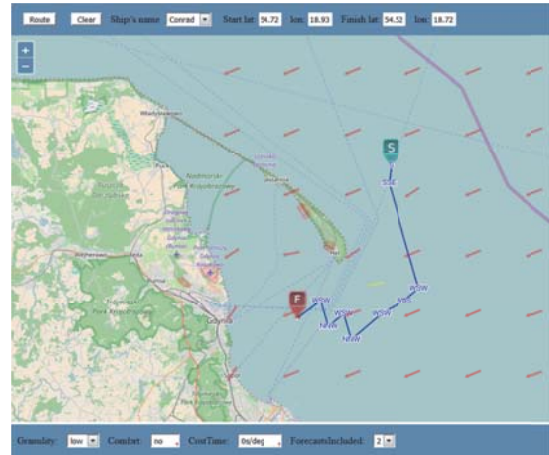


Fig. 12 Route 6, determined for the following settings: comfort criterion ignored, costs of course changes set to 0, two successive weather forecasts taken into account

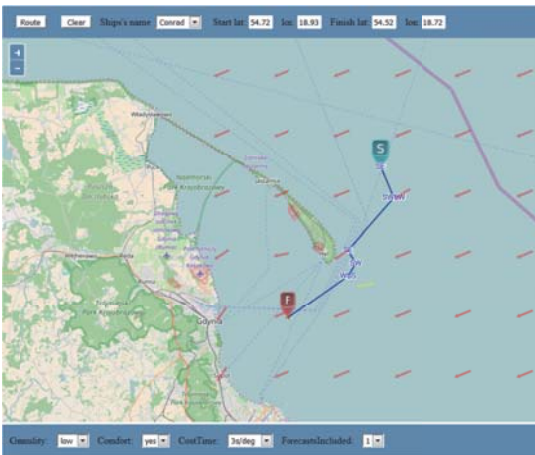


Fig. 10 Route 4, determined for the following settings: comfort criterion taken into account, costs of course changes set to 3 seconds per degree, only one weather forecast taken into account

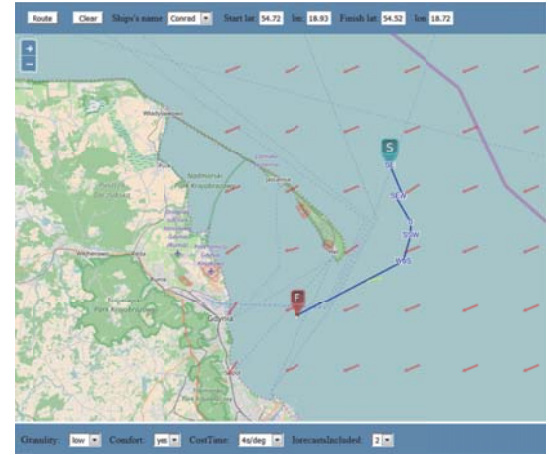


Fig. 13 Route 7, determined for the following settings: comfort criterion taken into account, costs of course changes set to 4 seconds per degree, two successive weather forecasts taken into account

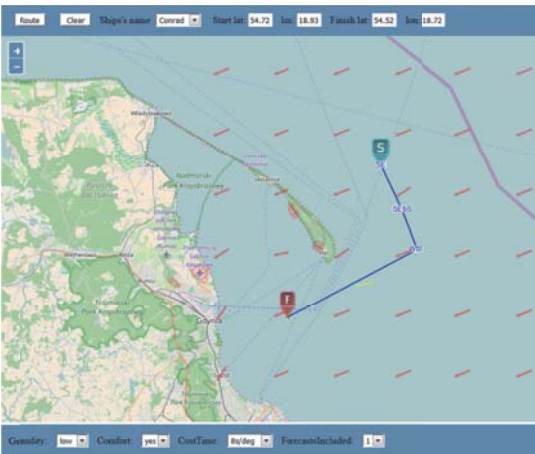


Fig. 11 Route 5, determined for the following settings: comfort criterion taken into account, costs of course changes set to 8 sec. per degree, only one weather forecast taken into account

Tab. 2 The example results

Route number	Comfort criterion taken into account	Cost of a course change [sec/deg]	Number of course changes	Number of weather forecasts taken into account	Total voyage time of a route (including assumed cost of course changes) [min]
1	No	0	5	1	121
2	Yes	0	4	1	165
3	Yes	1	4	1	168
4	Yes	3	4	1	180
5	Yes	8	2	1	231
6	No	0	8	2	286
7	Yes	4	4	2	304

CONCLUSIONS

The obtained results allow us to draw the following conclusions:

- as expected, the number of course changes is decreasing with the increased cost of a course change resulting in the longer tacks for increased costs (Figures 8 to 11),
- taking into account comfort criterion results in longer routes and increased total voyage time (Figures 7 and 8)
- applying two successive weather forecasts instead of just one results in greatly different results, if the second forecast differs significantly from the first one (Figures 8 and 12)

The above observations show that the proposed method gives largely different results depending on the user-configured values of the considered parameters. The proposed method is flexible, as it is able to take into account the particular user's needs like comfort. Finally, taking into account a number of successive weather forecasts, instead of assuming static weather, results in significantly different routes if the two forecasts differ drastically. This means that the routes determined for the static weather may in practice take more time than was predicted (total voyage time is not always reliable if static weather is assumed) or may even be unrealizable in some extreme cases. Further research on the method is planned and it is supposed to focus on applying a more accurate model of vessel's dynamics.

ACKNOWLEDGMENTS

The authors would like to thank Dr Bogusław Oleksiewicz for determining polar diagrams of sailing vessels used in this research.

BIBLIOGRAPHY

1. Arribas, F.L.P., A.L. Piniro: Seasickness prediction in passenger ships at the design stage, *Ocean Eng.* 34 (2007) 2086–2092.
2. Daniel, K., A. Nash, S. Koenig, A. Felner: Theta *: Any-Angle Path Planning on Grids, 39 (2010) 533–579.
3. Dębski, R.: An adaptive multi-spline refinement algorithm in simulation based sailboat trajectory optimization using onboard multi-core computer systems, *Int. J. Appl. Math. Comput. Sci.* 26 (2016) 351–365.
4. Dijkstra, E.W.: A Note on Two Problems in Connexion with Graphs, *Numer. Math.* 1 (1959) 269–271.
5. Disser, Y., M. Müller–Hannemann, M. Schnee: Multi-criteria Shortest Paths in Time-Dependent Train Networks, in: *Exp. Algorithms*, Springer Berlin Heidelberg, Berlin, Heidelberg, 2008: pp. 347–361.
6. Geisberger, R.: *Advanced Route Planning in Transportation Networks*, (2011) 227.
7. Johnson, B.: *Operator Guidance Based on Assessing the Wind - Heel Angle Relationship of Traditionally - Riggged Sailing Vessels*, (n.d.).
8. Jurdziński, M.: *Podstawy Nawigacji Morskiej*, Wydawnictwo Akademii Morskiej w Gdyni, 2003.
9. Kerwin, J.: A velocity prediction program for ocean racing yachts revised to February 1978, M.I.T. *Ocean Eng. Rep. Number 78-11*, MIT, Cambridge, MA. (1978).
10. Lee, T., H. Chung, H. Myung: Multi-resolution path planning for marine surface vehicle considering environmental effects, *Ocean. 2011 IEEE - Spain.* (2011) 1–9.
11. Lisowski, J.: Sensitivity of Computer Support Game Algorithms, *Int. J. Appl. Math. Comput. Sci.* 23 (2013) 439–446.
12. Lisowski, J.: ScienceDirect Computational intelligence methods of a safe ship control, *Procedia - Procedia Comput. Sci.* 35 (2014) 634–643.
13. Mannarini, G., G. Coppini, P. Oddo, N. Pinardi: A Prototype of Ship Routing Decision Support System for an Operational Oceanographic Service, *TransNav, Int. J. Mar. Navig. Saf. Sea Transp.* 7 (2013) 53–59.
14. Marchaj, C.: *Teoria żeglowania. Aerodynamika żagla, IV*, Alma-Press Sp. z o.o., Warszawa, 2016.
15. Neumann, T.: Method of Path Selection in the Graph - Case Study, *TransNav, Int. J. Mar. Navig. Saf. Sea Transp.* 8 (2014) 557–562.
16. Philpott, A., A. Mason: Optimising yacht routes under uncertainty, *Proc. 15th Chesap. Sail. Yacht Symp. Annapolis, MD.* (2001).
17. Philpott, A.B., R.M. Sullivan, P.S. Jackson: Yacht velocity prediction using mathematical programming, *Eur. J. Oper. Res.* 67 (1993) 13–24.
18. Ramalingam, G., T. Reps: On the computational complexity of dynamic graph problems, *Theor. Comput. Sci.* 158 (1996) 233–277.
19. Skriver, A.J.V., K.A. Andersen: A label correcting approach for solving bicriterion shortest-path problems, *Comput. Oper. Res.* 27 (2000) 507–524.
20. Specht, C., A. Weintrit, M. Specht, Y. Wo: A History of Maritime Radio- Navigation Positioning Systems used in

Poland, (2017).

21. Stelzer, R.: Novel Algorithms and Experimental Demonstration, De Montfort University, Leicester, 2012.
22. Stelzer, R., K. Jafarmadar: The robotic sailing boat asv roboat as a maritime research platform, Proc. 22nd Int. HISWA Symp. Yacht Des. Yacht Constr. (2012).
23. Szlapczynska, J.: Multi-objective Weather Routing with Customised Criteria and Constraints, J. Navig. 68 (2015) 338–354.
24. Szlapczynski, R.: A New Method of Ship Routing on Raster Grids, with Turn Penalties and Collision Avoidance, J. Navig. 59 (2006) 27–42.
25. Weintrit, A., P. Kopacz: Computational Algorithms Implemented in Marine Navigation Electronic Systems, in: Springer, Berlin, Heidelberg, 2012: pp. 148–158.
26. Weintrit, A., R. Wawruch: Polish Approach to e-Navigation Concept, Communications. 1 (2007) 327–335.
27. Wilcox, B.H., T. Litwin, J. Biesiadecki, J. Matthews, M. Heverly, J. Morrison, J. Townsend, N. Ahmad, A. Sirota, B. Cooper: ATHLETE: A Cargo Handling and Manipulation Robot for the Moon, J. F. Robot. 24 (2007) 421–434.
28. Życzkowski, M.: Sailing Vessel Routing Considering Safety Zone and Penalty Time for Altering Course, TransNav, Int. J. Mar. Navig. Saf. Sea Transp. 11 (2017) 49–54.
29. Życzkowski, M.: METHOD OF ROUTING SHIPS SAILING IN DEDICATED ENVIRONMENT, Annu. Navig. 24 (2017) 147–159.

CONTACT WITH THE AUTHOR

Rafał Szlapczyński

Marcin Życzkowski

Gdańsk University of Technology
11/12 Narutowicza St.
80 - 233 Gdańsk
POLAND

PERFORMANCE ANALYSIS OF A MEDIUM FREQUENCY OFFSHORE GRID FOR IDENTIFICATION OF VESSELS SAILING ON HIGH DENSITY MARITIME EUROPEAN ROUTES

Alfonso López¹

Miguel Gutiérrez¹

Andrés Ortega²

Cristina Puente³

Alejandro Morales⁴

Diego Gonzalez⁴

Emma Díaz²

¹ Catholic University of Ávila UCAV, Spain

² University of Cantabria UC, Spain

³ ICAI, Pontifical Comillas University, Spain

⁴ University of Salamanca, Spain

ABSTRACT

The paper analyses the performance of an Automatic Vessel Identification System on Medium Frequency (AVISOMEF), which works with the Grid Method (GM) on high density maritime European routes using real data and uniformly distributed data. Compared to other systems, AVISOMEF is a novelty, as it is not a satellite system, nor is it limited by a given coverage distance, in contrast to the Automatic Identification System (AIS), though in exceptional circumstances it leans towards it. To perform the analysis, special simulation software was developed. Moreover, a number of maritime routes along with their traffic density data were selected for the study. For each route, two simulations were performed, the first of which based on the uniform traffic distribution along the route, while the second one made use of real AIS data positioning of vessels sailing on the selected routes. The obtained results for both simulations made the basis for formulating conclusions regarding the capacity of selected routes to support AVISOMEF.

Keywords: Ships Identification Systems; Grid Method; Traffic Control Centre; SITOR

INTRODUCTION

The work described in the paper was preceded by several earlier research stages:

Firstly, in our past publications [1], [2], [3], [4], [5] we described the proposal of a new Automatic Identification System for Medium Wave Vessels (AVISOMEF). A brief synthesis of this system is given in this paper.

Next, we created a software tool which was able to simulate the analysed system, as we demonstrated in several publications [6], [7], [8]. We deal briefly with it in this aspect.

The objective of this work is was to perform a stress test of AVISOMEF and obtain reliable results concerning its operability.

To complete this objective, first we implemented the system to study an extensive, international route with adequate traffic density. It was, as shown, the route that surrounds Europe.

Next, we provided the information on the selected area to the maritime traffic data simulator. These data were of two types: uniformly distributed over an area, and obtained in real time. The obtained simulation results made the basis for formulating conclusions on the operability of AVISOMEF for the selected area.

THE AUTOMATIC IDENTIFICATION SYSTEM OF VESSELS IN MEDIUM WAVE BY THE GRID METHOD (AVISOMEF)

The system, whose applicability to study European high-density routes is discussed in the paper, is a result of an academic analysis of the Global Maritime Distress Safety System (GMDSS). We concluded that that system was obsolete when applying to vessels. We were aware of high investment needed and serious difficulties faced to reach world-wide agreements to remove an already existing system. So, we decided instead to improve the existing system by complementing it with new equipment which will make it a large input/output communication portal for the vessel. Combined with proper equipment and part of the already existing GMDSS equipment, it will have high potential for increasing the security and control of navigation. [2].

AVISOMEF is an automatic vessel identification system on medium frequency, MF. Compared to other systems, it is a novelty as it is neither a satellite system nor is it limited by a given coverage distance, unlike the Automatic Identification System (AIS) [9], [10], [11], though in exceptional circumstances it leans towards it.

Since the introduction of AIS, it has turned out to be an effective way of traffic control. Its only weakness is the visual range limit (more/less 30 miles), characteristic of Very High Frequency (VHF) range within which AIS works. This limit can be overcome through the use of frequencies from the High Frequency (HF) band, or by the use of some satellite-based techniques if the target does not have coverage limitations, like the system LRIT (Long-Range Identification and Tracking). The former solution is ruled out despite its global coverage, as it depends on different times of day, or even seasons. It would not be possible to reach vessels located at a smaller distance than that estimated due to the atmospheric rebound. Moreover, some side effects, like fading, for instance, could appear. The latter solution is acceptable from the technical point of view, but its disadvantage is that satellite connections are rather expensive and that the space is saturated.

AVISOMEF is the result of the symbiosis of one transmitter, four receivers – two of which include a Digital Selective-Calling system (DSC) – and a control computer, capable of supporting a determined digital mapping that should be implemented [12].

This mapping describes the maritime area to be controlled, and has the form of a grid composed of square cells of 44 nautical miles in length (thus achieving that the two furthest points from two contiguous cells are not more distant than by 100 miles, a distance which is the medium wave propagation limit). The only condition is that the message radiated at the beginning of each cell reaches the end of the following one. The grid has one row and as many columns as needed to cover the controlled mapping area. All vessels situated on this unit surface (cell) adjust the AVISOMEF transmitters and receivers automatically in order to work in a series of channels already predetermined for each cell, corresponding to the MF frequency assigned to the Maritime

Mobile Service. The information of these channels is provided to the computer integrated into the digital mapping of the controlled area [13], [14].

The system allows the ships sailing in the area inside the squares to act as receivers – and therefore acknowledgement emitters – of a message launched from the Traffic Control Centre (TCC). But they can also work as simple repeater stations for a message that is not targeted to them, making the message advance in the grid and arrive on the ship that has been called.

To avoid conflict between possible repeaters when gaining access to the respective channel, it is important to establish a relevant criterion, for example the vessel working as a repeater is the one located further to the south and further from the following cell. Any criterion can be applicable here, the only important thing is establishing one. The waiting times are controlled by the computer from the positioning information given by the G.P.S. (Global Positioning System) or another positioning system [15].

The aim of the AVISOMEF system is to identify a ship through the radio-packet launched by the Traffic Control Centre (TCC). This radio-packet is aimed at a certain ship using its call sign, the one corresponding to the digital selective calling (DSC), Maritime Mobile Service Identity (MMSI). This radio-packet moves forward from cell to cell until a certain vessel detects that it is for it, and therefore it will not work as a repeater of the message for the ships located in the following cell in the same line. Automatically, the ship in question launches a message in the opposite direction before other ships act as repeaters. This acknowledgement moves back from cell to cell until it arrives at the receiving antenna in the Traffic Control Centre from which the initial message started.

The message included in the acknowledgement is created based on a dump from a real-time data acquisition system indicative of the state of the vessel at that time, and delivers the information related to entering or leaving the cell in which the vessel has been located.

In order to run correctly, the system should be introduced to maritime routes with traffic density of at least one ship in each cell. After several simulations performed using the static level data from the maritime traffic density in the controlled area, the system is becoming operative in the studied zone.

As mentioned above, to work properly the AVISOMEF system should be introduced to maritime routes with traffic density of at least one ship per each cell. However, if at any time there is no vessel in a cell, AVISOMEF is able to auto-reset, although this situation is highly improbable. As a rule, it has to be implemented in routes with high traffic density.

The message passed from the TCC to the vessels is transmitted by the Simplex Teletype Over Radio with Forward Error Correction, SITOR-B (FEC), data communication system. This TCC sends an open collective message containing MMSI of the vessel to be located. This message also includes the MMSI of each vessel acting as a repeater in each cell, until the vessel to be located is found.

The return message from the vessel to the TCC is sent back using the SITOR with Automatic Repeat Request, SITOR-A

(ARQ), which is a peer to peer system. This return can be done in ARQ mode, as the message, until it reaches the vessel destiny, stores the identities of all stations that have acted as repeaters, so it can establish the way back.

When sending the message, each vessel knows if it is being sent, regardless the direction of the message. If the message is sent in the SITOR - B mode, in order to identify a vessel, the system listens to the assigned working channel of the next cell to check its progress two cells beyond. If, instead, there are no vessels continuing the retransmission process, the silence is understood as a gap of vessels in the next cell (one beyond). During the message return (SITOR-A), the analysis of possible gaps in cells is more evident, as each vessel is bound to pass the confirmation message to the previous vessel.

When a gap in a cell is confirmed by the identification message, the initiated reset process includes a protocol by which the verifying station transmits the message to the vessels located two cells away in the forward direction of the message, in its channel. The minimum propagation on medium frequency (MF) in the worst weather conditions is 100 nautical miles. In warm weather, it can reach 200 nautical miles, and this amount can quadruple on a summer night. As cells are squares of 44 miles in dimension, the propagation problem is solved most of the times.

If a gap is detected during the message return, the protocol establishes sending the message again, in this case to a vessel situated two cells away from the vessel which has detected the problem. However, activation of this protocol is highly improbable, as the system is designed for routes with maritime traffic density of at least one vessel per cell, a condition which is easily fulfilled on medium density routes. For the studied routes this situation cannot occur, as they have high to very high traffic density. However, if the problem persists, the protocol will perform the same action but advancing one cell more than in the previous situation. This is to take advantage of good propagation conditions in MF.

If despite all above described measures there is still a gap of vessels, the system makes decision to use AIS, leaning on it. In this case the Traffic Control Centre (TCC) is in charge of rebuilding the communication chain, locating the first vessel approached by AIS within a maximum of 30 miles, after surpassing the gap. After this, normal operation is restored.

The number of the required channels is a double of the number of cells in each grid, and the bandwidth required for provision of working channels is below 1800 Khz, within the segment assigned to the Maritime Mobile Service. This way, the communication is not affected by undesirable phenomena like fading. The segment of the required radio spectrum is not occupied by any other system [1], [2], [16]. The used modulation is F1B or J2B (digital modulation of information systems), and in regard to the transmission rate, 100 bauds are used to be in tune with the Global Maritime Distress Security System (GMDSS).

At the end of the system description, it is noteworthy that all messages are transmitted or received through antennas located at the beginning of each row of cells. The antennas are arranged in the so-called field of antennas. In Figs. 2, 3

and 4, these antennas are marked by points located at the centres of circular areas, indicative of the minimum coverage provided by each antenna in MF.

In our system, we outline basic aspects of electronic navigation (E-navigation):

- On-board systems that are able to integrate the information from different sensors.
- They should make use of electronic mapping in addition to electronic positioning systems, and make them appear integrated in the new systems.
- These systems will serve to improve the management of vessels traffic, by improving the support services from the ground and favouring data exchange.
- E-navigation will provide a platform for information transfer between vessels and between vessels and shore-based operators [17].

SOFTWARE CAPABLE OF GENERATING THE SIMULATIONS

The objective of the simulation software is to calculate the degree of operability of the vessel identification grid. This software allows modelling of different implementations of the AVISOMEF system, making performance calculus by means of uniformly distributed data [18] or real AIS data, along the selected maritime routes.

For the implementation of the software, we have used the architecture proposed in Figure 1. This is a client/server architecture, where the client is the simulation programme. It uses an external server, Web Map Services (WMSs) [19], [20], and a database manager system (DBMS) storing the AIS data. The WMS server provides the mapping to place the elements for the simulation via the OSM service of the standard, while the DBMS stores the maritime traffic data in the studied days. In the cases when the uniform distribution for maritime traffic routes is used, having access to the DBMS is not necessary.

The simulation software consists of four main modules:

- Mapping module, which represents all elements of the simulation.
- Representation Module, which overlaps the mapping and the layers by adding elements of AVISOMEF implementation. For that purpose, three components are used, which are:
 - Maritime traffic density: obtained from the database for each time interval for which the system wants to perform the calculus, or introduced by the user as uniformly distributed data.
 - Grids: elements that use the Automatic Vessel Identification System and the Grid Method (AISGM) for the division of the maritime space.
 - Traffic Control Centres (TCC): each centre is in charge of one or more grids of the simulation environment.
- Calculus Module, which performs all required calculus to evaluate the performance of AVISOMEF response times, number of identified vessels, etc.

- Event Controller Module, which enables the interaction of all user events with the application.

Depending on the user interaction with the application, the system displays a given mapping obtained from the external OSM WMS service. The user can include different elements conforming AVISOMEF, and the representation module will display both the elements of the system and the mapping where placed. Finally, when the user concludes that the implementation is correct, he performs the calculus to evaluate the performance according to the proposed design. The calculus module includes validation of the implementation, done by checking some required features of any implementation within these requirements. For example, it checks whether all grids are controlled by TCC, or whether the designed grids belong to the maritime traffic routes, etc. [6], [7] [8] [18], [21].

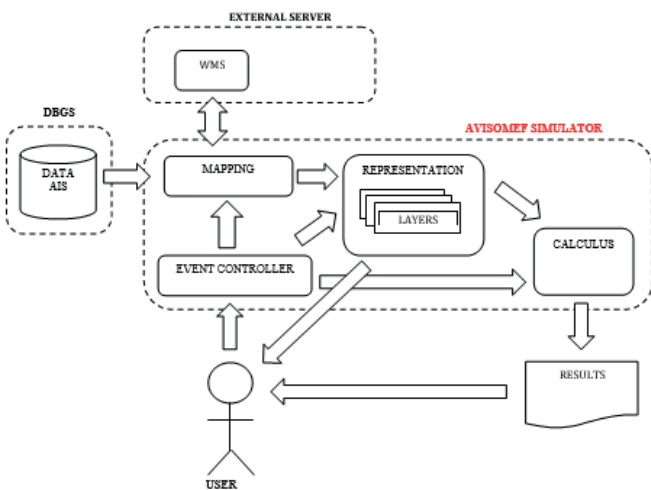


Fig. 1. Software architecture of the AVISOMEF simulator

GRID IMPLEMENTATION

Figure 2 shows in detail different segments of the European maritime route to be implemented by AVISOMEF, and their traffic densities, uniformly distributed vessels per day, being part of the route between two consecutive vertices [18].

The route selected for the analysis can be arbitrary. We have chosen this one firstly because certain density requirements that seemed a priori to be appropriate for the study were fulfilled, and secondly because of its European, international and extensive character.

The objective of the involved TCC is to identify the vessels sailing in each cell belonging to the controlled grid [3], [4], [5].

In the simulator, the layout of different grids is hand-laid. However, in real cases when the system is established in a given area, the grid formation is made based on exact coordinates.

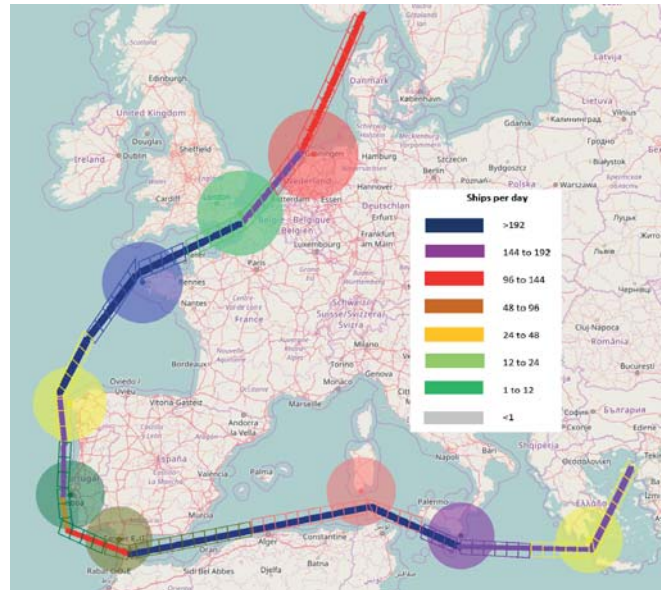


Fig. 2. European maritime routes to be implemented by AVISOMEF, indicating the traffic density uniformly distributed per segment. All segments have traffic density greater than 96 vessels/day

Figure 3 shows AVISOMEF implementation using real maritime traffic data obtained by AIS.



Fig. 3. First snapshot of European maritime traffic routes in which AVISOMEF is going to be implemented through non-uniformly distributed data

As seen in Figure 3, we have used nine TCC's for implementing AVISOMEF in the main European maritime routes. Each route has two grids associated to control the maritime traffic in that area. In Figure 2, TCC's are differentiated by circles of different colours, indicating the coverage area in the indicated medium wave frequency. The scope for this frequency range is 100 miles in the least favourable situations, and is larger than the dimensions of the first cell of the grid (44 miles), controlled by TCC, and covering the first cell in both directions.

Figure 3 shows a snapshot selected from thousands of them used by the simulator. It worked with 27.000 snapshots, each

composed by hundreds of AIS data, indicative of the position of the vessels at the given time in the study area. In the North African Mediterranean route, vessels suddenly disappear and reappear near Sicily. This is because countries in that zone do not collect AIS data, or at least do not share them for monitoring. The data for this area are obtained by European receivers, thanks to good propagation conditions at that moment. This last phenomenon can be observed in Fig. 4.

Gaps can also occur in the areas without the previously mentioned problems, for example between Finisterre and Brest, see Fig. 4, where a gap can be observed in the intermediate cells. It does not mean that there are no vessels in that area, it only means that no AIS information has been received by any receiver, as all of them are at a distance greater than 30 miles, out of the AIS range. However, in other times when the propagation is better, the same area can be full of vessels.

These are the reasons why in high density maritime routes we can find some ‘hypothetical’ gaps of vessels, despite knowing that there must be plenty of them at that time and area, as they are monitored before and after the gap. Obviously, not all of them end their journey at this midpoint.

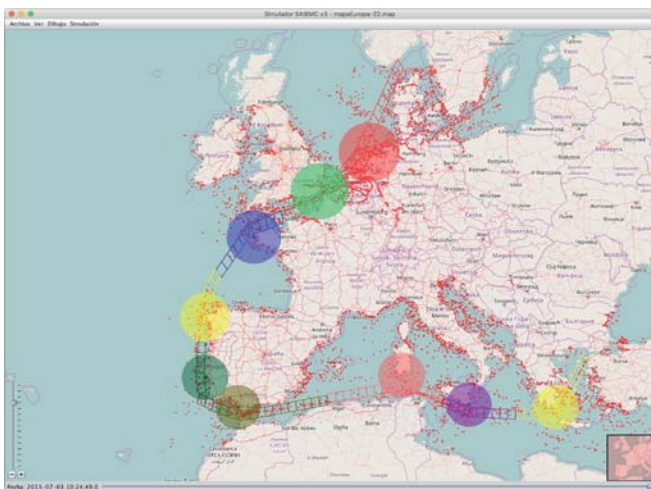


Fig. 4. Second snapshot of European maritime traffic routes in which AVISOMEF is going to be implemented through non-uniformly distributed data

RESULTS

Table 1 displays the obtained results through uniformly distributed data, beginning the analysis from TCC No. 1, which is the one located most northerly up to Rotterdam, finishing orderly with TCC No. 9 located at the south of Greece.

Each TCC has control over two previously assigned grids, built by one row of cells represented in the same colour as the belonging TCC. They are named as A and B, following the path previously explained for the TCC.

The uniformly distributed data are presented through each segment, being one of two parts of the route between two consecutive vertices.

The first column in Table 1 belongs to Traffic Control Centres (TCC), nine in all. As previously said, the first TCC is located further north, and from there, following the set direction, the second is in the English Channel, third in Brest, fourth in Finisterre, fifth in Lisbon, sixth in Cadiz, seventh in Sardinia, eighth in Sicily, and the final ninth TCC is in the south of Greece.

The second column indicates the two grids associated with each TCC. Named “A” and “B”, they always follow the set direction, being first A and then B. In this column, we can also see the number of cells per grid.

The third column displays the information about the highest traffic density in the area of interest. This column is divided into two sub-columns, one of which showing the number of vessels per day in the portion of segment controlled by the TCC, against the number of vessels per day and cell in that portion of segment. The other sub-column displays the number of vessels per day existing in the segment between two consecutive TCC’s. This information is relevant as a segment is often not covered by a single TCC, but two, so this data indicates the total number of vessels existing between two consecutive vertexes (segment), as the result of addition of all vessels existing in each of the two grids composing the segment. These two grids are not controlled by the same TCC, and this situation is repeated, except for TCC No. 1, grid A and TCC No. 9, grid B, whose segments are controlled by a single TCC.

The segments in which traffic densities reach the maximum provide data regarding their minimum traffic density, but not their maximum (Fig. 2). That is why in Table 1 some cells have the message “No data on maximum density in the segment”.

Noteworthy is the case of grid B associated with TCC No. 5. It is composed of more than one segment, and in this case the calculus takes into account the maritime traffic density data for the first segment, and then adds the portion of segments composing this grid.

The fourth column displays the information about the minimum traffic density in that area, following the same criteria as for the previous column.

The fifth and last column displays the operability of each grid for the maritime traffic density uniformly distributed along the segment. It was determined based upon the existence of at least one vessel per cell.

Tab. 1. Conclusion on the operability of AVISOMEF in the routes controlled by TCC implemented by uniformly distributed data

TCC	GRID	HIGHER TRAFFIC DENSITY		LOWER TRAFFIC DENSITY		OPERABILITY of each grid (based upon the existence of at least one vessel per cell)
		Number of vessels/day in the portion of segment controlled by TCC against the number of vessels/day per cell.	Total number of vessels in the segment between two consecutive TCC's.	Number of vessels/day in the portion of segment controlled by TCC against the number of vessels/day per cell.	Total number of vessels in the segment between two consecutive TCC's.	
N° 1	A (8 cells)	144/18	144	96/12	96	100%
	B (3 cells)	96/32	192	72/24	144	100%
N° 2	A (3 cells)	96/32		No data on maximum density in the segment		72/24
	B (5 cells)	No data	96/19		100%	
N° 3	A (4 cells)	No data	No data on maximum density in the segment	96/24	192	100%
	B (6 cells)	No data		115/19		100%
N° 4	A (5 cells)	No data	192 vessels in the segment	76/15	144	100%
	B (3 cells)	96/32		72/24		100%
N° 5	A (3 cells)	96/32	96+144=240 vessels in two segments between both TCC's	72/24	48+96=144 vessels in two segments between both TCC's	100%
	B (7 cells)	1° tramo: 96/24 2° tramo: 86/28		1° stretch: 48/12 2° stretch: 57/19		100%
N° 6	A (2 cells)	57/28	No data on maximum density in the segment	38/19	192	100%
	B (11 cells)	No data		100/9		100%
N° 7	A (10 cells)	No data	No data on maximum density in the segment	91/9	192	100%
	B (5 cells)	No data		120/24		100%
N° 8	A (3 cells)	No data	192	72/24	144	100%
	B (6 cells)	104/17		78/13		100%
N° 9	A (5 cells)	87/17	192	65/13	144	100%
	B (7 cells)	192/27		144/20		100%
PERFORMANCE IN LOW AND HIGH DENSITY		100 %		100 %		TOTAL PERFORMANCE
						100%

Based on these results, we can conclude that the chosen maritime routes are suitable for AVISOMEF implementation, and due to this we have performed another simulation with real data. To do so, we introduced to the AVISOMEF simulator selected pieces of AIS information, uniformly distributed throughout the year, of the six odd months of 2014 with a refresh rate of 10 minutes, in order to be representative of the total traffic in the area. The results are presented in Table 2. The maximum and minimum data of the detected targets are presented, as well as the average of all processed data. This last value is used to corroborate the conclusion previously obtained by means of uniformly distributed data and related to the operability of the system on each grid.

In Table 2, the numbers of grids are displayed that should work simultaneously in the same area to hold the existing traffic in that zone, in order to perform at least one identification per vessel and per cell. Along with this information, the numbers of channels needed for the grids

to operate in the same area (double numbers of cells) are also shown.

The first column in Table 2 displays nine TCC's following the previously explained order.

The second column indicates two grids associated with each TCC. Named "A" and "B", they always follow the set direction, being first A and then B. In this column, we can also see the number of cells per grid.

The third column shows the maximum and minimum number of vessels recorded in the grid during the studied time interval.

The fourth column displays the average of vessels per grid.

The fifth column shows the number of grids implemented in each controlled area, and the number of used channels. When the number of vessels exceeds a given value in the grid of interest, the system estimates that it is unable to give identification per vessel and per staying in cell. In this case, a second grid, identical to the first one but with different

working channels, is automatically established. Consequently, if the number of vessels exceeds a maximum value, the system directs the next vessels entering that area to work with the first duplicated grid for that area. This way, they are monitored without excessive delays, which otherwise would lead to situations when vessels pass cells without being identified by the system in more than one occasion.

When establishing the maximum number of vessels that a grid can hold before the duplicated grid of the area starts to work, the average speed established for the vessels in that area plays an important role. As shown before, to verify whether a route is suitable for AVISOMEF, an in-depth study of the subject is required. However, if it is difficult to obtain an average speed, the best option is to set a high average speed value in the system to make sure that it functions properly. When this value is set too high, the system will just perform more identifications than needed to monitor each vessel.

When the level of maritime traffic in the area decreases, the duplicated grid is removed, redirecting the new vessels entering the zone to the original grid.

The number of channels is calculated by multiplying the number of cells of each grid by two. It is important to know how many grids assigned to each zone have been working, if it is more than one, the number of channels is to be calculated as the double number of cells multiplied by the number of grids used for the area.

As previously shown, AVISOMEF just had to activate the first duplicated grid in some occasions, just in the area controlled by TCC No. 1, grid A.

The sixth column indicates the average number of vessels existing in each grid's cell.

Based on the previous data, in the seventh and last column the established operability degree of AVISOMEF per grid is presented. 100% is not reached only in TCC No. 7, grid A. As seen before, this is the area belonging to the major North African maritime traffic routes. The traffic existing in this area is has not been monitored because the countries in this area do not collect AIS data, or at least do not share them for monitoring.

The data from vessels in this area, appearing at certain times, are collected by European receivers thanks to good propagation conditions.

Note that the other area in which monitoring of the existing traffic is incomplete, but for different reasons, is between Brest and Finisterre (TCC No. 3, grid B and TCC No. 4, grid A). Nevertheless, full operability has been obtained for this area, despite the above inconvenience.

In both situations, the system performs a linear analysis, taking into account that the input and output of the traffic have similar values. For this reason, the 100% operability is estimated in the European area, and a little lower, but still very good, in the North African zone.

Tab. 2. Conclusion on the operability of AVISOMEF in the routes controlled by TCC implemented by real data

TCC	GRID	MAXIMUM AND MINIMUM NUMBER OF VESSELS IN THE GRID	AVERAGE OF VESSELS IN THE GRID	IMPLEMENTED GRIDS AND USED CHANNELS	NUMBER OF VESSELS PER CELL EXISTING IN EACH GRID WITH AVERAGE DATA	OPERABILITY of each grid (based upon the existence of at least one vessel per cell)
N° 1	A (8 cells)	123/38	79	2/32	9	100%
	B (3 cells)	120/69	95	1/6	31	100%
N° 2	A (3 cells)	129/70	96	1/6	32	100%
	B (5 cells)	166/93	135	1/10	27	100%
N° 3	A (4 cells)	119/48	88	1/8	22	100%
	B (6 cells)	113/6	36	1/12	6	100%
N° 4	A (5 cells)	52/15	27	1/10	5	100%
	B (3 cells)	40/28	27	1/8	9	100%
N° 5	A (3 cells)	37/26	31	1/6	10	100%
	B (7 cells)	62/43	53	1/14	7	100%
N° 6	A (2 cells)	31/10	16	1/4	8	100%
	B (11 cells)	106/49	71	1/22	6	100%
N° 7	A (10 cells)	24/0	9	1/20	0,9	90%
	B (5 cells)	80/22	37	1/10	7	100%
N° 8	A (3 cells)	83/22	39	1/6	13	100%
	B (6 cells)	67/1	19	1/12	3	100%
N° 9	A (5 cells)	17/5	11	1/10	2	100%
	B (7 cells)	64/0	35	1/14	5	100%

CONCLUSIONS AND FUTURE RESEARCH

To conclude, we can state that it is possible to establish traffic control by means of AVISOMEF for the selected European maritime routes, with the highest degree of operability.

This implies that we can establish a real-time control without using satellite techniques. This control is much cheaper, and automatic, for more than 90% of vessels sailing throughout European routes. It can be extended to a large number of vessels identified by the system and their surroundings, being previously detected by electronic devices located onboard.

Finally, it is important to state that there are more possibilities to explore Radio Systems installed aboard vessels. As demonstrated, little-changes open up possibilities to set up a new system to help navigation. The next step will be analysing the worldwide maritime routes, to select those that, by their traffic density, are able to support the system and allow its proper implementation.

REFERENCES

1. A. López, A. Ortega, M. Gutiérrez, F. Blanco, C. Puente, "Automatic identification system of vessels using the grid method", *Journal of Maritime Research*, vol. 9, no. 1, pp. 71-76, 2012.
2. A. López, "Planteamiento de un nuevo sistema, resultado de la interacción de GMDSS con otros dispositivos", *Academica Española*, 2012.
3. A. López, M. Gutiérrez, A. Ortega, F. Blanco, M. Graña, "Proposal of a medium frequency offshore grid for identification of vessels sailing in high density maritime Spanish routes", *OCEANS 2011 IEEE - Spain*. 2011.
4. A. López, M. García, F. Herráez, F. Blanco, "Análisis medioambiental derivado de un control en tiempo real de las rutas marítimas españolas fundamentales", *CONAMA 10 Congreso Nacional del Medio Ambiente*, 2010.
5. A. López, M. Gutiérrez, F. Herráez, "Constitución de una red marítima en onda media capaz de albergar el tráfico necesario para la identificación de buques que naveguen por rutas canarias". *XVIII Congreso Nacional de Ingeniería Mecánica*, 2010.
6. M. Gutiérrez, A. López, A. Morales, V. Carro, "Arquitectura software para el desarrollo de aplicaciones de control de tráfico marítimo", *6ª Conferência Ibérica de Sistemas e Tecnologias de Informação*, 2011.
7. M. Gutiérrez, "Aplicación de modelado de un sistema de identificación de buques", *Académica Española*, Madrid. 2011,
8. M. Gutiérrez, A. López, F. Herráez, C. Puente, S. Zubelzu, "Aplicación para el estudio de implantación de un sistema no satelitario de identificación de buques", *Revista Iberoamericana de Automática e Informática industrial*, vol. 9, pp. 244-248, 2012.
9. G.K. Høye, T. Eriksen, B.J. Meland, B.T. Narheim, "Space-based AIS for global maritime traffic monitoring", *Acta Astronautica*, vol. 62, no. 2-3, pp. 240-245, 2008.
10. K. Inoue, H. Usui, K. Hirono, W. Sera, "A ship monitoring system using a communication satellite for maritime safety", *Maritime Security and MET*, pp. 205-217, 2005.
11. J.L. Larrabel, M.A. Gómez, I. Sotés, F.J. Alvarez, M.C. Rey, V.E. Mielgo, I. Sotes, Basogain, "Vessel condition monitorization through satellite using principal X. component analysis", *Journal of Maritime Research*, vol. 7, no. 3, pp. 3-14, 2010.
12. R. Hekmat, P. Van Mieghem, "Connectivity in wireless ad-hoc networks with a log-normal radio model", *Mobile Networks and Applications*, vol. 11, no. 3, pp. 351-360, 2006.
13. I.F. Akyildiz, X. Wang, W. Wang, "Wireless mesh networks: A survey", *Computer Networks*, vol. 47, no. 4, pp. 445-487, 2005.
14. Y. Ge, P. Kong, C. Tham, J.S. Pathmasuntharam, "Connectivity and route analysis for a maritime communication network", *6th International Conference on Information, Communications and Signal Processing, ICICS*, 2007.
15. A. López, "La medida del tiempo. Un aliado para conseguir una relación más sostenible entre el tráfico marítimo, el medio ambiente y la economía", *IX Congreso Nacional del Medio Ambiente (CONAMA IX)*, pp. 978, 2009.
16. P. Santi, D.M. Blough, "The critical transmitting range for connectivity in sparse wireless ad hoc networks", *IEEE Transactions on Mobile Computing*, vol. 2, no. 1, pp. 25-39, 2003.
17. D. Patraiko, "The Development of e-Navigation", *International Journal on Marine Navigation and Safety of Sea Transportation*, vol. 1, no. 3, pp. 257-260, 2007.
18. United States Coast Guard, "Amver Density Plot Display". Available: <http://www.amver.com/Reports/DensityPlots>. 2017, May, 15.
19. United Nations, Statistical Division 2000, "Handbook on Geographic Information Systems and Digital Mapping". Homepage of United Nations Publications, On line. Available: http://unstats.un.org/unsd/publication/SeriesF/SeriesF_79E.pdf. 2011, March, 15.

20. Open Geospatial Consortium (2006), OpenGIS® Web Map Server Implementation Specification. Available: <http://www.opengeospatial.org/standards/wms>. 2017, May, 15.
21. S. Wen, P. Kong, J. Shankar, H. Wang, Y. Ge, C. Ang, "A novel framework to simulate maritime wireless communication networks", Oceans Conference Record (IEEE), 2007.

CONTACT WITH THE AUTHORS

Alfonso López

Catholic University of Ávila UCAV
SPAIN

Miguel Gutiérrez

Catholic University of Ávila UCAV
SPAIN

Andrés Ortega

University of Cantabria UC
SPAIN

Cristina Puente

ICAI, Pontifical Comillas University
SPAIN

Alejandro Morales

University of Salamanca
SPAIN

Diego Gonzalez

University of Salamanca
SPAIN

Emma Díaz

University of Cantabria UC
SPAIN

AN INNOVATIVE STEERING SYSTEM FOR A RIVER PUSH BARGE OPERATED IN ENVIRONMENTALLY SENSITIVE AREAS

Teresa Abramowicz-Gerigk

Gdynia Maritime University, Faculty of Navigation, Department of Ship Operation

Zbigniew Burciu

Gdynia Maritime University, Faculty of Navigation, Department of Ship Operation

Jacek Jachowski

Gdynia Maritime University, Faculty of Navigation, Department of Ship Operation

ABSTRACT

The paper presents an innovative steering system for a river push barge dedicated for operation in environmentally sensitive inland waterways. Development of the inland waterborne transport in Poland is dependent on the exploitation of rivers which can be adapted to navigation in the limited range because a high percent of their length is classified within special environment protection areas of Natura 2000 network. This is now the main reason that their better exploitation cannot be obtained without an introduction of a new generation of waterborne environment friendly inland units. In naturally winding rivers with differing and rapidly changing depths and widths it is important to equip a push barge with an efficient steering system that has a low environmental impact. The innovative steering system proposed in the paper is composed of main steering devices located at the pusher stern, auxiliary steering devices installed on the barge bow and a mechanical coupling system.

Keywords: river push barge, manoeuvring area, bow rotor, integrated steering system

INTRODUCTION

The development of sustainable inland waterborne transport (IWT) covers the improvement of the complex framework of inland navigation, hydraulic engineering and protection of natural environment. Many years of negligence in river training and maintenance are the reasons that a big part of inland waterways has become wildlife areas. The main bottle necks in inland navigation on Polish rivers are the restricted water depth, different flow rates at different water levels; restricted fairway width on river bends and the Natura 2000 special environment protection areas located along the rivers.

The areas length within the Natura 2000 network as a percent of the total river length for Odra and Vistula are

73.46% and 30.86% respectively [5]. All the factors influencing environmental impact of inland shipping in special protection areas should be considered along with the natural river processes which can increase or decrease the influence of ship traffic.

Polish rivers can be adapted for navigation in limited range and their better exploitation can be obtained mainly by the introduction of a new generation of waterborne inland units along with integrated traffic management and logistic systems [2, 14]. The regular navigation can decrease the amount of required maintenance works – dredging, winter ice-breaking and support flood protection.

In Poland the most important issue is now IWT on Lower Vistula River due to untapped transport potential [2]. The innovative solutions in IWT will be developed

and implemented on the market i.e. within the frames of the research and development projects included in “The Lower Vistula” horizontal project venture within “Smart Specialisation of Pomerania Region – offshore technology, ports and logistics” Regional Operational Programme for the Pomeranian Voivodeship for the period 2014-2020.

The first project is “Research, design and construction of a prototype of an innovative push train: pusher with hybrid propulsion with innovative ship’s boat with changing draft and fuel cells power supply, innovative pushed barge for heavy oversized goods transport with an anti-heeling system for ro-ro operations and bow thruster (with dimensions matched the Przegalina lock)”.

The priorities formulated in the resolution “Assumptions for the plans of inland waterways development in Poland in the years 2016-2020 with the 2030 perspective” [6] included i.e. development and implementation of E-30 waterway into the international waterways network, improvement of navigational conditions on the Vistula River, preparation for the modernization of E-40 and E-70 waterways and implementation of RIS (River Information System). The Vistula River Warsaw-Gdansk section will become an international waterway until 2030. After the first stage of modernization of the Lower Vistula the transport of goods is expected to reach the level 7.8 – 12 mln tonnes/year [16]. The fast growth of the handling capacity of the container terminals in Ports of Gdansk and Gdynia can speed up this process. The oversized heavy goods transport is the main demand for the Middle and Lower Vistula River IWT at the moment.

The investigations presented in the paper were conducted in order to define possibilities of handling a pushed barge train on natural rivers and obtain an early estimate of the manoeuvrability of the river push barge equipped with bow rudders.

RIVER BARGE TRAINS OPERATED IN THE MIDDLE AND LOWER VISTULA RIVER

The maximum dimensions of vessels and pushed convoys which may be accommodated are length, breadth, draft. These are dependent on river parameters and air draft depends on height of the space under bridges. All sections of the Lower Vistula River are classified as free flowing. The section from Bydgoszcz to Wloclawek (772.4 km – 674.8 km) requires the lowest values of ship draft - about 0.8 m, depending on the water level (LWL – Low Water Level) [7].

Tab.1. The main dimensions of locks on Gdansk –Warszawa section of E-40 waterway

Lock	Przegalina	Wloclawek
Length [m]	188.37	115.00
Width [m]	11.91	12.00
Depth at sills [m]	3.60 / 3.28 LWL	3.50

Barge train formations operated on the Middle and Lower Vistula River are different combinations of pushing-towing units. The main dimensions of the barges operated in these pushing-towing units, described by Rabant et al. [15] are presented in table 2.

Tab. 2. Main dimensions of the barges used in pushing-towing units on the Lower Vistula River

Main dimensions	Barge type			
	BP-1000	BP-500 Zegluga Wyszogrodzka	BP-500 Zegluga Bydgoska	BP-400
Length [m]	73.0	56.0	44.0	35.0
Breadth [m]	10.2	10.2	8.0	8.5
Draft [m]	0.9	0.9	0.9	0.7

A predominantly used push barge consists of a pusher and barge with couplings made of cable ropes, winches and hydraulic cylinders with the coupling force 800-1200 kN. An example of the coupling used for the container push barge on the Lower Vistula River in April 2017 [9] is presented in figure 1.



Fig. 1. Push barge – pusher boat “Hetman” and barge “Galar-2” coupling system including cable lines and hydraulic cylinders, on the Lower Vistula River in April 2017

The operability of a new design environment friendly push barge depends on its good propulsive and manoeuvring properties both in shallow and deep water conditions. The push barge should generate waves of acceptable significance to reduce the influence on river banks, and low velocity propeller thrust streams to avoid river-bed scouring.

In naturally winding rivers with differing and rapidly changing depths and widths it is important to equip a push barge with an efficient steering system having low environmental impact.

THE INNOVATIVE PUSH BARGE BOW STEERING SYSTEM

The innovative steering system proposed in the paper is composed of auxiliary steering devices installed on the barge

bow, dynamic coupling system and main steering devices located at the pusher stern.

BOW ROTORS AUXILIARY STEERING DEVICE

The conventional auxiliary steering devices are mainly bow thrusters. They produce high velocity thrust streams and their efficiency drops sharply at ship speed above 2 m/s in open water conditions (Fig. 2).

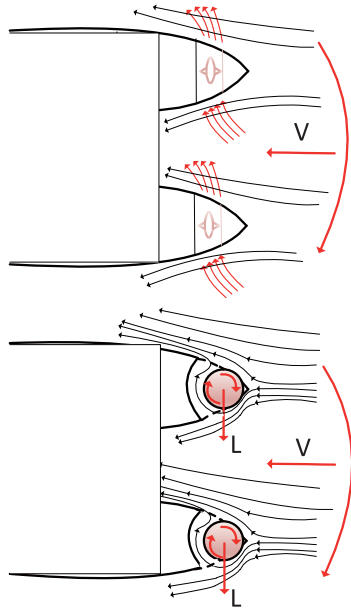


Fig. 2. Effects of barge bow steering systems: 1 – bow thrusters; 2 – bow rotors, v – inflow speed, L – hydrodynamic lift force [3]

The rotor bow rudder system based on the Magnus effect results in a significant enhancement in manoeuvrability. The rotating cylinder in oncoming water currents produces a lift force larger than a conventional rudder.

The most effective operational configuration without the ventilation effects influence is the configuration with the rotor extruded below the bow. The existing vertical and retractable versions of rotor bow rudder [10, 20] are not suitable for shallow water conditions, therefore the steering system of rotors integrated with the barge bow has been proposed.

RESISTANCE OF A PUSH BARGE WITH DIFFERENT CONFIGURATIONS OF BOW ROTORS

Barges with vertical or slightly inclined stems have greater resistance than the streamlined forms [12, 18], however at this stage of investigations, the simple straight inclined bow which could be modified to test different configurations of bow rotors has been assumed.

To determine the ship manoeuvring performance the existed IMO criteria based on the standard trials are used in general. The criteria are not designed specifically for pusher-barge or tug-barge formations and the assumptions should be made regarding the method of their application. Liu et al. [13] proposed the standard maneuvers and parameters for

the evaluation of inland push barge maneuverability. The length of the ship originally defined as the length measured between perpendiculars was assumed for the pusher-barge combination as the distance measured between the aft perpendicular of the pusher and the forward perpendicular of the barge.

The resistance of the barge with straight inclined bow without rotors has been compared with the resistance of the barge with central bow skeg with rotor, twin bow skegs with rotors, twin cylindrical bulbs without and with rotors. The hull forms of the first three configurations and their resistance predicted using CFD FlowVision solver [22] at 10 km/h speed are presented in figures 3-6. The main particulars of the push barge model are presented in table 3.

Tab. 3. Main dimensions of the push barge model used in CFD simulation for resistance prediction

Dimension	Push barge model	Push barge
Length [m]	4.966	100
Breadth [m]	0.55	11
Draft [m]	0.06	1.2
Buoyancy [kg]	160	1280000
Model scale	1:20	1:1

The 3-dimensional CFD flow simulations were performed in full scale, based on the reverse flow method using overlapping meshes. The VOF method in the free surface modelling and semi-empirical $k-\epsilon$ turbulence model were applied.

For the purpose of the simulation the calculations were carried out in the domain of discretized structural mesh consisting of 1.4 million cells.

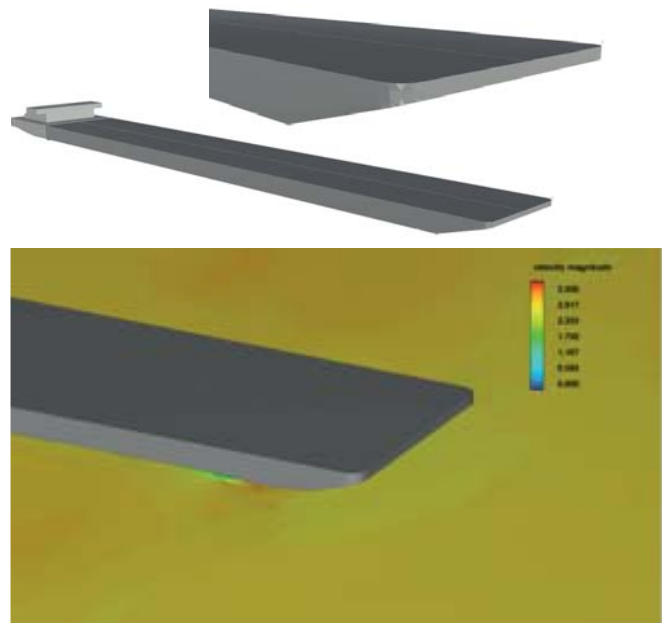


Fig. 3. Push-barge with a straight inclined bow

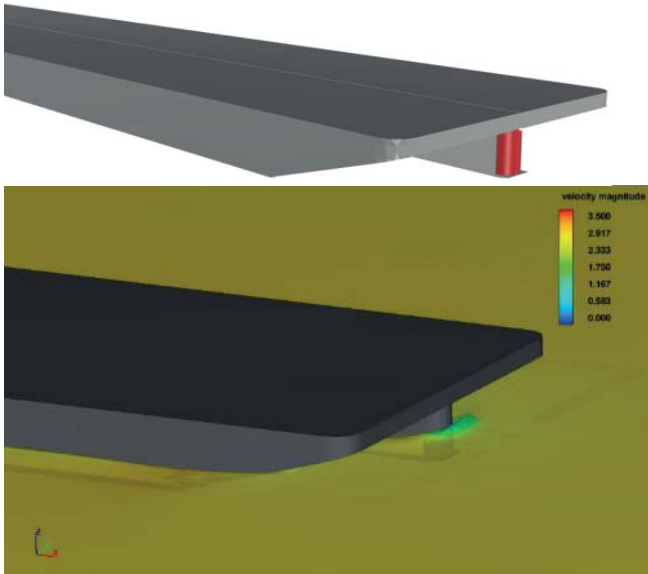


Fig. 4. Push-barge with a central bow skeg and rotor

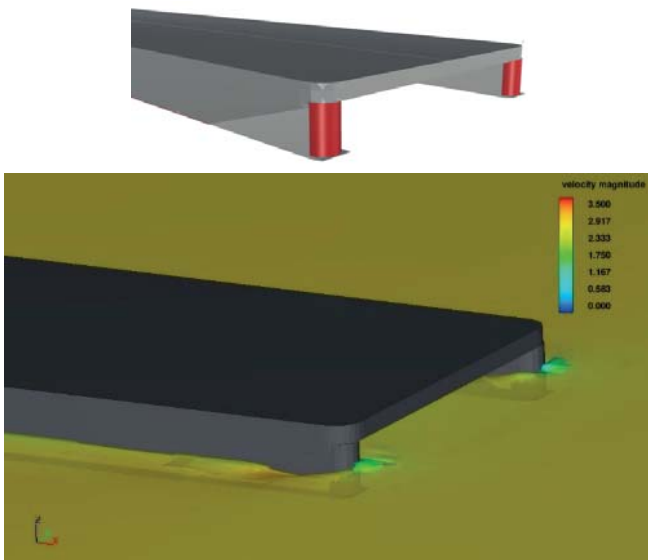


Fig. 5. Push-barge with twin bow skegs and rotors

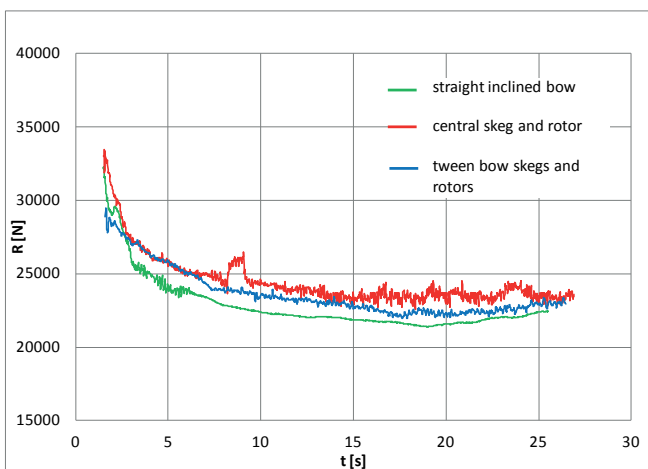


Fig. 6. Resistance of the push barge with different bow configurations at 10 km/h speed: R – resistance, t – time of simulation

The twin bow rotors integrated with cylindrical bulbs give much smaller steering force and almost the same resistance in shallow water (Fig. 7). This observation suggests that the favourable configuration from the point of view of push barge hull resistance is the bow with twin bow skegs and rotors.

The resistances at 15 km/h in 5 m shallow water at 0.6 critical speed assumed as square root of the product of water depth and ship speed are presented in figure 7.

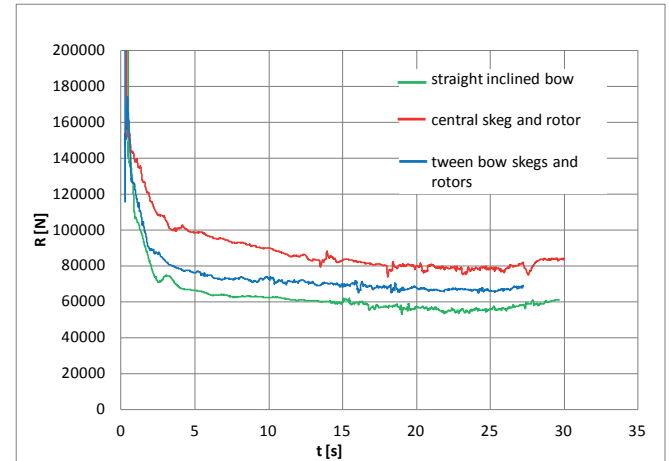


Fig.7. Resistances of the push barge with different bow configurations at 15 km/h speed: R – resistance, t – time of simulation

TURNING ABILITY OF PUSH BARGE WITH BOW ROTORS

The results of experiments presented in the literature [19] show a significant decrease of the lift coefficient of a steadily rotating rotor due to the wake separation. The numerical investigations and model tests of the proposed rotor bow steering system confirm the conclusions from the previous research.

The results of CFD simulations of rotor with 1 m diameter and aspect ratio of 1 performance at 5.55 m/s inflow speed are presented in figures 8-11. The flow field for the motionless cylinder is presented in figure 8. The flow field for the cylinder rotating with the linear velocity of rotation 4 times greater than the inflow speed – in open water conditions, with a front horn (front guard) and integrated with a cylindrical bulb are presented in figures 9, 10 and 11 respectively.

The lift force of a steadily rotating rotor in open water conditions is very small due to the wake separation and ventilation effects. In the case of rotor integrated with the bow cylindrical bulb the opposite sign of a lift force was observed.

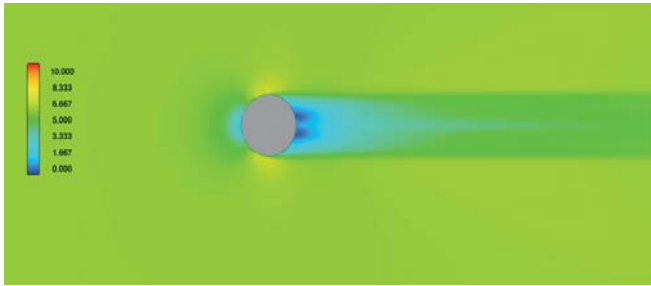


Fig. 8. CFD simulation of rotor performance: flow field around the motionless cylinder

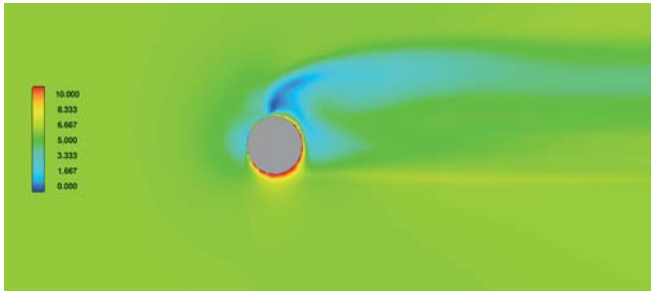


Fig. 9. CFD simulation of rotor performance: flow field around a rotor at the linear velocity of rotation 4 times greater than the inflow speed in open water conditions

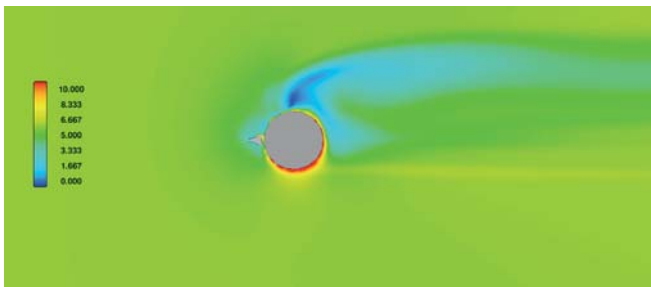


Fig. 10. CFD simulation of rotor performance: flow field around a rotor with a front guard at the linear velocity of rotation 4 times greater than the inflow speed in open water conditions

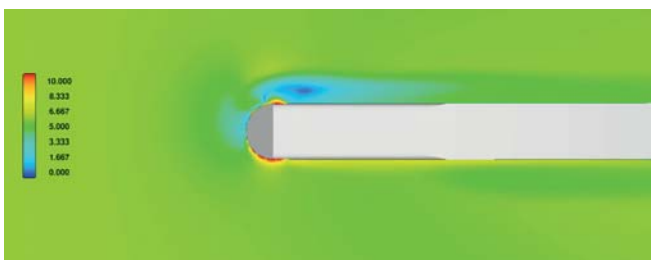


Fig. 11. CFD simulation of performance of a rotor integrated with a cylindrical bulb: flow field around the rotor at the linear velocity of rotation 4 times greater than the inflow speed

The lift forces generated on the rotor for the above cases are presented in figure 12.

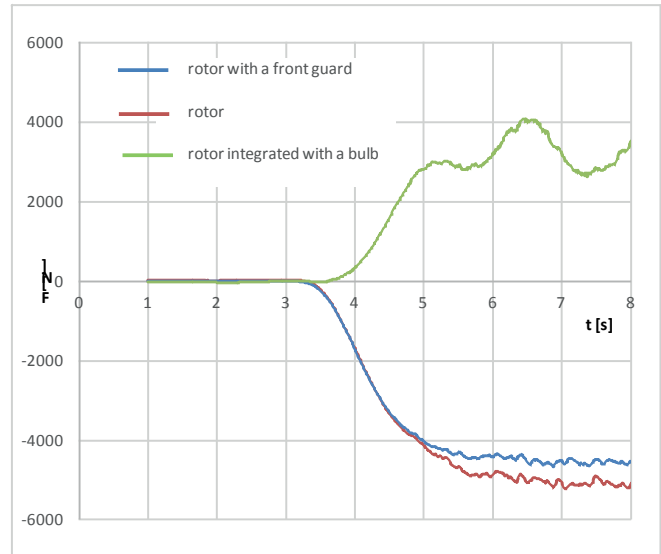


Fig. 12. CFD calculation of the lift force generated on the rotors in different configurations: F – lift force, t – time

The phenomena were discussed in [19] and they were confirmed by physical model tests, where the unsteady effects significantly increased the observed lift force.

During the early stage of the concept study the test of turning ability was crucial to ensure the possibility to handle the push barge using bow rotors. At this stage the tests were conducted with an arbitrary hull form representative for pushers and barges under consideration with the main particulars presented in table 3 assumed in CFD simulation

A pusher model was equipped with twin rudders and twin fixed pitch propellers with 0.04 m diameter and 8000 rpm rotational speed each. The main engine power of the pusher was 2×150 kW.

The physical model of the push barge is presented in figure 13.



Fig. 13. Physical model of the push barge

The example of a turning trial using only bow rotors steering system at the initial speed 0.5 m/s is presented in figure 14.

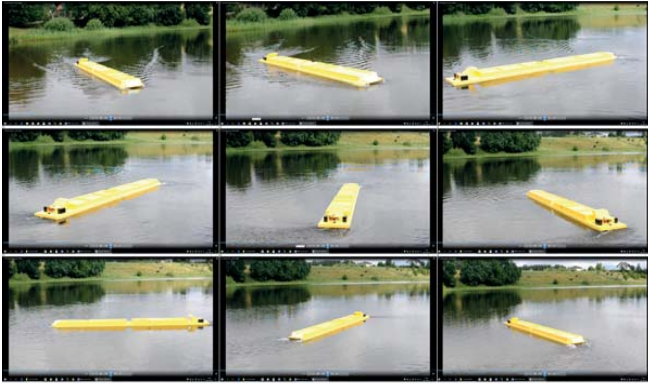


Fig. 14. Turning circle manoeuvre using bow steering unit

The push barge initially starts turning immediately after the rotors start to rotate. The lift force generated by the bow rotors in the second phase of circulation, when the push barge has changed its heading gets the longitudinal stopping component, resulting in tight turn due to the transfer of the pivot point astern and decrease of push barge speed. Then the rotors steering force drops due to the small inflow speed, the barge stops turning and then after the lift force increases it starts a very tight turn again. The tighter turning was observed when both the coupled twin rudders and bow steering system were used simultaneously.

To determine the manoeuvring performance the qualitative investigations on turning and yaw-checking abilities of the push barge should be followed by detail measurements.

PUSHER-BARGE COUPLING

The pushing system has an impact on the operational efficiency and safety of a push barge. It has an influence on the running speed and time needed for berthing, unberthing and exchanging barges. In sheltered, wide waters simple methods of mechanical connection using wire ropes winches and hydraulic cylinders can be applied to assure satisfactory performance. The rope-connection is rigid, mechanically locked and has an absolute limit in the horizontal plane.

The mechanically connected pusher-barge combination can be designed and constructed for unrestricted service [21, 17]. The proposed coupling system presented in figure 15 incorporates the use of a steering mechanism secured between a pusher and a barge for the purpose of pivoting the barge with respect to the pusher. It gives the possibility to control relative movements of the pusher and barge in horizontal plane and increases the manoeuvrability performance of the formation.

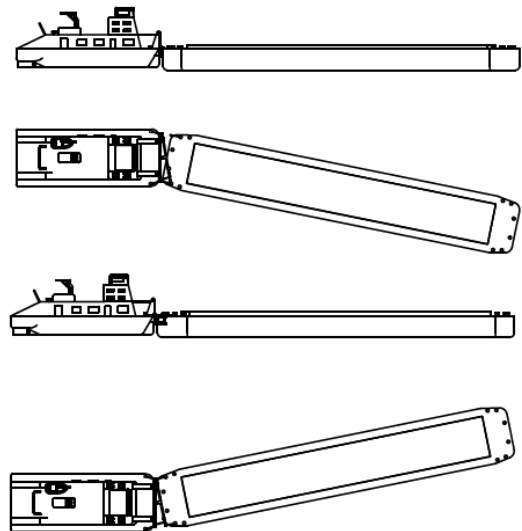
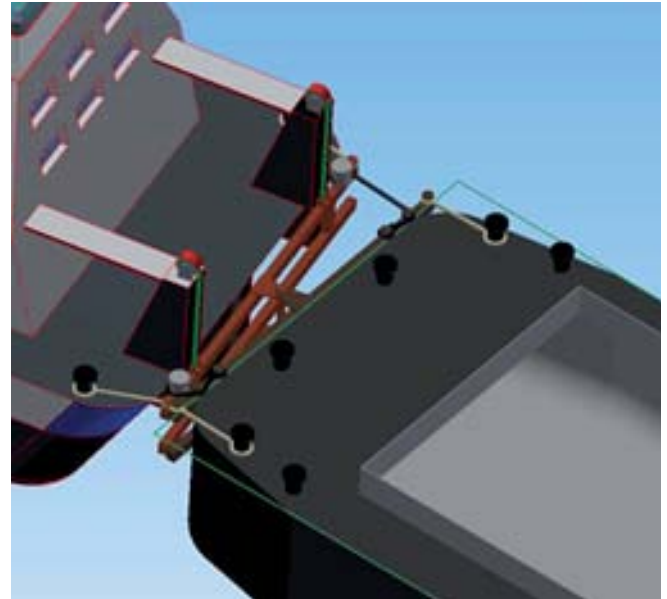


Fig. 15. Coupling system for a waterborne inland barge [4]

Effective steering depends on a reliable hydrodynamic model of the push barge motions and an integrated handling system including the mechanical coupling and steering devices both at the bow and at the aft. The system is now under development within the R&D project R.P.P.M.01.01.01-22-0075/16-00.

CONCLUSIONS

The preliminary study concerning the manoeuvrability of the concept push barge was divided into a CFD study phase and a model test phase. The results showed a big potential of the innovative steering system that includes a mechanical coupling system and bow rotors.

The different manoeuvring performance of the push barge needs to be further investigated for the optimal use of bow

rotors and the steering system. The most important issues are the tight turns at different speeds and pivot turns performed at slow speeds.

The proposed bow rotors system has much less influence on the river bed than bow thrusters. It has much less influence on small boats in narrow passages and canals than bow thrusters. The presented push barge is a promising innovation in terms of the economic and ecological potential for the inland waterway sector.

ACKNOWLEDGEMENT

The research presented in this paper has been financially supported by the Regional Operational Programme for the Pomeranian Voivodeship for the period 2014-2020: "Smart Specialisation of Pomerania Region program – offshore technology, ports and logistics"; within the frames of the R&D project: R.P.P.M.01.01.01-22-0075/16-00 "Research, design and construction of a prototype of an innovative push train: pusher with hybrid propulsion with innovative ship's boat with changing draft and fuel cells power supply, innovative pushed barge for heavy oversized goods transport with an anti-heeling system for ro-ro operations and bow thruster (with dimensions matching the Przegalina lock)".

BIBLIOGRAPHY

1. Abramowicz-Gerigk T., Błachuta J., Burciu Z., Granatowicz J., Jacyna M., Kulczyk J., Mazurek M., Nowakowski T., Picińska-Fałtynowicz J., Skupień E., Tubis A., Werbińska-Wojciechowska S., Więckowska M., Winter J. WP5 of European project INVAPO "Upgrading of Inland Waterway and Sea Ports" – coordinated by Gdynia Maritime University, Gdynia 2014.
2. Abramowicz-Gerigk T., Burciu Z. 2016. *The influence of regular river navigation in special protection areas of NATURA 2000 Network*. Journal of KONES. Vol. 23 No. pp 9-16.
3. Abramowicz-Gerigk T., Burciu Z., Krata P. "Steering system for a waterborne inland unit" Patent application P. 420664. 2017
4. Abramowicz-Gerigk T., Burciu Z., Stefurak W. *Coupling system of a pusher and waterborne barge*. Patent application P. 420684. 2017
5. *Assessment of plans and projects significantly affecting Natura 2000 sites Methodological guidance on the provisions of Article 6(3) and (4) of the Habitats Directive 92/43/EEC*. http://ec.europa.eu/environment/nature/natura2000/management/docs/art6/natura_2000_assess_en.pdf
6. *Assumptions for the plans of inland waterways development in Poland in 2016-2020 with the perspective to 2030*. Ministry of Maritime Economy and Inland Navigation. Document accepted by the Council of Ministers 14 June 2016.
7. "Blue Book". *Second draft of the Inventory of Main Standards and Parameters of the E Waterway Network ("Blue Book")*, 2016. Third revision Working Party on the Standardization of Technical and Safety Requirements in Inland Navigation Forty-ninth session, Geneva, 22–24 June 2016. Item 5 (b) of the provisional agenda Inland waterways infrastructure. https://www.nece.org/fileadmin/DAM/trans/doc/2016/sc3wp3/ECE-TRANS-SC3-WP3-2016-inf_30e.pdf
8. Burciu Z., Gąsior A. 2015. *The analysis of the possibility of revitalization of the Lower Vistula river based on INVAPO European Project*. *Scientific Journals of Gdynia Maritime University No. 92/2015*, in Polish.
9. EMMA - *Enhancing freight Mobility and logistics in the BSR by strengthening inland waterway and river sea transport and promoting new international shipping services* - project funded by the Interreg Baltic Sea Region Programme 2014-2020.
10. Keuning F. W. *Motion control of small fast boats in following waves*. SNAME Symposia Papers. 2016. <http://www.sname.org/HigherLogic/System/DownloadDocumentFile.ashx?DocumentFileKey=ef3cb5a3-350b-e385-d7a2-a91fddd0589a>.
11. King K. K., Yasukawa H., Hirata N., Kose K. *Manoeuvring simulations of pusher-barge systems*. *Journal of Marine Science and Technology*, 2008, Volume 13, Issue 2 pp. 117–126.
12. Kulczyk J., Werszko R. *Influence of ship motion on waterway backward current velocity*. *Polish Maritime Research*, Special Issue 2006/S2.
13. Liu J., Hekkenberg R., Rotteveel E. *A Proposal for Standard Manoeuvres and Parameters for the Evaluation of Inland Ship Manoeuvrability*. European Inland Waterway Navigation Conference 2014, Budapest, Hungary.
14. PIANC Report N° 99. 2008. *Considerations to reduce environmental impacts of vessels navigation*. Inland Navigation Commission. www.pianc.org.
15. Rabant H., Habel M., Babiński Z. *Transport of the oversized goods on the Vistula waterway. The basic waterway parameters and main difficulties*. *Works of Commission Of Communication Geography PTG 2016*, 19(3), pp. 7-17, in Polish.
16. *Resolution on acceptance of "Assumptions for the plans of inland waterways development in Poland in 2016-2020 with the perspective to 2030"*. <https://www.premier.gov.pl/wyda-znania/decyzje-rzadu/uchwala-w-sprawie-przy>

jecia-zalozen-do-planow-rozwoju-srodladowyc h-drog.
html.

17. Smith W. J. 1959. *Steering connection between a barge and a pusher tug*. US Patent 3035537 A
18. Tabaczek T., Kulczyk J., Zawislak M. *Analysis of hull resistance of pushed barges in shallow water*. Polish Maritime Research 1(51) 2007, Vol 14, pp. 10-15
19. Tokumaru T., Dimotakis P. E. *The lift of a cylinder executing rotary motions in a uniform flow*. J. Fluid Mech. (1993), vol. 255, pp. 1-10
20. <http://www.vdvelden.com/products/product/rotor-bow-rudder.html>
21. http://www.articouple.com/5-articouple_fr.html
22. <http://www.fv-tech.com>

CONTACT WITH THE AUTHORS

Zbigniew Burciu

e-mail: zbj@am.gdynia.pl
Gdynia Maritime University
Morska, 81-225 Gdynia
POLAND

Teresa Abramowicz-Gerigk

e-mail: tagerigk@am.gdynia.pl
Gdynia Maritime University
Morska, 81-225 Gdynia
POLAND

Jacek Jachowski

e-mail: jj@o2.pl
Gdynia Maritime University
Morska, 81-225 Gdynia
POLAND

ACOUSTIC IMAGING OF SELECTED AREAS OF GDANSK BAY WITH THE AID OF PARAMETRIC ECHOSOUNDER AND SIDE-SCAN SONAR

Grażyna Grelowska²

Eugeniusz Kozaczka²

Wojciech Szymczak¹

¹ Polish Naval Academy, Poland

² Gdansk University of Technology, Poland

ABSTRACT

The article presents and analyses the data recorded during sounding of the Gdansk Bay seabed with the aid of a parametric echosounder and a side-scan sonar. The accuracy of seabed structure examination, as a condition for obtaining valuable results, requires correct configuration of echolocation devices and proper calibration of peripheral devices, such as the survey unit geographical position sensor – GPS, the navigation unit, the MRU-Z sensor of pitch, roll and heave, and the sound velocity meter, which deliver the data to the bathymetric measurement system. Parametric seabed profilers deliver two types of data: the envelope, and the detailed echo signal without processing. The envelope is used for data visualisation in the form of online echograms, while the echo signal is stored for further analyses, to be performed using dedicated software or, after relevant conversion, in arbitrary programming environment¹. The presented data analysis is illustrated by selected sample images recorded by the parametric echosounder and the side-scan sonar during Gdansk Bay sounding.

Keywords: echolocation, acoustic imaging, seabed structure examination

INTRODUCTION

Although hardly assessable, the deep sea becomes more and more interesting for people. Numerous reasons for this growing interest can be named, starting with the willingness to gain more information about the seabed and its environment^{2,3,4,5} and ending with the sailing safety, especially in relatively shallow water regions. Another possible reason is the historical and archaeological research, frequently related with the search for wrecks of ships or airplanes, or other objects resting on the seabed^{6,7}.

The next important aspect of underwater exploration is the search for natural resources the inland access to which is limited and which are available under the seabed. This refers to both inanimate natural resources, such as raw energy materials or polymetallic minerals, and animate resources.

Exploitation of undersea energy resources, especially crude oil and natural gas, carries the danger of leaking of those harmful substances to the seawater⁸. To reduce the threat of appearance of such a situation, the areas surrounding drilling platforms and bore-holes, as well as those in the vicinity of submarine pipelines used for long-distance transport of gas and crude oil, are under continuous monitoring.

Such a wide interest in the research and observation of the underwater space facilitates the development of devices and methods for underwater research^{9,10,11,12}. The overwhelming majority of these devices make use of acoustic waves as information carriers.

Generally, we try to systematise the knowledge about the underwater world, which we build by analogy to the perception of the space around us on the Earth's surface, in the form of images. These images can be created as graphical

presentation of the processed acoustic signals¹³. The article shows the seabed images of selected areas of the Gdansk Bay which were obtained with the aid of devices making use of most recent research methods, including those based on the theory of nonlinear acoustics.

MEASURING SYSTEM

The rig for sea trials was assembled on the 9-m deck of a small survey vessel *s/y Windspeel* (Fig.1.). The main measuring instrument was the parametric sub-bottom profiler SES-2000 standard, consisting of two components: the main unit integrating the probing pulse generation system, and the receiving unit with analogue-to-digital signal conversion elements, complemented by a matrix of converters - antenna - mounted on starboard side of the vessel, in a specially prepared holder.



Fig. 1. Survey vessel *s/y Windspeel*

The profiler emits low-frequency acoustic signals of adjustable time duration. The signal frequency can be set by the user within the range between 4 and 15 kHz. Taking into account that the measurements were expected to deliver information on the structure of seabed sediment layers, a relatively long time of signal duration was to be chosen. On the other hand, when searching for objects laying on or buried under the seabed, i.e. in cases when the in-depth resolution is of high importance, short pulses and higher frequencies are to be used. An interesting option, which was used in the research, is the sounding data recording along a set trajectory with the aid of, alternately, two or three different sounding signals. In that case the longitudinal resolution decreases, but the use of two or three different sounding pulses of given frequencies makes it possible to record different data during one survey. The sounding frequencies used during the reported sea trials were equal to 4 kHz, 8 kHz and 12 kHz. Due to the fact that the optimal measuring conditions refer to calm sea, a phenomenon which cannot be controlled by the research worker, the emitted beam is to be controlled to compensate ship's rolls and gain the information on heave in order to eliminate it. The recorded data were stored on

the hard disc in two formats: *.SES files, which contained the data concerning the signal envelope, and *.RAW files with the complete time-history of the detailed echo signal. The measuring unit was supplied with 230V (AC) voltage delivered from the DC-AC converter connected to a set of three 110 Ah gel batteries. During the sea trials, the batteries were charged from solar panels and from the engine driven electric current generator, while during the measurement intervals they were additionally charged from the 230 V(AC) current generator Honda. Additional seabed insonification was done using the side-scan sonar Simrad Structure Scan. Moreover, such equipment as the MRU-Z sensor of pitch, roll and heave, and the precise GPS with position sensor were installed on the survey ship and calibrated. The signals from the sensors were transmitted to the devices using RS-232 distributors. The research included measurements of sound velocity profiles with the aid of the measuring instrument MIDAS SVX2 produced by Valeport (Fig. 2.).



Fig. 2. Sound velocity probe - MIDAS

The collected profiles were immediately entered to the programme controlling the operation of the parametric echosounder. The analysed area and the transects, along which the soundings were planned to be made, were selected based on the geological maps of the Polish Geological Institute. Relevant data were delivered to the navigation software (Nobeltec) connected to the autopilot, which ensured satisfactory accuracy of survey vessel navigation along the set paths.



Fig. 3. Operator panel inside the survey vessel

The operator panel where the recorded data were visualised on monitors, Fig. 3, was assembled inside the survey vessel. Additionally, two screens were installed on the deck to display the navigation chart, the AIS and radar data images (Fig. 4), and the results of parametric echosounder sounding, this way facilitating operator's and steersman's work. Before the beginning of sea measurements, the system was fully calibrated in the harbour, along with checking whether the electrical supply system does not affect negatively the recorded data. This check included correctness of earthing, operation of DC/AC converter, etc.



Fig. 4. Navigation device – radar

LABORATORY TESTS

The laboratory tests, which preceded real in-situ measurements, aimed at, among other aspects, verification of sounding pulses generated by the parametric echosounder transceiver, with further analysis of the effect of changes of individual parameters (pulse duration time – number of generated intervals, frequency, amplification of received signal - TVG) on on-line imaging presented to the operator based on the signal envelope. Another goal of these tests was to determine transmission characteristics for both primary waves, and the frequency difference wave.

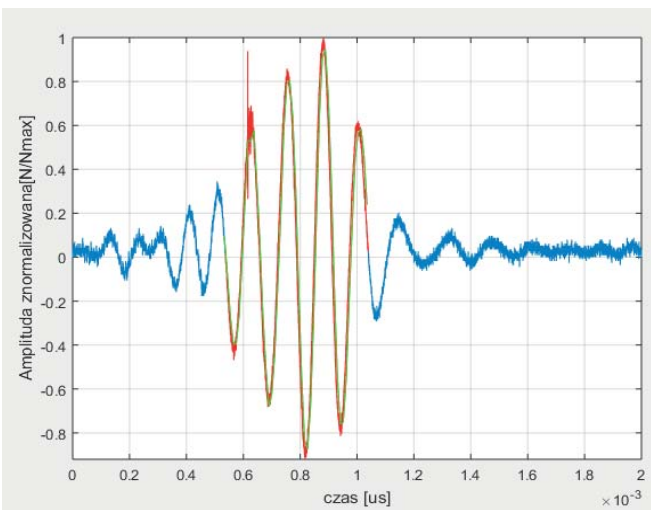


Fig. 5. Sounding pulses: 8kHz, 4 intervals

Because of the properties of parametric wave generation, the main beam of the echosounder was directed horizontally along the largest dimension of the basin. Since the depth and width of the basin were limited, the first important point was proper directing of main lobes of the wave radiating system. A measuring principle was adopted that the antenna was kept in fixed position, while the moving object was the measuring hydrophone. The measuring area was scanned using a precise device made by ISEL, which allowed space scanning with the accuracy of up to 20 μm .



Fig. 6. Parametric echosounder antenna on support

The motion of the hydrophone was controlled using a computer code which enabled precise characteristics to be recorded. The next goal of the tests was to determine acoustic impedances of materials representing typical seabed sediments expected to be found in the water region chosen for in-situ measurements. Figure 7 shows the model of the measuring basin with the drawn directional transmission characteristic.

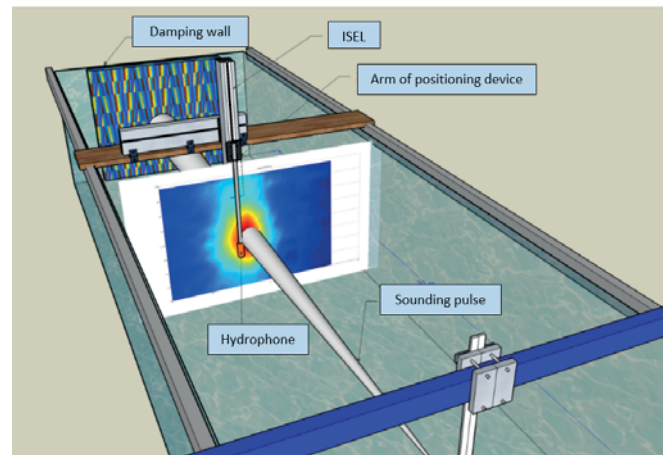


Fig. 7. 3D characteristic of frequency difference wave

According to the theory, the generated pulse of the frequency equal to the frequency difference between primary pulses (in this case, frequencies 100 and 108 kHz, for instance) has a similar beam width and no side lobes.

Figure 8 compares directional characteristics measured in the horizontal plane at a distance of 4 metres from the parametric echosounder transceiver. The red curve represents the primary wave characteristic, while the blue curve – the frequency difference wave. The recorded results confirm similar properties concerning beam width and the absence of side lobes for the pulse whose properties make it possible to penetrate seabed sediments.

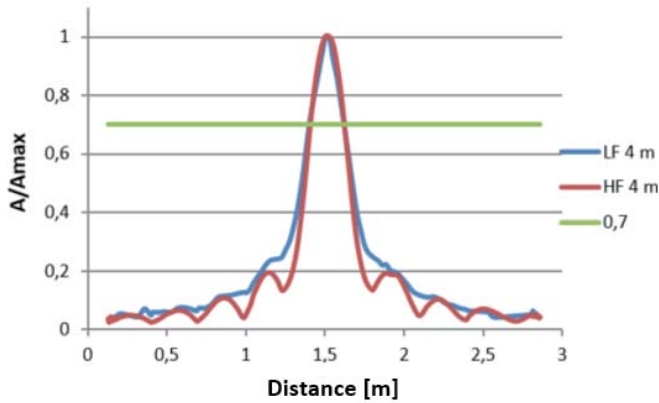


Fig. 8. Horizontal directional characteristic

Specially prepared frames (Fig. 9.), which enabled positioning of seabed sediments taken from selected points of the measuring water region, were used for measuring acoustic impedances of individual materials and assessing the in-depth resolution.

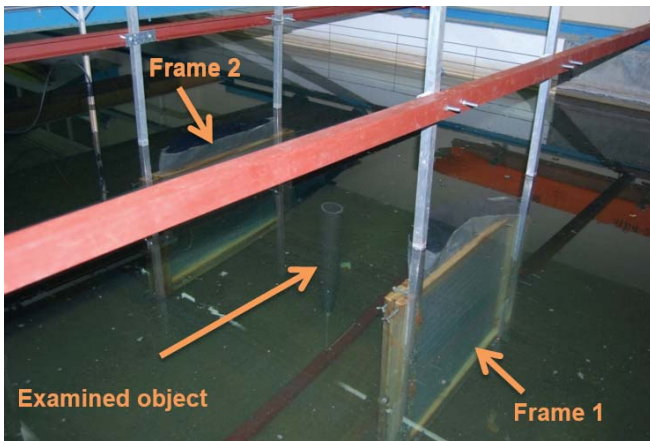


Fig. 9. Frames simulating seabed sediment layers

Figure 10 shows the results of sounding of two frames separated by 1 m from each other. The tests were performed for the empty space between the frames, and when an object (cylinder made of non-absorbent sponge with air bubbles) was inserted between them. Comparing these two cases revealed very precise and stable object positioning between the two sediment layers.

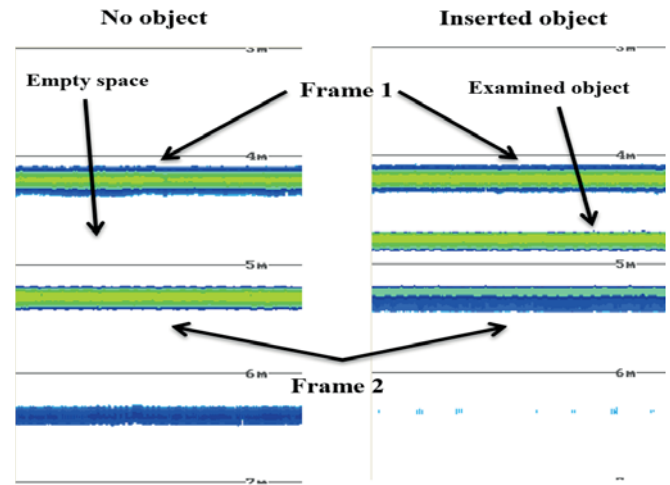


Fig. 10. Result of in-depth resolution test

RESULTS OF IN-SITU MEASUREMENTS

Two sample results of sounding were selected for presentation as characteristic for sounding in the Gdansk Bay area. The former result is closely related with the geological map developed based on the analysis of the content of sediment samples taken by the Polish Geological Institute using invasive methods¹⁴. The image of the results collected by the parametric echosounder (Fig. 11.) shows the seabed as a highly reflective surface, and mud sediments in the upper seabed layer. In selected fragments of the echogram, of several kilometres in length, we can observe stratification resulting from the fact that the echo is obtained from the upper mud layer and from the highly reflective sandy bottom situated about 2 m below. This situation made the sound penetration to deeper seabed layers practically impossible.

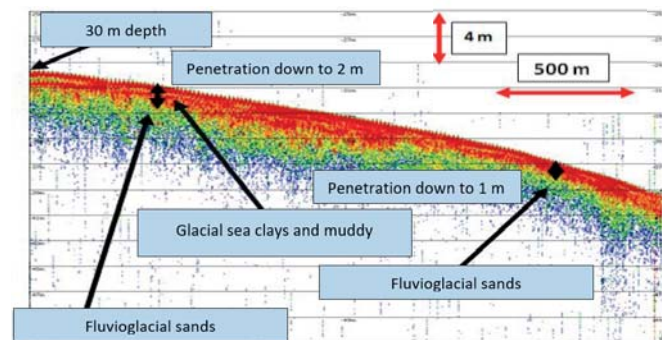


Fig. 11. Sounding: 1–2 m layer of mud and sand

When analysing the second part of sounding (Fig. 12) we can clearly see high stratification resulting from the presence of layers having lower acoustic impedance than that of sand or clay. This allowed deeper penetration into seabed sediment layers. This image is well correlated with the results of the geological research performed by the Polish Geological Institute, from which we can conclude that the

sediment structure image reaches the layer of boulder clays and glacial sands.

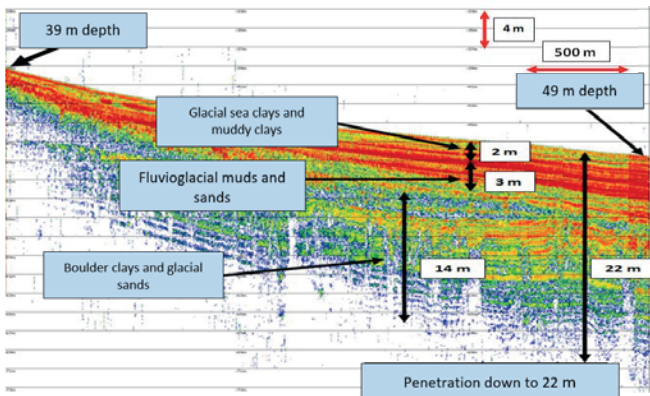


Fig. 12. Muds and clays accumulated under the seabed down to 22 m

When analysing the seabed image recorded with the aid of the side-scan sonar, we can clearly observe changes in the image of the top layer of sediments (Fig. 13.). This is related with two aspects, which are: the acoustic impedance of sediments (decreasing with the increasing depth), and the depth dependent high-frequency attenuation ratio. We should bear in mind, however, that the latter factor is not dominating in the given case. Consecutive layers represent the results of sounding recorded in water regions of increasing depths.

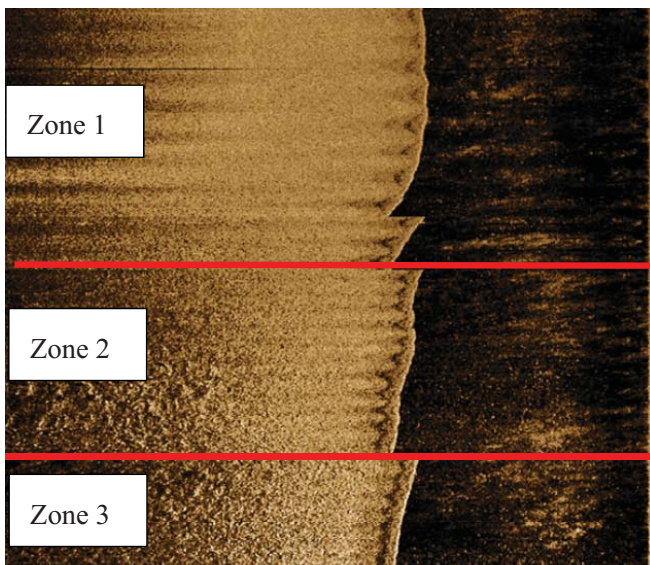


Fig. 13. Sonar image, change in deposit impedance

The image in Fig. 14, Zone 5, shows the results collected at the maximum depth of 49 m.

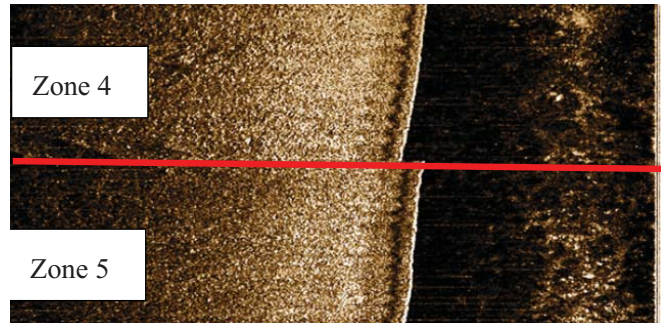


Fig.14. Sonar image, change in deposit impedance

The other selected sample image presents the results recorded at the depth of 10 metres, in the water region situated near the Orlowo cliff. Because of small depth, the image obtained from the side-scan sonar reveals high resolution, which makes it possible to visualise wavy forms created on the sandy sea.

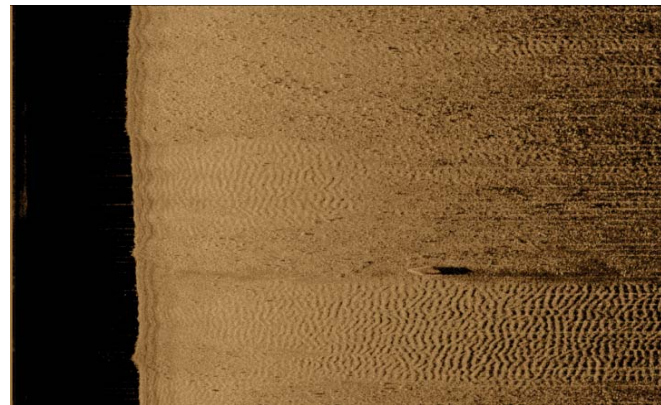


Fig. 15. Clearly visible sandy and wavy seabed

In those conditions (sand – extremely high reflectance) the echosounder image reveals strong reflection from the top layer (Fig. 16.) When the consolidated sandy layer is damaged, (Fig. 16 – zone B), the difference related with the structural seabed change and the resultant sounding pulse scattering is clearly visible.

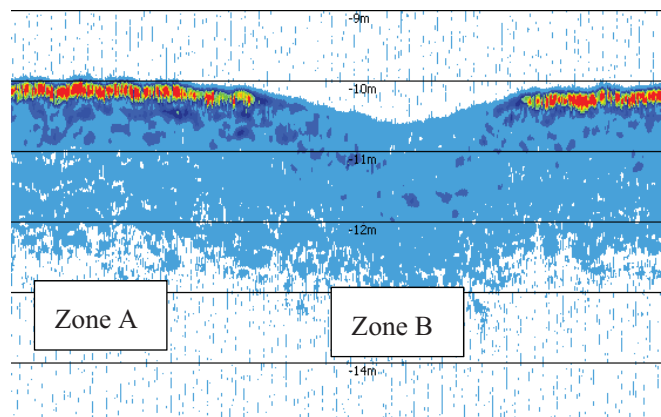


Fig. 16. Image of sandy seabed and excavation

SUMMARY

A number of technologies and devices are known which are used for imaging the seabed and the structure of sediments accumulated under its surface. However, obtaining a comprehensive image of the underwater world with the aid of any of these methods is not possible. The article presents two methods for seabed exploration and the analysis of results making use of precise laboratory tests of sounding pulses. Based on the data collected using different devices in the same area, we received different images of the same environment. The presented results confirm that each underwater imaging method delivers only a partial picture, due to limitations resulting from the applied technology. Comprehensive information can only be obtained using a number of complementary techniques. It is noteworthy that parametric echosounders, which belong to the new class of devices working based on the theory of nonlinear acoustics, make it possible to image the structure of sediments and localise objects buried under the seabed, a task which is impossible when using other underwater observation devices.

ACKNOWLEDGEMENTS

The research was supported in part by the Ministry of Science and Higher Education, within the framework of funds for statutory activities of the Gdansk University of Technology and the Polish Naval Academy.

BIBLIOGRAPHY

1. E. Kozaczka, G. Grelowska, W. Szymczak, S. Kozaczka, Processing data on sea bottom structure obtained by means of the parametric sounding, Polish Maritime Research, Vol. 19, No 4, 3-10, 2012
2. Peter C. Wille: Sound Images of the Ocean in Research and Monitoring, 2005.
3. L. Hamilton, P. Mulhearn, R. Noecker: Comparison of RoxAnn and QTC-view acoustic bottom classification system performance for the Cairns area, Great Barrier Reef, Australia. Continental Shelf Research 19, 1577÷1597, 1999
4. Leighton T., Mantouka A., White P., Klusek Z., Towards field measurements of populations of methane gas bubbles in marine sediment: an inversion method required for interpreting two-frequency insonification data from sediment containing gas bubbles, Hydroacoustics, 11, 203–224, 2008.
5. G. Grelowska, E. Kozaczka, Underwater acoustic imaging of the sea, Archives of Acoustics, Vol. 39, 4, 439-452, 2014.
6. Kozaczka E., Grelowska G., Kozaczka S., Szymczak W., Detection of Objects Buried in the Sea Bottom with the Use of Parametric Echosounder, Archives on Acoustics, 38, 1, 99–104, 2013.
7. Wunderlich J., Müller S.: High-resolution sub-bottom profiling using parametric acoustics. International Ocean Systems, 7 (4), 6÷11, 2003
8. P. Blondel, A. Caiti: Buried Waste in the Seabed Acoustic Imaging and Bio-Toxicity. University of Bath, UK, 2007
9. Tegowski J., Lobbies Z., Seabed characterization using spectral moments of the echo signal, Acta Acustica united with Acustica, 88, 5, 623-626, 2002.
10. Zacharias M. and Dybedal J., The parametric side-scan sonar instrument and synthetic aperture sonar processing, [in:] Buried waste in the seabed. Acoustic imaging and Bio-toxicity, P. Blondel and A. Caiti [Eds.], Springer 2007.
11. G. Grelowska, S. Kozaczka, W. Szymczak: Some methods of the sea bottom recognition. Hydroacoustics, Vol. 12, 69÷76, 2009
12. G. Grelowska, E. Kozaczka, S. Kozaczka, W. Szymczak, Gdansk Bay seabed sounding and classification of its results, Polish Maritime Research No 3 (79) Vol 20, s. 45-50, 2013
13. E. Kozaczka, G. Grelowska, S. Kozaczka: Images of the seabed of the Gulf of Gdansk obtained by means of the parametric sonar. Acta Physics Polonica A, Vol. 118, No 1, 91÷94, 2010
14. Uścińowicz S., Zachowicz J. (1994), Geological map of the bottom of the Baltic Sea, 8 sheets and pamphlet, scale 1:200 000, Polish Geological Institute, Warsaw.

CONTACT WITH THE AUTHORS

Grażyna Grelowska

e-mail: koe@o2.pl
Gdansk University of Technology
ul. G. Narutowicza 11/12
80-233 Gdansk
POLAND

Eugeniusz Kozaczka

e-mail: koe@o2.pl
Gdansk University of Technology
ul. G. Narutowicza 11/12
80-233 Gdansk
POLAND

Wojciech Szymczak

e-mail: ws2@o2.pl
Polish Naval Academy
ul. Śmidowicza 69
81-127 Gdynia
POLAND

VISUALIZATION OF A LIFEBOAT MOTION DURING LOWERING ALONG SHIP'S SIDE

Aleksander Kniat

Gdańsk University of Technology, Faculty of Ocean Engineering and Ship Technology, Poland

ABSTRACT

This paper presents description of a computer program for motion visualization of a lifeboat lowered along ship's side. The program is a post-processor which reads results of numerical calculations of simulated objects' motions. The data is used to create scene composed of 3D surfaces to visualize mutual spatial positions of a lifeboat, ship's side and water waving surface. Since the numerical data contain description of a simulation as a function of time it is possible to screen a static scene showing the simulated objects in an arbitrary instance of time. The program can also reproduce a sequence of scenes in the form of animation and control its speed. The static mode allows to view an arbitrary cross-section of the scene, rotate and enlarge specific details and make the image more realistic by hiding invisible lines or shading. The application of the program is aimed at making it possible to assess and analyze numerical calculation results in advance of their experimental verification.

Keywords: three-dimensional visualization, kinematics, computer animation, lifeboat lowering , numerical simulations

INTRODUCTION

Spatial visualization and animation of images in the form of a film represents computer techniques which are commonly applied to present numerical calculation results. This was made possible as a result of increasing computing power of PCs and universal window environment dedicated to graphic applications ensured by operating systems. Fast development of the technology has been stimulated first of all by the market of entertainment and games. Examples of highly sophisticated techniques used in cartoon films for home cinema can be found in [12]. In this context it is a natural trend of professional users to see results of their work not in the form of numbers but in a graphic form of imagination appealing pictures.

Theoretical background for solutions in the field of mechanics is contained in [8]. An example of simulation of human body motions are given in [9]. The application of simulation of crane operation in building industry is presented in [1]. In [10] a similar technique is shown for simulating interaction of many devices present at construction site. The

visualization found its application also in robotics and CNC (Computerized Numerical Control). There are many programs which allow to carry out simulations of robot or machine tool operation in advance of their implementation to industrial tasks. Such approach makes it possible to avoid errors which may cause expensive failures of machines or destruction of valuable materials. An example of open source program applicable to simulation of robot operation is described in [15]. A broader analysis of programs available in this domain is given in [3]. Commercial programs examples for instance K-Roset program for Kawasaki robots or Italian universal program Eureka by Roboris can be found in [11] and [6]. Visualizations of results of operation of an algorithm for automatic routing the pipelines in three-dimensional space are presented in [14]. Above mentioned cases exemplifies design applications.

Making use of computer visualization becomes especially important when complex mathematical multi-parameter models are analyzed because description of their state contains yet greater number of data. The finite element method (FEM) as well as boundary element method (BEM) can be

distinguished as an excellent example of such problems. Today nobody can imagine to work with a FEM solver without using a pre- and post-processor. Functional assumptions for such visualizing programs are presented in [2]. Many commercial programs are in use today for this purpose. The application concerning visualization of ship hull strength calculations [13] represents work made by the author in the domain in question. Further development of computer techniques in the field of visualization is inevitable. It proceeds especially dynamically in the area of home entertainment where virtual reality constitutes basis for computer games and animated cartoons. There is no reason for which the same technique could not be applied in professional domain. Additionally computer simulations are less expensive than physical experiments.

KINEMATIC MODEL AND RESULTS OF CALCULATIONS

This work concerns a particular issue which is visualization of lowering a lifeboat along ship's side. The kinematic model of the process includes the following objects:

- lifeboat,
- fender bar installed on boat's side,
- lines on which the lifeboat is hung,
- mechanism for lowering the lifeboat,
- boat hook which allows to set the lifeboat free after its launching,
- boat davits from which the lifeboat is lowered,
- ship's side along which the lifeboat is lowered,
- water waving surface onto which the lifeboat falls.

Each of the above specified objects was described by an appropriate set of parameters defining its features. A comprehensive description and results of operation of RESBO program which performs numerical simulation of behavior of the system composed of the so defined objects are given in [4]. A mathematical model of kinematics of the entire system can be found there too. The program produces numerical data which represent, in given time intervals, the state of the system characterized by forces and moments acting on the objects, as well as their velocities and locations. Description of the system's states as a function of time is recorded by the program in disk text files. Hence, to assess results of simulation produced by RESBO program it is necessary to analyze numerical data in the files. At first the results have been analyzed by presenting them on diagrams. Unfortunately, when it was necessary to analyze results of more difficult cases or their larger number, as e.g. in [5], difficulties in interpretation and correlation of relevant diagrams occurred. It was especially troublesome to check in which direction the lifeboat is rotated, having only numerical values of co-ordinates of its center of gravity and co-ordinates of the three versors of local reference frame.

Contemporarily there are available ready-to-use programs for kinematic simulation and spatial visualization, such as e.g.

ADAMS discussed in [16]. However the author did not decide to apply any of them to the case in question. The reason was that it was impossible to simulate interaction between the lifeboat and water surface (slamming) and behavior of the lifeboat floating in waves.

ASSUMPTIONS FOR VISUALIZATION PROGRAM

To make analysis of calculation results obtained from RESBO program easier it was decided to prepare a new program called VRBS which makes it possible to visualize spacial location of objects taking part in simulation. The following functions were assumed for the program:

- visualization of an arbitrary scene composed of spacial objects represented by quadrangular and triangular mesh in the form of axonometric view;
- presentation of the scene in four different forms:
 - transparent (only edges of the mesh are visible),
 - hidden lines removed (edges of the mesh are obscured by elements located closer to observer),
 - opaque (interior of each mesh element is filled with color and only non-hidden elements or their fragments are visible)
 - shaded with lighting (interior of each mesh element is filled with color, tint of color depends on light incidence angle and only non-hidden elements are visible);
- shaping of water free surface onto which the lifeboat is lowered, in an arbitrary instant;
- positioning ship's side and ends of arms of boat davits from which the lifeboat is lowered, in an arbitrary instant;
- positioning and orientation of the lifeboat itself, in an arbitrary instant;
- simulation of motion of the objects in the form of a film by sequential projecting of following scenes based on calculation results obtained from RESBO program;
- stopping motion simulation, jumping to an arbitrary instant and continuing the motion simulation.

SPATIAL MODEL AND METHODS OF VISUALIZATION

The computational model of the scene consists of the objects specified in section „Kinematic model and results of calculations”. Since not all of them are necessary for visualization, graphic representations were prepared only for:

- lifeboat,
- ship's side and davits by which the lifeboat is lowered,
- waving water surface onto which the lifeboat falls.

Each of the above mentioned objects is graphically represented as a 3D surface. Shape is assumed to be mapped by a quadrangular mesh. Since the spatial model will be imported from a CAD program and in order not to lose solution generality it was assumed that quadrangular mesh will be presented as NURBS surface of the first degree,

described in [17]. In such case control points of the surface are the same as mesh vertices. This approach makes it possible to import from a CAD program not only mesh but also smooth surfaces. VRBS program uses the OpenGL library [18] to achieve professional effects of 3D object's visualization. Such approach let the author to focus on the details of the scene and motion but not on issues of geometrical transformations, projection and rendering. An exemplary image of a ready 3D scene consisting of objects subjected to motion simulation is presented in Fig. 1.

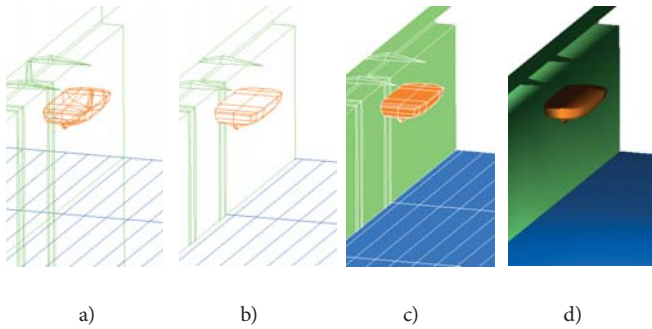


Fig. 1. Image of scene shown in axonometric parallel projection: a) edge transparent, b) edge one with hidden invisible lines, c) colour filled, d) shaded

MOTION AND TIME RELATIONS

Because the surfaces are assumed to be the NURBS surfaces the visualization program is to operate in the space of homogenous co-ordinates. If 3D space is taken into account in which the system under simulation is considered, then every point of the space is represented by four co-ordinates. The fourth co-ordinate is interpreted to be a weight. In kinematic system, objects have six degrees of freedom. These are three translations and three rotations with respect to each axis of co-ordinate frame. Superposition of appropriate translations and rotations makes it possible to obtain an arbitrary location of the simulated objects. The translation matrix used in geometrical transformations looks always similarly. It is represented by the expression (1).

$$\mathbf{T}(x, y, z) = \begin{bmatrix} 1 & 0 & 0 & x \\ 0 & 1 & 0 & y \\ 0 & 0 & 1 & z \\ 0 & 0 & 0 & 1 \end{bmatrix} \quad (1)$$

where: x, y, z - co-ordinates of translation vector.

The rotation is generally composed of three rotations. It is represented by the expression (2).

$$\mathbf{R}(\chi, \beta, \alpha) = \mathbf{R}_x(\chi) \cdot \mathbf{R}_y(\beta) \cdot \mathbf{R}_z(\alpha) = \begin{bmatrix} 1 & 0 & 0 & 0 \\ 0 & \cos(\chi) & -\sin(\chi) & 0 \\ 0 & \sin(\chi) & \cos(\chi) & 0 \\ 0 & 0 & 0 & 1 \end{bmatrix} \quad (2)$$

$$\begin{bmatrix} \cos(\beta) & 0 & \sin(\beta) & 0 \\ 0 & 1 & 0 & 0 \\ -\sin(\beta) & 0 & \cos(\beta) & 0 \\ 0 & 0 & 0 & 1 \end{bmatrix} \begin{bmatrix} \cos(\alpha) & -\sin(\alpha) & 0 & 0 \\ \sin(\alpha) & \cos(\alpha) & 0 & 0 \\ 0 & 0 & 1 & 0 \\ 0 & 0 & 0 & 1 \end{bmatrix}$$

As numerical results obtained from RESBO program do not contain the rotation angles χ, β, α but only directions of versors of objects' local co-ordinate frame the rotation matrix is described by the expression (3) acc. [7].

$$\mathbf{R}(\mathbf{V}_x, \mathbf{V}_y, \mathbf{V}_z) = \begin{bmatrix} x_{vx} & x_{vy} & x_{vz} & 0 \\ y_{vx} & y_{vy} & y_{vz} & 0 \\ z_{vx} & z_{vy} & z_{vz} & 0 \\ 0 & 0 & 0 & 1 \end{bmatrix} \quad (3)$$

where:

$$\mathbf{V}_x = \begin{bmatrix} x_{vx} \\ y_{vx} \\ z_{vx} \end{bmatrix}, \quad \mathbf{V}_y = \begin{bmatrix} x_{vy} \\ y_{vy} \\ z_{vy} \end{bmatrix}, \quad \mathbf{V}_z = \begin{bmatrix} x_{vz} \\ y_{vz} \\ z_{vz} \end{bmatrix}$$

are versors of object's local coordinate frame.

Therefore the translation of the object from its original location in the point O and orientation consistent with current reference frame to a new point Q and new orientation $\mathbf{V}_x, \mathbf{V}_y, \mathbf{V}_z$, is described by the following matrix \mathbf{M} , acc. to the formula (4).

$$\mathbf{M} = \mathbf{T}(x_q, y_q, z_q) \cdot \mathbf{R}(\mathbf{V}_x, \mathbf{V}_y, \mathbf{V}_z) \cdot \mathbf{T}(-x_o, -y_o, -z_o) \quad (4)$$

where:

$$\mathbf{O} = \begin{bmatrix} x_o \\ y_o \\ z_o \end{bmatrix} \quad \mathbf{Q} = \begin{bmatrix} x_q \\ y_q \\ z_q \end{bmatrix}$$

Initial location of all points \mathbf{P}_i belonging to scene objects is known. Hence, if at any instance of time t a new location of the origin of object's co-ordinate frame, i.e. the point $\mathbf{Q}(t)$, and its versors $\mathbf{V}_x(t), \mathbf{V}_y(t), \mathbf{V}_z(t)$ are known, then by using the matrix \mathbf{M} acc. (4) one is able to find a new location of any point of the scene at this instance of time.

$$\mathbf{P}_i(t) = \mathbf{M}(t) \cdot \mathbf{P}_i = \mathbf{T}(x_a(t), y_a(t), z_a(t)) \cdot \mathbf{R}(\mathbf{V}_x(t), \mathbf{V}_y(t), \mathbf{V}_z(t)) \cdot \mathbf{T}(-x_o, -y_o, -z_o) \cdot \mathbf{P}_i \quad (5)$$

Numerical results from RESBO program contain subsequent states of the system in given time intervals. If a motion visualizing program has to make it possible to show the motion with its real velocity it must adjust time of displaying subsequent states to real time. The problem consists in that recalculation of new locations of scene points and displaying them on screen does not for sure last precisely as long as the time step used during numerical simulations. In the case when displaying a new scene lasts shorter than time step during numerical calculations, the program waits appropriately long before it starts to display the next scene. When scene displaying lasts longer than the time step there is no other possibility except to omit some of calculated system's states and to display the one which is consistent with capability of the visualization program. However it may cause the effect of lack of motion smoothness as a result of neglecting the intermediate states.

SIMULATION RESULTS

Fig. 2 shows selected subsequent states of simulation of motion of a lifeboat being lowered. Results of the numerical calculations covered the time period lasting 35 s. The calculation time step was equal to 1 ms but only every 10th state was recorded in text files of the results. In such a case the visualizing program should display one by one 3500 states in the real time of 35 s. Unfortunately it turned out that the displaying time of a single scene on an available computer was equal to 16 ms. For this reason it appeared necessary to neglect every second state/scene. In spite of that the final effect was better than satisfactory. Scenes were displayed smoothly, without stopping and jumping, and their animation made impression of real motion.

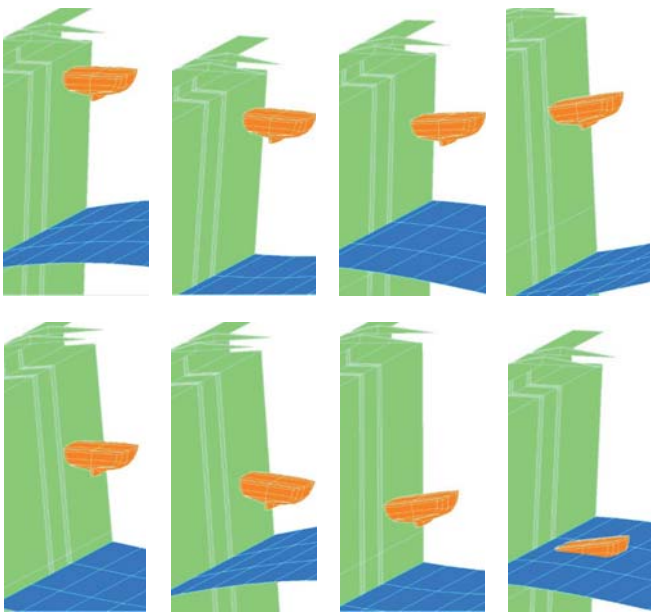


Fig. 2. Single scenes of animation showing motion of lifeboat under lowering

SUMMARY

The VRBS program has been created and it enables visualization of selected scenes and motion of lifeboat being lowered along ship's side. Tests on a few selected results of numerical calculations produced by RESBO program have been done. As the program allows to control motion of visualized objects in time it is possible to directly compare the motion with the film recorded during experiment in real conditions. Synchronizing the visualization of simulation and the recorded film, one is able to compare motion trajectories of objects and analyze differences in mutual location of the objects taking part in the entire process. Therefore it can be stated that the visualizing program VRBS makes possible:

- to analyze various scenarios of lowering lifeboat without incurring cost of real experiments,
- to easily identify dangerous moments during lowering process – impacts against ship's side, capsize of lifeboat,
- to check visually what has happened just before a dangerous situation and to verify motion parameters (acceleration, velocity, distance).

The information obtained this way is a very important element of analysis of considered case. It allows to interpret the data more comprehensively and faster than in the case of using numerical quantities only. Having at one's disposal both the program for numerical calculations (RESBO) and that for visualization of their results (VRBS), one is able to perform simulations which may be helpful in finding optimum scenarios for lifeboat lowering process and avoiding situations which may be hazardous to life and health of evacuated persons.

BIBLIOGRAPHY:

1. Al-Hussein M., Niaz M. A., Yu H., Kim H., Integrating 3D visualization and simulation for tower crane operations on construction sites. *Automation in Construction*, 15(5), pp. 554-562, (2006).
2. Benzley S. E., Merkley K., Blacker T. D., Schoof L., Pre- and post-processing for the finite element method. *Finite elements in analysis and design*, 19(4), pp. 243-260, (1995).
3. Craighead J., Murphy R., Burke J., Goldiez B., A survey of commercial & open source unmanned vehicle simulators. *2007 IEEE International Conference on Robotics and Automation*, pp. 852-857, (2007).
4. Dymarski P., Dymarski Cz., Computational model for simulation of lifeboat motions during its launching from ship in rough seas. *Polish Maritime Research*, Vol. 19 No. 3(75), pp. 45-52, DOI: 10.2478/v10012-012-0030-6, (2012).
5. Dymarski C., Dymarski P., Kniat A., Searching for critical conditions during lifeboat launching – simulations. *Polish Maritime Research*, Vol. 24 Special Issue 2017 S1 (93), pp. 53-58, DOI: 10.1515/pomr-2017-0021, (2017).

6. Roboris, <https://www.roboris.it/en/product/eureka-robot>.
7. Foley J. D., Van Dam A., Feiner S. K., Hughes J. F., Phillips R. L., Introduction to computer graphics. Addison-Wesley, (1994).
8. Haber R. B., Visualization techniques for engineering mechanics. Computing Systems in Engineering, 1(1), pp. 37-50, (1990).
9. Jan S. V. S., Clapworthy G. J., Rooze M., Visualization of combined motions in human joints. IEEE Computer Graphics and Applications, 18(6), pp. 10-14, (1998).
10. Kamat V. R., Martinez J. C., Dynamic 3D visualization of articulated construction equipment. Journal of computing in civil engineering, 19(4), pp. 356-368, (2005).
11. Kawasaki, <https://robotics.kawasaki.com/en1/products/other/simulation-OLP/index.html>.
12. Kerlow I. V., The art of 3D: computer animation and effects. John Wiley & Sons, (2004).
13. Bogdaniuk M., Kniat A., Puch W., Effective pre- and post-processors for FEM strength analysis using AutoCAD possibilities. MARINE TECHNOLOGY III, Book Series: MARINE AND MARITIME edited by: Graczyk T., Jastrzebski T., Brebbia CA., 3rd International Conference on Marine Technology (ODRA 99), 1, pp. 35-43, (2000).
14. Kniat A., Optimization Of Three-Dimensional Pipe Routing. Schiffstechnik (ShipTechnology Research), 47, pp. 111-114, (2000).
15. Koenig N., Howard A., Design and use paradigms for gazebo, an open-source multi-robot simulator. 2004 Proceedings of IEEE/RSJ International Conference on Intelligent Robots and Systems (IROS 2004), vol. 3, pp. 2149-2154, (2004).
16. Li Z., Kota S., Virtual Prototyping and Motion Simulation with ADAMS. J. Comput. Inf. Sci. Eng., 1(3), pp. 276-279, (2001).
17. Piegl L., Tiller W., The NURBS Book. Second Edition, Springer, (1997).
18. Shreiner D., Sellers G., Kessenich J., Licea-Kane B., OpenGL Programming Guide: The Official Guide to Learning OpenGL, 8th Edition, Addison-Wesley, (2013).

CONTACT WITH THE AUTHOR

Aleksander Kniat

Gdańsk University of Technology
11/12 Narutowicza St.
80 - 233 Gdańsk
POLAND

PROBLEMS OF THE STARTING AND OPERATING OF HYDRAULIC COMPONENTS AND SYSTEMS IN LOW AMBIENT TEMPERATURE (PART V)

METHODS ENSURING CORRECT START-UP OF HYDRAULIC COMPONENTS OF SHIP'S ONBOARD DEVICES IN LOW AMBIENT TEMPERATURES

Ryszard Jasiński
Gdańsk University of Technology, Poland

ABSTRACT

A large number of hydraulic devices and systems are started in low ambient temperatures. A good example of such a device is the hoisting winch on the ship. Starting hydraulic drive units in thermal shock conditions (rapid supply of hot oil to the cold unit) may lead to incorrect operation of the actuating system, for instance, due to the loss of clearance between cooperating elements. The article presents methods to prevent the disappearance of effective clearance in a hydraulic motor started in thermal shock conditions. For this reason, the structure of the hydraulic satellite motor was complemented by elements creating special channels through which hot oil could flow and additionally heat fixed parts of the motor. This solution ensures faster heating of motor housing, thus decreasing the temperature difference between the housing and the satellites during motor start-up in thermal shock conditions.

Keywords: hydraulic drive, hydraulic components, thermal shock, computer simulation

INTRODUCTION

Hydraulic drive is becoming more and more frequently used for driving ship's onboard devices [1, 2, 15], including various types of anchor, mooring, trawl-net, and loading winches, as well as deck cranes. The power of the hydraulic unit can reach 500 kW and more. High efficiency of hydraulic motors makes them competitive with other driving systems.

Compared to the electric drive, the hydraulic drive used in anchor and loading installations reveals the following advantages:

- high energy efficiency from mass or volume unit,
- simple structure,
- simple and effective overload protection,
- possibility to assemble the device from standard components,
- shorter start-up and shut-down times of hydraulic motors, compared to electric motors,
- lower power consumption during start-up.

Basic components of the hydraulic system of the ship's onboard equipment are pumps, hydraulic motors, and valves. In each of those components energy losses take place, which are defined as volumetric, pressure and mechanical losses. Exact values of these losses for a given hydraulic device are determined in steady-state conditions, neglecting, as a rule, the effect of heat transfer inside the device on the total energy loss balance [13, 14, 16-22, 25]. During the hydraulic machine start-up, the heat transfer between the working medium and machine elements affects significantly the efficiency of energy conversion in this machine, especially in the case of cold machine supplied with hot working medium, which was proved in [3-10], among other sources. Therefore, analysing the issues concerning start-ups of hydraulic components of ships onboard devices in low ambient temperatures is advisable and justified.

Some disadvantages of deck installations with hydraulic drives can also be named. One of them is difficult start-up

in low ambient temperatures. In lower temperatures the resistance of the flow of hydraulic medium through hydraulic installations and components is higher, due to higher viscosity of the medium. Consequently, situations frequently occur in which the heated working medium is supplied to cold onboard units (thermal shock conditions) [3-10, 24]. These situations may lead to incorrect operation of the installation, which is impermissible from the safety point of view. Hydraulic motors should meet the requirements of Polish Standard [30] and Polish Register of Shipping [26-28].

The article presents methods to prevent incorrect operation of hydraulic components started in thermal shock conditions.

STARTING HYDRAULIC MOTORS IN THERMAL SHOCK CONDITIONS

When a hydraulic unit is started in low ambient temperatures, certain difficulties in its correct operation can be observed. Among other cases, Fig. 1, the cold hydraulic motor can be supplied with oil having higher temperature than the motor, all this leading to thermal shock conditions. Moreover, this start-up can be accompanied by uneven heating of component elements, due to different structural and material properties, which is also a possible source of incorrect component operation.

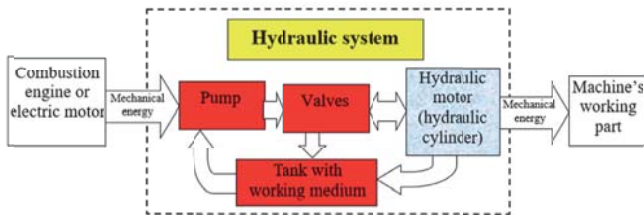


Fig. 1. Structure of hydraulic system: marked cold hydraulic motor supplied with hot working medium [3]

Low-speed hydraulic motors without axial clearance compensation, such as: satellite motor SOK [29, 31] or orbital motors [32], can work incorrectly when started in thermal shock conditions. The behaviour of some motors in those

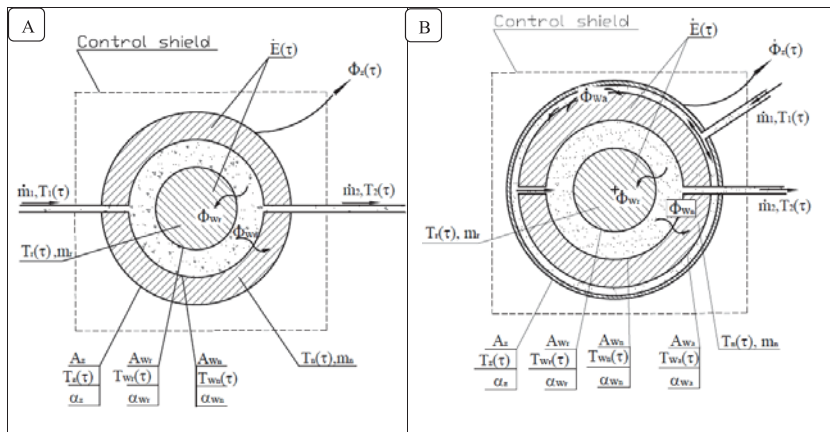


Fig. 2. Models of cold motor heating by the flowing hot fluid [3, 4, 6, 10]: (A) without additional channels in fixed elements (housing); (B) with additional channels in fixed elements (housing) (A – surface, T – temperature, m – mass, α – heat transfer coefficient, \dot{m} – mass flux, $\dot{\Phi}$ – thermal energy flux, \dot{E} – flux of energy increase of motor elements,

Symbols: W_n – inner surface of fixed elements without additional channels, W_a – inner surface of additional channels, W_r – outer surface of mobile elements, z – outer, r – mobile elements, n – fixed elements, a – additional element (overlay) creating additional channels in fixed elements, 1 – inlet, 2 – outlet

conditions and the accompanying phenomena are described in [3, 6-10].

METHODS TO PREVENT THE DISAPPEARANCE OF EFFECTIVE CLEARANCE IN HYDRAULIC MOTORS STARTED IN THERMAL SHOCK CONDITIONS

There are several methods to prevent the disappearance of effective clearance between cooperating elements in hydraulic motors during their start-up in thermal shock conditions. This can be obtained by:

- using a hydraulic motor with a large heat transfer surface between oil and fixed motor elements (housing), which will ensure relatively small changes of effective clearance between cooperating elements during motor start-up,
- designing and manufacturing special motor,
- using structural materials with different linear thermal expansion for hydraulic motor elements,
- additional heating of fixed hydraulic motor elements (housing) before and during the start-up. This can be obtained by using additional elements to create special channels and thus increase the heat transfer surface between the flowing oil and the fixed motor elements (housing),
- electric heating of the housing,
- heating the motor elements before the start-up by hot oil flowing through the inner space of the motor housing (casing space).

MODELS OF HEATING OF HYDRAULIC MOTOR ELEMENTS

The hydraulic motor comprises two groups of elements: mobile and fixed. Figure 2 shows models of hydraulic motor heating. The difference between them is that in the second model, Fig. 2.B, the fixed elements of the motor (housing) have additional channels through which the hydraulic fluid flows. During the motor start-up in thermal shock conditions,

the hot oil flowing through these channels created by the element placed on the motor intensifies the heating of motor housing. The additional heat transfer surface between the oil and the fixed elements, Fig. 2.B, causes their faster heating than in the case shown in Fig. 2.A.

In the motor model shown in Fig. 2, the inlet and outlet mass fluxes are equal: $m_1 = m_2$.

During the motor start-up in thermal shock conditions, the thermal energy flux from oil $\dot{\Phi}_\alpha$ to mobile elements $\dot{\Phi}_{wr}$ and fixed elements $\dot{\Phi}_{wn}$ of the motor without additional channels in housing is equal to [3, 5, 6, 10, 23]:

$$\dot{\Phi}_\alpha(\tau) = \dot{\Phi}_{wr}(\tau) + \dot{\Phi}_{wn}(\tau) \quad (1)$$

$$\dot{\Phi}_\alpha(\tau) = \alpha_{wr} \cdot A_{wr} \cdot (T_{ol} - T_{wr}(\tau)) + \alpha_{wn} \cdot A_{wn} \cdot (T_{ol} - T_{wn}(\tau)) \quad (2)$$

where:

T_{ol} - average temperature of oil,
r- refers to mobile elements,
n- refers to fixed elements.

The thermal energy flux from oil to fixed elements of the motor with additional channels in housing, $\dot{\Phi}_N$, is equal to the sum of the thermal energy flux from oil to the inner surfaces of fixed elements of the motor, $\dot{\Phi}_{wn}$, and that to the surfaces of additional channels, $\dot{\Phi}_{wa}$ [3, 6]:

$$\dot{\Phi}_N(\tau) = \dot{\Phi}_{wn}(\tau) + \dot{\Phi}_{wa}(\tau) \quad (3)$$

Assuming that the conditions of heat transfer from oil to the surfaces of additional channels are similar to those in the channels of fixed motor elements:

$$\alpha_{wn} = \alpha_{wa} \quad (4)$$

Equation (3) can be written in the form:

$$\dot{\Phi}_{wn}(\tau) + \dot{\Phi}_{wa}(\tau) = \alpha_{wn} \cdot (A_{wn} + A_{wa}) \cdot (T_{ol} - T_{wn}(\tau)) \quad (5)$$

where:

A_{wa} - outer surface of the motor washed by the flowing oil (motor with overlay)

The energy flowing from oil to fixed elements of the motor increases their internal energy (temperature) and the thermal energy flowing out through the outer surface to the environment:

$$\begin{aligned} (\dot{\Phi}_{wn}(\tau) + \dot{\Phi}_{wa}(\tau))d\tau &= (\alpha_{wn} \cdot (A_{wn} + A_{wa}) \cdot (T_{ol} - T_{wn}(\tau))) \cdot d\tau = \\ &= m_n \cdot c_n \cdot dT_n + \dot{\Phi}_z \cdot d\tau \end{aligned} \quad (6)$$

where:

c_n - average specific heat of fixed elements,

dT_n - increase of average temperature in fixed elements.

In Equation (6), the flux of energy flowing to the environment, $\dot{\Phi}_z$, is omitted as very small during the motor start-up, since the external temperature of the motor is approximately equal to the ambient temperature $T_z(\tau) \approx T_{ot} \rightarrow \dot{\Phi}_z \approx 0$. The use of overlay decreases the outer surface of the motor which is in direct contact with the environment.

After transforming Equation (6), the relationship between the temperature of fixed elements and time takes the form [5, 10]

$$T_n(\tau) = T_{ol} - \Delta T_{ol-ot} \cdot e^{-\sigma_n \cdot \tau} \quad (7)$$

where:

$\sigma_n = \frac{\alpha_n \cdot (A_{wn} + A_{wa}) \cdot \psi_n}{m_n \cdot c_n}$ - the rate of heating of fixed elements

[3, 5, 10] (the mass of overlay is neglected due to its small contact with fixed elements of the motor),

$\Delta T_{ol-ot} = T_{ol} - T_{ot}$ - difference between oil temperature T_{ol} and ambient temperature T_{ot} ,

ψ_n, ψ_r - coefficient of non-uniform temperature distribution in fixed and mobile motor elements, respectively [3, 5, 10],

c_n, c_r - specific heat of fixed and mobile motor elements, respectively.

The effective clearance l_e between cooperating motor elements depends on the assembly clearance l_m , the difference of thermal expansion Δl_t of elements, and deformations of elements Δl_p caused by the action of pressure:

$$l_e(\tau) = l_m + \Delta l_p(\tau) - \Delta l_t(\tau) \quad (8)$$

$$\begin{aligned} l_e(\tau) &= l_m + \Delta l_p(\tau) + (T_{ol} - T_0) \cdot (h_n \cdot \beta_n - h_r \cdot \beta_r) + \\ &+ \Delta T_{ol-ot} \cdot (h_r \cdot \beta_r \cdot e^{-\sigma_r \cdot \tau} - h_n \cdot \beta_n \cdot e^{-\sigma_n \cdot \tau}) \end{aligned}$$

Making use of Equations (7) and (8) along with Equation: $T_r(\tau) = T_{ol} - \Delta T_{ol-ot} \cdot e^{-\sigma_r \cdot \tau}$, the effective clearance can be given as:

$$\quad (9)$$

where:

$\sigma_r = \frac{\alpha_r \cdot A_{wr} \cdot \psi_r}{m_r \cdot c_r}$ - rate of heating of mobile element [3, 5, 10].

β_r, β_n - linear thermal expansion coefficient of mobile element (r) and fixed element (n), respectively.

When starting the motor in thermal shock conditions, the effective clearance will not disappear ($l_c > 0$), assuming that the effect of pressure on motor elements is small, if the following inequality is fulfilled [3, 10]:

$$l_m + (T_{ol} - T_0) \cdot (h_n \cdot \beta_n - h_r \cdot \beta_r) + \Delta T_{ol-ot} \cdot (h_r \cdot \beta_r \cdot e^{\frac{-\alpha_r \cdot A_{Wr} \cdot \psi_r \cdot \tau}{m_r \cdot c_r}} - h_n \cdot \beta_n \cdot e^{\frac{-\alpha_n \cdot (A_{Wn} + A_{Wn}) \cdot \psi_n \cdot \tau}{m_n \cdot c_n}}) > 0 \quad (10)$$

According to Equation (10), the dimension of the effective clearance is affected by: heat transfer surfaces, masses of elements, specific heats of elements, heat transfer coefficient from oil to motor surfaces, initial clearance, and the difference between oil temperature and ambient temperature.

ADDITIONAL HEATING OF HYDRAULIC MOTOR HOUSING

The housing of the hydraulic component started in thermal shock conditions can be additionally heated to prevent the disappearance of the effective clearance. This heating can be executed by the flow of hot oil through the inner space of the housing, or heating the housing in another way, electrically, for instance.

Both methods consist in delivering additional heat to the housing (fixed elements) of the hydraulic motor.

The housing of the satellite motor SOK does not have an inner chamber through which hot oil could flow and heat it before the start-up. This solution would allow to increase the temperature of motor elements before the motor start-up in low ambient temperatures. In terms of safety, the best method is the use of an additional element (overlay) placed on the satellite motor SOK to create special channels through which hot oil can flow and heat the outer surface of the motor

housing, (Fig. 3). This way the total surface of heat transfer from oil to fixed motor elements (housing) is increased.

Compared do other types of low-speed motor structures, the advantage of satellite motors is their small overall dimension with respect to absorbency, and easy assembling of the overlay over the motor. The article presents a selected structure of the overlay [4, 6, 11, 12, 24].

Hot oil flows in through the overlay connector (Fig. 3) and flows around the outer surface of the motor, heating it. After leaving the overlay through the other connector, the oil flows via a pipe (not shown in the figure) to the motor collector. By using the overlay on the satellite motor SOK 100, the heat transfer surface from oil to fixed elements is increased by nearly twice.

TESTING THE SATELLITE MOTOR SOK IN THERMAL SHOCK CONDITIONS

Some publications [3-10] describe the performance of the motor SOK 100 (geometric working volume 0,4 dm³/rev) in thermal shock conditions, along with the accompanying phenomena. Satellite motors SOK are produced without axial clearance compensation.

The satellite motors SOK are sensitive to thermal shock conditions. The start-up at large temperature difference between hot oil and cold motor can lead to incorrect operation of the motor.

The operation of the satellite motor SOK 100 was tested at the ambient temperature equal to -20 °C (in the cooling chamber) and the oil temperature equal to 50 °C.

During this test, incorrect operation of the hydraulic motor was recorded in the form of the disappearance of effective clearances between satellites and covers, and between rotor and covers.

Initially, the pressure at motor inlet increased to about 7,2 MPa (Fig. 4). Then, after about 150 seconds from the start-up, the operation of the motor stabilised. The inlet and outlet pressures were equal to 2 MPa, and 1 MPa, respectively.

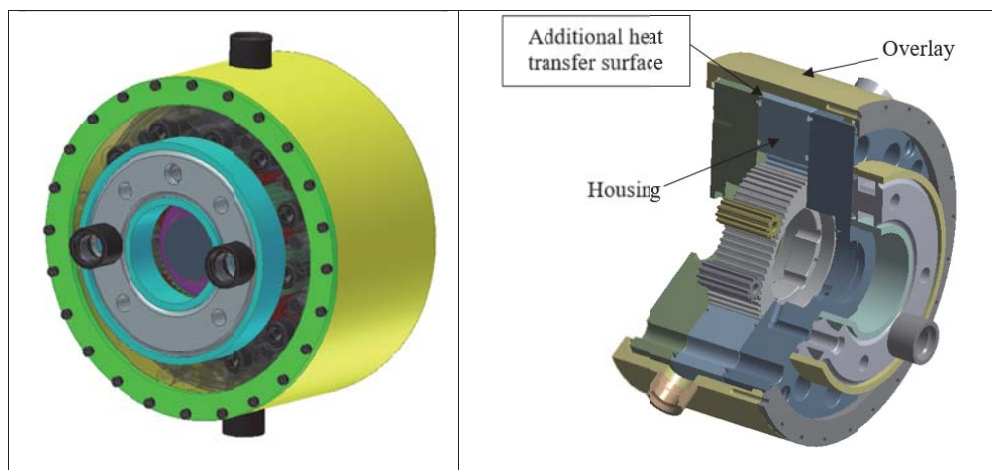


Fig. 3. Model of satellite motor SOK with heating system of fixed elements [4, 6, 11, 12]

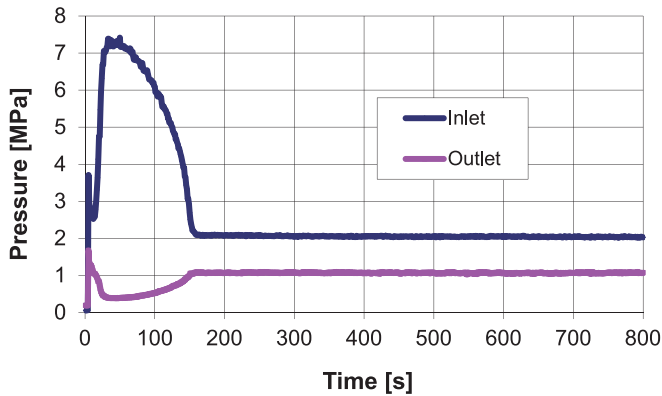


Fig. 4. Inlet and outlet pressure time-histories of unloaded motor [5, 8]

During the first few seconds after the motor start-up, the rotational speed increased to nearly 250 rpm and then decreased to about 90 rpm (Fig. 5). Between second 35 and 150 from the start-up, the rotational speed increased gradually to about 255 rpm and then remained stable.

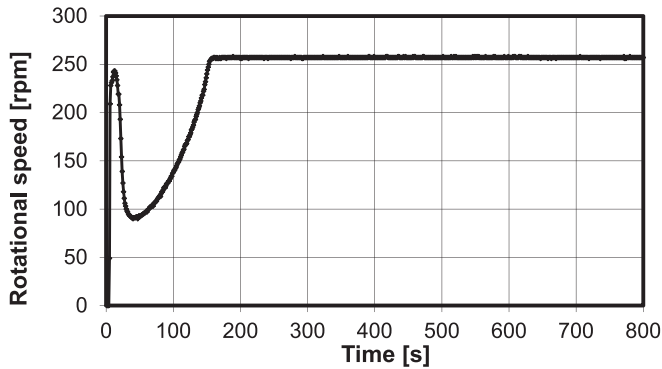


Fig. 5. Time-history of rotational speed [5]

The rotor temperature in the initial time interval increased rapidly to reach 60 °C after 120 seconds. The friction between the rotor, satellites, and covers led to the temperature increase, mainly in mobile elements. At second 120, the rotor temperature was higher by 10 °C than the temperature of oil supplied to the motor (Fig. 6).

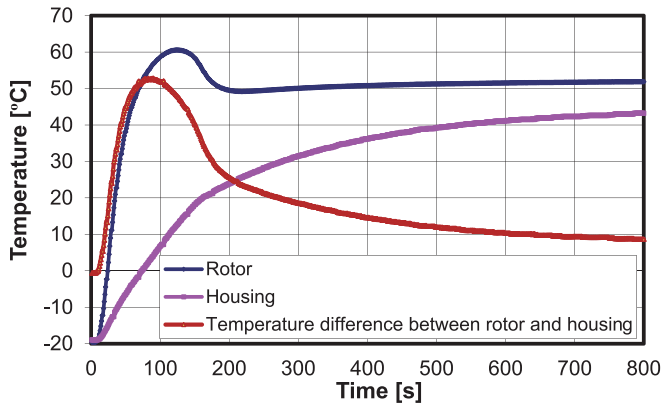


Fig. 6. Temperature of rotor and housing, and temperature difference between these elements, for start-up parameters [5, 9]: initial motor temperature -20 °C, oil temperature 50 °C, rotational speed in steady-state conditions 255 rpm

The effective clearance between the cooperating elements was determined using Equation (8).

At second 60, the effective clearance between the rotor and the covers disappeared, and this state lasted until second 130 (Fig. 7).

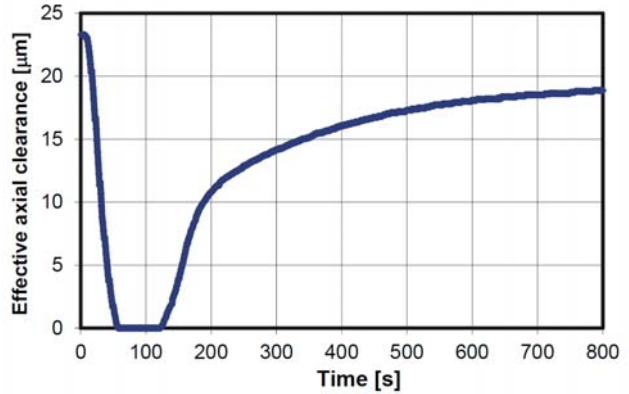


Fig. 7. Effective clearance between rotor and covers, for start-up parameters [5, 9]: initial motor temperature -20 °C, oil temperature 50 °C, rotational speed in steady-state conditions 255 rpm

The results of experimental tests made the basis for determining heat transfer coefficients from oil to mobile and fixed elements of the satellite motor SOK 100. These data were used for computer simulation of heating of SOK 100 motor elements.

A computer simulation test was performed for the following start-up parameters: initial motor temperature -20 °C, oil temperature 50 °C, rotational speed in steady-state conditions 255 rpm. The following boundary conditions were assumed: heat transfer coefficient from oil to fixed elements 1460 W/m²K, heat transfer coefficient from oil to mobile elements 1150 W/m²K, and heat transfer coefficient from outer surface to environment 12 W/m²K.

Based on the obtained results of computer simulation, including temperature characteristics of mobile and fixed motor elements, the analysis of the course of motor heating was performed. The element which warmed up the fastest was the satellite. At second 80, in nominal operating conditions its temperature should become already stable, (Fig. 8), while during incorrect motor operation, mobile elements warmed up to temperatures higher than the oil temperature (Fig. 6).

The satellite, rotor, and housing temperature characteristics obtained from computer simulation (Fig. 8) were used for determining temperature differences between satellites and housing, and between rotor and housing, (Fig. 9).

ANALYSING THE HEATING PROCESS DURING START-UP OF SATELLITE MOTOR SOK WITH ADDITIONAL HEATING OF HOUSING IN THERMAL SHOCK CONDITIONS

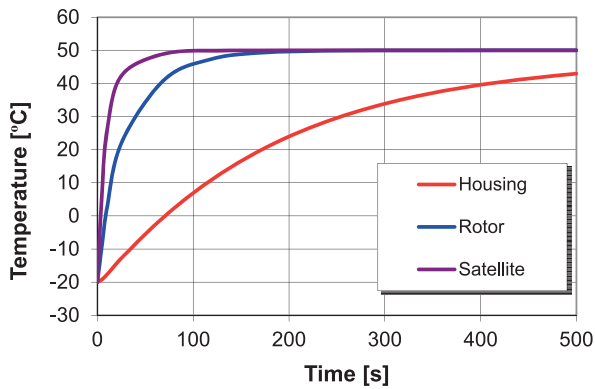


Fig. 8. Temperature changes in housing, rotor and satellite obtained from computer simulation, for start-up parameters: initial motor temperature -20°C , oil temperature 50°C , rotational speed in steady-state conditions 255 rpm

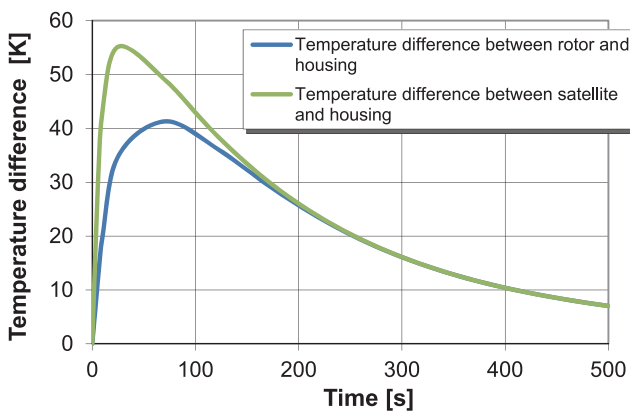


Fig. 9. Temperature differences between rotor and housing, and between satellite and housing, for start-up parameters: initial motor temperature -20°C , oil temperature 50°C , rotational speed in steady-state conditions 255 rpm

Based on the temperature difference between satellite and housing, the effective clearance between satellites and covers was calculated from Equation (8). At second 15, the effective clearance between satellites and covers disappeared, and this lack of clearance lasted until second 75 (Fig. 10). In fact, incorrect motor operation could last longer, as the computer simulation neglected the heat of friction between satellites and covers, and between rotor and covers.

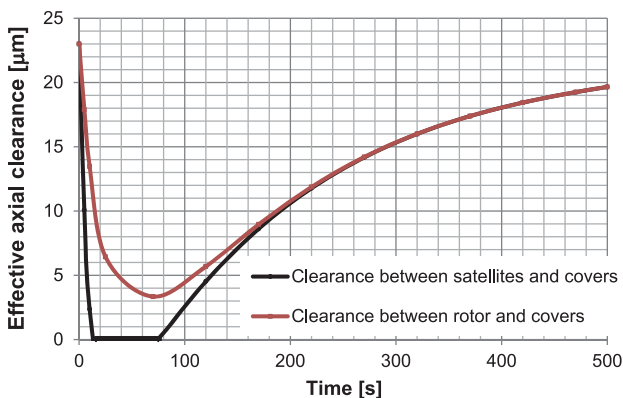


Fig. 10. Effective clearance between satellites and covers, and between rotor and covers, for start-up parameters [6]: initial motor temperature -20°C , oil temperature 50°C , rotational speed in steady-state conditions 255 rpm

A computer simulation test was performed to study the heating of elements of the satellite motor SOK 100 with additional heating of housing executed with the aid of an overlay. The test was performed for the same start-up conditions in which incorrect motor operation had been recorded: ambient temperature -20°C , oil temperature 50°C , and rotational speed in steady-state conditions 255 rpm (Fig. 11).

The shape of the overlay was designed in such a way as to obtain a similar average flow velocity in the channel created by the overlay and the housing to that observed in inner motor channels. This assumption justified assuming the same value of heat transfer coefficient as for the inner motor channels, i.e. $1460\text{ W/m}^2\text{K}$. For mobile elements, the assumed heat transfer coefficient from oil to elements was $1150\text{ W/m}^2\text{K}$, while on the outer motor and overlay surfaces this coefficient was assumed equal to $12\text{ W/m}^2\text{K}$.

The use of an additional channel in the motor through which hot oil could flow resulted in faster heating of the motor housing. In Fig. 12, after second 320 from motor start-up, steady-state heat flow conditions can be already observed, unlike the case of motor without overlay (Fig. 6).

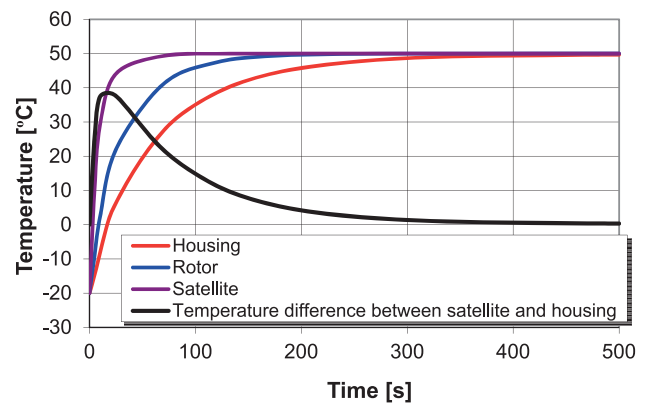


Fig. 12. Temperature changes in housing, rotor and satellite, and temperature difference between satellite and housing during start-up of satellite motor SOK 100 with overlay

The highest temperature difference between satellite and housing was recorded at second 18 and was equal to 38 K (Fig. 12). For the assumed high difference between the cold motor SOK 100 and the supplying hot oil, which amounted to 70 K, the effective clearance between satellites and covers was not entirely closed. It only decreased by $18\text{ }\mu\text{m}$ at second 18, to the value of $5\text{ }\mu\text{m}$ (Fig. 13).

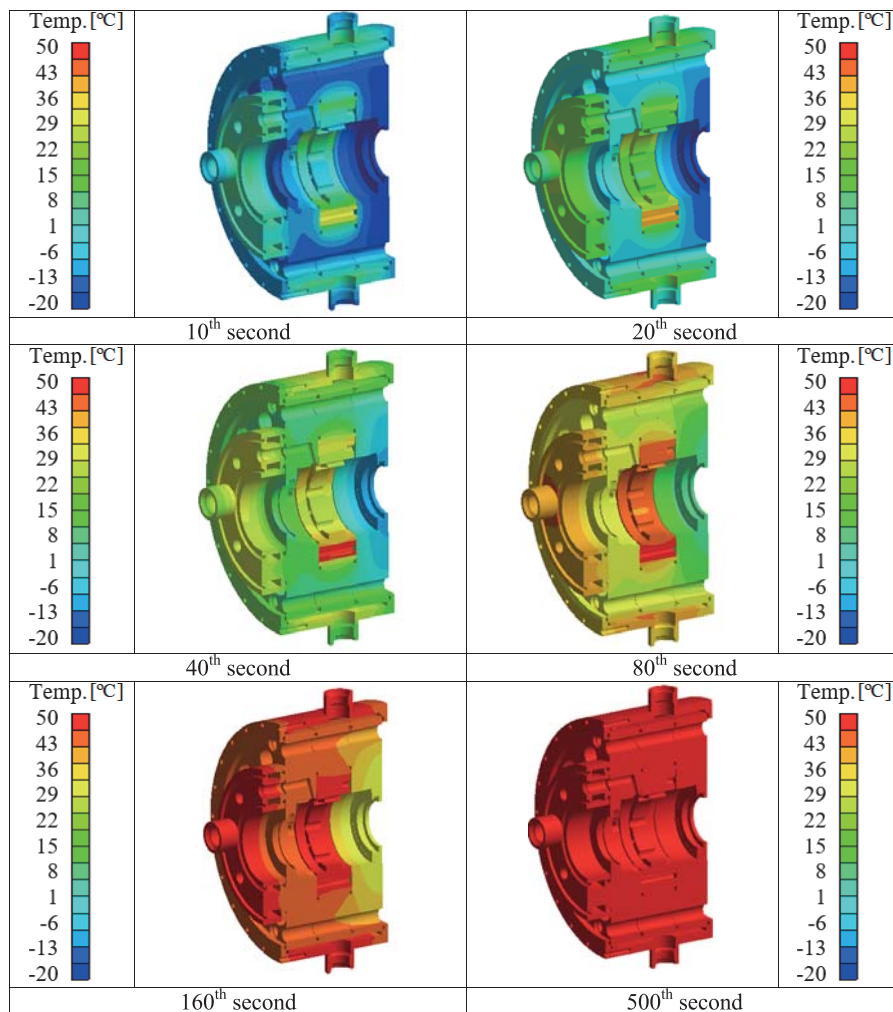


Fig. 11. Temperature distribution in warmed elements of satellite motor SOK 100 with overlay (initial motor temperature -20 °C, rotational speed in steady-state conditions 255 rpm) at 10th, 20th, 40th, 80th, 160th and 500th second after the supply of oil of temperature 50°C [6]

ANALYSING THE HEATING PROCESS OF SOK MOTOR WITH OVERLAY FIXED TO HOISTING WINCH FRAME IN THERMAL SHOCK CONDITIONS

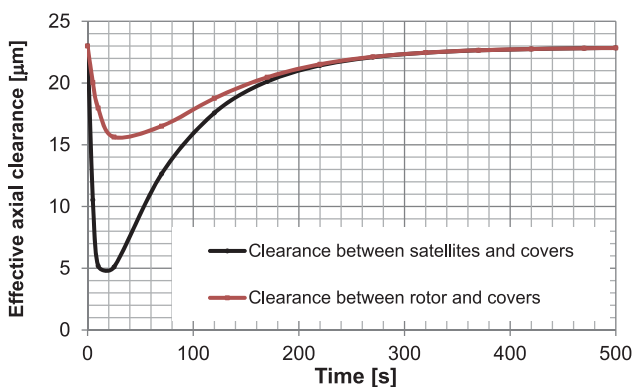


Fig. 13. Effective clearance between satellites and covers, and between rotor and covers, for start-up parameters of motor with overlay [6]: initial motor temperature -20 °C, oil temperature 50 °C, rotational speed in steady-state conditions 255 rpm

Analysing the heating process, in thermal shock conditions, of a motor which is not fixed to any machine or installation frame does not provide comprehensive information on the real course of heating of motor elements, and on changes of effective clearance between cooperating elements. That is why a model test was performed to study heating of elements of the SOK 100 motor with overlay fixed to the hoisting winch frame. During the start-up, the heating of fixed motor elements is expected to take a slower course due to the heat flux flow from these elements to the machine frame.

A computer simulation test was performed for the initial conditions: ambient temperature -20 °C, oil temperature 50 °C, rotational speed in steady-state conditions 255 rpm.

A numerical model of SOK 100 motor fixed to the frame being structural part of the hoisting winch was developed. The following boundary conditions were assumed in the calculations: heat transfer coefficient from oil to fixed elements equal to 1460 W/m²K, heat transfer coefficient from oil to mobile elements equal to 1150 W/m²K, and heat

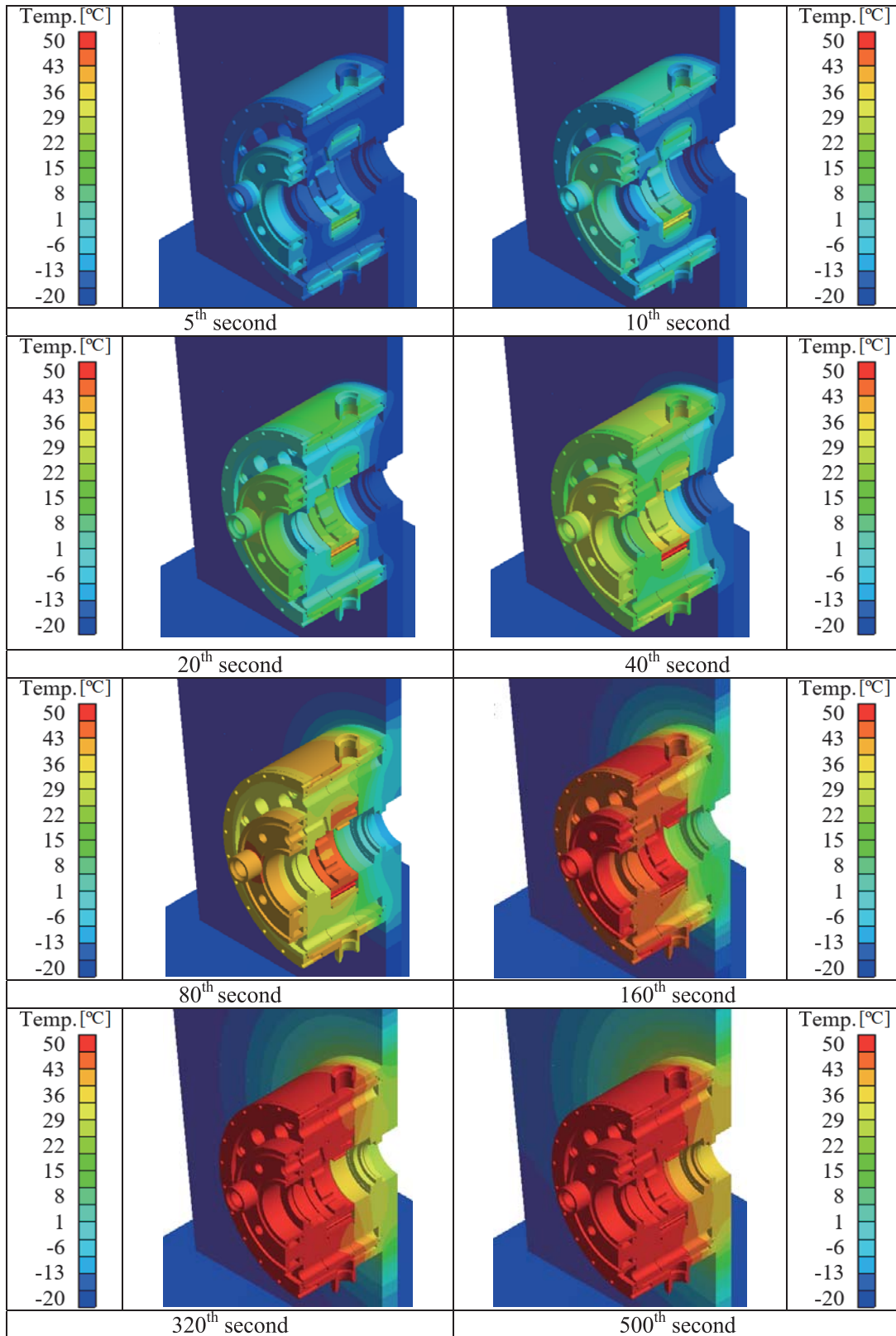


Fig. 14. Temperature distribution in warmed elements of satellite motor SOK 100 with overlay fixed to hoisting winch frame (initial temperature $-20\text{ }^{\circ}\text{C}$, rotational speed in steady-state conditions 255 rpm) at 5th, 10th, 20th, 40th, 80th, 160th, 320th and 500th second after the supply of oil of temperature $50\text{ }^{\circ}\text{C}$

transfer coefficient from outer surface to environment equal to $12\text{ W/m}^2\text{K}$.

In Fig.14, the flow of heat flux from the motor (front plate)

to the hoisting winch frame appears only at second 20 from the start-up and then gradually increases. After 320 seconds, the temperature of some fixed elements of the motor stabilises, while the warming up of the frame is continuing.

For the same start-up conditions, Fig. 15 shows the housing temperature time-histories for three models of satellite motor SOK 100:

- without overlay and without fixing to the hoisting winch frame,
- with overlay but without fixing to the hoisting winch frame,
- with overlay and fixed to the hoisting winch frame.

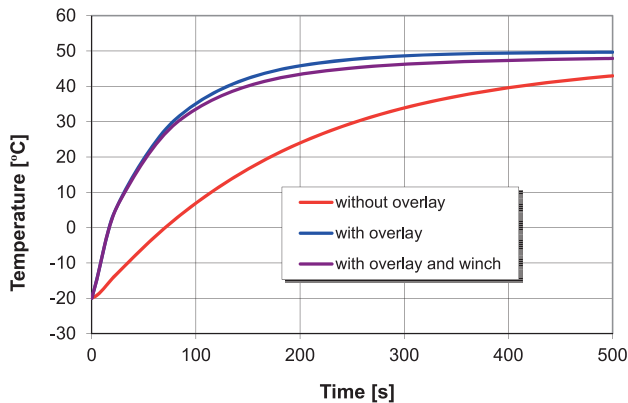


Fig. 15. Temperature of SOK motor housing during start-up in thermal shock conditions, for start-up parameters: initial motor temperature -20 °C, oil temperature 50 °C, rotational speed in steady-state conditions 255 rpm

The heating process of the SOK motor without overlay takes a much slower course than that of the motor with overlay. Additional elements which create channels through which hot oil flows make it possible to affect the operation of hydraulic components in different ambient conditions and the accompanying phenomena.

Fixing the motor to the hoisting winch frame does not cause considerable outflow of heat (and resultant cooling of motor housing), especially at the beginning of the start-up, when incorrect operation of the motor is mostly expected to occur. After 100 seconds, the housing temperature difference for the motor with overlay fixed and not fixed to the hoisting winch frame approximately equalled 2 K. This suggests that neglecting the heat outflow to the hoisting winch frame when modelling the process of motor heating in thermal shock conditions does not cause large error in assessing permissible conditions of correct start-up.

CONCLUSIONS

The structure of hydraulic motors affects their clearance change limits and, consequently, their operation in low ambient temperatures. When starting the motor in thermal shock conditions, the effective clearance between cooperating elements can totally disappear.

By using additional inner channels in the motor housing, the motor can be protected against the disappearance of clearances between cooperating elements (incorrect motor operation) during the start-up in thermal shock conditions.

Placing an overlay on the hydraulic motor increases the surface of heat transfer from hot oil, which contributes to better protection of the motor against incorrect operation in

thermal shock conditions, as shown for the case of the motor SOK 100 as an example.

The use of overlay on the motor increases the oil flow resistance and overall dimensions of the hydraulic component. The increase of oil flow resistance can be large when the motor is started in low ambient temperatures.

The most effective method to start the motor in thermal shock conditions is its earlier heating by the hot working medium flowing through the inner space of the housing (casing space) or through additional channels of the motor. Although it extends the time of motor preparation for correct start-up, this method is very effective, as it does not generate additional oil flow resistance during the start-up.

BIBLIOGRAPHY

1. Dymarski C.: An integrated hydraulic drive system of a novel device for launching lifeboats from large passenger ship. Polish Maritime Research. Vol. 19, 1/2012.
2. Dziejwski W.: Outline of machine hydraulics in shipbuilding industry (in Polish), Wydawnictwo Morskie, Gdansk 1985.
3. Jasiński R.: Influence of design of hydraulic motors on their operation in low ambient temperatures (in Polish). International Scientific-Technical Conference „Hydraulics and Pneumatics'2007”, Wrocław, 2007.
4. Jasiński R.: Research and method for assessment of operation of hydraulic drive components started in low ambient temperature and supplied with hot working medium (in Polish). Report on execution of the research project financed by Polish Ministry of Science and Higher Education (in Polish), No. 4 T07C042 30, Gdansk 2010.
5. Jasiński R.: Operation of selected low-speed hydraulic motors in thermal shock conditions (in Polish). Ph.D. thesis, supervisor: A. Balawender. Gdansk 2002.
6. Jasiński R.: Influence of design of hydraulic components on their operation in low ambient temperatures. Key Engineering Materials, Fundamentals of Machine Design, Vol. 490, 2012.
7. Jasiński R.: Methodology of examination of low-speed hydraulic motors in thermal shock conditions (in Polish), IX Seminar on drives and control 2003, Gdansk, 2003.
8. Jasiński R.: Problems of the starting and operating of hydraulic components and systems in low ambient temperature (Part I). Polish Maritime Research, 4/2008.
9. Jasiński R.: Problems of the starting and operating of hydraulic components and systems in low ambient temperature (Part II). Determining the clearance between

- cooperating elements during the hydraulic components start-up in extremely low ambient temperatures on the grounds of experimental research. Polish Maritime Research, 1/2009.
10. Jasiński R.: Problems of the starting and operating of hydraulic components and systems in low ambient temperature (Part III). Methods of determining parameters for correct start-ups of hydraulic components and systems in low ambient temperatures. Polish Maritime Research, 4/2009.
 11. Jasiński R.: System for heating a cold hydraulic satellite motor (in Polish). Patent no. 214740. Patent application no. P.393921 accepted by UP RP in 2011.
 12. Jasiński R., Zelewski J.: Protection system for a hydraulic satellite motor started in thermal shock conditions (in Polish). Patent PL 224464. Patent application P393922 accepted by UP RP in 2011.
 13. Landvogt B.; Osiecki L.; Patrosz P.; Zawistowski T.; Zylinski B.: Numerical simulation of fluid-structure interaction in the design process for a new axial hydraulic pump. Progress in Computational Fluid Dynamics. Vol. 14, No. 1, 2014. Doi: 10.1504/PCFD.2014.059198.
 14. Pobedza J., Sobczyk A.: Properties of high pressure water hydraulic components with modern coatings. Advanced Materials Research. Trans Tech Publications Ltd, 849/2014. doi: 10.4028/www.scientific.net/AMR.849.100.
 15. Smotrycki S.: Marine hydraulic drives (in Polish), Wydawnictwo Morskie, Gdansk, 1970.
 16. Śliwiński P.: Influence of water and mineral oil on the leaks in satellite motor commutation unit clearances. Polish Maritime Research, vol. 24, 3(95) 2017. Doi: 10.1515/pomr-2017-0090.
 17. Śliwiński P.: The influence of water and mineral oil on the mechanical losses in a hydraulic motor. Chinese Journal of Mechanical Engineering. Article accepted for publication.
 18. Śliwiński P.: The influence of water and mineral oil on volumetric losses in a hydraulic motor. Polish Maritime Research, vol. 24, 2017. Doi: 10.1515/pomr-2017-0041.
 19. Śliwiński P.: The basics of design and experimental tests of the commutation unit of a hydraulic satellite motor. Archives of Civil and Mechanical Engineering, No 16/2016, DOI: 10.1016/j.acme.2016.04.003.
 20. Śliwiński P.: The flow of liquid in flat gaps of satellite motors working mechanism. Polish Maritime Research, No 2/2014.
 21. Śliwiński P.: New satellite pumps. Key Engineering Materials, No 490/2012.
 22. Walczak P., Sobczyk A.: Simulation of water hydraulic control system of Francis turbine. American Society of Mechanical Engineers, 2014. doi: dx.doi.org/10.1115/FPNI2014-7814.
 23. Wiśniewski S., Wiśniewski T.: Heat transfer (in Polish). WNT, Warsaw 2000.
 24. Zelewski J.: Modernisation project of a satellite motor without axial clearance compensation, resistant to thermal shock conditions, in application to hydraulic ship deck hoisting winch (in Polish). Diploma thesis, supervisor: R. Jasiński, Gdansk University of Technology, 2004.
 25. Złoto T., Nagorka A.: An efficient FEM for pressure analysis of oil film in a piston pump. Applied Mathematics and Mechanics, vol.30, No 1/2009.
 26. Environmental tests of ship equipment (in Polish). Polish Register of Shipping, Gdansk, 1975.
 27. Polish Register of Shipping, "Publication 11P" (in Polish), 1994.
 28. Polish Register of Shipping, "Rules for the Classification and Construction of Sea-going Ships" (in Polish), 2002.
 29. Technical information documentation: Hydraulic motors SOK produced by ZUO Hydroster (in Polish).
 30. PN-86/M-73079 "General conditions of use of unified hydraulics system" (in Polish).
 31. Information on <http://hydro-precyzja.pl>.
 32. Catalogues of companies: Bosch-Rexroth, Sauer-Danfoss, Parker.

CONTACT WITH THE AUTHOR

Ryszard Jasiński

Gdańsk University of Technology
11/12 Narutowicza St.
80 - 233 Gdańsk
POLAND

FEATURES OF LOAD AND WEAR OF MAIN PROPULSION DEVICES ON SEA-GOING SHIPS WITH PISTON COMBUSTION ENGINES AND THEIR IMPACT ON CHANGES IN TECHNICAL STATES OF THE SYSTEMS

Jerzy Girtler

Gdańsk University of Technology, Poland

ABSTRACT

The paper presents the specificity of operation of propulsion systems of seagoing ships which causes the need to control the load on them, especially on their engines called main engines. The characteristics of the load on the propulsion systems, especially on the main engines as well as on the shaft lines and propellers driven by the engines, along with the process of wear in tribological joints (sliding tribological systems) of the machines have been described herein. Using examples of typical types of wear (both linear and volumetric) for the tribological systems of this sort, interpretation of states of their wear has been provided with regards to the wear levels defined as acceptable, unacceptable and catastrophic. The following hypotheses have been formulated: 1) hypothesis explaining necessity to consider the loads on the systems under operation as stochastic processes; 2) hypothesis explaining a possibility of considering the processes as stationary; and 3) hypothesis explaining why it can be assumed that a given technical state of any tribological system can be considered as dependent only on the directly preceding state and stochastically independent of the states that existed earlier. Accepting the hypotheses as true, a four-state continuous-time semi-Markov process has been proposed in the form of a model of changes in condition of a propulsion system (PS) of any ship. The model includes the most significant states affecting safety of a ship at sea, such as: s_0 – PS ability state, s_1 – PS disability state due to damage to the main engine (ME), s_2 – PS disability state due to damage to the shaft line (SL) and s_3 – PS disability state due to damage to the propeller (P). Probability of occurrence (changes) of the states has also been demonstrated.

Keywords: load, reciprocating internal combustion engine, seagoing ship, propulsion system of a ship, wear

INTRODUCTION

Propulsion systems on sea-going ships are consisted of one propulsion unit (Fig. 1) or many propulsion units of various design solutions [1, 18, 37]. In case of large commercial ships like general cargo ships, bulk carriers, containerships, tankers, the one-engine, one-shaft (one-propeller) propulsion systems without reduction gear are used. The main devices of such propulsion systems are: main engine (SG), screw propeller (SN) and shaftline connecting SG with SN (Fig. 1). The main engine is a slow-speed, self-ignition combustion engine of large or great power, and the screw propeller more and more often is that of controllable pitch (CPP). The shaftline of the propulsion systems in question is consisted of such devices

as: thrust shaft and propeller shaft (sometimes intermediate shaft), thrust bearing and shaft journal bearings, clutch, brake and turning gear. Excessive linear (surface) wear and/or volumetric wear of any of the above mentioned devices of an arbitrary propulsion system of every ship, causes failure of the system.

Rational operation of propulsion systems on sea-going ships consists in, a.o., the appropriate controlling of changes in their energy states and, resulting from them, thermal and mechanical loads affecting their devices, especially their main tribological links (systems). In the case of engines, the following belong to such links: pistons – piston rings – cylinder sleeves as well as main and crankshaft bearings. In the case of controllable pitch propellers (SNoSN) with

electro-hydraulic control over the propeller pitch change mechanism (MZSS), the following should be counted among the crucial tribological links: piston- cylinder link of MZSS ram, piston-cylinder link of distribution slider and propeller blade bearings. And, in the case of shaftline the most important tribological links are: thrust bearing and journal bearings [4, 13, 15, 27, 36, 37, 43].

Run of wear processes in the above mentioned systems, both concerning surface and volumetric wear, strictly depends on execution of control process over thermal and mechanical loads of the specified devices of ship propulsion systems. Wear processes of any propulsion system of any ship result in change of technical state of the system. In the most simple manner, the following states may be distinguished: the serviceability state (s_0) of the propulsion system (UN), its unserviceability state (s_1) resulting from failure of the main engine (SG), its unserviceability state (s_2) resulting from failure of the shaftline (LW) and its unserviceability state (s_3) resulting from failure of the controllable pitch propeller (SNoSN). In this situation it is interesting for propulsion system's user how big probabilities (respectively – P_0, P_1, P_2, P_3) of occurrence of the mentioned technical states in a longer duration time of its operation (theoretically for $t \rightarrow \infty$), are.

The probabilities mean: P_0 – probability of UN serviceability, P_1 – probability of UN unserviceability due to SG failure, P_2 – probability of UN unserviceability due to LW failure, P_3 – probability of UN unserviceability due to SN failure. Determination of the probabilities requires to use a mathematical model assumptions for which would be appropriate to features of load and wear processes in such devices of ship propulsion systems (Fig. 1) as the main engine (SG), shaftline (LW) and controllable pitch propeller (SNoSN).

FEATURES OF LOADS OF PROPULSION SYSTEMS ON SEA-GOING SHIPS, WHICH ARE MAIN CAUSES OF THEIR FAILURES

Features of loads of propulsion systems on sea-going ships, considered to be main causes of their failures, may be described in a similar way like qualities of loads of tribological links in piston-crankshaft systems of main engines (SG), which were already discussed in detail in [18]. A schematic diagram of a propulsion system, such as that shown in Fig. 1, was presented in [1, 42]. Fig. 1 shows also exemplary causes of UN unserviceability state: a – failure of SNoSN, b – failure of SG. In the case of large commercial ships (tankers, bulk carriers, containerships) such units simultaneously serve as their propulsion systems. Loads on propulsion systems of every sea-going ship are also so significantly varying during ship operation as loads in SG tribological links [11, 15, 18, 26, 27, 36, 37, 40, 41]. The loading depends on atmospheric and sea conditions which are especially unfavourable during storm weather, as well as on effective power of the engine loaded within a given working area. The power output depends

on fuel dose as well as wear of tribological links, especially those of main engines, such as pistons, rings and cylinder sleeves as well as main and crankshaft bearings.

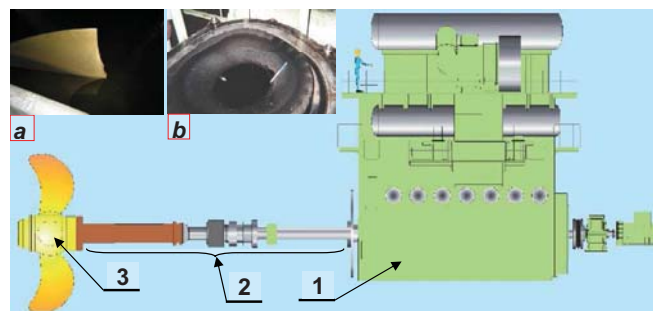


Fig. 1. Propulsion system (UN) usually applied on large commercial ships (tankers, general cargo ships, bulk carriers, containerships):
1 – slow-speed, two-stroke main engine (SG),
2 – shaftline (LW), 3 – controllable pitch screw propeller (SNoSN),
a – a view on a broken blade of the SNoSN, b – a view on a SG piston head with a burnt-through hole

Excessive wear and a failure resulting from the loading upon any device of the propulsion system (SG, LW, SNoSN) causes failure of the system. The determining of the mentioned probabilities P_0, P_1, P_2, P_3 requires to work out such mathematical model as to reflect physical feature of the loading upon the system UN and first of all on tribological links of the SG – the crucial device.

Both the mechanical (Q_M) and thermal (Q_C) loads upon elements of tribological links of the controllable pitch propellers (SNoSN), shaftline (LW) [41, 43, 47] and main engines (SG) vary randomly, sometimes in a broad range, along with time [6, 16, 21, 24, 22, 30, 40].

Therefore during operation phase the loading $Q(t)$ upon tribological links of such engines as well as those of shaftlines and screw propellers should be considered to be a stochastic process comprising its mechanical component $Q_M(t)$ and thermal one $Q_C(t)$, that may be expressed as follows [18]

$$Q(t) = f[Q_M(t), Q_C(t)] \quad (1)$$

where:

- Q – loading upon the engine;
- Q_M – mechanical loading upon the engine;
- Q_C – thermal loading upon the engine ;
- t – duration time of engine operation.

Hence, in empirical investigations on the loading, two stochastic processes $\{Q_M(t); t \geq 0\}$ and $\{Q_C(t); t \geq 0\}$ being components of the process $\{Q(t); t \geq 0\}$, can be considered [18].

As results from the considerations presented in [18], it is possible to formulate a hypothesis H_1 which says that: loading process of any propulsion system (i.e. its main engine, shaftline, screw propeller) is stochastic process because values of the loading upon the system, assigned to arbitrary time instant t , are random variables.

In case of every self-ignition engine, different values of its operational indices (parameters) which characterize the

loading upon devices of a given propulsion system, can be recorded. The indices are random variables and the events of reaching a given or another value of the indices are random [15, 18, 41].

As results from the investigations have been made so far, some quantities, e.g. p_e , c_{sr} [18, 26, 32, 34], characterize both mechanical and thermal loading. It obviously means that between mechanical loading and thermal loading some relations exist. As they are random processes, it may be concluded that the relations may be expected stochastic. The problem was highlighted in the work [18] in the form of a hypothesis from which it results that between the mechanical loading $Q_M(t)$ and thermal loading $Q_C(t)$ a stochastic relation takes place. As results also from this work, for a longer time of operation of the system, the hypothesis H_2 which says that: “the loading upon the propulsion system is a stationary process because in a longer time of its operation there is no monotonicity of changes in the loading upon its main engine as well as of changes in the loading upon its screw propeller and shaftline, which are strictly associated with the engine loading”, may be considered true. [18, 22, 27].

The hypothesis can be considered true because, as it results from the so far conducted tests of self-ignition engines, when the time interval (Θ), called range, between particular loads increases then correlation between them decreases. Therefore load values measured in the mutually far-distant time intervals may be considered independent. This feature is called asymptotic independence of load value. It occurs if the range Θ increases (Fig. 2 and 3). The independence may be proved by analyzing engine load values in the time intervals mutually far distant (e.g. by the Θ). Dependence between the loads will be low and the lower the greater the time interval (range) Θ . An example of such relation is shown in Fig.1 where changes in temperature, pressure, heat emission rate and fuel dose in cylinder (engine working space) during compression of fresh charge, fuel combustion and decompression of exhaust gas, are illustrated. The experiment whose result is given in Fig. 3, revealed consequences of lessening tension in injector spring. The lessening of the injector spring tension was simulated by applying a thinner choke. As a result, a lower pressure at injector’s opening and lower injection pressure was obtained, that results in a lower velocity of fuel flow from spray nozzles and consequently a lower quality of fuel spraying. This is effected in increasing delay of self ignition [44] and in consequence in increasing maximum combustion pressure and its occurrence angle becomes close to GMP. It is accompanied sometimes with significant increase of pressure rate ($dp/d\alpha$) in cylinder as well as increase of exhaust gas temperature (t_w) and mean indicated pressure (p_i). As a result, engine working space and consequently its piston-crankshaft system is thermally overloaded (Q_C) and mechanically (Q_M) as well [26, 27, 33, 34, 36, 41, 43].

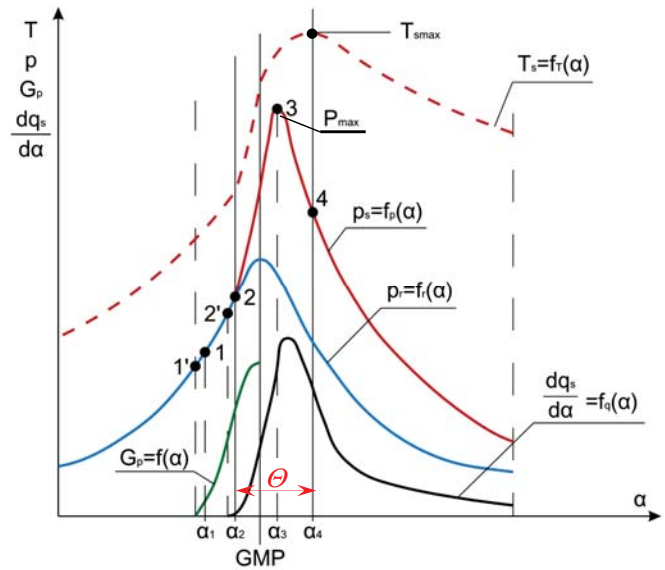


Fig. 2. Schematic diagram of run of changes in pressure and temperature as well as fuel dose and heat emission rate in cylinder of self-ignition engine, dealing with the parameters:

p - pressure, T - temperature, α - crankshaft rotation angle, $p_s = p_{max}$ - maximum combustion pressure, T_{smax} - maximum temperature, G_p - fuel dose, q_s - specific heat emitted during combustion, $dq_s/d\alpha$ - heat emission rate values in cylinder, 1 - beginning of fuel pressure by injection pump, 1' - beginning of fuel injection into combustion chamber, 2 - formation of first sources of fuel self-ignition, 2' - beginning of fuel combustion in cylinder, 3 - maximum combustion pressure, 4 - maximum combustion temperature, Θ - duration time of engine operation

The asymptotic independence of load values increases when engine wear grows. The question was signalled with growing injector spring wear which causes the lowering of injector’s opening, as an example. (Fig. 3) [44].

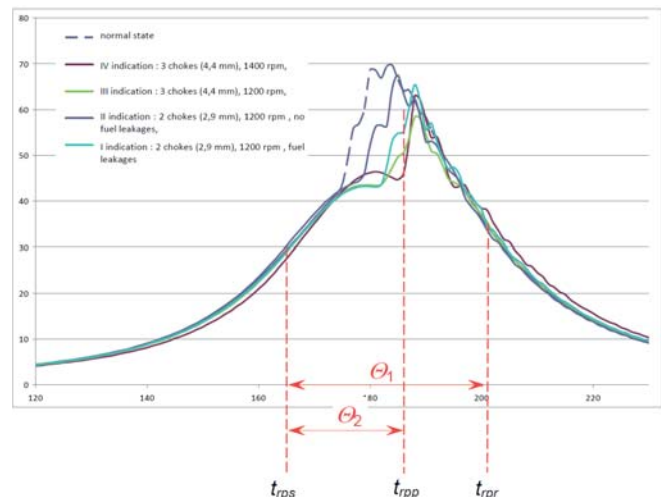


Fig. 3. Real image of indicator diagram's deformation resulting from a lower opening pressure of injector of the laboratory engine of ZS Faryman Diesel, type D [44], t_{rps} - a selected instant of execution of fresh charge compression process, t_{rpp} - a selected instant of execution of fuel combustion process t_{rpr} - a selected instant of execution of exhaust gas decompression process, Θ_1, Θ_2 - ranges of engine operation time intervals in whose beginnings and ends loads are determined.

As results from the presented considerations (Fig. 3), if the time interval (range) $\Delta t = \Theta$ increases, the loads upon the

propulsion system (*UN*), which occur in the instants being the ends of the interval, e.g. (t_{rps}, t_{rpp}) or (t_{rps}, t_{rpr}) , are more and more independent to each other. And, it is obvious that if the instants are the beginnings and ends of small intervals, i.e. when $dt = d\Theta$, then the loads in such instants will be mutually dependent. Therefore it may be acknowledged that the Markov condition in relation to the loading upon the *UN* may be formulated as follows: the load (thermal and mechanical) upon the propulsion system (*UN*) and simultaneously upon every device belonging to the system, i.e. the main engine (*SG*), shaftline (*LW*) and controllable pitch screw propeller (*SNoSN*), occurring in a given time instant, and its duration time depend only on the load directly preceding it and not on the loads which occurred earlier and their duration time intervals. Moreover, from the above presented hypothesis H_1 results that the loading which occurs during operation of the *UN* may be considered a stochastic process. It means that for description of the loads in function of time the theory of semi-Markov processes may be used. The conclusion may also implicate that for description of *UN* wear resulting from its loading during service of the system, the semi-Markov processes theory may be also applied.

Differentiated (random) loads (see e.g. Fig. 3) cause irregular run of wear process in particular tribological links as well as random spread of wear rate in the combustion engine systems [6, 11, 16, 25, 39]. For this reason it is necessary to identify features of the wear processes in tribological links of propulsion systems, especially in their main engines.

FEATURES OF WEAR PROCESS IN TRIBOLOGICAL LINKS OF ENGINES

The run of wear process in an arbitrary tribological link of the main engine (*SG*), shaftline (*LW*) and controllable pitch screw propeller (*SNoSN*) is influenced by initial quality of the system as well as random spread of its wear rate resulting from varying loads and lubrication conditions [6, 15, 25, 35, 39].

The run of wear process in tribological links of an arbitrary device of propulsion system (*SG*, *LW*, *SNoSN*) may be generally represented by the commonly known Lorence curve which is one of many models applicable to investigation of changes in states of such systems in a given time instant [6, 15, 35, 39]. In such case, while considering run of surface (linear) wear process in a given tribological link, the following states may be taken into account: the state z_0 – in which grinding-in takes place, state z_1 – in which usual stable wear occurs, state z_2 – in which quasi-failure wear happens, state z_3 – which may lead to failure-generating wear (accelerated, disastrous) and is undesired for this reason (Fig. 4).

Run of surface wear process in all the states $z_i \in Z (i = 0, 1, 2, 3)$ depends on many factors but first of all on loads upon particular tribological links. While analyzing wear process in any tribological link according to Lorence curve (Fig. 4), some its limit values may be distinguished, i.e. such wear values of a given system whose exceedance results in qualitative change in features of the system.

The following values may be certainly counted among those of practical usefulness:

- the initial wear value (z_p) which occurs after passing the time interval $(0, t_p]$ during which the tribological system's wear z_0 assuring its correct grinding-in, was present;
- the permissible wear value (z_d) which occurs after passing the time interval $(t_p, t_d]$ during which the tribological system's wear z_1 (called quasi-stable, normal wear) was present;
- the inadmissible wear (failure-generating, ultimate) value (z_n) which occurs after passing the time interval $(t_d, t_n]$ in which the tribological system's wear z_2 being in – between stable and disastrous one, takes place – i.e. that in which the initial wear of friction surfaces of the system appears, e.g. due to occurrence of initial symptoms of the seizing-up in the system,
- the disastrous wear value (z_k) which appears after passing the time interval (t_n, t_k) during which accelerated (failure-generating, disastrous) wear showing initial phase of wearing the friction surfaces of the system took place first, that in consequence leads to growth of the seizing-up of surfaces of the system; the wear z_k occurred at the instant (t_k) is equivalent to disastrous (final) failure, e.g. due to seizing the system, bonding, welding its elements or melting its interacting surfaces etc., that makes its further work entirely impossible.

In case of volumetric wear, the value of disastrous wear ($Z_{k(b)}$) showing first micro-cracks and then macro-cracks, appears after passing the time interval $(0, t_k)$.

Interpretation of the above mentioned limit values is presented in Fig.4.

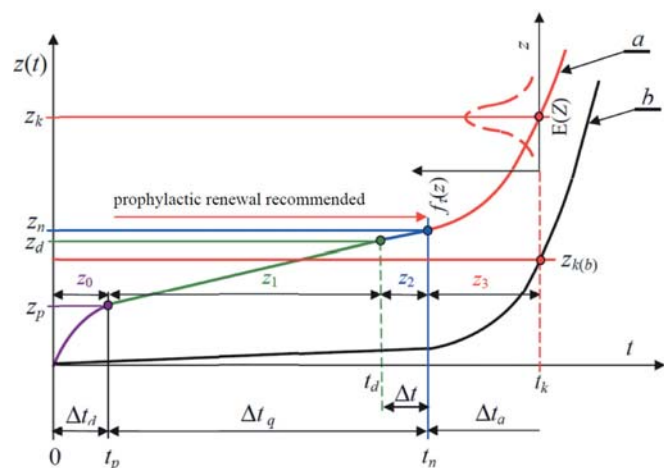


Fig. 4. Exemplary curves of typical runs of wear of slide tribological systems: a – linear wear curve, b – volumetric wear curve, z_p – permissible wear value, z_n – inadmissible wear value (failure generating, ultimate), z_k – disastrous wear value which causes failure of the system, $Z_{k(b)}$ – disastrous value of volumetric wear which causes failure of the system, Δt_d – time interval of grinding-in process, Δt_q – quasi-static (normal, stable) wear time interval, Δt_a – failure generating (accelerated, disastrous) wear time interval, z_0 – state of the system in which grinding-in takes place, z_1 – state of the system in which stable wear takes place, z_2 – state of the system in which quasi-failure wear takes place, z_3 – state of the system which is leading to failure-generating (accelerated, disastrous) wear, $f_i(z)$ – wear density function of the system, $E(Z)$ – expected wear value, z – wear random variable, Δt – time interval in which prophylactic servicing should start, t_p – the instant at which the value z is reached, t_d – the instant at which the value z_d is reached, t_n – the instant at which the value z_n is reached

For practical reasons every tribological system should be considered failed when its surface (linear) wear value reaches the permissible value (z_d). This results from that mean rate of surface (linear) wear of the system, in case of occurrence of the state z_3 , grows along with its operation time (curve "a" in Fig. 4). The same happens in case of volumetric wear (micro- and macro-cracks) (curve "b" in Fig. 4).

In order to prevent tribological systems (SG, LW, SNoSN) against failures appropriate servicing operations are applied to the UN devices leading to renewal of particular tribological systems. The servicing operations may be undertaken (depending on a decision situation) in the time when tribological systems are in the failure-generating wear state (z_3) or also when the systems are in the stable wear state (z_2). The second case occurs when it results from predictions of duration time of the state z_2 of a given tribological system that it is highly probable that the remaining duration time of the state will be shorter than the time necessary to complete the ship's task which can be fulfilled then and only then when in the above mentioned system the failure-generating (disastrous) wear does not appear. In case of occurrence of such wear a failure may happen in any tribological system and consequently also in the UN device containing such system. Every such failure is random event [6, 11, 15, 25, 39]. Therefore the process of subsequently following technical states should be considered to be the random process $\{W(t): t \geq 0\}$ whose values are the above distinguished states $s_i \in S(i = \overline{0,3})$ of the following interpretation:

- s_0 – serviceability state of the propulsion system (UN),
- s_1 – unserviceability state of the UN resulting from main engine (SG) failure,
- s_2 – unserviceability state of the UN resulting from shaftline (LW) failure and
- s_3 – unserviceability state of the UN resulting from failure of controllable pitch screw propeller (SNoSN).

The process $\{W(t): t \geq 0\}$ is characteristic of that the duration time T_i of the states $s_i \in S(i = \overline{0,3})$ is a non-odd random variable having the distribution function $F_i(t) = P(T_i < t)$, continuous density function $f_i(t) = \frac{dF_i(t)}{dt}$ and positive expected value $E(T_i) = \int_0^{\infty} t f_i(t) dt$.

The distributions $F_i(t)$ of random variables T_i and their expected values $E(T_i)$ can be determined by using results of properly conducted measurements of wear of particular tribological systems as well as the relationships (formulae) presented e.g. in the publications [6, 25, 35, 39, 45, 46, 47]. The duration time T_0 of the state s_0 depends on run (realization) of load and wear processes in the tribological systems of the UN. Whereas the duration times T_i of the states $s_i \in S(i = \overline{1,3})$ depend on run of servicing operations and resulting UN renewal. The renewal events are necessary in the case of appearing the above mentioned states $s_i \in S(i = \overline{1,3})$ resulting from failures in the UN devices, i.e. SG, LW and SNoSN, respectively.

As results from the presented analysis of loads upon the tribological systems the loads are random and for this reason it is not possible to precisely predict their values in an arbitrary

instant of operation. This results from unavoidable random changes in external factors as well as mutual interaction of friction elements of every tribological system and lubricating oil present between its elements. In case of considering loads upon an arbitrary tribological system (Fig. 2 and 3) in the instants far distant from each other by the time interval Θ , it may be assumed that the relation between the loads is insignificant and the lower the greater value of the above mentioned interval Θ [4, 5, 25, 30, 33]. It means that the loading of tribological systems is a process of asymptotically independent increases. Therefore the following hypothesis H_3 may be accepted: "every technical state $s_i \in S(i = \overline{0, 1, 2, 3})$ of an arbitrary tribological system as well as its duration time significantly depends on the state directly preceding it, but not on the earlier occurred states and their duration time intervals because its loading and both the rate and increases of wear, implicated by it, are processes of asymptotically independent values".

It means that it is possible to work out such model of changes in states (important for user) of every tribological system of the UN (in this case the states $s_i \in S(i = \overline{0, 1, 2, 3})$) as to make duration time of an arbitrary state of the process existing in the instant τ_n and that of the state possible to be obtained in the instant τ_{n+1} stochastically independent on the states which occurred earlier and their duration time intervals. To fulfil the conditions is possible by applying the theory of semi-Markov processes to determining reliability and lifetime of the considered tribological systems [13, 14, 15], and this way also of the UN. The presented features of loads and wear processes occurring in tribological systems of UN components (SG, LW, SNoSN) as well as existing possibilities to measure loads and wear of the systems [6, 15, 21, 25, 29, 31, 34, 36, 39] made it possible to formulate the conclusion that the semi-Markov process of an appropriate functional matrix and known initial distribution whose values are the earlier distinguished states $s_i \in S(i = \overline{0,3})$ may serve as a model of the process of changes in technical state of propulsion systems on sea-going ships.

MODEL OF CHANGES IN TECHNICAL STATES OF DEVICES CRUCIAL FOR SHIP SAFETY

In operation phase of propulsion systems (UN) their devices such as main engines (SG), shaftlines (LW) and controllable pitch scw propellers (SNoSN) suffer failures. The devices usually undergo renewal (of course if it is justified) as a result of appropriate servicing. Hence in the case of the devices in question, like in the case of other shipboard devices, model of process of changes in their reliability states may be considered to be the semi-Markov process $\{W(t): t \geq 0\}$ of the set of states $S = s_i; i = \overline{0, 1, 2, 3}$. Interpretation of the states $s_i \in S(i = \overline{0, 1, 2, 3})$, as already mentioned, is as follows:

- s_0 – serviceability state of propulsion system (UN),
- s_1 – unserviceability state of propulsion system (UN) resulting from main engine failure (SG),

s_2 – unserviceability state of propulsion system (UN) resulting from shaftline failure (LW) and
 s_3 – unserviceability state of propulsion system (UN) resulting from failure of controllible pitch sciew propeller (SNoSN).

Changes in the specified states $s_i (i = 0, 1, 2, 3)$ occur in subsequent instants $t_n (n \in \mathbb{N})$, whereas in the instant $t_0 = 0$ all the mentioned devices of the UN are in the state s_0 . The state s_0 lasts till the instant of failure of any of the devices. But the states $s_i (i = 1, 2, 3)$ last as long as one of the mentioned devices is renewed or replaced if its renewal is not justified. Changes of the states s_i into the states $s_j (i, j = 0, 1, 2, 3; i \neq j)$ occur after passing the time T_{ij} which is a random variable. Taking the situation into account in the operation phase of an arbitrary ship UN requires to use probabilistic description with accounting for probabilities of possible occurrence of the mentioned states $s_i (i = 0, 1, 2, 3)$ in particular instants $t_0, t_1, \dots, t_{n-1}, t_n$ of ship's UN operation time [2, 5, 6, 20, 23, 38]. As results from the presented considerations the mentioned states $s_i (i = 0, 1, 2, 3)$ so appear in particular instants of propulsion system's operation time as it is possible to state that:

- 1) the Markov condition is satisfied, namely, the future evolution of technical states of any device of ship propulsion system, i.e. its main engine, shaftline and screw propeller (and – consequently – process of changes in their technical states) depends only on a state existing in a given instant but not on functioning that propulsion system in the past, hence the future of the devices in question does not depend on its past but only on its present ;
- 2) the random variables T_i and T_{ij} have distributions other than exponential, where: T_i – stands for duration time of the state s_i irrespective of which state will follow it, and T_{ij} – stands for duration time of the state s_i under condition that the next state of the process will be the state s_j .

Hence it may be assumed that the state of the UN and consequently the state of the devices in question (SG, LW, SNoSN) in the instant t_{n+1} as well as the duration time interval of the state reached in the instant t_n does not depend on the states which occurred in the instants t_0, t_1, \dots, t_{n-1} as well as on their duration time intervals. Therefore the four-state, time-continuous, semi-Markov process $\{W(t): t \geq 0\}$ of the states s_0, s_1, s_2, s_3 may serve as a model of the real process $\{V(t): t \geq 0\}$ of changes in UN states [9, 15, 10, 12, 13, 30]. The graph of the process is given in Fig. 5.

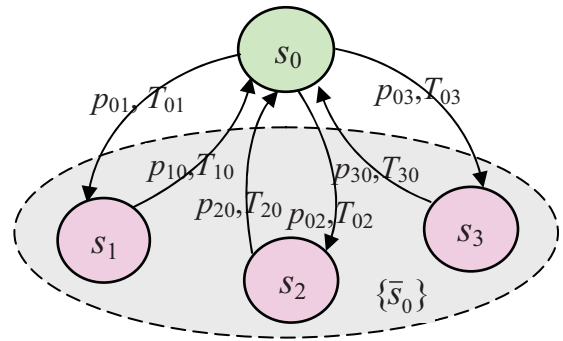


Fig. 5. Graph of changes in the states of the process $\{W(t): t \in T\}$:
 s_0 – serviceability state of UN, $\{\bar{s}_0\}$ – the set of unserviceability states of the devices (SG, LW, SNoSN): $\{\bar{s}_0\} = \{s_1, s_2, s_3\}$,
 $s_i \in S (i = 0, 1, 2, 3)$ – states of the following interpretation: s_0 – serviceability state of UN, s_1 – unserviceability state of UN due to main engine failure (SG), s_2 – unserviceability state of UN due to failure of shaftline (LW) and s_3 – unserviceability state of UN due to screw propeller failure (SNoSN),
 T_{ij} – duration time of the state s_i under condition that the next will be the state $s_j (i, j = 0, 1, 2, 3; i \neq j)$, p_{ij} – probability of passing the process $\{W(t): t \in T\}$ from the state s_i to the state $s_j (i, j = 0, 1, 2, 3; i \in j)$.

The initial distribution of the process is as follows:

$$P\{W(0) = s_i\} = \begin{cases} 1 & \text{dla } i = 0 \\ 0 & \text{dla } i = 1, 2, 3 \end{cases} \quad (2)$$

and its functional matrix has the following form:

$$Q(t) = \begin{bmatrix} 0 & Q_{01}(t) & Q_{02}(t) & Q_{03}(t) \\ Q_{10}(t) & 0 & 0 & 0 \\ Q_{20}(t) & 0 & 0 & 0 \\ Q_{30}(t) & 0 & 0 & 0 \end{bmatrix} \quad (3)$$

The functional matrix $Q(t)$ constitutes mathematical description of changes in the UN reliability states and consequently its devices in question. The non-zero elements $Q_{ij}(t)$ of the functional matrix $Q(t)$ depend on distributions of random variables which are time intervals of staying the process $\{W(t): t \geq 0\}$ in the states $s_i (s_i \in S)$. Elements of the matrix are probabilities of passing the considered process from the state s_i to the state $s_j (s_i, s_j \in S)$ during the time not longer that t , which are determined as follows [13, 15, 19]:

$$Q_{ij}(t) = P\{W(\tau_{n+1}) = s_j, \tau_{n+1} - \tau_n < t | W(\tau_n) = s_i\} = p_{ij} F_{ij}(t) \quad (4)$$

where:

p_{ij} – probability of passing the Markov uniform chain in one step:

$$p_{ij} = P\{W(\tau_{n+1}) = s_j | W(\tau_n) = s_i\} = \lim_{t \rightarrow \infty} Q_{ij}(t),$$

$F_{ij}(t)$ – distribution function of the random variable T_{ij} determining the duration time of the state s_i of the process $\{W(t): t \geq 0\}$ under condition that its next state will be the state s_j .

As results from the functional matrix $Q(t)$ (2), the matrix P of probabilities of passing the Markov chain inserted into the process, is the following [8, 9, 15, 19, 38]:

$$P = \begin{bmatrix} 0 & p_{01} & p_{02} & p_{03} \\ 1 & 0 & 0 & 0 \\ 1 & 0 & 0 & 0 \\ 1 & 0 & 0 & 0 \end{bmatrix} \quad (5)$$

In the process $\{W(t); t \geq 0\}$ the random variables T_{ij} have determined positive expected values. Therefore its distribution is limited [8, 9, 15, 19] as follows:

$$P_j = \lim_{t \rightarrow \infty} P_{ij}(t) = \lim_{t \rightarrow \infty} P\{W(t) = s_j\}, s_j \in S(j = 0, 1, 2, 3) \quad (6)$$

and has the following form:

$$P_j = \frac{\pi_j E(T_j)}{\sum_{k=0}^3 \pi_k E(T_k)} \quad (7)$$

The probabilities $\pi_j(j = 0, 1, 2, 3)$ in the formula (7) are limit probabilities of Markov chain inserted into the process $\{W(t); t \geq 0\}$. Whereas $E(T_j)$ and $E(T_k)$ are expected values of random variables in the state s_j and s_k , respectively, irrespective of which state the system will pass in the future to.

Determination of the limit distribution (7) requires to solve the set of equations which contain the above mentioned limit probabilities $\pi_j(j = 0, 1, 2, 3)$ of inserted Markov chain into the process $\{W(t); t \geq 0\}$ as well as the matrix P of probabilities of passing from the state s_i to the state s_j , determined by the formula (5). Such set has the following form:

$$\left. \begin{aligned} [\pi_0, \pi_1, \pi_2, \pi_3] &= [\pi_0, \pi_1, \pi_2, \pi_3] \cdot \begin{bmatrix} 0 & p_{01} & p_{02} & p_{03} \\ 1 & 0 & 0 & 0 \\ 1 & 0 & 0 & 0 \\ 1 & 0 & 0 & 0 \end{bmatrix} \\ \sum_{k=1}^4 \pi_k &= 1 \end{aligned} \right\} \quad (8)$$

As a result of solving the set of equations (8) it is possible to obtain, by using the formula (7), the following relations:

$$\left. \begin{aligned} P_0 &= \frac{E(T_0)}{E(T_0) + \sum_{k=1}^3 p_{0k} E(T_k)}, P_1 = \frac{p_{01} E(T_1)}{E(T_0) + \sum_{k=1}^3 p_{0k} E(T_k)}, P_2 = \frac{p_{02} E(T_2)}{E(T_0) + \sum_{k=1}^3 p_{0k} E(T_k)}, \\ P_3 &= \frac{p_{03} E(T_3)}{E(T_0) + \sum_{k=1}^3 p_{0k} E(T_k)} \end{aligned} \right\} \quad (9)$$

The probability P_0 is limit probability that in a longer time of operation (theoretically at $t \rightarrow \infty$) the devices in

question (SG, LW, SNoSN) remain in the state s_0 . Therefore the probability determines a technical operational availability factor of the UN as well as of the devices in question. Whereas the probabilities $P_j(j = 1, 2, 3)$ are limit probabilities of existence of the states $s_j \in S(j = 1, 2, 3)$ of the devices in question at $t \rightarrow \infty$, i.e. the probabilities of their passing to unavailability states due to failure.

Fig. 6 shows an exemplary realization of the process $\{W(t); t \geq 0\}$, which illustrates appearing the reliability states $s_j \in S(j = 1, 2, 3)$ of any UN and consequently its devices during operation. In order to obtain values of the probabilities $P_j(j = 0, 1, 2, 3)$ (of course approximate ones) it is necessary to estimate p_{ij} as well as $E(T_j)$.

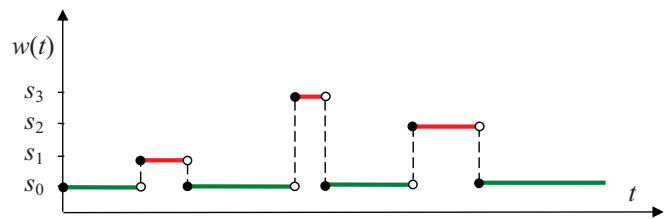


Fig. 6. Exemplary realization of the process $\{W(t); t \geq 0\}$ of ship's UN and its devices (SG, LW, SNoSN): s_0 - serviceability state of UN and its devices, s_1 - unavailability state of SG, s_2 - unavailability state of LW, s_3 - unavailability state of SNoSN.

To estimate the probabilities p_{ij} and the expected values $E(T_j)$ is possible after obtaining realization of $w(t)$ of the process $\{W(t); t \geq 0\}$ in an appropriately long time interval of observation, i.e. for $t \in [0, t_b]$, where the observation time of the process: $t_b \gg 0$. It is then possible to determine the numbers $n_{ij}(i, j = 0, 1, 2, 3; i \neq j)$ of transition of the process $\{W(t); t \geq 0\}$ from the state s_i to s_j in an appropriately long time and to determine values of the estimator \hat{P}_{ij} of unknown probability p_{ij} . The below given statistics [15, 19] is the highest credibility estimator for the transition probability p_{ij} :

$$\hat{P}_{ij} = \frac{N_{ij}}{\sum_j N_{ij}}, \quad i \neq j; \quad i, j = 0, 1, 2, 3, \quad (10)$$

whose value $\hat{p}_{ij} = \frac{n_{ij}}{\sum_j n_{ij}}$ is the valuation of unknown transition probability p_{ij} .

From the run $w(t)$ of the process $W(t)$ the realizations $t_j^{(m)}$, $m = 1, 2, \dots, n_j$ of the random variables T_j can be obtained. Due to application of point estimation it possible to easily estimate $E(T_j)$ as mean arithmetic value of the realizations $t_j^{(m)}$.

In order to obtain required information for estimation of the probabilities in question it is necessary to apply an appropriate diagnostic system (SDG) to the considered devices of the UN, which, in this case, are the diagnosed systems (SDN) [13, 15, 42, 43, 45, 46, 47].

FINAL REMARKS AND CONCLUSIONS

The formulae for determining the reliability indices of propulsion systems were worked out on the basis of application of limit distribution of the semi-Markov process $W(t): t \geq 0$. To determine such distribution is easier than the instantaneous distribution constituted by the functions $P_k(t)$ ($k = 0, 1, 2, 3$) which determine probabilities of the event that in an arbitrary instant t the process will be in the state $s_i \in S$ ($i = 0, 1, 2, 3$). Such distribution can be determined by using the initial distribution (2) of the process in question as well as the functions $P_{ij}(t)$ which determine the conditional probabilities (4), called also the probabilities of transition of the process from the state s_i to the state s_j ($s_i, s_j \in S, i, j = 1, 2, 3; i \neq j$). Calculation of the probabilities $P_k(t)$ consists in solving the set of Volterra 2nd kind integral equations [19] whose known quantities are (in this case) elements of the functional matrix (3).

Generally, when number of states is rather low and functional matrix – rather non-sophisticated in mathematical sense then the above mentioned set of equations can be solved by using operational calculus with the aid of Laplace-Stieltjes transform. A larger number of states or more complicated stochastic matrix makes that such set can be only solved in an approximate way by means of an appropriate numerical procedure.

The proposed semi-Markov process is the simplest model of changes in crucial states of ship propulsion systems (UN) and their devices such as SG , LW and $SNoSN$. Obviously, the model may be modified depending on needs resulting from utilitarian aims and/or cognitive ones assumed for investigations concerning every kind of the considered devices.

The presented model of the process of changes in states of UN devices is the four-state, time-continuous semi-Markov process.

The offered considerations concern first of all tribological systems of main engines (SG) such as their main and crankshaft bearings as well as the piston-piston rings-cylinder sleeve systems. However they are also applicable to thrust and journal bearings of shaftline (LW) as well as bearings of controllable pitch screw propellers ($SNoSN$), i.e. of such their units as pitch changing mechanism ($MZSS$), blade rotation mechanism ($MOSS$) and propeller transmitter (NSN).

Hypotheses have been proposed as to why it may be assumed that loading process of any propulsion system can be considered a stationary stochastic process of asymptotically independent increases as well as that there is a stochastic dependence between its thermal and mechanical loads.

The presented considerations concerning features of wear in propulsion systems (UN) were focused mainly on surface (linear) wear of slide bearings, but it was also mentioned that such features may be also assumed characteristic for volumetric wear (micro- and macro-cracks) of UN devices.

BIBLIOGRAPHY

1. Aeberli K.: *New high-economy engines for Panama containerhips and large tankers*, Wartsila Switzerland Ltd, Winterthur, September 2007.
2. Benjamin J. R., Cornell C. A.: *Probability calculus, mathematical statistics and decision theory for engineers* (in Polish). WNT, Warszawa 1977.
3. Bielaczyc P., Merkisz J., Pielecha J.: *Thermal state of combustion engine and emission of noxious compounds* (in Polish). Wydawnictwo Politechniki Poznańskiej, Poznań 2001.
4. Brun R.: *High-speed diesel engines* (in Polish). WKiŁ, Warszawa 1973. Original edition : Science et Technique du Moteur Diesel Industriel et de Transport. Copyright by Societe des Editions Technip ? et Institut Francais du Petrole, Paris 1967.
5. Firkowicz S.: *Statistical assessment of quality and reliability of electronic lamps* (in Polish). WNT, Warszawa 1963.
6. Gercbach I.B., Kordonski Ch.B.: *Reliability models of technical objects* (in Polish). WNT, Warszawa 1968.
7. Gichman I.I., Skorochod A.W.: *Introduction to theory of statistical processes* (in Polish) . PWN, Warszawa 1968.
8. Girtler J., Kuzmider S., Plewiński L.: *Selected issues of operation of sea-going ships in the aspect of navigation safety* (in Polish). Monograph. WSM, Szczecin 2003.
9. Girtler J., Kitowski Z., Kuriata A.: *Ship safety at sea. System's approach* (in Polish). WKiŁ, Warszawa 1995.
10. Girtler J.: *Probability as a measure of operational safety of technical objects* (in Polish). Materials of 7th Scientific Conference „ Safety of systems”. PTBiN, PTC, SPE KBM PAN, STST KT PAN, Wydział Transportu PW, ITWL, Warszawa-Zakopane-Kościelisko 1998, pp.163-168.
11. Girtler J.: *Stochastic model of load spectrum of self-ignition engine* (in Polish). Zagadnienia Eksploatacji Maszyn, PAN quarterly, iss. 1/97, 1994.
12. Girtler J.: *A concept of decision-making process with taking into account reliability and safety of sea transport means* (in Polish). Materials of Domestic Conference on Safety and Reliability, Vol.1. ITWL, Warszawa-Zakopane-Koscielisko 1999, pp. 289-296.
13. Girtler J.: *Diagnostics as a condition for control over ship combustion engines in operation* (in Polish). Studies No. 28. WSM, Szczecin 1997.

14. Girtler J.: *Physical aspects of application and usefulness of semi-Markov processes for modelling the processes occurring in operational phase of technical objects*. Polish Maritime Research, No. 3 (41)/2004, Vol. 11, pp. 25-30.
15. Girtler J.: *Control over ship combustion engines in operation on the basis of diagnostic decision – making process* (in Polish). ZN AMW, No. 100A, Gdynia 1989.
16. Girtler J.: *Stochastic model of operation process of ship combustion engine* (in Polish). ZEM, PAN, quarterly, iss. 2/1989, s. 79-88.
17. Girtler J.: *Quantum issues in diagnostics of marine energy machines and devices*. Zeszyty Naukowe Akademii Morskiej w Szczecinie, No. 30 (102), 2012, pp. 37-45.
18. Girtler J.: *Identification of damages of tribological associations in crankshaft and piston systems of two-stroke internal combustion engines used as main propulsion engines on sea-going vessels and proposal of probabilistic description of loads as causes of these damages*. Polish Maritime Research. No. 2 (86)/2015, Vol. 22, pp. 44 – 54.
19. Grabski F.: *Theory of semi-Markov processes of operation of technical objects* (in Polish). ZN WSMW, No. 75A, Gdynia, 1982.
20. Gniedenko B.W., Bielajew J.K., Sołowiew A.D.: *Mathematical methods in theory of reliability* (in Polish). WNT, Warszawa, 1968.
21. Höglund P.G., Ydstedt A.: *Reduced Air Pollution and Fuel Consumption with Preheated Car Engines*. Urban Transport and the Environment for the 21st Century, International Conference, Lisbon 1998.
22. Korczewski Z.: *Exhaust gas temperature measurements in diagnostics of turbocharged marine internal combustion engines. Part II: Dynamic measurements*. Polish Maritime Research. No. 1 (89)/2016, Vol. 23, pp. 68 – 76.
23. Krzysztofiak M., Urbanek D.: *Statistical methods* (in Polish). PWN, Warszawa 1979.
24. Lewitowicz J.: *Impact of physical processes onto diagnostic systems of technical objects* (in Polish). Materials of 3rd School of Systems Engineering. Warszawa-Kiekrz, ITWL 1987, pp. 71-85.
25. Niewczas A.: *Background for stochastic model of friction wear in issues of lifetime of machine elements* (in Polish). Zeszyty Naukowe, Mechanika, No. 19, Politechnika Radomska 1989.
26. Piotrowski I.: *Ship combustion engines* (in Polish). WM, Gdańsk 1971.
27. Piotrowski I., Witkowski K.: *Operation of ship combustion engines* (in Polish). Maritime Academy, Gdynia, 2002.
28. Plewiński L.: *Accidents at sea. Collisions of ships* (in Polish). Publ. WSM, Szczecin, 2000.
29. Rozanov Ju.A.: *Stacionarnyje slučajnyje processy* (in Russian). Fizmatgiz, Moskva 1963.
30. Rudnicki J.: *Application issues of the semi-Markov reliability model*. Polish Maritime Research. No. 1 (85)/2015, Vol. 22, pp. 55 – 64.
31. Voinov A.N.: *Sgoranie v bystrochodnych poršnevych dvigateliach* (in Russian). Mašinostroenie, Moskva, 1977.
32. Voznickij I.B., Ivanov Ł.A.: *Predotvrascenie avarij sudovych dvigatelej vnutrennego sgorania* (in Russian). Transport, Moskva, 1971.
33. Wajand J.A., Wajand J.T.: *Medium- and high-speed combustion engines* (in Polish). WNT, Warszawa, 2005.
34. Wieszkielski S.A., Łukianczenko B.S.: *Techniczeskaja ekspluatacja dvigatelej vnutrennego sgorania* (in Russian). Maszinostroenie, Leningrad, 1978.
35. Włodarski J.K.: *Piston combustion engines. Tribological processes* (in Polish). WKiŁ, Warszawa, 1981.
36. Włodarski J.K.: *Operational states of ship combustion engines* (in Polish). WSM, Gdynia, 1998.
37. Wojnowski W.: *Ship power plants* (in Polish). Publ. AMW, Gdynia, 1998.
38. *Reliability handbook* (in Polish). Multi-author work. Ed.: J. Migdalski, Wydawnictwa Przemysłu Maszynowego „WEMA”, Warszawa, 1982.
39. *Selected issues concerning wear of materials in sliding joints of machines* (in Polish). Multi-author work. Ed.: W. Zwierzycki. PWN, Warszawa-Poznań, 1990.
40. *Marine Chamber's statements on failures of main and auxiliary self-ignition combustion engines* (in Polish).
41. Girtler J.: *Identification of operational conditions of crankshaft-piston systems of ship main engines* (in Polish). A stage report on realization of the project No. N N509 494638 financed by MNiSW. The author's research project on: „Decision – making control over operation of crankshaft-piston systems of main propulsion engines on sea-going ships with application of technical diagnostics and taking into account safety and protection of the environment”. Project's supervisor: J. Girtler. Prace badawcze No. 1/10/PB. Faculty of Ocean

Engineering and Ship Technology, Gdańsk University of Technology, 2010.

42. Girtler J., Łosiewicz Z.: *Analysis of diagnostic model of engine crankshaft-piston systems, adjusted to needs of control of operation process of the engines in the aspect of ship and environment safety (in Polish). A stage report on realization of the project No. N N509 494638 financed by MNiSzW. The author's research project on: „Decision – making control over operation of crankshaft-piston systems of main propulsion engines on sea-going ships with application of technical diagnostics and taking into account safety and protection of the environment”*. Project's supervisor: J. Girtler. Prace badawcze No. 6/10/PB. Faculty of Ocean Engineering and Ship Technology, Gdańsk University of Technology, 2010.
43. Girtler J., Frydrych J.: *Analysis and assessment of usability of the worked out diagnostic system for ship main engines, intended for control of operation process of such engines in the aspect of assuring safety of ships and marine environment (in Polish). The author's research project on: „Decision – making control over operation of crankshaft-piston systems of main propulsion engines on sea-going ships with application of technical diagnostics and taking into account safety and protection of the environment”*. Project's supervisor: J. Girtler. Prace badawcze No. 4/12/PB. Faculty of Ocean Engineering and Ship Technology, Gdańsk University of Technology, 2012.
44. Korczewski Z.: *Determination of principles for verification of diagnostic model and its possible modification for needs of rational control over operation process of engines (in Polish). The work done within frames of the author's research project titled: „Decision – making control over operation of crankshaft-piston systems of main propulsion engines on sea-going ships with application of technical diagnostics and taking into account safety and protection of the environment”*. Project's supervisor: J. Girtler. Prace badawcze No. 28/11/PB. Faculty of Ocean Engineering and Ship Technology, Gdańsk University of Technology, 2011.
45. UP RP Patent No. 211232 issued for the invention: „The stand for preparation of classifiers for identification failure states of bearings, especially these in self-ignition engines, based on application of acoustic emission to form diagnostic signal “ (in Polish) Its authors: Jerzy Girtler, Wojciech Darski, Ireneusz Baran, Marek Nowak, Artur Olszewski, Jerzy Schmidt, Gdańsk University of Technology. The patent was worked out as a result of realization of the authors' research project No. N504 043 31/3480 financed by MNiSzW.
46. UP RP Patent No. 224702 issued for the invention: „The diagnostic system adjusted to identification of technical state of sleeves of slide bearings of piston combustion engines, based on application of acoustic emission to form diagnostic signal “ (in Polish). Its authors: Girtler J., Darski W., P. Darski, Gdańsk University of Technology. The patent was worked out as a result of realization of the authors' research project No. N N509 494638 financed by MNiSzW.
47. UP RP Patent No. 223940 issued for the invention: „The diagnostic system adjusted to identification of technical state of controllable pitch screw propeller for the needs of its operation control, especially on sea-going ships “ (in Polish). Its authors: Girtler J., Darski W., Frydrych J., Gdańsk University of Technology. The patent was worked out as a result of realization of the authors' research project No. N N509 494638 financed by MNiSzW.

CONTACT WITH THE AUTHOR

Jerzy Girtler

Gdańsk University of Technology
11/12 Narutowicza St.
80 - 233 Gdańsk
POLAND

METHOD OF BUILDING A MODEL OF OPERATIONAL CHANGES FOR THE MARINE COMBUSTION ENGINE DESCRIBING THE IMPACT OF THE DAMAGES OF THIS ENGINE ON THE CHARACTERISTICS OF ITS OPERATION PROCESS

Bogdan Landowski

UTP University of Science and Technology, Poland

Michał Pająk

University of Technology and Humanities in Radom, Poland

Bogdan Żółtowski

UTP University of Science and Technology, Poland

Łukasz Muślewski

UTP University of Science and Technology, Poland

ABSTRACT

This article deals with the modeling of the processes of operating both marine main and auxiliary engines. The paper presents a model of changes in operating conditions of ship's internal combustion engine. The semi-Markov decision process was used to mathematically describe the process model of the engine. The developed model describes the effect of engine damage on the characteristics of its operation.

A change in the input parameters of the model can simulate the influence of internal and external factors on the course of the analyzed process. A simplified calculation example is also presented for illustration purposes.

The presented method together with developed algorithms and IT tools can be used to solve a wide range of problems related to the operation of marine main engines and other marine equipment as well as maritime and port facilities. This concerns primarily the economic, risk management and operational security issues of complex technical systems, as well as the readiness and reliability analysis of technical facilities.

Keywords: process of operation, stochastic process, compression ignition engine, condition of object, operating condition

INTRODUCTION

Although shipping covers the transport of passengers and cargo is carried out between sea ports by ships, it is in the process of transport outside the ships in which other means of transport, equipment and handling systems and other complex technical facilities are used. Many of these means of transport and other technical facilities use compression-ignition internal combustion engines in their propulsion systems.

The paper presents the basic assumptions of the method of constructing a model of changes in operating conditions of a technical object describing the influence of its damage on the characteristics of the operation process. The analyzed technical object is a self-ignition internal combustion engine.

The paper deals with selected issues related to modeling, forecasting and controlling the operation process of a certain class of technical objects. Assisting the decision maker in the decision-making process is to evaluate the impact of the decision-making options on the course of the operation.

The study analyzed the process of change operating states of the internal combustion engine used in transport. As a result of the identification of the process of exploitation of the analyzed object, it was found that this is a non-homogeneous process.

Due to the purpose of research and the need to model sequences of object states in which the next state and process characteristics depend not only on the previous state but also on other factors for the mathematical modeling of the analyzed process of exploitation, the theory of Markov and semi-Markov processes was used.

The article presents the construction method and example of the model of the process of operation of technical objects, for which the periods of time of analyzed operating states, sequence of consecutive states, revenues and expenses related to staying in states depend not only on the current state but also on other factors.

As a result of the identification of the operation process of means of transport, finite sets of states and operations relevant to the efficiency of their operation were distinguished [14-18, 20].

The model describes, inter alia, the impact of the damage to the propulsion system, in particular its combustion-ignition internal combustion engine, on the course of the operation of such an important means of transport as a seagoing ship.

The operational process model was built on the basis of state space analysis and operational events on the analyzed facilities. The source data sets needed to develop the assumptions of the model and their initial verification were obtained as a result of performing operational research using a passive experiment.

Preliminary operational tests were conducted on a diesel self-combustion engine.

The change of the input parameters of the model can simulate the influence of internal and external factors on the course of the analyzed process. A simplified calculation example is also presented for illustration purposes.

MODELING THE PROCESS OF CHANGES IN ENGINE STATES

A natural model of the operation of many categories of technical objects is the random process $X(t)$ with a finite set of states S and a set of parameters R^+ (subset of real numbers ≥ 0) [15, 26, 27]. Stochastic homogeneous processes, including homogeneous Markov and semi-Markov processes [6, 8, 12-13, 18-20, 24-27] are commonly used for modeling changes in operating states. The use of the homogeneous Markov process to determine the means of decision-making for transport means is illustrated, inter alia, in [19]. This is an important simplification of real processes, which are generally characterized by heterogeneity. In the work on the use of Markov models and semi-Markov models, the assumed assumption of uniformity of modeled processes is generally not verified.

In the study, the states S_i ($i = 1, 2, 3, 4$) belonging to the set $S = \{s_1, s_2, s_3, s_4\}$ with the following interpretation were included:

s_1 – use status,

s_2 – correction state (fitness restoration),

s_3 – standby to use state,

s_4 – after repair state (so called after repair diagnosis), i.e. the state in which, after the restoration of the fitness of certain motor systems the engine state is examined.

The correctness of the execution of correction processes for damaged subsystems is assessed.

It was assumed that the initial model of the operation of the compression ignition engine used in maritime means of transport is a semi-Markov process that is continuous over time and discrete in the states. The operation state codes of the engine are in correlation to the states of the analyzed stochastic process $\{X_t, t \in T\}$, $t \geq 0$. It is assumed that the analyzed process $\{X_t, t \in T\}$, $t \geq 0$ with a finite set of states $S = \{s_1, s_2, s_3, s_4\}$ is a homogeneous process.

From the Markov property, for the analyzed process $\{X_t, t \in T\}$, $t \geq 0$ with a finite set of states S , the probability of transition is defined as follows [1,2,3,12,13,27]:

$$P\{X(\tau_{n+1})=s_j, \tau_{n+1}-\tau_n < t / X(\tau_n)=s_i\} = P\{X(\tau_{n+1})=s_j, \tau_{n+1}-\tau_n < t / X(\tau_n)=s_i, X(\tau_{n-1}), \dots, X(\tau_1), X(\tau_0), \tau_n - \tau_{n-1}, \dots, \tau_1 - \tau_0, \tau_0\} \quad (1)$$

where:

$S = \{s_1, s_2, s_3, s_4\}$ – set of process states $X(t)$,

$0 = \tau_0 < \tau_1 < \dots < \tau_{n-1} < \tau_n$ – random variables representing moments in which process state changes occur $X(t)$,

j, i – numbers of states, which are the values of the process $X(t)$, $j, i = 1, 2, 3, 4$,

n – the number of the step in which the process state changes $X(t)$, $n \in N$,

N – set of natural numbers.

The initial distribution of the process $X(t)$ can be expressed by the relation:

$$p_i = P\{X(0)=s_i\}, \quad s_i \in S, \quad i = 1, 2, 3, 4, \quad \sum_{i=1}^4 p_i = 1.$$

For a homogeneous semi-Markov process, a sequence of random variables $X(\tau_n)$, $n \in N$ is a homogeneous Markov chain with the probability of passing between states (in n -step) of the form:

$$p_{ij} = P\{X(\tau_{n+1})=s_j / X(\tau_n)=s_i\}, \quad i, j = 1, 2, 3, 4. \quad (2)$$

All Markov chain probability crossovers can be written together in the form of a matrix P called the probability matrix of the inserted Markov chain:

$$P=[p_{ij}] = \begin{bmatrix} p_{11} & p_{12} & p_{13} & p_{14} \\ p_{21} & p_{22} & p_{23} & p_{24} \\ p_{31} & p_{32} & p_{33} & p_{34} \\ p_{41} & p_{42} & p_{43} & p_{44} \end{bmatrix}, \quad i, j = 1, 2, 3, 4. \quad (3)$$

T_{ij} random variable representing the duration of the i -th state of the process $X(t)$ provided that the next state j , is expressed by the dependence:

$$F_{ij}(t) = P\{T_{ij} < t\} = P\{\tau_{n+1} - \tau_n < t / X(\tau_{n+1}) = s_j, X(\tau_n) = s_i\} \quad (4)$$

The factors based on the probability limits placed in the Markov chain's semi-Markov process and the values of the expected random variables representing the time intervals of the states are mainly determined.

Among many works [18, 20, 26, 27] as a criterion function z (the function of the target) a function is assumed whose value is the average profit (loss) that will bring per unit of time used in the system under investigation. This function is expressed by relation:

$$z = \frac{\sum_{i=1}^4 z_i p_i^* ET_i}{\sum_{i=1}^4 p_i^* ET_i}, \quad (5)$$

where:

z_i – profit per time unit associated with staying in a state s_i ,
 p_i^* – limit probability of an inserted Markov chain,
 ET_i – expected value of the random variable representing the residence time of the object in the process state s_i .

In many works, including [6-8, 12-13, 18, 20, 24-27] general properties of semi-Markov processes are described and their applicability to the analysis of processes of exploitation of technical objects is justified.

The use of semi-Markov processes to model the change process in operating and/or technical conditions of an internal combustion engines, including marine diesel engines, has been reported in [7, 10].

In many cases, changes in the technical condition or operating facility, including the internal combustion engine, are made in certain operations, decisions or occurrences of certain operational events affecting sequences of successive states, duration or economic characteristics of the process. In this case, decision-making stochastic processes may be useful for modeling changes in the state of an internal combustion engine.

Many researchers have taken up the problem of using both Markov chains [5], Markov processes [19, 22-23] and semi-Markov [1-3, 10, 11, 14, 16, 17, 20, 28] for mathematical modeling real processes, including the modeling of processes of changes in operating conditions of technical objects. In the literature of the subject one will find many articles concerning both theoretical description and examples of practical applications of this type of models. The use of decision-making semi-Markov processes for modeling changes in operating states and/or technical internal combustion engines, including main engines used for propulsion of ships, is presented, inter alia, in [9, 10, 24].

SELECTED FEATURES OF THE CHANGE PROCESS OF AN INTERNAL COMBUSTION ENGINE OPERATIONAL STATUS

As a formal description of the process of changing the technical and operational conditions of complex technical objects such as compression-ignition internal combustion engines and the model of this process in the form of a stochastic process, the values of which are the operational and operational statuses of practical importance, [18, 20, 26, 27], only selected features of the analyzed process are presented in this paper.

As a result of the identification of the operation process of the analyzed combustion-ignition internal combustion engines, finite sets of states and operational events are significant for their efficient operation.

Possible transition between states have been determined. Operational states are characterized by distributions of random variables indicating their duration, expenditures and revenues per unit of time associated with staying in states. Entry into the state can be related to revenue or effort.

In the computational example, the selected subsets of these states and events were analyzed.

As a result of the identification of the analyzed process of exploitation and carried out operational research, the following regularities were observed [14, 16, 17]:

- after the repair of specific engine systems, it is necessary to perform a status check, i.e. the status of the engine status check is only possible after repairs of the identified engine failures;
- if, after the execution of the engine condition check, the continuation of work is prevented by the object being repaired, the workpiece is subject to repairs at the workstation where the condition of the work has been carried out;
- the cost per unit of time associated with the performance of the engine repair is related to the type of damaged subsystem;
- repair time depends on the type of the damaged engine subsystem;
- maintenance time depends on the outcome of the status check, i.e. whether the engine will be allowed to perform tasks or will be repaired again;
- the cost per unit of time associated with the execution of a repaired object is related to the result of its state control.

Based on preliminary operational research [14, 18, 20, 28] it can be concluded that an example of a means of transport that damages sequences of successive states of operation and their characteristics is the drive system. In the analyzed object with relatively high frequency there is damage to the engine power supply system requiring adjustment of the injection pump. The correction procedure used for this system provides for the necessity of carrying out a maintenance diagnosis.

For the purposes of the simplified computational example (Section 6), the combustion engine subsystem (damage to its components) was divided into three subsets denoted by U_u , $u = 1, 2, 3$, i.e. [14, 16, 17]:

- subsystems (damage to their components) characterized by low labor-intensive repairs, which average repair time is relatively short; Restoring fitness does not require the engine to be transferred to specialized technical facilities; A subset of these subsystems is marked with code U_1 ;
- subsystems which, after failure and recovery, require remediation processes; A subset of these subsystems is marked with code U_2 ,
- subsystems with high repair workloads which average repair time is relatively long (multiple subsystems classified under subset U_1); A subset of these subsystems is designated U_3 .

Selected characteristics of operating states and semi-Markov model of the change process of operating states of the means of transport, in which the impact of damage on the course of the exploitation process is analyzed is presented in the papers [18, 27].

MATHEMATICAL MODEL OF ENGINE OPERATION PROCESS

It was assumed that the engine can, at a given time $t, t > 0$, be present in only one of the distinguished states, constituting a finite set of operating states of the object.

The operating state change process model of the engine is a stochastic process $\{X_t, t \in T\} t \geq 0$ for a finite set of states $S = \{s_1, s_2, s_3, s_4\}$.

The probability of change of state in one step of the process $\{X_t, t \in T\}$ from the state $s_i, s_i \in S$ to the state $s_j, s_j \in S$ at the occurrence of the condition $a, a \in A$ is marked $p_{ij}^a, \sum_{j=1}^4 p_{ij}^a = 1, p_{ij}^a \geq 0$ for $i, j = 1, 2, 3, 4$ and $a \in A$.

Continued process states $\{X_t, t \in T\}$ is heterogeneous Markov chain.

If all random variables signifying the duration of process states $\{X_t, t \in T\}$ have exponential distributions then such a defined stochastic process is a special case of the non-stationary decision-making process of Markov process [23, 26]. If the random variables signifying the duration of process states $\{X_t, t \in T\}$ can have any distribution, then the analyzed stochastic process is a special case of the non-stationary decision of the semi-Markov process [1-3].

Semi-Markov decision processes are used, inter alia, for modeling the process of changes in operating states and technical conditions of complex technical systems. These processes according to [10] are a convenient mathematical tool for analyzing decision problems related to the operation of marine combustion engines.

Due to the character of the paper, only selected assumptions of the simplified model of the engine operation process are presented.

The main assumptions used to describe the stochastic process $\{X_t, D_t, t \in T\}, t \geq 0$ are the mathematical model of the analyzed process of operation.

It has been assumed that the process of changing the operating conditions of the engine is described by the stochastic process:

$$\{X_t, t \in T\}, t \geq 0, \quad (6)$$

with finite state space:

$$S = \{s_1, s_2, s_3, s_4\}, \quad (7)$$

where:

T – subset of real numbers.

In this paper we assume that the states of the stochastic process under consideration correspond to the states of engine operation.

$a_{ik}, (i = 1, 2, 3, 4, k \in N)$ denotes the action (decision) k taken at s_i . Each is made up of $s_j, s_j \in S$ corresponding to a finite set of actions A_i (decisions).

It was assumed that elements of the set $A_i, i = 1, 2, 3, 4$ are the elements $a_{ik}, (i = 1, 2, 3, 4, k \in N)$, i.e.:

$$A_i = \{a_{i,1}, a_{i,2}, \dots, a_{i,i}\}, \quad (8)$$

where:

i – means power of the set A_i .

The set of all subsets of actions is denoted by A , i.e.:

$$A = \bigcup_{i=1}^4 A_i \quad (9)$$

In the general case, a_{ik} action taken at process input $\{X_t, t \in T\}$ to s_i can affect both the process state and the state of s_j , the type and the distribution parameters of the random variable representing the dwell time, costs, or gains in this state, etc.).

Actions may represent the way in which operations, tasks, events, decisions are made, etc., which can be attributed to the state of the modeled process [14-18, 27-29]. In the actual operating system there may be different ways of servicing, repairs, inspections, ranges of activities performed or usage of an object, etc. Adoption of a given action can affect: costs incurred, revenues, frequencies and types of damage of an object, sequences of states, etc. [27-29].

For the analyzed object, the elements of a_{ik} subsets A_i were interpreted in step 6 of the work. Considered in the computational example (point 6), set A has the form $A = \{a_{1,1}, a_{2,1}, a_{2,2}, a_{2,3}, a_{3,1}, a_{4,1}, a_{4,2}\}$.

Stochastic process:

$$\{D_t, t \in T\}, t \geq 0, \quad (10)$$

with a finite set of actions A describes how $a \in A$ is chosen.

The change of the state of the process $\{D_t, t \in T\}$ occurs at t times of process states $\{X_t, t \in T\}$. At moments $t_n, n \in N$ of process states changes $\{X_t, t \in T\}$, the action $a \in A$ is selected.

If at the moment t_n the state of the process $\{X_t, t \in T\}$, s_i is the state of being, then $a \in A_i$.

Process $\{X_t, D_t\}$, $t \geq 0$ with finite sets of states S and finite set of actions A , is called a decision-making stochastic process. As a result of this process from the initial time t_0 to the moment t_n , a sequence of states and decisions is obtained, which is called the process history until t_n :

$$h_{t_n} = \{s_{i_{t_0}}, a_{t_0}, s_{i_{t_1}}, a_{t_1}, \dots, s_{i_{t_n}}, a_{t_n}\}, \quad (11)$$

where:

- t_m – moments in which process conditions change $\{X_t, D_t\}$, $m = 0, 1, \dots, n$,
- $s_{i_{t_m}}$ – process state $\{X_t, t \in T\}$ at moment t_m , e.g. $X(t_m) = s_i$, $s_i \in S$,
- a_{t_m} – the process state $\{D_t, t \in T\}$ at moment t_m , i.e. $D(t_m) = a$, $a \in A$,
- m – the number of step in which the process $\{X_t, D_t\}$ states change.

For the mathematical modeling of the described process of changes in the state of a technical object, Markov decision-making processes [19, 22-23] or semi-Markov [1-3, 9-11, 14, 16-17, 19-20, 22-23, 28] can be used. Based on the analysis of the results of the conducted studies on the duration of operating states, the hypothesis about the compatibility of time distributions with the exponential distribution was rejected, it was further assumed that the analyzed decision-making process of stochastic:

$$\{X_{t_n}, D_{t_n}\}_{n=1}^{\infty}, \quad (12)$$

is a semi-Markov decision-making process. Accepting such an assumption implies, inter alia, that random variables describing the duration of process states $\{X_t, t \in T\}$ can have any distribution. The set of possible realizations of the analyzed decision process is $W = \{S \times A\}^{\infty}$ set. It has also been assumed that the probability of action $a_{t_n} \in A$ selection depends only on the state $s_{i_{n-1}} \in S$, and does not depend on the history $h_{t_{n-1}}$ of the process.

In this case, the process state sequence $\{X_t, t \in T\}$ is a non-homogeneous Markov chain [3-5].

In order to define the analyzed stochastic decision process $\{X_t, D_t\}$, $t \geq 0$ one should also define:

- the way of choosing a process action $\{D_t, t \in T\}$,
- initial distribution of the process $\{X_t, t \in T\}$,
- conditional probabilities of process state changes $\{X_t, t \in T\}$,
- random variables representing the duration of process states $\{X_t, t \in T\}$.

In a very simplified way, the rule that determines how to choose when entering the state of action is called a strategy. The method of selecting action at the input of the process state may be random or determined.

By:

$$p = [p_1, p_2, p_3, p_4], \quad \sum_{i=1}^4 p_i = 1, \quad p_i \geq 0, \quad (13)$$

the initial distribution of the process $\{X_t, t \in T\}$ is determined.

Given the value p_i of elements of the initial distribution vector p , the probability of finding the process $\{X_t, t \in T\}$ at time $t = 0$ in the state s_i .

The probability of change of state in one step of the process $\{X_t, t \in T\}$ from state $s_i, s_i \in S$ to $s_j, s_j \in S$ when taken at input s_i and $a \in A_i$ are determined as p_{ij}^a .

The condition is fulfilled:

$$\sum_{j=1}^4 p_{ij}^a = 1, \quad p_{ij}^a \geq 0, \quad \text{for all } i, j = 1, 2, 3, 4 \text{ and } a \in A_i. \quad (14)$$

For each state $s_i, s_i \in S$ and action $a, a \in A_i$, a stochastic matrix $P^{(i,a)}$ can be assigned to determine the conditional probability of the transition p_{ij}^a . The array of matrices attributed to the $s_i, s_i \in S$ state is the power equal i (the power of the set A_i).

The matrix $P^{(i,a)}$ is a matrix of stochastic lines that determines the probability of transition from state s_i (index and state s_i corresponds to the row of the matrix $P^{(i,a)}$) to all remaining states. The element p_{ij}^a at the intersection of the line with the number i and the column j with the matrix $P^{(i,a)}$ is the probability of transition from state $s_i, s_i \in S$ to $s_j, s_j \in S$ if when entering state $s_i, s_i \in S$, $a \in A_i$ is applied.

The random variable signifying the duration of the process $\{X_t, t \in T\}$ state $s_i \in S$, when the next state is the state $s_j \in S$, and when entering the $s_i \in S$ state, with undertaken action $a \in A_i$ determined by the distribution $F_{ij}^a(t)$, is determined by the symbol T_{ij}^a .

For the sake of simplicity in further consideration it was assumed that:

$$F_{ij}^a(t) = F_i^a(t) = F_{ia}(t), \quad i, j = 1, 2, 3, 4, \quad a \in A_i. \quad (15)$$

This means that the duration of the process $\{X_t, t \in T\}$ state does not depend on the next state in which the process will be located. The function $F_{ia}(t)$ is the distribution of the time distribution of the states of $s_i, s_i \in S$, provided that upon entry into this state the action a is taken.

The random variable signifying the duration of the $s_i, s_i \in S$ state of the distribution determined by the distribution $F_{ia}(t)$ is denoted by the symbol T_{ia} .

In order to assess the economic aspects associated with the implementation of the modeled operation process, it is necessary to additionally determine the relevant economic category values associated with the way in which the process states enter and stay in the process.

In addition, it was assumed that the model of changes in operating states of a homogeneous n set from the

point of view of the objective of testing technical objects are independent processes $\{X_t, t \in T\}$. The random vector $X(t) = [X_1(t), X_2(t), \dots, X_n(t)]$ describes the process of changing the operation states of a set of objects [15].

In practical applications, it is necessary to verify that there are no grounds for rejecting assumptions resulting from the applied mathematical apparatus.

A computer program has been developed to simulate the realization of a particular stochastic process. In the course of the simulation, the values of selected sets of indicators are determined which allow analysis of the modeled process of changing the engine states.

SIMULATION OF THE OPERATIONAL PROCESS IMPLEMENTATION

Analytical determination of the characteristics of the process of operation, which model is described decision stochastic process is a complex problem. In literature, the most commonly studied models are of small numbers of states and actions, and at the same time, there are limited opportunities for transition between states. Analysis of the operating conditions of complex technical facilities, including means of transport and the ongoing exploitation process often points to the need to consider more states considered significant and actions taken in states.

The authors of papers [18, 20, 27] consider more numerous states of space containing up to a dozen states of operation and analyze the characteristics of the process of operation of a technical object as a result of simulation of the process of stochastic process as a model of the process of changing the state of an object.

It seems that the numerical simulation of the process of changes in operating and technical states and the determination of selected values of characteristics on the basis thereof may be helpful in analyzing the process of operation of an object [14-18, 20-21, 27-29].

For the described assumptions, the simulation of the engine operation process consists of simulating the implementation of the described stochastic decision-making process, which is a model of the process of changing the engine operating states.

Numerical simulation algorithms of the decision-making process of the stochastic process have been developed. The data necessary for the simulation are the data necessary to determine the described process $\{X_t, D_t\}, t \geq 0$.

A computer program has been developed to simulate the realization of a particular stochastic process. During the implementation of the simulation, the values of the selected indicators allowing to analyze the modeled process of changing the state of objects are determined.

The algorithm and computer program developed enable the decision-making process of the semi-Markov process to be performed for both the number of states and actions that can be applied at the entry of particular states, and types of timestamps that are implemented in the program. The above values are given as input parameters of the simulation

program. The collection of all input data needed to execute the simulation experiments is prepared in the form of Excel spreadsheets.

With regard to decision strategies, the program enables the implementation of stationary strategies determined by the distribution of the probability of choosing a particular action (decision) for each state. A particular case of stationary strategy is a deterministic strategy for which a state is always used for a particular state with probability equal to one and the same action.

Using the developed program, it is possible to simulate the execution of stationary processes in the sense that one matrix of probabilities of transitions between process states $\{X_t, t \in T\}$ and non-stationary ones for the duration of the whole simulation ($p_{ij}^a = p_{ij}$) – and non-stationary states, i.e. for each state and action (decision), a different probability matrix is used.

The characteristics of the developed simulation program and examples of numerical simulations are presented in [15-17, 20, 28].

As a result of the numerical simulation of the process of changing the operating conditions of the engine, the following are measured for the time interval: inter alia, the number of faults of the analyzed engine subsystems, the total repair time of the damaged subsystems, the readiness of the engine and the time between faults.

CALCULATION EXAMPLE

For illustration purposes, the influence of the type of damaged object subsystem on the likelihood of transition between analyzed states and time intervals and the costs of staying in states is modeled.

Due to the nature of the study, the presented calculation example is characterized by considerable simplification. The selected features of the process of alteration of operating conditions of the internal combustion engine (section 3) have been modeled.

In the analyzed example, process states $\{X_t, t \in T\}$ correspond to the highlighted operating states $S_i, i = 1, 2, 3, 4$ of the engine.

The states s_1 and s_3 of the process $\{X_t, t \in T\}$ are so-called non-decisive states. This means, that the subsets of actions A_1 and A_3 are one-element. In these states, actions are only formal (consistency of writing) and have no influence on the course of the analyzed process $\{X_t, D_t\}, t \geq 0$.

In state s_2 , the actions $a \in A_2$ of the process $\{D_t, t \in T\}$ correspond to the code of the damaged subsystems of the engine and map its faults (point 3). The set A_2 contains the following elements $A_2 = \{a_{2,1}, a_{2,2}, a_{2,3}\}$. Actions $a_{2,1}, a_{2,2}, a_{2,3}$ denote damage to the selected motor subsystems U_1, U_2 , and U_3 , respectively. Interpreting the input at time t to process $\{X_t, t \in T\}$ state s_2 and occurrence of action $a_{2,3}$ of process $\{D_t, t \in T\}$ is as follows: engine has been damaged and serviced and damaged subsystem is marked with code U_3 . Interpretation of actions $a_{2,1}, a_{2,2}$ possible to occur in this state is analogous and concerns respectively the subsystems U_1 and U_2 .

In state s_4 , the actions $a \in A_4$ of the process $\{D_t, t \in T\}$ correspond to the engine status control codes. The set A_4 contains the following elements $A_4 = \{a_{4,1}, a_{4,2}\}$. By $a_{4,1}$ and $a_{4,2}$, respectively, the positive status of the engine status check and the need for re-handling are indicated.

The rule of action a selection in the state of $s_i, i = 1, 2, 3, 4$ determines the distribution of the probability of occurrence of the analyzed actions. It has been assumed that $q_{ik}, i = 1, 2, 3, 4, k \in N$ denotes the probability of a_{ik} action at the s_i input.

By

$$q_i = [q_{i1}, q_{i2}, \dots, q_{ik}], \quad q_{ik} \geq 0, \quad i = 1, 2, 3, 4, \quad k \in N, \quad (16)$$

the vector of the distribution of the occurrence of the action i is determined. The vector elements q_i satisfy the condition:

$$\sum_{i=1,2,3,4; k \in N} q_{ik} = 1. \quad (17)$$

In the example under consideration, the elements of this vector for $i = 2$ denote the probability of damage to the engine subsystem denoted by code k .

In order to illustrate the considerations, simulation experiments were performed for the scenario under consideration.

In the simulation experiments it was assumed that the random variables T_{ia} for $i = 1, 2, 3, 4, a \in A$ have gamma distributions with different parameters, and the process state is related to obtaining revenue (state s_1) and the expenditure of the system in which objects are operated. The values determining the conditional probabilities of the transition p_{ij}^a of the stochastic matrix $P^{(i,a)}$ $i, j = 1, 2, 3, 4, a \in A$ were estimated on the basis of the results of preliminary operational tests.

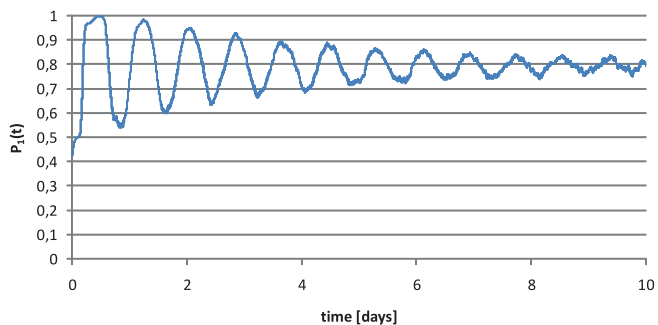


Fig. 1. Probability of $P_1(t)$ the analyzed engine occurring in use state

The probability values of $q_{ik}, i = 2, k = 1, 2, 3$ of the a_{ik} actions were determined on the basis of the results of the investigations of damage of the analyzed internal combustion engines.

The remaining parameter values used for the simulation experiments were estimated on the basis of the preliminary results.

It should be assumed that the values used for the distribution of random variables $T_{ia}, i = 1, 2, 3, 4, a \in A$ are hypothetical. Values of parameters were estimated on the basis of a low-volume dataset.

Figures 1 to 4 show the course of changes in probability values $P_i(t)$ of the analyzed process $\{X_t, D_t\}, t \geq 0$ in the states of $S_i, i = 1, 2, 3, 4$.

Presentation of the full set of input data used to perform simulation experiments and numerical simulation results goes beyond the scope of the study.

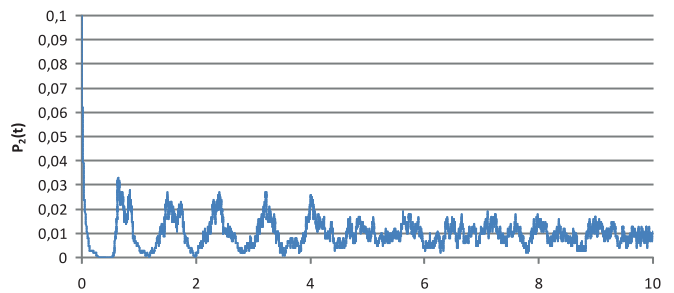


Fig. 2. Probability of $P_2(t)$ the analyzed engine occurring in the state of maintenance control

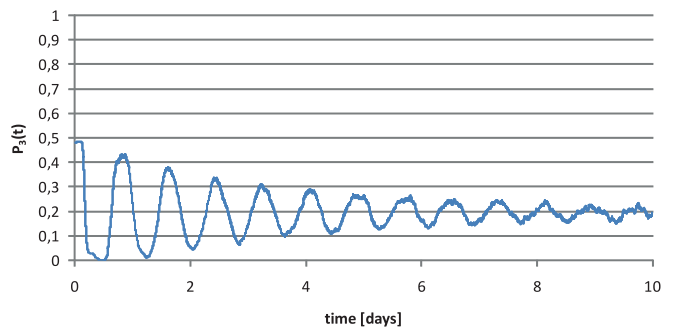


Fig. 3. Probability of $P_3(t)$ the analyzed engine occurring in standby state

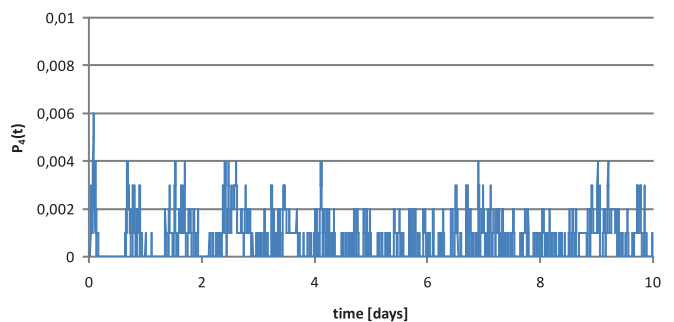


Fig. 4. Probability of $P_4(t)$ the analyzed engine occurring in the state of repair

SUMMARY

The purpose of this paper, among others, was to describe the possibilities of using semi-Markov decision-making theories for modeling the operation of internal combustion engines for main propulsion of ships, including propulsion systems of such means and other equipment that have a significant impact on the reliability and safety of maritime transport.

The method proposed in the article can be used to build similar models of other marine propulsion systems, as well as any means of maritime transport.

In the operation phase, such models can be used to predict changes in the characteristics of the modeled process description, as well as to estimate the value of the reliability and safety indicators and other operating indicators.

Numerical simulation of the semi-Markov decision-making process as a model of the process of change of the state of the analyzed combustion engine used in marine means of transport enables to determine the characteristics of the process which cannot be determined by the analytical method.

It seems possible and appropriate to use this type of tool to analyze multi-tasking processes and assist decision-makers in the decision-making process regarding the operation of internal combustion engines, means of transport and other complex technical objects, e.g. by predicting the behavior of an object after a change of control forces.

The set of possible indicators includes subsets of indicators for: readiness, repair time, performance, costs, and more.

The presentation of the full set of input data needed to simulate the analyzed stochastic process and how the model parameter values that are estimated based on the results of actual operational data is beyond the scope of this study. Due to the nature of the work and the extensive range of results generated, only selected results of simulation experiments are presented. The simulation results presented are illustrative.

The model presented in the paper has been designed in such a way that it can be used in a wide range of problems related to the operation of technical objects, including both the description of the effect of damage on the characteristics of the operation of the main engine and marine auxiliary engines.

The presented method together with developed algorithms and IT tools can be used to solve a wide range of problems related to the operation of marine main engines and other marine equipment as well as maritime and port facilities. This concerns primarily the economic, risk management and operational security issues of complex technical systems, as well as the readiness and reliability analysis of technical facilities.

BIBLIOGRAPHY

1. Baykal-Gürsoy M.: *Semi-Markov Decision Processes*. Wiley Encyclopedia of Operations Research and Management Sciences, 2010.
2. Baykal-Gürsoy M., Gürsoy K.: *Semi-Markov Decision Processes: Nonstandard Criteria*, Probability in the Engineering and Informational Sciences, Vol. 21:4, pp. 635-657.
3. Bernaciak K.: *Zastosowanie decyzyjnych procesów semimarkowskich do optymalizacji eksploatacji pewnego urzędnienia*. Zagadnienia Eksploatacji Maszyn, Zeszyt 3 (75), 1988.
4. Buslenko, N., Kałasznikow, W., Kowalenko, I.: *Theory of complex systems*, PWN, Warsaw 1979.
5. Chrzan P.: *Łącuchy decyzyjne Markowa i ich zastosowania w ekonomii*. Akademia ekonomiczna, Katowice 1990.
6. Girtler J.: *Application of theory of semi-Markov processes to determining distribution of probabilistic process of marine accidents resulting from collision of ships*. Polish Maritime Research 2014 nr 1, pp. 9-13.
7. Girtler J.: *Stochastyczny model procesu eksploatacji okrętowego silnika spalinowego*. Zagadnienia Eksploatacji Maszyn 1989 nr 2, s. 79-88.
8. Girtler J.: *Physical aspect of application and usefulness of semi-Markovian processes for modeling the processes occurring in operational phase of technical objects*. Polish Maritime Research 2004, nr 3(41), vol. 11, pp. 25-30.
9. Girtler J.: *Possibility of estimating the reliability of diesel engines by applying the theory of semi-Markov processes and making operational decisions by considering reliability of diagnosis on technical state of this sort of combustion engines*. Combustion Engines. 2015, vol. 163(4), pp. 57-66.
10. Girtler, J.: *Usefulness of semi-Markov processes as models of the operation processes for marine main engines and other machines of ship power plants*. Journal of Polish CIMAC, 9(2), Gdańsk 2014, pp. 57-67.
11. Grabski F.: *Analiza ryzyka w decyzyjnych semi-markowskich modelach procesu eksploatacji*. XXXVIII Zimowa Szkoła Niezawodności, Szczyrk, 2010.
12. Grabski F.: *Semi-markowskie modele niezawodności i eksploatacji*. PAN IBS, seria: Badania Systemowe, t. 30, Warszawa 2002.

13. Grabski F.: *Teoria semi-markowskich procesów eksploatacji obiektów technicznych*. Zeszyty Naukowe AMW, nr 75 A, Gdynia 1982.
14. Kostek R., Landowski B., Muślewski Ł.: *Simulation of rolling bearing vibration in diagnostics*. Journal of Vibroengineering 2015, volume 17, issue 8, pp. 4268-4278, ISSN 1392-8716.
15. Landowski B.: *An example of a technical object operation process model describing influence of engine damages on the operation process course*. Journal of POLISH CIMAC Vol. 9, No. 3, Gdańsk 2014.
16. Landowski B.: *Example of applying Markov decision process to model vehicle maintenance process*. Journal of KONES Powertrain and Transport, Vol. 20, No. 4, 2013, European Science Society of Powertrain and Transport Publication, Warsaw 2013.
17. Landowski B.: *Example of Markov decision process use for modelling of operation and maintenance process*. Interdisciplinary Integration of Science in Technology, Education and Economy. Monograph: edited by Shalapko J. and Żółtowski B., Khmelnytsky – Jaremche 2013, ISBN 978-617-70-94-07-3.
18. Landowski B.: *Method of determination values of the chosen decision variables to control rationally the operation and maintenance process in the transport system*. Doctoral thesis, Academy of Technology and Agriculture, Bydgoszcz 1999.
19. Landowski B., Perczyński D., Kolber P., Muślewski Ł.: *An example of Markov model of technical objects maintenance process*. Engineering Mechanics 2016, 22nd International Conference, may 9 – 12, 2016, Svratka, Czech Republic, Book of full texts, Institute of Thermomechanics Academy of Sciences of the Czech Republic, 2016, pp. 346-349, ISBN 978-80-87012-59-8, ISSN 1805-8248.
20. Landowski B., Woropay M., Neubauer A.: *Sterowanie niezawodnością w systemach transportowych*. Biblioteka Problemów Eksploatacji, Wydawnictwo Instytutu Eksploatacji Maszyn, Bydgoszcz – Radom 2004.
21. Łukasiewicz M., Kałaczyński T., Musiał J., Shalapko J.: *Diagnostics of buggy vehicle transmission gearbox technical state based on modal vibrations*. Journal of Vibroengineering 2014, volume 16, issue 6, pp. 3137-3145, ISSN 1392-8716.
22. Puterman M. L.: *Markov decision processes*. John Wiley, New York, 1994.
23. Puterman M. L.: *Markov decision processes: discrete stochastic dynamic programming*. John Wiley & Sons 2014.
24. Rudnicki J.: *Application issues of the semi-markov reliability model*. Polish Maritime Research 2015, nr 1(85), vol. 22, pp. 55-64.
25. Rudnicki J.: *The time of the first transition of the semi-Markov process in the evaluation of diesel engine operation*. Silniki Spalinowe 2011, tom R. 50, nr 3, pp. 89-98.
26. Woropay M., Grabski F., Landowski B.: *Semi-Markov model of the vehicle maintenance processes in an urban transport system*. Scientific Publishers of the Polish Scientific Association of Automotive Engineering, Archives of Automotive Engineering Vol. 7, No 3, 2004.
27. Woropay M., Knopik L., Landowski B.: *Modelowanie procesów eksploatacji w systemie transportowym*. Biblioteka Problemów Eksploatacji. Wydawnictwo Instytutu Eksploatacji Maszyn, Bydgoszcz – Radom 2001.
28. Woropay M., Landowski B., Neubauer A.: *Applying semi-Markov decision processes to model and simulate the bus operation and maintenance processes*. Scientific Publishers of the Polish Scientific Association of Automotive Engineering, Archives of Automotive Engineering Vol. 7, No. 1, 2004.
29. Woropay M., Landowski B., Neubauer A.: *Simulation of the method to optimise the operation and maintenance process of the buses in an urban transport system*. International Scientific Conference “Transport of the 21st Century”, section5, Warsaw 2004.

CONTACT WITH THE AUTHOR

Bogdan Landowski

e-mail: bl-sluzbowy@wp.pl

Uniwersytet Technologiczno-Przyrodniczy
im. Jana i Jędrzeja Śniadeckich w Bydgoszczy
Al. prof. S. Kaliskiego 7
85-796 Bydgoszcz
POLAND

Michał Pająk

e-mail: m.pajak@pr.radom.pl

Uniwersytet Technologiczno-Humanistyczny
im. Kazimierza Pułaskiego w Radomiu
Malczewskiego 29
26-600 Radom
POLAND

Bogdan Żółtowski

e-mail: bogdan.zoltowski@utp.edu.pl

Uniwersytet Technologiczno-Przyrodniczy
im. Jana i Jędrzeja Śniadeckich w Bydgoszczy
Al. prof. S. Kaliskiego 7
85-796 Bydgoszcz
POLAND

Łukasz Muślewski

e-mail: lukasz.muslewski@utp.edu.pl

Uniwersytet Technologiczno-Przyrodniczy
im. Jana i Jędrzeja Śniadeckich w Bydgoszczy
Al. prof. S. Kaliskiego 7
85-796 Bydgoszcz
POLAND

ENERGY EFFICIENT AND ENVIRONMENTALLY FRIENDLY HYBRID CONVERSION OF INLAND PASSENGER VESSEL

Wojciech Litwin

Wojciech Leśniewski

Jakub Kowalski

Gdańsk University of Technology, Faculty of Ocean Engineering and Ship Technology, Poland

ABSTRACT

The development and growing availability of modern technologies, along with more and more severe environment protection standards which frequently take a form of legal regulations, are the reason why attempts are made to find a quiet and economical propulsion system not only for newly built watercraft units, but also for modernised ones.

Correct selection of the propulsion and supply system for a given vessel affects significantly not only the energy efficiency of the propulsions system but also the environment – as this selection is crucial for the noise and exhaust emission levels.

The paper presents results of experimental examination of ship power demand performed on a historic passenger ship of 25 m in length. Two variants, referred to as serial and parallel hybrid propulsion systems, were examined with respect to the maximum length of the single-day route covered by the ship. The recorded power demands and environmental impact were compared with those characteristic for the already installed conventional propulsion system.

Taking into account a high safety level expected to be ensured on a passenger ship, the serial hybrid system was based on two electric motors working in parallel and supplied from two separate sets of batteries. This solution ensures higher reliability, along with relatively high energy efficiency.

The results of the performed examination have revealed that the serial propulsion system is the least harmful to the environment, but its investment cost is the highest. In this context, the optimum solution for the ship owner seems to be a parallel hybrid system of diesel-electric type.

Keywords: ship propulsion, hybrid propulsion, green shipping, zero emission, solar power

INTRODUCTION

Mechanically driven ships proved their advantage over sailing ships as early as in the nineteenth century, but sailing cargo ships were still built until the 1930s. However, since the mechanical propulsion has become popular in shipping industry, engineers and designers fast came to the conclusion that the key parameter for a ship is energy efficiency of the entire propulsion system, starting from the engine and ending at the screw propeller. A case which happened in the nineteenth century is known when there was no enough coal for burning steam boilers on a steam ship and the wooden deck was completely burned for this purpose, along with all wooden furniture, to reach the destination. This story may

seem funny, and rather unimaginable in these days, when the safety of a ship is controlled by reputable classification societies before they grant the authorisation for placing it into service. Nevertheless, the authors are aware of events when a modern electrically driven ship had to interrupt the voyage, let go the anchor and wait for a tug due to the lack of energy.

In a few recent decades, electric propulsion has successfully been used on ships, especially on special watercraft units such as ice-breakers and warships. In these decades, the development of new technologies has made it possible to design light electric devices with low energy loss. This mainly refers to AC electric motors and frequency converters needed for their control. Despite high price, such solutions are being more and more frequently used now. A good example here

can be ships designed and built for oil industry, for instance so-called SPV's (Supply Platform Vessels) [1]. The responsibility related with the operation of these vessels affects technical advancement of the installed systems. The construction costs of these vessels are high, but the resultant operating potential is also extremely high, and practically unattainable for earlier designs. An example worth mentioning here is the dynamic positioning system which allows the ship to be kept at a given position, even in storm conditions.

The experience gained in past centuries indicates that each new technology is initially applied in the military industry. The first successful application of a parallel hybrid propulsion system had place in a submarine at the beginning of the twentieth century. For years, electric machines have been improved. Until recently, lead-acid batteries have been used as the energy source in conventional submarines during underwater navigation. And only at the end of the twentieth century attempts were made to install fuel cells [2][3]. Despite the passage of time, the use of fuel cells as energy sources has not become popular in the maritime industry for some reasons, such as high price for instance. As a consequence, those solutions still remain the object of theoretical and experimental research [4][5][6][7].

A significant breakthrough, with serious implications for civil use of hybrid propulsion systems, had place quite recently, due to the development of mobile technologies. Tens of millions of mobile phones, tablets, and portable computers needed a reliable and safe energy source with limited dimensions and mass. The solution was the use of successive generations of lithium batteries. Initially, little attention was paid to the importance of so-called BMS's (Battery Management Systems) controlling the battery charging/discharging processes. However, it soon turned out that these processes have to be permanently controlled, which now is frequently executed by displaying main charging parameters, such as voltage, electric current, and temperature on the screen [8]. At present, hybrid propulsion systems are being developed by various companies all over the world, they are also the object of numerous research activities worldwide [9][10].

For years, a large amount of research has been performed upon photovoltaic panels, which are considered sources of clean, „green” electric energy. Now, they can be seen not only on the roofs of buildings, but also on some vehicles. The voyage of the catamaran PLANETSOLAR around the world, which ended in 2012, is the best example proving that the solar energy can be a significant source of energy for a moving vehicle [11].

An obvious reason why modern hybrid technologies are being more and more widely used is growing awareness of societies regarding the increasing environment pollution, with the resultant more and more severe standards concerning permissible exhaust emission limits. Numerous publications by authors from all over the world can be found in recent literature which focus on economic issues of applications of propulsion systems on inland and sea-going vessels and their effect on the environment [12][13][14][15][16][17]. More and

more attention is also paid to noise emission by watercraft units [18][19]. This issue is of special importance in inland navigation, in which the waterways frequently lead through densely urbanised areas. In those conditions, hybrid drive can reveal its advantages. Unlike large water regions, in which high-power diesel engines can generate relatively high ship speeds, canal navigation has often speed restrictions. This prefers the use of quiet and environment friendly electric propulsion systems.

GENESIS OF THE PROJECT

The authors of the paper have over 10-years' experience in designing and building, together with students of the Gdansk University of Technology, untypical watercraft units with solar energy supplied electric propulsion systems. They witnessed and actively participated in the revolution concerning propulsion and supply of the watercraft used for competitive purposes. During the first edition of the Frisian Solar Challenge – Holland 2006 sailing races, use was usually made of simple brushed DC motors, lead-acid batteries, and components of inland solar systems and photovoltaic panels, the efficiency of which was approximately equal to 10%. By contrast, in 2016 the use of AC motors with permanent rare earth magnets, frequency converters, lithium batteries, and advanced converters of energy generated by photovoltaic panels became a standard in propulsion systems. The average speed on the route of the race, the length of which exceeded 200 km, almost doubled. The maximum speed of the solar energy fed watercraft units taking part in the sailing race in 2016 was greater than 56 km/h (Fig.1.). Despite rainy weather, keeping the average speed above 30 km/h was quite possible due to the energy accumulated in batteries.

A valuable source of experience was the executed project of the Poland first passenger boat with hybrid propulsion based on solar and power network supply, so-called plug-in hybrid [20].



Fig.1. Solar hydrofoil boat "Clafis" during Dutch Solar Challenge 2016

In response to the demand of owners of smaller inland ships, a prototype propulsion system has been designed which

can be easily installed not only on newly built units, but also, what is more important, on the units already in operation [20]. In the meantime, the classification societies which grant the authorisation for placing the watercraft unit into passenger service radically changed the regulations. Firm emphasis was placed on safety issues. One of key modifications concerned the propulsion system, where a necessary condition became the use of two independent, autonomous propulsion units, which forced in practice the use of two independent diesel engines with independent systems for fuelling, cooling, exhaust, etc.

Changes in regulations have increased the interest of ship owners in new solutions. This especially refers to the owners of ships with propulsion systems based on one, most often, diesel engine. The parallel hybrid propulsion turns out to be able to solve their problems concerning the necessary existence of two independent propulsion units on the ship. Advantages of this solution also are becoming more and more evident for them.

ORIGIN AND PURPOSE

The authors of the paper have been challenged by the task commissioned by an owner of inland passenger ships to modernise the propulsion system and renovate a historical passenger ship of 25 m in length. The propulsion of this ship consisted of a 74-kW diesel engine and a single screw propeller, driven via a reduction gear. According to owner's expectations, the new ship propulsion system should be fully electric.

That is why, based on the concept of two engines working for one shafting, which is the solution accepted by classification societies, a propulsion system was proposed in which two electric motors drive a single propeller via a summarising gear. Each motor has an independent supply system, consequently the proposed solution meets the requirements of classification societies concerning passenger ship propulsion, which should consist of two independent systems. Due to the fact that a set of photovoltaic panels, being an additional source of energy, and an emergency power generator are going to be installed on the ship (according to the requirements of the classification society), the propulsion and supply system can be classified as a serial hybrid system. This results from the fact that three sources (network, generator, photovoltaic panels) are used to charge the batteries.

The system in universal configuration is shown in Fig. 2 in the form of block diagram.

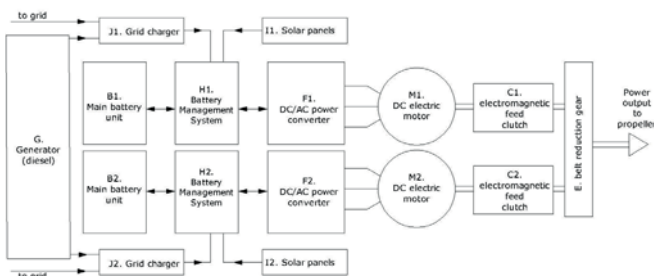


Fig. 2. Modular scheme of the designed propulsion and supply system

Of special interest are the details composing the supply system (modules B, H, I, J). When in use, lithium batteries require an additional Battery Management System (BMS) which protects the entire battery of cells against damage due to overheating or excessively deep charge/discharge by monitoring the operating parameters of each cell. What is also very important is that the BMS controls the charging process in such a way that all cells are equally charged. The latter process is frequently referred to as balancing.

The installed power generator has very important tasks to perform. It is expected to work as emergency power supply in case of complete discharge of the batteries. Even a precisely calculated power balance sheet, along with installation of a larger battery of accumulators, do not ensure sufficient energy reserves to reach the destination in any conditions which may occur during multi-years operation. The next task is ensuring security of the ship and crew, the awareness of which will allow the crew to make rational decisions. What is more, installing the emergency power generator eliminates the risk of an event known from sailing races of solar boats, when the BMS cuts off motor supply a few hundred meters before the finish and the boat begins to drift. This event occurs quite often when the batteries are already heavily discharged and one cell has unacceptably low voltage. There are several possible reasons for this situation, the most frequent of which is that the battery balancing process was not performed during battery charging and significant differences between capacities of individual cells can be observed as a result of poor quality of the cells or their wear-out.

MEASURING POWER DEMAND – EXPERIMENTAL EXAMINATION

In order to design properly the propulsion and supply system, the experimental examination of the real ship offered by the owner was performed. The goal of this research was to identify the power demand of the ship propulsion system and evaluate the quality of the used screw propeller by calculating its efficiency.

The experiment was executed in the following way: during the voyage, when the ship sailed at constant known speed calculated based on the GPS system, the propeller shaft torque and rotational speed measurements were performed. The torque was measured using the strain gauge method. For this purpose, two double strain gauge sensors, so-called rosettes, were stuck to the propeller shaft. The applied system was unaffected by temperature changes and possible shaft bending.

The measuring system was developed in such a way as to provide opportunity for simultaneous additional measurement of the longitudinal force in the propeller shaft. The known value of the propeller thrust force (i.e. the longitudinal force) made it possible to calculate the so-called “towing power”. Comparing the towing power with the power on propeller shaft made it possible, in turn, to calculate the approximate propeller efficiency.

To allow the measurement, basic components of the recording unit, including:

- strain gauge sensor amplifiers,
 - radio transmitter of the measured signal to the recording computer,
 - batteries composing the system supply,
- were placed on a special handle fixed to the rotating shaft, (Fig. 3).



Fig.3. Torque and thrust measurement system rotating with the propeller shaft during the measurements

In order to ensure the highest possible accuracy of measurements, a model of the examined shaft was manufactured in real scale in the laboratory of the Faculty of Ocean Engineering and Ship Technology. The measuring sensors were placed on this model and then loaded in a controlled way to calibrate the system.

Power measurements were done in favourable light-wind conditions. For this purpose, the ship sailed to a sufficiently large water region in which it could sail steady course at a given constant speed for a few minutes. When the ship speed stabilised, its value was estimated from GPS data. Simultaneously, the propeller shaft torque, thrust and rotational speed were measured. To assess the effect of wind, the measurements were done twice: for upwind and downwind course.

The ship speeds for which the measurements were done were equal to 6, 8, 10, 12 and 13 km/h. The thrust was measured only for speeds above 10 km/h, due to the concerns that the measurements of small torque values at lower speeds would be burdened with unacceptably large error resulting from relatively small compressive stresses of the shaft.

The results of the measurements are given in Table 1.

Table 1. Propeller shaft power, towing power, and propeller efficiency calculated from strain gauge measurements

ship speed	shaft speed	torque on propeller shaft	power on propeller shaft	thrust force in propeller shaft (towing force)	towing power	estimated propeller efficiency
km/h	rev/s	Nm	kW	N	kW	%
6,0	5,9	200,4	7,4	-	-	-
8,0	7,4	315,1	14,6	-	-	-

ship speed	shaft speed	torque on propeller shaft	power on propeller shaft	thrust force in propeller shaft (towing force)	towing power	estimated propeller efficiency
km/h	rev/s	Nm	kW	N	kW	%
10,0	9,8	537,9	33,2	2086,3	5,8	17
12,0	11,2	684,8	48,1	4526,7	15,1	31
13,0	12,8	919,6	73,8	6435,9	23,2	32

What is noteworthy, the sailing resistance characteristic has a typical nonlinear shape (Fig. 4). This is a typical situation in general, but in the examined case it has special meaning. Another noteworthy fact is rapid increase of power demand with the increasing speed, and low propeller efficiency, not exceeding 32%. This low efficiency results from the use of a very simple welded propeller, the geometry of which was designed using simple parametric methods to estimate ship resistance.

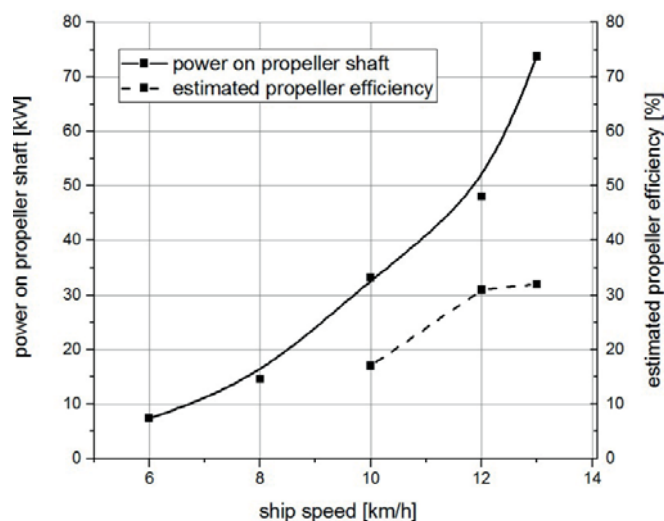


Fig. 4. Measured propeller shaft power and propeller efficiency vs. ship speed

RESULTS AND DISCUSSION

The examined ship is intended to sail on inland waters, with frequent speed restrictions resulting from the need to protect the shoreline and bed structures. The speed limit in force along a large part of the route leading along historical canals is 6 km/h. Moreover, it was agreed with the ship owner that the cruising speed of the ship in open waters will be 12 km/h. Taking into account the experimentally determined towing power equal to 15,1 kW for the speed of 12 km/h (Table 2), and assuming 60% efficiency of the dedicated screw propeller, the expected mechanical power of the propulsion system was calculated as equal to 25,2 kW. The ship was assumed to be driven by the above described dual propulsion system 2 x 15kW, which should provide sufficient power margin and facilitate the performance of manoeuvres. Untypical operating conditions of the ship sailing with two different

cruising speeds provide opportunities for well-balanced use of the propulsion system, as the lower speed equal to 6 km/h is reached by the ship operating on one motor. To reach the higher speed, both motors are to be started up. When analysing the power demand, the longest possible single-day trip of the ship was taken in to account. Its total length is 80 km, with 45 km leading along canals with speed limits. The diagram in Fig. 5 shows ship speed profiles in different propulsion variants: the presently installed conventional propulsion system, and parallel and serial hybrid systems. Based on the power demand as a function of ship speed, the power demand needed to select battery capacities was calculated, Fig. 6. The results of these calculations are given in Table 2. What is noteworthy, decreasing the cruising speed in open waters from 13 to 12 km/h leads to substantial energy saving, due to the decreased ship resistance, Fig. 4. The increased travel time in this case, from 10h10' to about 10h30', seems acceptable.

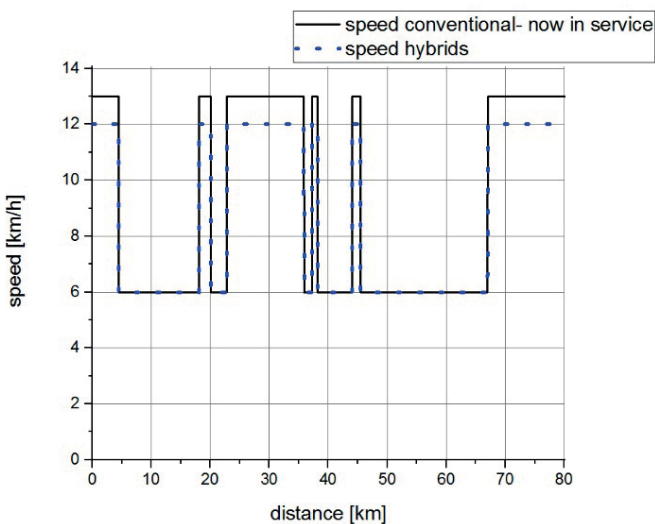


Fig. 5. Diagram of ship speed during longest single-day trip

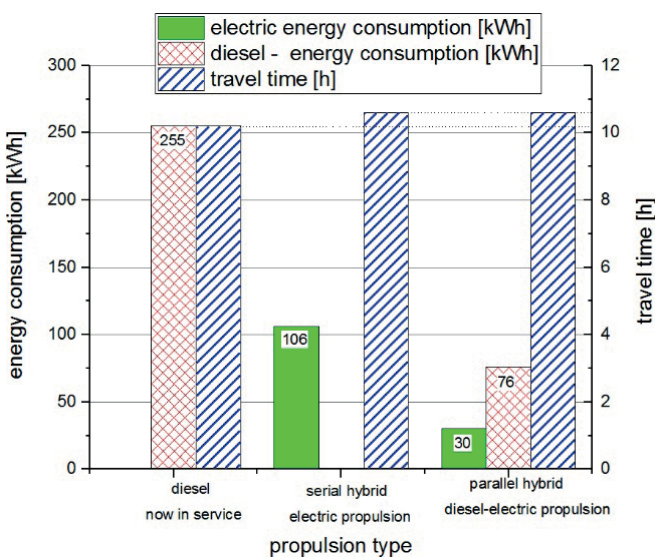


Fig. 6. Power distribution and travel time of longest single-day trip

Table 2. The calculated power demand and electric energy consumption on the ship with hybrid propulsion system

Ship speed	Towing power (thrust power)	Propeller efficiency	Motor power (power on shaft) [kW]	Motor and controller efficiency	Electric power
[km/h]	[kW]	%		%	[kW]
6,00	4,00	60	6,67	80	8,33
12,00	15,10	60	25,17	85	29,61
13,00	23,40	60	39,00	85	45,88

What is noteworthy here is low efficiency of the presently used system. The cause for this low efficiency, and the resultant large power consumption, is ineffective screw propeller. Increasing its efficiency from 30% to 60% would instantaneously lead to the decrease in fuel consumption – even by as much as a half. The energy demand from the serial hybrid system is about 148 kWh (Table 3). However, this value was calculated based on 60% screw propeller efficiency and 100% efficiency of the electric propulsion system. To calculate the capacity of batteries which are to be installed on the ship, real efficiency of the propulsion system as the function of load is to be taken into account, Fig. 7.

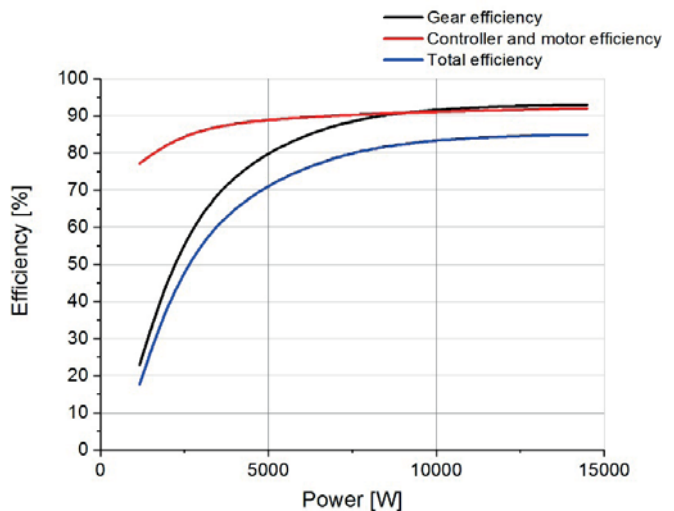


Fig. 7. Propulsion efficiency as a function of power

In practice, at least 20% battery capacity margin is to be added. The batteries can be installed on the ship but this solution is extremely expensive. The calculated battery capacities are given in Table 3.

Table 3. Calculated power demands for different propulsion types, and capacities of propulsion motor supply batteries

Type of drive	energy -diesel engine [kWh]	energy -electric motor [kWh]	battery capacity with 20% margin [kWh]
conventional – present state	260,02		
conventional – after screw propeller replacement	147,78		

Type of drive	energy -diesel engine [kWh]	energy -electric motor [kWh]	battery capacity with 20% margin [kWh]
serial hybrid		147,78	177
parallel hybrid	87,9	59,88	72

The data shown in the table reveals that in terms of investment, a solution which would be favourable for the ship owner is installing the parallel hybrid diesel-electric propulsion. In this case the battery is more than twice as small as for the serial hybrid solution. The size of battery capacity margin can also be reconsidered. It can be small, as the voyage can be continued on a diesel engine in case of battery discharge. Moreover, in the case of parallel hybrid propulsion, when the diesel engine is in operation, the electric motor can be started up in generator mode to charge the batteries during the voyage. This way the size of the battery can be even more reduced, at the expense of its shorter lifetime connected with the number of charging cycles.

What is noteworthy, a relatively large set of light photovoltaic panels can be placed on such a big ship. Their total peak power could reach even as much as 10kW. In the summer season, at good weather, battery charging from the shore may turn out unnecessary. This solution increases the investment cost, but significantly decreases the operating costs.

Ship reconstruction to pure electric drive eliminates the present exhaust emissions by the conventional low-efficiency propulsion system. The quantity of exhaust emissions for conventional propulsion was calculated using approximate methods [21][22][23]. Real quantities depend on the type of burned fuel and the engine generation [24][25].

Replacing the screw propeller to the dedicated, specially designed unit would reduce the exhaust emissions by half, while applying the parallel hybrid propulsion system would lead to further reduction by 30% (Fig. 8).

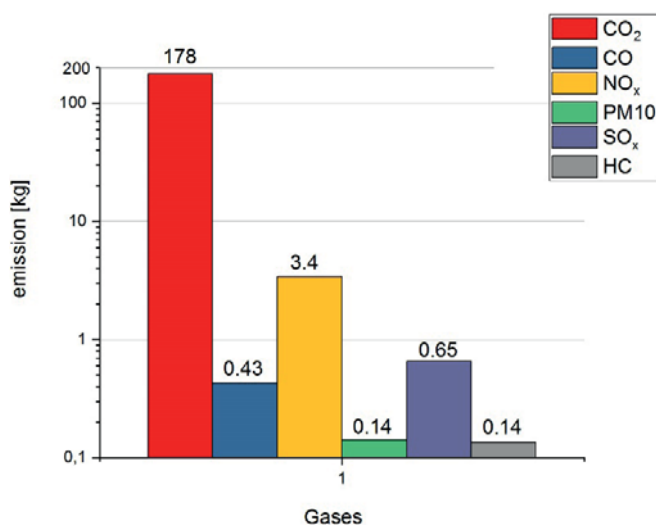


Fig. 8. Calculated exhaust emissions to the atmosphere for different propulsion variants

One more aspect concerning the voyage on the examined ship is worth noticing. The purely electric propulsion makes the ship travel in practically complete silence. The passengers can stay on the weather deck without fear of breathing the exhaust gas.

CONCLUSIONS

In authors' opinion, reasonably performed ship modernisation consisting in propulsion system replacement from conventional to electric or hybrid system, should involve screw propeller replacement. Only comprehensive modernisation can provide a good effect in the form of decreased consumption of the energy collected in batteries, the amount of which is limited on the ship.

Slower – means more economically. If possible, decreasing the maximal speed is always profitable when the low fuel consumption is a priority.

The propulsion system which seems rational in both operating and investment terms is the parallel hybrid system with battery charging from a set of photovoltaic panels. It should be kept in mind, however, that, for instance, lines of trees growing along the waterway can significantly reduce the amount of energy generated by the panels. It is enough to overshadow a fragment of one panel for the entire set of panels connected in series to stop working. That is why proper connection of panels is crucial for the efficiency of the entire system.

The assumed 20% battery capacity margin should suffice to cover the increased power demand resulting from, for instance, difficult sailing conditions, ship hull fouling, rapid manoeuvres, and/or minor screw propeller damages which frequently take place during voyages along inland waterways.

REFERENCES

1. M. C. Díaz-de-Baldasano, F. J. Mateos, L. R. Núñez-Rivas, and T. J. Leo, "Conceptual design of offshore platform supply vessel based on hybrid diesel generator-fuel cell power plant," *Appl. Energy*, vol. 116, pp. 91–100, 2014.
2. G. Sattler, "Fuel cells going on-board," *J. Power Sources*, vol. 86, no. 1, pp. 61–67, 2000.
3. A. Psoma and G. Sattler, "Fuel cell systems for submarines: From the first idea to serial production," *J. Power Sources*, vol. 106, no. 1–2, pp. 381–383, 2002.
4. C. H. Choi et al., "Development and demonstration of PEM fuel-cell-battery hybrid system for propulsion of tourist boat," *Int. J. Hydrogen Energy*, vol. 41, no. 5, pp. 3591–3599, 2016.
5. Y. M. A. Welaya, M. M. El Gohary, and N. R. Ammar, "A comparison between fuel cells and other alternatives

- for marine electric power generation,” *Int. J. Nav. Archit. Ocean Eng.*, vol. 3, no. 2, pp. 141–149, 2011.
6. N.-C. Shih, B.-J. Weng, J.-Y. Lee, and Y.-C. Hsiao, “Development of a small fuel cell underwater vehicle,” *Int. J. Hydrogen Energy*, vol. 38, no. 25, pp. 11138–11143, 2013.
 7. N. C. Shih, B. J. Weng, J. Y. Lee, and Y. C. Hsiao, “Development of a 20 kW generic hybrid fuel cell power system for small ships and underwater vehicles,” *Int. J. Hydrogen Energy*, vol. 39, no. 25, pp. 13894–13901, 2014.
 8. C. R. Lashway, A. T. Elsayed, and O. A. Mohammed, “Hybrid energy storage management in ship power systems with multiple pulsed loads,” *Electr. Power Syst. Res.*, vol. 141, pp. 50–62, 2016.
 9. J. Wilflinger, P. Ortner, R. Johannes, K. Universität, M. Aschaber, and S. Motors, *Simulation and control design of hybrid propulsions in boats*, vol. 43, no. Ljung, IFAC, 1999.
 10. G. Seenumani, H. Peng, and J. Sun, “A reference governor-based hierarchical control for failure mode power management of hybrid power systems for all-electric ships,” *J. Power Sources*, vol. 196, no. 3, pp. 1599–1607, 2011.
 11. Dante D’Orazio, “An inside look at the world’s largest solar-powered boat,” *The Verge*, vol. 2013, pp. 1–13, 2013.
 12. W. Sihn, H. Pascher, K. Ott, S. Stein, A. Schumacher, and G. Mascolo, “A Green and Economic Future of Inland Waterway Shipping,” *Procedia CIRP*, vol. 29, pp. 317–322, 2015.
 13. E. K. Dedes, D. A. Hudson, and S. R. Turnock, “Assessing the potential of hybrid energy technology to reduce exhaust emissions from global shipping,” *Energy Policy*, vol. 40, no. 1, pp. 204–218, 2012.
 14. D. A. Cooper, “Exhaust emissions from high speed passenger ferries,” *Atmos. Environ.*, vol. 35, no. 24, pp. 4189–4200, 2001.
 15. Y. Shi, “Reducing greenhouse gas emissions from international shipping: Is it time to consider market-based measures?,” *Mar. Policy*, vol. 64, pp. 123–134, 2016.
 16. J. Yuan, S. H. Ng, and W. S. Sou, “Uncertainty quantification of CO₂ emission reduction for maritime shipping,” *Energy Policy*, vol. 88, pp. 113–130, 2016.
 17. B. Zahedi, L. E. Norum, and K. B. Ludvigsen, “Optimized efficiency of all-electric ships by dc hybrid power systems,” *J. Power Sources*, vol. 255, pp. 341–354, 2014.
 18. D. Borelli, T. Gaggero, E. Rizzuto, and C. Schenone, “Analysis of noise on board a ship during navigation and manoeuvres,” *Ocean Eng.*, vol. 105, pp. 256–269, 2015.
 19. A. Badino, D. Borelli, T. Gaggero, E. Rizzuto, and C. Schenone, “Airborne noise emissions from ships: Experimental characterization of the source and propagation over land,” *Appl. Acoust.*, vol. 104, pp. 158–171, 2016.
 20. J. Kowalski, W. Leśniewski, and W. Litwin, “Multi-source-supplied parallel hybrid propulsion of the inland passenger ship STA.H. Research work on energy efficiency of a hybrid propulsion system operating in the electric motor drive mode,” *Polish Marit. Res.*, vol. 20, pp. 20–27, 2013.
 21. I. S. Seddiek and M. M. Elgohary, “Eco-friendly selection of ship emissions reduction strategies with emphasis on SO_x and NO_x emissions,” *Int. J. Nav. Archit. Ocean Eng.*, vol. 6, no. 3, pp. 737–748, 2014.
 22. I. S. Seddiek, M. Mosleh, and A. A. Banawan, “Thermoeconomic approach for absorption air condition onboard high-speed crafts,” *Int. J. Nav. Archit. Ocean Eng.*, vol. 4, no. 4, pp. 460–476, 2012.
 23. M. Morsy El Gohary and I. S. Seddiek, “Utilization of alternative marine fuels for gas turbine power plant onboard ships,” *Int. J. Nav. Archit. Ocean Eng.*, vol. 5, no. 1, pp. 21–32, 2013.
 24. M. A. Kalam and H. H. Masjuki, “Emissions and deposit characteristics of a small diesel engine when operated on preheated crude palm oil,” *Biomass and Bioenergy*, vol. 27, no. 3, pp. 289–297, 2004.
 25. M. Mikulski, K. Duda, and S. Wierzbicki, “Performance and emissions of a CRDI diesel engine fuelled with swine lard methyl esters-diesel mixture,” *Fuel*, vol. 164, no. x, pp. 206–219, 2016.

CONTACT WITH THE AUTHORS

**Wojciech Litwin
Wojciech Leśniewski
Jakub Kowalski**

Gdansk University of Technology
Faculty of Ocean Engineering and Ship Technology
Gabriela Narutowicza 11/12
80-233 Gdańsk
POLAND

OPERATION OF TWO-SHAFT GAS TURBINE IN THE RANGE OF OPEN ANTI-SURGE VALVE

Marek Dzida

Jacek Frost

Gdańsk University of Technology, Faculty of Ocean Engineering and Ship Technology, Poland

ABSTRACT

This paper presents experimental tests of full-scale two-shaft gas turbine in the range of open anti-surge valve (ASV). The tests were carried out in a laboratory gas-turbine test stand belonging to Department of Automation and Power Engineering, Faculty of Ocean Engineering and Ship Technology, Gdańsk University of Technology. The tests covered the start-up and low load operation of the turbine set in the range of open anti-surge valve.

Keywords: gas turbine, anti-surge valve, laboratory stand, experimental studies

INTRODUCTION

Power plants based on gas turbines are applied into many driving devices : in power industry – for driving electric generating sets working in simple or combined gas-steam systems, in aeronautics – gas turbine serves as a basic engine, in military applications, especially in shipbuilding, in ocean engineering as well as in intermediate pumping stations of piping networks for transporting gas or crude oil products etc. They are used in a micro-scale beginning from a few hundred watts, up to several hundred megawatts available from a single driving engine. Main aspects of application of gas turbines are the following : low values of ratio of their mass and volume to unit of power output, high easiness of application of automation, possible fast start-ups and cyclic-mode operation, low or full independence from cooling water, possible freedom in selecting location place within the engine room, especially in power generation applications, low failure frequency, low emission of contaminations, especially NO_x and sulphur compounds, to the atmosphere.

Gas turbine plants can operate in a broad range of load changes, hence in diagnostics of such engines much attention is placed to the issues of partial loads. For gas turbines partial loads are more important than for steam power plants as in the steam turbines change of power is achieved mainly by changing dose of working medium, i.e. water steam, whereas the remaining parameters of the medium at inlet to turbine are rather invariable. In gas turbines a change in their power output is accompanied with broad changes in all cycle parameters and engine efficiency. Calculation of operational parameters of gas turbine under partial loads either in steady conditions (static characteristics) or transient ones (dynamic characteristics) becomes a difficult and very complex task.

Especially difficult case of gas turbine operation is its work in the range of open anti-surge valve. The gas turbine operation in the range of open anti-surge valve (ASV) occurs at a low load from the side of consumer as well as during starting-up and stopping the turbine. This is the range of turbine operation in which anti-surge valve is automatically (i.e. without any interference of operator) activated to cause increasing air flow

rate from rotary compressor in order to shift its working point off the unstable work area into stable work one. An air surplus behind the compressor is discharged to the atmosphere, Fig. 1.

In the range of open ASV, gas turbine characteristics, especially gas turbine cycle efficiency, are radically changed. The efficiency drops fast and the gas turbine as a rule should not operate at all in this range. The work with open ASV occurs rather rarely and results from the reasons for safe operation of turbine set [2,3].

In the subject-matter literature there are only scarce publications concerning gas turbine operation in the range of open anti-surge valve [5]. This paper covers issues dealing with the problem and describes experimental tests performed on the test stand including full-scale gas turbine.

TWO-SHAFT GAS TURBINE

For aircraft drives, application is usually made of the two-shaft system in which a separate part of turbine is devoted to drive compressor only, Fig. 1.

The unit consisted of a compressor, combustion chamber and compressor turbine serves as a gas generator. Its aim is to produce hot gas of the parameters (p_3, t_3), which, expanding in the compressor turbine, transforms a part of its thermal energy into mechanical one. The role of the gas generator is similar to that of a steam boiler with supply pump in a steam turbine power plant. Further expansion occurs in a power turbine which delivers its output to a consumer. In the above described system the air (working medium) is absorbed from the atmosphere and sent back to the atmosphere in the form of exhaust gas therefore such cycles are called open cycles. The cycles are usually used in gas turbines driving mechanical devices including those in ship power plants.

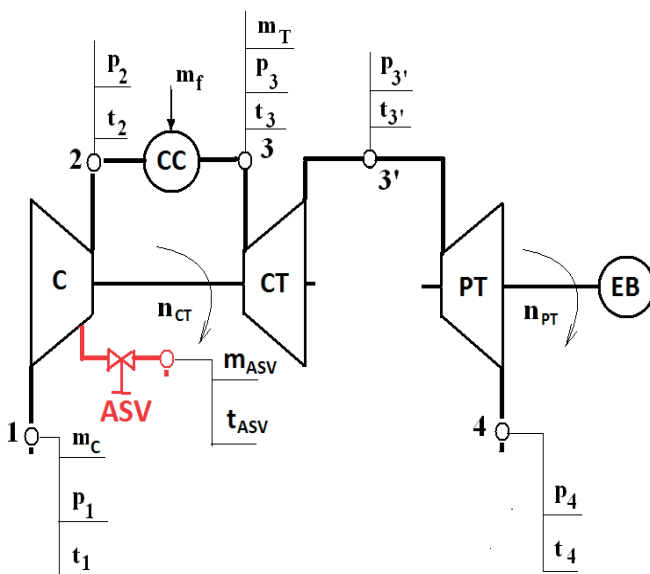


Fig. 1. Schematic diagram of two-shaft gas turbine. Simple open cycle (see Designations)

OPERATION OF TWO-SHAFT GAS TURBINE IN THE RANGE OF OPEN ANTI-SURGE VALVE

A two-shaft gas turbine installed on the engine test bed of the Department of Automation and Power Engineering, Faculty of Ocean Engineering and Ship Technology, Gdańsk University of Technology, was used for the tests. The gas turbine is of a light -aircraft type; it is applicable to driving the helicopter and operates according to simple cycle (Fig. 1) [1].

The gas turbine is consisted of (see Fig. 1):

- the compressor (C) of seven axial stages and one radial stage,
- the combustion chamber (CC) consisted of the body with collecting scroll and air pipes, flame tube, working injector and flame igniter,
- the compressor turbine (CT) – axial, one-stage,
- the power turbine (PT) – axial, two-stage,
- the eddy-current brake (EB) directly coupled with the turbine's shaft.

Nominal parameters of the turbine in ISO conditions are the following [4]:

- the power $N_e = 235 \text{ kW}$
- the compressor turbine shaft rotational speed $n_{CT} = 90\%$ (39375 rpm)
- the power turbine shaft rotational speed $n_{PT} = 101\%$ (24240 rpm)
- the exhaust gas temperature behind the combustion chamber, $t_3 = 870 \text{ }^\circ\text{C}$
- the fuel flow rate $m_f = 0,0808 \text{ kg/s}$

In order to assure a required static operation reserve for the compressor in all gas turbine operation ranges, an anti-surge valve which releases air flow from behind 6th stage of the compressor, was applied. The engine operates with open anti-surge valve during start-up and idle run down till a determined low rotational speed of compressor turbine, n_{CT} . Fig. 2.1 presents the range of compressor turbine rotational speed in function of atmospheric conditions (air temperature), which causes the shutting- up of the anti-surge valve [4].

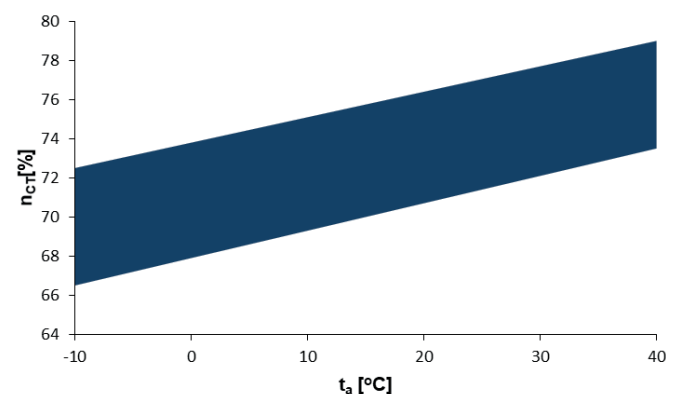


Fig. 2.1. The range of compressor turbine rotational speed in function of atmospheric conditions (air temperature) in which the anti-surge valve is shut up (acc. producer's data [4])

In the presented engine control of air extraction is executed by means of an automatic air extraction controller which starts the hydraulic valve to extract air from behind 6th compressor stage, Fig. 2.2.

To the stub pipe „A” the air pressure p_2 is applied from behind the compressor; the pressure is reduced by inlet and outlet nozzles placed in the pump controller of the fuel control system of the engine. To the stub pipe „B” the total air pressure p_2 is applied from behind the rotary compressor.

To the stub pipe „C” fuel is supplied under high pressure from the pump controller, and from the stub pipe „E” control pressure is sent into the mechanism actuating air extraction valve.

As long as the engine turbocompressor does not yet reach the rotational speed determined from Fig. 2.1, the slider „S” remains in its upper point. When the demanded pressure ratio p_2/p_1 is obtained, the slider „S” is displaced down. In this position the lower edge of the slider opens fuel flow under high pressure into the stub pipe „E” ; the pressure controls the anti-surge valve switching-on. The air - extraction valve is now closed. Operation of the air - extraction valve is controlled by the air - extraction automatic controller where the poppet valve connected with the piston is made open due to high pressure of the fuel delivered through the stub pipe „E” connected with the working space of the piston and the air-extraction automatic controller. The stub pipe „D” is connected with the discharge stub pipe of the pump controller.

Photo 1 shows location of the anti-surge valve within the gas turbine.



Photo 1. Air extraction from behind 6th stage of the compressor
1. Air-extraction automatic controller; 2. Anti-surge valve.

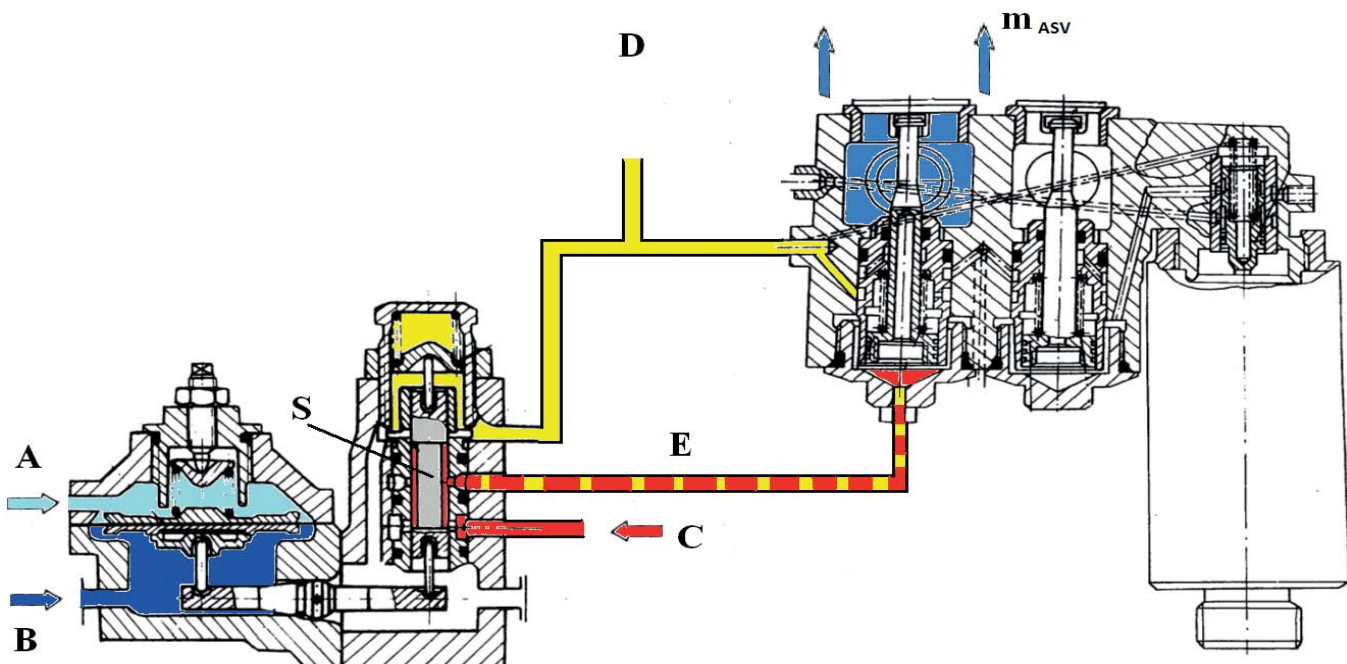


Fig. 2.2. Schematic diagram of the air-extraction control system [4] A – the air pressure p_2 ; B – the air pressure from behind the compressor, p_2 ; C – fuel high pressure from the pump controller; D – discharge stub pipe; E– the crossover between the air-extraction control device and air-extraction valve; S- slider; m_{ASV} –extraction air flow rate.

MEASUREMENT STAND [1]

The gas turbine measurement stand is shown in Photo 2. The stand was equipped with control and measurement systems as well as auxiliary devices including eddy-current brake, control and measurement software as well as data

recording and visualization software delivered by ODIUT Automex Co. Ltd¹. The stand contains also the gas turbine engine² coupled with the eddy-current brake. The engine absorbs air from outside of the building through the suction pipe fitted with a filter at its end ; exhaust gas from PT is directed to the atmosphere through an outlet funnel combined with a silencer. The eddy-current brake is cooled with water flowing in a closed system.

The turbine is controlled from an acoustically insulated cabin. The engine may be loaded by acting upon fuel system with the use of the gas charge lever or by loading the eddy-current brake, directly. The setting of the gas lever and of the brake may be changed simultaneously by using electronic control.



Photo 2. The test and didactic stand containing the two-shaft gas turbine

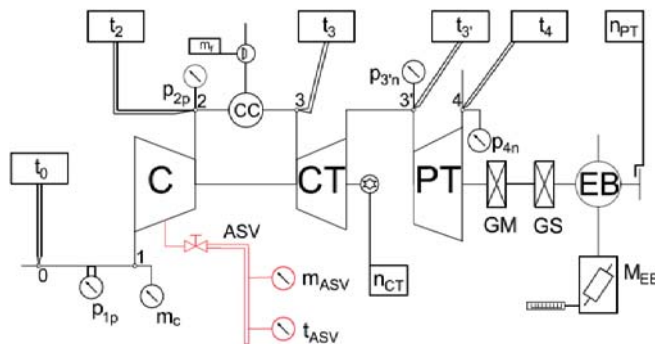


Fig. 3. Schematic diagram of the measurement system of the gas turbine test stand with possible measurement of the extraction air parameters [1]

The engine is controlled from the control cabin by means of digital controllers (controlling module) connected together by CAN bus which makes it possible to control simultaneously the two-dimensional object: the gas turbine and eddy-current brake as well as the measurement module, by means of a computer system.

The engine was specially adjusted to experimental tests by introducing additional measurement points to the standard engine instrumentation.

Fig. 3 presents the measurement scheme of the gas turbine test stand. To make it possible to measure parameters of air extraction from the rotary compressor, an additional measurement line allowing to determine the parameters was adjoined to the existing measurement system. In Fig. 3 additional measurement channels are distinguished by bold lines. In the outlet from the anti-surge valve a pipe for discharging air to the atmosphere was installed. On the pipe a sensor for measuring the extraction air flow rate m_{ASV} and its temperature t_{ASV} was attached (Sensor of Non-Incendive Type 4X, Model: ST50-AG12B000), Photo 3.

The test stand allows to measure not only static characteristics but also dynamic ones with a short time of signal sampling.



Photo 3. Measurement of extraction air parameters on the gas turbine test stand

EXPERIMENTAL TESTS OF GAS TURBINE PARAMETERS IN THE RANGE OF OPEN ANTI-SURGE VALVE

During start up of the turbine set as well as under low loads the gas turbine operates with open anti-surge valve which assures stable operation of the turbine set. The tests in question are aimed at the measuring of gas turbine parameters, especially air flow rate from anti-surge extraction point. The usual instrumentation of the gas turbine test stand makes it possible to measure only the air flow rate at the inlet to the turbine set, m_c , Fig. 3, because of the air inlet. location place. At the open anti-surge valve, the air flow rate to the combustion chamber, m_2 is not known.

The air flow rate m_2 delivered to the combustion chamber results from the relation:

$$m_2 = m_c - m_{ASV}$$

¹ ODIUT Automex sp. z o.o. (Ltd) designed and equipped the turbine station. All screenshots come from the company's own design.

² The GTD-350 turbine engine in the property of the Gdansk University of Technology was modernised and prepared for the tests in accordance with the instructions of the Department of Automatics and Turbine Propulsion by WSK "PZL-Rzeszów" S.A

In the range of open anti-surge valve, accurate knowledge of the air flow rate m_2 allows to calculate quantities which depend on the flow rate.

In the subject-matter literature there are only a few publications concerning this range of gas turbine operation. The completion of the test stand by possible additional measurement of air flow extracted from anti-surge valve makes it possible to measure gas turbine basic parameters. The test stand in question is one of the full - scale gas turbine stands the best instrumented in measurement points in Poland.

START - UP OF THE TURBINE SET

During start-up and transition to idle work the turbine set operates with open anti-surge valve. The valve is controlled automatically by comparing the air pressure from behind the compressor with that reduced according to the scheme presented in the previous section. In the start-up initial phase the valve is open, but it is choked when the pressure p_2 behind the compressor increases, Fig. 4. During start-up all the measured parameters become readjusted. The ASV is choked and opened again along with changes in the pressure p_2 .

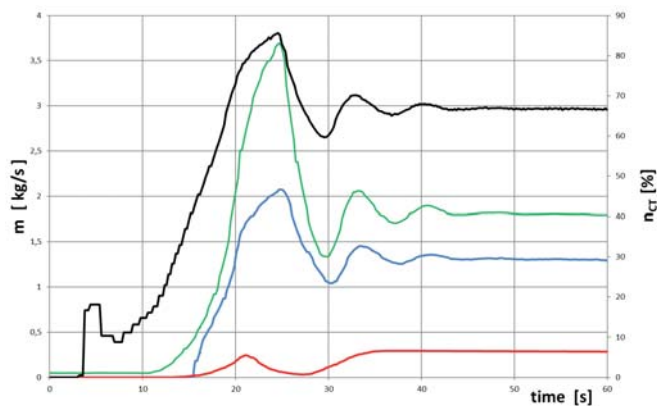


Fig. 4. Changes in the parameters of air flow rate at inlet to compressor, rotational speed of compressor turbine as well as air pressure at outlet from compressor and extraction- air flow rate during start-up of the turbine set

The start-up lasts about 30 seconds counting from the instant of switching-on the start-up apparatus till the transition to idle work. Character of changes in the air flow rate m_C , pressure p_2 and compressor turbine rotational speed n_{CT} is similar, Fig. 4.

Fig. 5 shows time runs of air flow through the compressor during start-up. The air flow rate m_2 delivered to the combustion chamber is equal to the air flow rate m_C at inlet to the turbine set reduced by the extraction-air flow rate m_{ASV} . The ratio of extraction air flow rate and air flow rate at inlet, m_{ASV}/m_C , changes in time beginning from 0 up to 0,22 during idle work, Fig. 5.

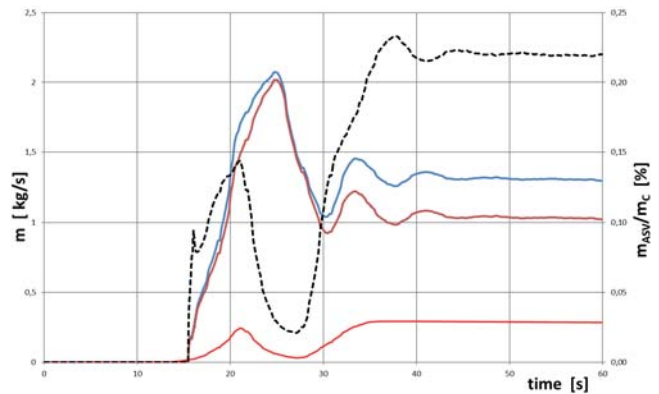


Fig. 5. Changes in air flow rates in the compressor during start-up

During start-up, temperatures of air flow and gas flow in particular points of the cycle are changing, Fig. 6. The gas flow temperatures : behind the combustion chamber, t_3 , in passage between the turbines, t_3' , at outlet from the power turbine, t_4 , have similar runs and repeat oscillations resulting from flowing gas, and their amplitudes become smaller along with increasing distance of measurement point from the combustion chamber. The smallest exhaust gas temperature oscillations occur behind the power turbine. Runs of air temperature behind the compressor, t_2 , do not show such oscillations like those of gas flow.

Results of measurements of air temperature at outlet from the compressor, t_2 , and extraction-air temperature t_{ASV} during start-up are given in Fig. 7. During start-up the extraction-air temperature t_{ASV} increases and its time run differs from that of the air behind the compressor, t_2 .

Fig. 8 presents changes in the rate of fuel flow delivered to the combustion chamber, m_p , on the background of the runs of the air flow rate m_C and compressor turbine rotational speed n_{CT} . The fuel flow during start-up is limited because of fast increasing gas temperature behind the combustion chamber, to reach finally a value relevant to idle work, in the end of the start-up process.

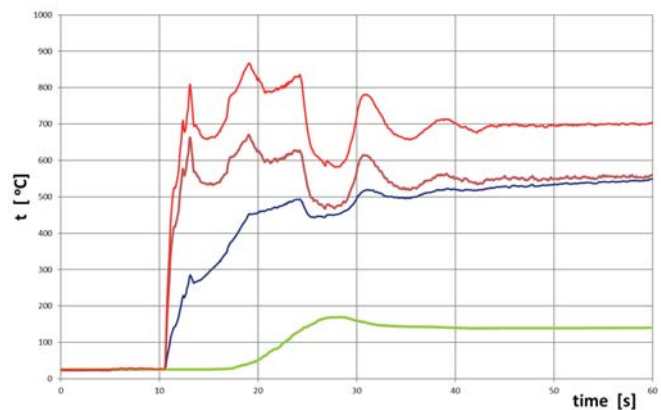


Fig. 6. Changes in air flow temperature and gas temperature in particular points of gas turbine cycle during start-up

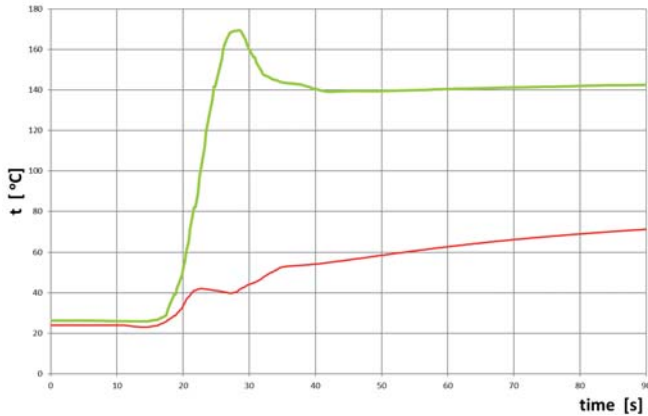


Fig. 7. Air temperature behind the compressor and in extraction valve during start-up
 — t_{ASV} — t_2

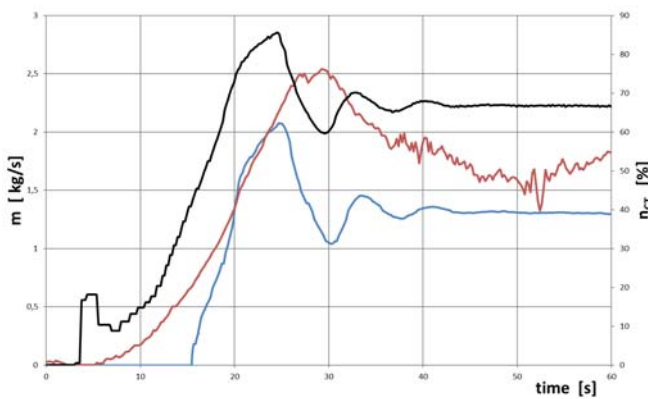


Fig. 8. Changes in the fuel flow rate and air flow rate at inlet to the compressor as well as in the rotational speed of the compressor turbine during start-up
 — n_{CT} — m_c — $m_j \cdot 100$

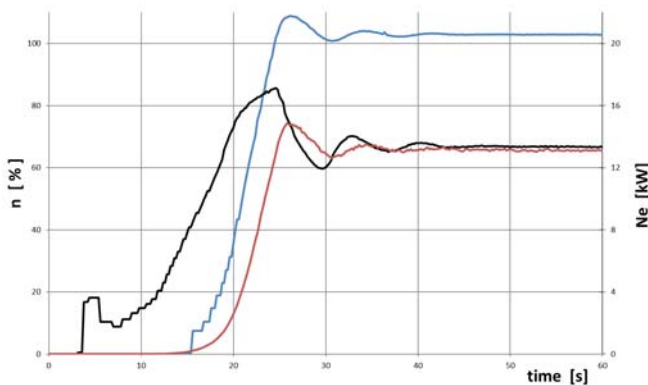


Fig. 9. Runs of the power output of the turbine set as well as of rotational speed of compressor turbine and power turbine during start-up
 — n_{CT} — n_{PT} — Ne

Fig. 9 presents changes in the rotational speed of compressor turbine n_{CT} and power turbine n_{PT} as well as in the effective power of the turbine set, Ne . During start-up the eddy-current brake was preliminarily loaded by the power of about 13 kW. Changes in the power Ne and the speed n_{PT} in time have similar character.

RANGE OF LOW LOADS OF THE TURBINE SET

In the range of low loads of the turbine set the anti-surge valve is open. Along with increasing load of the turbine set, which is equivalent to increasing the rotational speed of the compressor turbine, the valve is being closed at the rotational speed n_{CT} according to Fig. 2.1.

The experimental tests were conducted by loading the eddy-current brake step by step so as to shut the anti-surge valve up and then to make the valve to become open by unloading the turbine set.

Fig. 10 contains runs of the rotational speed of the compressor turbine, n_{CT} , and of the air pressure behind the compressor, p_2 , during shutting up and opening the anti-surge valve of the gas turbine. At the increasing of the speed n_{CT} up to about 79% the ASV starts shutting up, and its complete closure occurs at the speed of about 81%. At further load increasing the turbine set operates in the range of closed anti-surge valve. During the loading, Fig.10, the ASV starts to open at the speed n_{CT} equal to about 77,5% to be entirely open at the speed of about 7,5%.

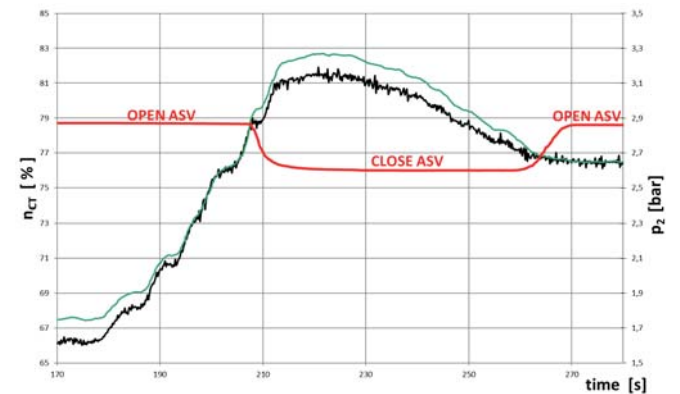


Fig. 10. Range of the turbine set's operation with closed and open anti-surge valve (ASV)
 — n_{CT} — p_2 — ASV

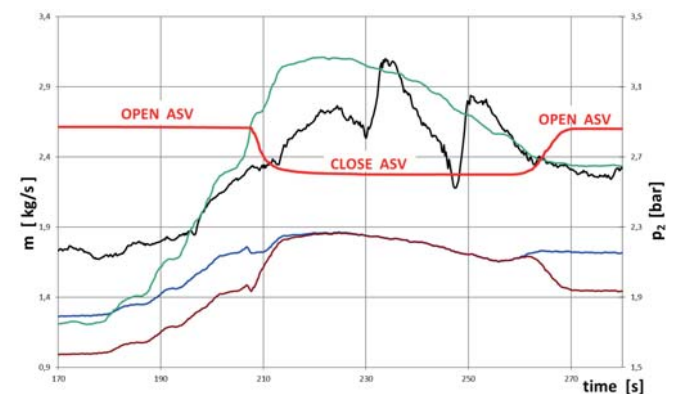


Fig. 11. Changes in air and fuel flow rates as well as the pressure p_2 in the range of closing and opening the ASV
 — m_c — p_2 — $m_j \cdot 100$ — m_2 — ASV

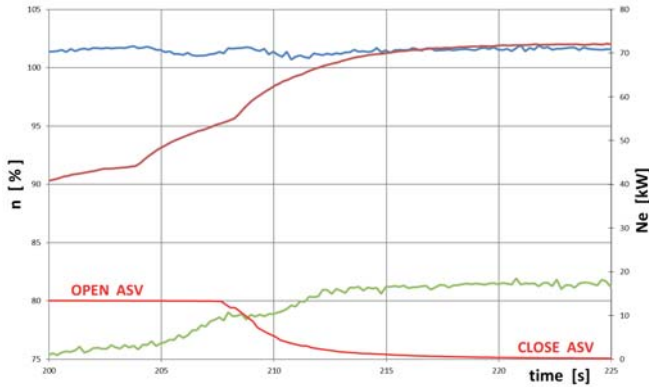


Fig. 12. Changes in gas turbine parameters in the range of closing the ASV
 — n_{CT} — n_{PT} — Ne — ASV

Fig. 11 presents changes in air flow through the compressor as well as in the pressure p_2 and fuel flow during opening and closing the ASV. At the closed ASV the air flow rate m_2 delivered to the combustion chamber is equal to the air flow rate at inlet to the compressor, m_C .

In the runs of changes in the power output Ne and the speed n_{CT} , changes associated with closing the ASV can be observed, however the speed n_{PT} is not susceptible to closing or opening the ASV, Fig. 12.

The static characteristics of the gas turbine in the range of open ASV are presented in Fig. 13 and 14. The extraction-air flow rate m_{ASV} is constant and amounts to 0,25 kg/s in the range of open ASV. However during loading the turbine set, the ratio m_{ASV}/m_C is varying because the air flow rate m_C increases along with increasing the speed n_{CT} (increasing power output of the gas turbine). The ratio drops beginning from idle work till the start of ASV closing operation and varies between 0,22 and 0,15. The temperature of the air mass flow m_{ASV} rises a little from the value of 80°C to 85 °C at closing the ASV. The temperature of the air behind the compressor, t_2 , in the same range of operation increases from about 145°C to 200°C, and, the gas temperature behind the combustion chamber varies within the range from 700°C to about 20°C.

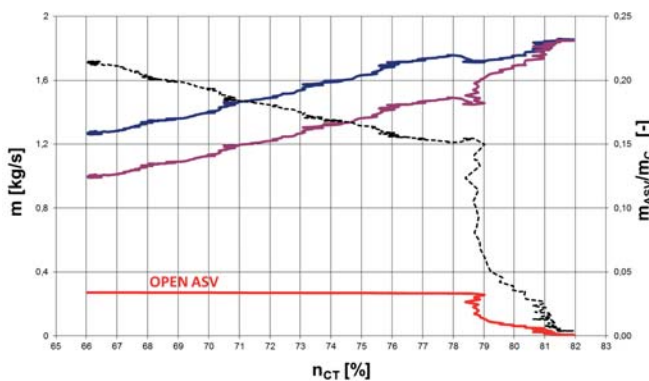


Fig. 13. Changes in air flow rates in function of changes in the speed n_{CT} in the range of open ASV (the ASV starts to close at the speed $n_{CT} = 79\%$)
 — m_C — m_2 — m_{ASV} — m_{ASV}/m_C

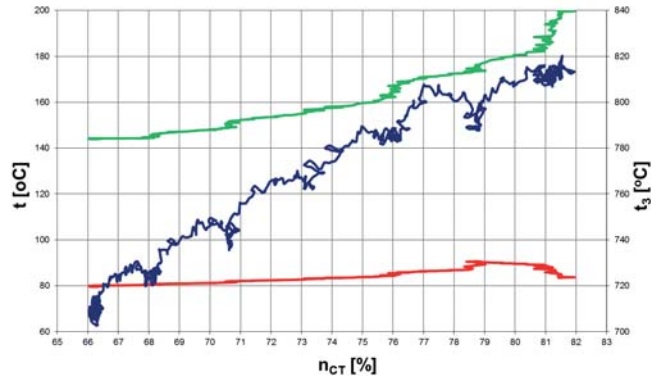


Fig. 14. Changes in exhaust air temperature in function of changes in the speed n_{CT} in the range of open ASV (the ASV starts to close at the speed $n_{CT} = \text{abt. } 79\%$)
 — t_2 — t_{ASV} — t_3

CONCLUSIONS

Experimental tests of gas turbine operation in the range of open anti-surge valve were performed. The tests covered two gas turbine operation ranges: the start-up range of the turbine set and the range of low loads on the gas turbine with open anti-surge valve.

The tests demonstrated that in start-up the range of the turbine set the gas turbine operates with open anti-surge valve. During start-up the ASV is choked depending on a value of the air pressure behind the compressor as it results from the control process of the valve.

In the range of low loads on the turbine with open ASV the measurements make it possible to determine the air flow behind the compressor, delivered to the combustion chamber. Knowledge of amount of the flow allows to determine the gas turbine characteristics in the range of open anti-surge valve. And, in this range the extraction- air flow rate m_{ASV} is constant irrespective of gas turbine loading.

Designations

m – mass flow	C – compressor
n – shaft rotational speed	CC – combustion chamber
Ne – power of gas turbine	CT – compressor turbine
p – pressure	EB – eddy - current brake
t – temperature	PT – power turbine
	ASV – anti-surge valve

Cycle points

- 1 – compressor inlet
- 2 – compressor outlet
- 3 – combustion chamber outlet
- 3' – crossover between turbines
- 4 – turbine outlet

Indexes

- f – fuel
- n – overpressure
- p – negative pressure

BIBLIOGRAPHY

1. Dzida M. Frost J.: Two-shaft Gas Turbine Teaching and Testing Station. Journal of POLISH CIMEEAC, Vol. 11 No. 1 (2016) pp. 31-46
2. Dzida M.: Impact of changes in gas turbine main parameters on accuracy of calculation of upper temperature of gas turbine cycle (in Polish). Zagadnienia Maszyn Przepływowych. Instytut Maszyn Przepływowych Polskiej Akademii Nauk, Gdańsk, 1993, pp.205-219.
3. Dzida M.: Possible Efficiency Increasing of Ship Propulsion and Marine Power Plant with the System Combined of Marine Diesel Engine, Gas Turbine and Steam Turbine. [Ed.] Ernesto Benini. Advances in Gas Turbine Technology. Rijeka : Published by InTech,, 2011, Chapter 3, pp. 45 -68.
4. Technical description of GTD-350 engine for Mi-2 helicopter (in Polish). Document No.16.0.381. Issued on 3 May 1978. Wytownia Sprzętu Komunikacyjnego „PZL Rzeszów”.
5. Cortinovis A., Ferrea H.J., Lewandowski D., Mercangöz M.: Experimental evaluation of MPC-based anti-surge and process control for electric driven centrifugal gas compressors. Journal of Process Control, 34 (2015), pp. 13–25.

CONTACT WITH THE AUTHORS

Marek Dzida
Jacek Frost

Faculty of Ocean Engineering and Ship Technology
Gdansk University of Technology
Gabriela Narutowicza 11/12
80-233 Gdańsk
POLAND

ASSESSMENT OF ENERGY USE AND ELIMINATION OF CO₂ EMISSIONS IN THE LIFE CYCLE OF AN OFFSHORE WIND POWER PLANT FARM

A. Tomporowski¹⁾

J. Flizikowski¹⁾

M. Opielak²⁾

R. Kasner¹⁾

W. Kruszelnicka¹⁾

¹⁾ University of Science and Technology, Faculty of Mechanical Engineering, Poland

²⁾ Lublin University of Technology, Faculty of Mechanical Engineering, Poland

ABSTRACT

Power stations in marine locations cause multi-faceted impact on the environment, man and the economy. There are not many studies devoted to modeling energy benefits for CO₂ emissions. The paper presents the issues of assessing the efficiency of offshore wind farms, defined as the ratio of benefits to life cycle inputs. The scientific goal was to develop a mathematical model for efficiency in the design, manufacture, use and management of offshore wind power. The papers practical purpose is the experimental designation of the impact of selected post-use management methods, time of use and maritime location, i.e. average annual productivity of wind power plants on the efficiency of energy benefits from greenhouse gas emissions. The mathematical model of the integrated cost-benefit ratio has been developed for energy use assessment, taking into account the benefits generated by electricity production and the life-cycle CO₂ emissions based on the LCA analysis using the CML method. Mathematical model validation was performed by determining the value of the indicator for an existing 2 MW offshore wind farm and comparatively for fossil fuel production: lignite, stone, fuel oil and natural gas. Analytical and research work carried out showed that the higher the efficiency index, the higher the value of the indicator. It has been shown that the location of the power station at sea produces more favorable CO₂ elimination rates, due to higher productivity compared to in-land wind power plants. A more favorable form of post-consumer management for CO₂ has been determined as recycling. It was found that for electricity generated from offshore wind farms, the value of the energy efficiency benefit from CO₂ emissions is higher than for fossil fuel energy production.

Keywords: energy efficiency, use of machines, offshore wind power plant farms, CO₂ emissions

INTRODUCTION

Efficiency is the goal, the postulated state of the technological energy, allowing estimation, optimization, modernization, innovation: ideas, constructions and processes: generation, use, power and decommissioning, by comparing the benefits and expenditures in their life cycle.

For the purposes of this paper, the benefits of offshore wind power (EW) include, inter alia, a product of power and energy, financial revenues, reduction of emissions to the marine environment, diversification of energy sources,

development and activation of the environment, and other potential benefits which cannot be determined today [2, 11, 13, 17, 24].

On the other hand, the costs of the operation included damage to the marine environment, energy consumed throughout the life cycle, incurred financial expenditures, harmful social outlays and potential costs that are currently unknown [10, 11, 34].

The benefits and costs of action are divided into rational and irrational, measurable and immeasurable, actual and potential. Such comparisons can be made in many ways, but

it is important to create a model that enables the analysis, evaluation and development of energy efficiency using expenditure and emissions throughout the life cycle [10, 11, 17, 18]. From the literature analysis of the subject comes the conclusion that there are no studies on the modeling of energy benefits from the emission of harmful gases as an outlay for obtaining these benefits [6, 10].

In light of the above findings, the objectives of the study were:

1. To develop a mathematical model of the cost-effectiveness of the outlay for the design, manufacture, use, and disposal of offshore wind power (EW) power plants;
2. Experimental determination of the influence of selected management methods, use time and maritime location, i.e. average annual productivity of wind power plants influence on energy efficiency benefits from greenhouse gas emissions.

Problems: In order to achieve the objectives of the study, it was proposed to formulate the following research problems:

1. Taking into account such variables as: design, manufacturing, use and management, is it possible to develop an adequate mathematical model of energy efficiency (energy production) from CO₂ emissions for the analysis, evaluation and development of marine EW?
2. What are the effects on the energy production efficiency from CO₂ emissions for EW offshore wind farms coming from:
 - power uses,
 - expenditures (emissions) during the design, manufacture, use and development of offshore EW potentials,
 - ways of utilizing post-use offshore EW potentials,
 - usage time of offshore EW,
 - maritime location, i.e. average annual productivity of offshore EW.

MATHEMATICAL MODEL

General assumptions: the basis for developing the mathematical model of energy efficiency of offshore EW for the purposes of design, manufacture, use and management were the assumptions of the general equation of development. The equation of the development of the renewable energy source efficiency according to the benefits and expenditures of energy, economy and ecology is [5-11, 17, 18, 29-34]:

$$L(H, E, R, \Theta, t) = P(s, z, \Theta, t - t_0), \quad (1)$$

where:

- H* – performance characteristics as output quantities (efficiency, process harmlessness, power and electricity quality, CO₂ emissions),
- E* – features of internal components: energy conversion units,

R – relations, interconnections of elements (the relations of elements of offshore (EW) wind power plants, materials, plastics, air, emissions, impact on operator health, system functionality, environment and accompanying devices);

$\Theta, t - t_0$ – time,

s – control, interference: design, manufacture, use, storage, recycling of EW off-shore material potential,

z – interference.

The left side of the equation (1) (model) describes the properties of the processing process, its physical characteristics, specific to the class of activity. These properties depend on the elements E_1, \dots, E_m , relationships (relations) between these elements R_1, \dots, R_n and are functions Θ and t (time of operation and dynamic process). The unknowns are the elements of the set characteristics of the inputs processes for the preparation of elements for use of offshore EW in accordance with the conditions and purpose, development and the advantages of the use of energy H as the response variables, which determine the effectiveness evaluation – lack of uniformity and inefficiency, the variable efficiency, unwarranted consumption and nature power, internal energy consumption, construction and operating materials etc.

The right side of the equation (1) is a description of internal and external interference. They may depend on: the developmental form of the interaction, the control by the signals from the *s* set (storage, recycling), interactive interaction, interaction of elements (material, machine, conversion process, conditions, marine environment, construction, ...), tensile-tension impact (associated with potential difference), which is the cause of compensatory processes; It may also occur as a disturbance of the system as expressed by *z*.

Taking into account the specific characteristics of the *U* benefits and the outlays *N* of using and operating wind turbines, equation (1) takes the form:

$$L(E, R, U, N, \Theta, t) = P(s, z, \Theta, t - t_0). \quad (2)$$

Starting from the descriptive definition of efficiency, the formal form of the indicator can be given as the quotient of the utility $U(t)$ to the directly incurred expenditure $N(t)$ related to the time of action [17, 29]:

$$E(t) = \frac{U(t)}{N(t)} \quad (3)$$

The values of $U(t)$ and $N(t)$ denote the values of the obtained positive and negative flows - the expenditures spent up to the time t from the beginning of the operation ($t = 0$).

The function $N(t)$ in time interval $(0, t)$ is a non-temporal function, i.e. in every elementary interval (Δt or dt) elementary value of inputs [17, 24]:

$$n(t) = \frac{dN(t)}{dt} \quad (4)$$

is not less than zero, and the value of the function $N(t)$, depending on whether the function $n(t)$ is continuous or discrete, is determined from the relation:

$$N(t) = \int_0^t n(\tau) d\tau, \quad (5)$$

$$N(t) = \sum_i^T n_i \cdot \Delta t_i.$$

The use function of offshore wind power plants $U(t)$ in the given time interval can take both positive and negative values and its values based on the values of the elementary functions

$$u(t) = \frac{dU(t)}{dt} \quad (6)$$

depending on its form (continuous or discrete), was determined from the dependence:

$$U(t) = \int_0^t u(\tau) d\tau, \quad (7)$$

$$U(t) = \sum_i^T u_i \cdot \Delta t_i.$$

In this consideration, the term “outlay” was defined as part of an engineering resource, i.e. energy-material-information-time, spent in a given activity [1, 3, 10, 13-18]. This can be expressed in different components in different units [26, 31].

The useful effect of off-shore wind power is interpreted as the part of the effect (effect, product) of the activity which has utility adequateness and which is the target of action, and the side effects of the action and its effects are subject to considerations of destructiveness [6, 18, 29].

It has been assumed that the time interval Δt , in which the operation of the test object and analysis is considered, tends to zero. The momentary efficiency of the energy system is therefore the limit value of the change in effect Δt by the increment of inputs ΔN in the time interval Δt when Δt tends to zero, in the form:

$$E(t) = \lim_{\Delta t \rightarrow 0} \frac{U(t + \Delta t) - U(t)}{N(t + \Delta t) - N(t)} \quad (8)$$

assuming that the interval is large enough, i.e.

$$\Delta t = T \gg 0,$$

then the equation of instantaneous energy efficiency takes the form:

$$E(t) = \frac{U(t+T) - U(T)}{N(t+T) - N(T)} = \frac{\Delta U}{\Delta N} = \frac{U(T)}{N(T)}. \quad (9)$$

Utilization quotient of the benefits $U(T)$ achieved in finite time interval T by $N(T)$ expenditure incurred at this time is the mean efficiency.

Assumptions of analysis, evaluation and development:

Efficiency in the construction and operation of energy machinery is a feature that expresses the rational ability of systems to meet specific needs, desires for human well-being, their functionality, product quality, product harmony and the process of action (attainment of intended goals, according to purpose and requirements).

For the evaluation of production, operation and decommissioning of offshore wind farms in the life cycle the integrated indicator of the efficiency benefits incurred from the creation to elimination i.e. renewable energy source, has been defined in the form:

$$E(t) = \frac{U(t)}{N(t)}, \quad (10)$$

where:

- $E(t)$ – integrated life cycle efficiency indicator,
- $U(t)$ – benefits in the life cycle,
- $N(t)$ – outlays in the life cycle,
- t – time of use.

Denoting by:

- U_i – benefits in the time of the i -th year of use,
 - m_w – outlays at the manufacturing stage,
 - N_i – outlays in the time of the i -th year of use,
 - m_z – outlays in the post use management,
- can be written as [10]:

$$E(t) = \frac{U(t)}{N(t)} = \frac{\sum_{i=1}^t U_i}{m_w + \sum_{i=1}^t N_i + m_z}. \quad (11)$$

For the considered offshore wind power plant, it is assumed that m_w and m_z are constants, whereas U_i and N_i are random values. It is also assumed that U_1, U_2, \dots have the same distribution, and N_1, N_2, \dots have the same distribution, and that U_1, U_2, \dots are independent, and N_1, N_2, \dots are independent. For the purposes of the analysis, the assumption is that both U_1 and N_1 have normal distributions with known mean and variances. So:

$$U_1, U_2, \dots \sim \mathcal{N}(\mu, \sigma) \text{ independent,}$$

$$N_1, N_2, \dots \sim \mathcal{N}(m, s) \text{ independent,}$$

where:

- \mathcal{N} – means normal distribution,
- μ – is the average benefit generated during the year of use,
- σ – is the standard deviation of the benefits generated during the year of use,
- m – is the average amount spent during the year of use,
- s – is the standard deviation of expenditures spent during the year of use.

Notes:

1. In this paper, benefits and expenditures are considered in one year because the research facility has annual, comparable, repeatable cycles of activity.
2. For the above reasons, the assumption of normality of distributions is substantiated. For the studies and analyzes of specific values of benefits and expenditures in the following years, one can test the hypothesis about the normality of distributions and then evaluate their parameters.
3. For the given i -th year of operation the offshore wind turbines U_i and N_i are correlated and their correlation values are not known.

Distribution of power and environmental expenditures in the use of offshore wind turbines (CO_{2eq} emission): Experimental determination of the influence of selected offshore wind farm designs on energy efficiency and benefits was determined by answering the question: what effect on off-shore EW efficiency from CO₂ emissions are generated by the use of energy and resources (emissions) of design, manufacture and management?

By dividing the numerator and denominator by t in equation (11), we obtain that

$$E(t) = \frac{\bar{U}_t}{(m_W + m_Z)/t + \bar{N}_t}, \quad (12)$$

where:

$$\bar{U}_t = \frac{1}{t} \sum_{i=1}^t U_i, \quad \bar{N}_t = \frac{1}{t} \sum_{i=1}^t N_i \quad (13)$$

are the average of generated benefits and average generated emissions (spent outlays) per year over the t years of use of offshore EW. The distributions \bar{U}_t and $((m_W + m_Z)/t + \bar{N}_t)$ are known:

$$\begin{aligned} \bar{U}_t &\sim \mathcal{N}(\mu, \sigma/\sqrt{t}), \\ ((m_W + m_Z)/t + \bar{N}_t) &\sim \mathcal{N}((m_W + m_Z)/t + m, s/\sqrt{t}). \end{aligned} \quad (14)$$

Justifying the choice of a normal distribution the consideration was carried out based on Figure 1, a) density f , b) the survival function \bar{F} random size X of an average a and standard deviation d .

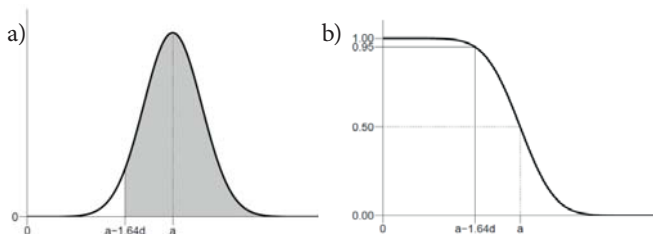


Fig. 1. Density (a) and survival function (b) of the normal distribution for the case in question with parameters a and d

To determine the probability that X reaches a value that is equal to or greater than a given value x , the field under density is determined/counted on the right of x and the value \bar{F} for x :

$$\Pr(X \geq x) = \int_x^{+\infty} f(x)dx = \bar{F}(x) \quad (15)$$

In this case, it is characteristic that the normal distribution considered is a “light tail” distribution, i.e. X is reluctant to take values far from the mean a . E.g.:

$$\begin{aligned} \Pr(X \geq a - 0,67d) &= 0,75, \\ \Pr(X \geq a - 1,28d) &= 0,9, \\ \Pr(X \geq a - 1,64d) &= 0,95, \\ \Pr(a - 4,06d \leq X \leq a + 4,06d) &= 0,99995. \end{aligned} \quad (16)$$

The considered integrated efficiency index of the test object $E(t)$ is the quotient of two variables with normal distributions. So constructed random value has so called double unoccupied student distribution. This distribution is very complicated and difficult to use. In particular, there is no formal so called expected value $\mathbb{E}E(t)$, which would naturally define the property $E(t)$. Therefore, in this paper, simplification is defined by the range to which $E(t)$ belongs with probability very close to one.

From (16) it has been concluded that:

$$\Pr\left(\mu - \frac{4,06\sigma}{\sqrt{t}} \leq \bar{U}_t \leq \mu + \frac{4,06\sigma}{\sqrt{t}}\right) = 0,99995, \quad (17)$$

$$\Pr\left(m + \frac{m_W + m_Z}{t} - \frac{4,06s}{\sqrt{t}} \leq (m_W + m_Z)/t + \bar{N}_t \leq m + \frac{m_W + m_Z}{t} + \frac{4,06s}{\sqrt{t}}\right) = 0,99995. \quad (18)$$

From inequality

$$\Pr(A \cap B) \geq P(A) + P(B) - 1 \quad (19)$$

it is therefore apparent that the

$$\Pr\left(\frac{\mu - \frac{4,06\sigma}{\sqrt{t}}}{m + \frac{m_W + m_Z}{t} + \frac{4,06s}{\sqrt{t}}} \leq E(t) \leq \frac{\mu + \frac{4,06\sigma}{\sqrt{t}}}{m + \frac{m_W + m_Z}{t} - \frac{4,06s}{\sqrt{t}}}\right) \geq 0,9999. \quad (20)$$

So if σ is much smaller than μ , and s is much smaller than $m + (m_W + m_Z)/t$, then with probability very close one, it can be written approximately that the integrated efficiency index of the test object is:

$$E(t) \approx \frac{\mu}{m + \frac{m_W + m_Z}{t}} = \frac{\mu \cdot t}{m_W + m \cdot t + m_Z}. \quad (21)$$

CASE STUDY

The integrated efficiency index of the offshore EW expenditure defined as electricity production efficiency from greenhouse gas emissions: a 2 MW wind turbine, a 90 m blade diameter, installed on a 105 m tower at a location for the integrated efficiency sea location. An integrated indicator of the efficiency of electricity production from CO_{2eq} emissions was defined. On the basis of the previously presented dependency, the integrated index of the efficiency of the production of electricity from CO_{2eq} emissions can be written as:

$$E(t) = \frac{U}{m_W + m_U + m_Z} \approx \frac{\mu \cdot t}{m_W + m \cdot t + m_Z}, \quad (22)$$

where:

- t – usage time in years,
- $E(t)$ – integrated efficiency index for t years of use,
- U – energy produced at the stage of use,
- μ – average annual energy output at the stage of use,
- m_W – CO_{2eq} emission at the manufacturing stage,
- m_U – CO_{2eq} emission at the stage of use,
- m – average annual CO_{2eq} emissions at the stage of use,
- m_Z – CO_{2eq} emission at the post use management stage.

The wind farm researched was started in 2012. The average annual production in the long run was determined on the basis of three years of production. CO_{2eq} emissions in the life cycle were determined using the LCA method using CML modeling. For this purpose SimaPro 7.1 software was used. The results of the study were based on criteria designed to develop the mathematical model of energy efficiency of offshore wind farms and to determine the impact of selected wind farm development methods on useful energy benefits and integrated CO₂ emissions.

The obtained results of the model variables of the integrated ecological efficiency model CO_{2eq} are presented in Table 1.

Tab. 1. Production of energy during use and CO_{2eq} emissions in the life cycle of an offshore wind power plant (source: own research)

No.	Indicator	Symbol	Unit	Value
1.	Average annual energy output at the stage of use,	μ	MWh·rok ⁻¹	5118
2.	CO _{2eq} emission at the manufacturing stage	m_W	Mg CO _{2eq}	2700
3.	Average annual CO _{2eq} emission at the stage of use	m	Mg CO _{2eq} ·rok ⁻¹	24
4.	CO _{2eq} emission at the post use management stage (storage)	m_Z^S	Mg CO _{2eq}	1150
5.	CO _{2eq} emission at the post use management stage (recycling)	m_Z^R	Mg CO _{2eq}	-704

On this basis, an integrated ecological efficiency of CO_{2eq} emissions was established for the 25-year cycle of use with the production and end-use of $E^S(25)$ and $E^R(25)$ recycling. The results are presented in Table 2. It also includes the comparison of the values of the integrated ecological efficiency of conventional power plants with CO_{2eq} emissions for [10, 19-23]:

- hard coal,
- brown coal,
- heating oil,
- natural gas.

The combined environmental efficiency of an off-shore wind power plant with CO_{2eq} emissions compared to a conventional coal-fired power plant in an estimated 25-year operating life with potable landfill disposal is 9.93 times higher. However, when managed through recycling - 16.8 times higher.

Tab. 2. Integrated ecological efficiency of offshore EW and conventional power plants with CO_{2eq} emissions in a 25-year lifecycle with different ways of managing the offshore wind potential of a wind farm (source: own research)

No.	Indicator	Symbol	Unit	Value
1.	Integrated ecological efficiency of off-shore EW with CO _{2eq} emission (storage)	$E^S(25)$	MWh·Mg CO _{2eq}	29,38
2.	Integrated ecological efficiency of off-shore EW with CO _{2eq} emission (recycling)	$E^R(25)$	MWh·Mg CO _{2eq}	49,73
3.	Integrated ecological efficiency of CO _{2eq} emission for the production of electricity from fossil fuels (hard coal)	–	MWh·Mg CO _{2eq}	2,96*
4.	Integrated ecological efficiency of CO _{2eq} emission for the production of electricity from fossil fuels (brown coal)	–	MWh·Mg CO _{2eq}	2,75*
5.	Integrated ecological efficiency of CO _{2eq} emission for the production of electricity from fossil fuels (heating oil)	–	MWh·Mg CO _{2eq}	3,61*
6.	Integrated ecological efficiency of CO _{2eq} emission for the production of electricity from fossil fuels (natural gas)	–	MWh·Mg CO _{2eq}	4,96*

* calculated on the basis of data [10]

Integrated off-shore wind power plant efficiency with CO_{2eq} emissions compared to a conventional lignite-fired power plant in an estimated 25-year operating life with a potential utilization of storage capacity is 10.68 times higher. On the other hand, utilization by recycling - 18.08 times higher.

The values of the integrated environmental efficiency of offshore wind power installation with CO_{2eq} emissions in comparison with a conventional power plant utilizing oil or natural gas attain slightly lower values.

A comparison of these data shows the high possibility of reducing CO_{2eq} emissions by designing, manufacturing and using off-shore wind power plants, replacing fossil fuel energy from offshore wind power.

As the integrated ecological efficiency of CO_{2eq} emissions in the life cycle largely depends on the length of the operation phase. Figure 3 illustrates this dependence on the offshore wind farm, taking into account storage and recycling at the

post-disposal stage, and uncertainty resulting from a forecast of productivity and consumption of energy and materials in use.

Figure 3 also shows the effectiveness of CO_{2eq} emissions for the production of electricity from hard coal and natural gas (2.90 for hard coal, 4.96 for natural gas respectively).

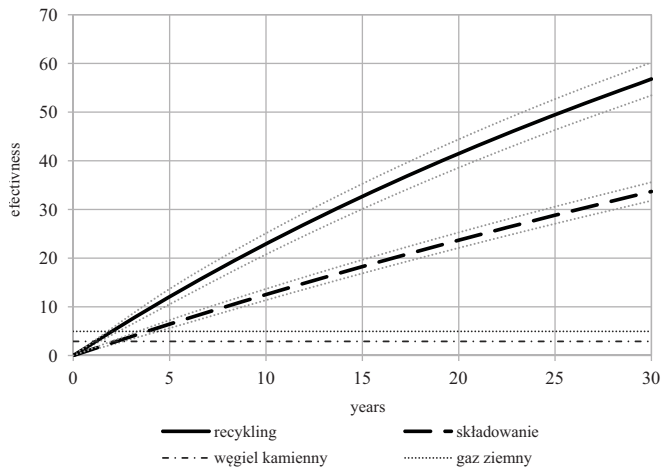


Fig. 2. The dependence of the integrated CO_{2eq} efficiency index on the use of different off-shore wind power plants for the various post-shore utilization patterns of the parameters listed in Table 1 (source: own research)

The increasing value of the integrated efficiency index from CO_{2eq} emissions as a function of the time of use for various off-shore utilization patterns of the analyzed off-shore wind turbine of $\mu = 5118 \text{ MWh} \cdot \text{year}^{-1}$ indicates the growing operational potential of offshore wind turbines, even over 25 years of use.

The equations of the lines shown in Figure 2 are mathematically described in Table 3. The values of the integrated energy efficiency index from CO_{2eq} emission are given for the analyzed, rated offshore wind turbine as average, minimum and maximum values for recycling and post-use management.

Tab 3. Integrated CO_{2eq} efficiency index for recycling and storage at offshore wind power plants (Source: own research)

No.	Model	Mathematical form
1.	recykling	$E^R(t) = \frac{5118 \left[\frac{\text{MWh}}{\text{rok}} \right] \cdot t}{2700[\text{Mg}] + 24 \left[\frac{\text{Mg}}{\text{rok}} \right] \cdot t - 704[\text{Mg}]}$
2.	storage	$E^S(t) = \frac{5118 \left[\frac{\text{MWh}}{\text{rok}} \right] \cdot t}{2700[\text{Mg}] + 24 \left[\frac{\text{Mg}}{\text{rok}} \right] \cdot t + 1150[\text{Mg}]}$
3.	recykling (max)	$E^{R\max}(t) = \frac{5118 \left[\frac{\text{MWh}}{\text{rok}} \right] \cdot t + 1440 \left[\frac{\text{MWh}}{\sqrt{\text{rok}}} \right] \cdot \sqrt{t}}{2700[\text{Mg}] + 24 \left[\frac{\text{Mg}}{\text{rok}} \right] \cdot t - 704[\text{Mg}] - 4 \left[\frac{\text{MWh}}{\sqrt{\text{rok}}} \right] \cdot \sqrt{t}}$
4.	recykling (min)	$E^{R\min}(t) = \frac{5118 \left[\frac{\text{MWh}}{\text{rok}} \right] \cdot t - 1440 \left[\frac{\text{MWh}}{\sqrt{\text{rok}}} \right] \cdot \sqrt{t}}{2700[\text{Mg}] + 24 \left[\frac{\text{Mg}}{\text{rok}} \right] \cdot t - 704[\text{Mg}] + 4 \left[\frac{\text{MWh}}{\sqrt{\text{rok}}} \right] \cdot \sqrt{t}}$
5.	storage (max)	$E^{S\max}(t) = \frac{5118 \left[\frac{\text{MWh}}{\text{rok}} \right] \cdot t + 1440 \left[\frac{\text{MWh}}{\sqrt{\text{rok}}} \right] \cdot \sqrt{t}}{2700[\text{Mg}] + 24 \left[\frac{\text{Mg}}{\text{rok}} \right] \cdot t + 1150[\text{Mg}] - 4 \left[\frac{\text{MWh}}{\sqrt{\text{rok}}} \right] \cdot \sqrt{t}}$

No.	Model	Mathematical form
6.	storage (min)	$E^{S\min}(t) = \frac{5118 \left[\frac{\text{MWh}}{\text{rok}} \right] \cdot t - 1440 \left[\frac{\text{MWh}}{\sqrt{\text{rok}}} \right] \cdot \sqrt{t}}{2700[\text{Mg}] + 24 \left[\frac{\text{Mg}}{\text{rok}} \right] \cdot t + 1150[\text{Mg}] + 4 \left[\frac{\text{MWh}}{\sqrt{\text{rok}}} \right] \cdot \sqrt{t}}$

The installation of a wind power plant also has a significant impact on the integrated ecological efficiency of CO_{2eq} emissions in the life cycle, and thus the average annual energy output. Figure 3 illustrates this relationship for the various post-use uses and duration of use. The effectiveness of CO_{2eq} emissions for the production of electricity from hard coal and natural gas has also been emphasized.

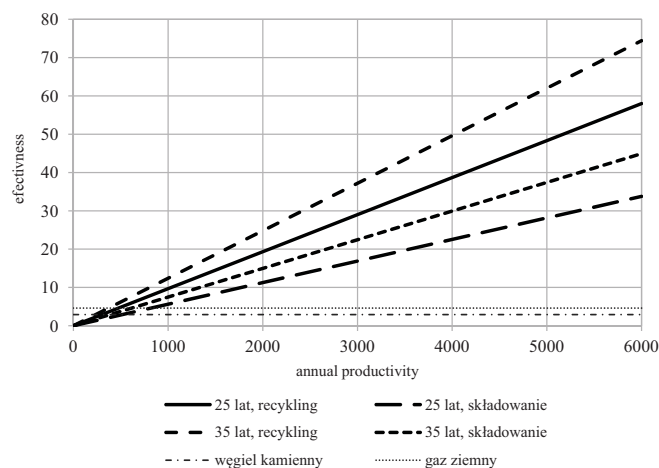


Fig. 3. Dependency of integrated CO_{2eq} efficiency index from average annual productivity of the offshore wind farm analyzed for different lengths of use and management (source: own research)

The equations of the lines shown in Figure 3 have the mathematical form as described in Table 4.

Tab. 4. Integrated CO_{2eq} efficiency index for recycling and storage at offshore development, for 25 and 35 years of operation (source: own research)

Lp.	Model	Mathematical form
1.	25 years, recycling	$E^R(25)(\mu) = \frac{25[\text{lat}] \cdot \mu}{2700[\text{Mg}] + 25[\text{lat}] \cdot 24 \left[\frac{\text{Mg}}{\text{rok}} \right] - 704[\text{Mg}]}$
2.	25 years, storage	$E^S(25)(\mu) = \frac{25[\text{lat}] \cdot \mu}{2700[\text{Mg}] + 25[\text{lat}] \cdot 24 \left[\frac{\text{Mg}}{\text{rok}} \right] + 1150[\text{Mg}]}$
3.	35 years, recycling	$E^R(35)(\mu) = \frac{35[\text{lat}] \cdot \mu}{2700[\text{Mg}] + 35[\text{lat}] \cdot 24 \left[\frac{\text{Mg}}{\text{rok}} \right] - 704[\text{Mg}]}$
4.	35 years, storage	$E^S(35)(\mu) = \frac{35[\text{lat}] \cdot \mu}{2700[\text{Mg}] + 35[\text{lat}] \cdot 24 \left[\frac{\text{Mg}}{\text{rok}} \right] + 1150[\text{Mg}]}$

SUMMARY AND CONCLUSIONS

In the light of the assumptions, results of research and accompanying calculations, analytical and research work was carried out to solve the problems formulated to achieve the objectives of the article by:

1. the solution of the first problem is the development of an adequate mathematical model for the efficiency of electricity production from CO₂ emissions for the purposes of analysis, evaluation and development of marine EW. The model incorporates variable indicators, supporting the design, manufacture, use and management of post-use potentials.
2. the solution to the second problem is to determine the experimental impact of the selected management, use and location, i.e. the average annual productivity of offshore wind power plants, on the energy benefits of CO₂ emissions. It was found that the efficiency of electricity production from CO₂ emission is influenced by the following factors occurring in the offshore EW:

a) methods of post-use management;

For two ways of managing post-use management (storage, recycling), the more favorable values of the efficiency index were obtained for recycling. Using the recycling for the tested EW and its useful life for 25 years, the CO_{2eq} energy efficiency index is $E^R(25) = 49,73$, and using storage $E^S(25) = 29,38$

The EW offshore efficiency rating for CO_{2eq} compared to the conventional coal-fired power plant in the estimated 25-year lifetime for storage capacity is 9.93 times higher (Table 2). On the other hand, in management by recycling 16.8 times higher. For lignite, these values are: 10,68 times when stored, recycled - 18.08 times.

b) Operating time;

The values of the integrated energy efficiency index from CO_{2eq} emissions as a function of the time of use for the different utilization patterns of the analyzed offshore wind power plant with an average annual production of energy $\mu = 5118$ indicate the increasing operational potential of offshore wind power plants, along with the increasing lifetime. For the period of use of 25 years, these indices are respectively $E^S(25) = 29,38$, $E^R(25) = 49,73$, and for long service life of up to 35 years $E^S(35) = 38,31$ and $E^R(35) = 63,48$.

c) Location - average annual productivity;

Choosing a location is crucial for achieving high electricity production from CO_{2eq} emissions. For comparison, if we assume that the operating life is 25 years, these rates, with a fluctuation in annual productivity around $\mu = 5118$ by 5118 by $\pm 10\%$, are respectively:

$$E^S(25)(90\%\mu) = 25,94, E^S(25)(110\%\mu) = 31,70,$$

$$E^R(25)(90\%\mu) = 44,53, E^R(25)(110\%\mu) = 54,43.$$

Compared to the results obtained, there is considerable potential for reducing CO_{2eq} emissions from the design, manufacture and operation of offshore wind farms, replacing fossil fuel energy with offshore wind power.

LITERATURE

1. Alberts H. Recycling of wind turbine rotor blades – fact or fiction? *Dewi Magazin* 2009; 2(34): 32-41.
2. Conconi M. Raport EWEA: Research note outline on recycling wind turbines blades. Brussels: The European Wind Energy Association, 2012.
3. Davidsson J, Hook M, Wall G. Review of life cycle assessments on wind energy systems. *The International Journal of Life Cycle Assessment* 2012; 17(6): 729–742.
4. Davis S, Peters G P, Calderia K. The supply chain of CO₂ emissions. *Proceedings of the National Academy of Sciences* 2011; 108(45): 18554–18559.
5. Flizikowski J, Sadkiewicz J, Tomporowski A. Charakterystyki użytkowe sześciowalcowego mielenia uziarnionych surowców dla przemysłu chemicznego i spożywczego. *Przemysł chemiczny* 2015; 94(1): 69-75.
6. Flizikowski J, Topoliński T, Opielak M, Tomporowski A, Mroziński A. Research and Analysis of Operating Characteristics of Energetic Biomass Micronizer. *Eksploatacja i Niezawodność – Maintenance and Reliability* 2015; 17(1): 19-26.
7. Garrett P, Rendc K. Life cycle assessment of wind power: comprehensive results from a state-of-the-art approach. *The International Journal of Life Cycle Assessment* 2013; 18(1): 37-48.
8. Gillingham K, Newell R, Palmer K. Energy efficiency, economics and policy. *Annual Review of Resource Economics* 2009; 1(1): 597-620.
9. Hau E. *Wind turbines: Fundamentals, technologies, application and economics*. Berlin: Springer-Verlag, 2006.
10. Kasner R. Ocena korzyści i nakładów cyklu życia elektrowni wiatrowej. *Dysertacja*. Poznań: Politechnika Poznańska, 2016.
11. Kłós Z, Małdziński L, Wisłocki K. *Rozprawy naukowe*. Poznań: Wydawnictwo Politechniki Poznańskiej, 2011.
12. Kosicka E, Kozłowski E, Mazurkiewicz D. The use of stationary tests for analysis of monitored residual processes. *Eksploatacja i Niezawodność – Maintenance and Reliability* 2015; 17(4): 604–609.
13. Malujda I. *Kierunki projektowania i badania cech konstrukcyjnych elementów maszyn*. Poznań: Wydawnictwo Politechniki Poznańskiej, 2006.

14. Mitchell R B. Technology is not Enough: Climate change, population, affluence and consumption. *Journal of Environment & Development* 2012; 21(1): 24-27.
15. Oexmann J. Post-combustion CO₂ capture: energetic evaluation of chemical absorption processes in coal-fired steam power plants. Hamburg: Epubli, 2011.
16. Petrakopoulou F, Tsatsaronis G, Morosuk T, Paitazoglou C. Environmental evaluation of a power plant using conventional and advanced exergy-based methods. *Energy* 2012; 45(1): 23-30.
17. Piasecka I. Badanie i ocena cyklu życia zespołów elektrowni wiatrowych. Dysertacja. Poznań: Politechnika Poznańska, 2014.
18. Piasecka I. Charakterystyki destrukcyjności Kujawsko-Pomorskich elektrowni wiatrowych. Rozdział w monografii: V Eko-Euro-Energia. Inżynieria Odnawialnych Źródeł Energii pod red. A. Mrozińskiego. Bydgoszcz: Wydawnictwo Fundacji Rozwoju Mechatroniki, 2013.
19. PN-EN ISO 14040:1997. Zarządzanie środowiskowe – Ocena cyklu życia – Zasady i struktura. Warszawa: PKN, 2000.
20. PN-EN ISO 14041:1998. Zarządzanie środowiskowe – Ocena cyklu życia – Określenie celu i zakresu oraz analiza zbioru. Warszawa: PKN, 2002.
21. PN-EN ISO 14042:2000. Zarządzanie środowiskowe – Ocena cyklu życia – Ocena wpływu cyklu życia. Warszawa: PKN, 2002.
22. PN-EN ISO 14043:2000. Zarządzanie środowiskowe – Ocena cyklu życia – Interpretacja cyklu życia. Warszawa: PKN, 2002.
23. Popczyk J. Bezpieczeństwo elektroenergetyczne w społeczeństwie postprzemysłowym na przykładzie Polski. Gliwice: Wydawnictwa Politechniki Śląskiej, 2009.
24. Popczyk J. Energetyka rozproszona – od dominacji energetyki w gospodarce do zrównoważonego rozwoju, od paliw kopalnych do energetyki odnawialnej i efektywności energetycznej. Warszawa: Polski Klub Ekologiczny Okręg Mazowiecki, 2011.
25. Price T J. UK large-scale wind power programme from 1970 to 1990: The carmarthen bay experiments and the musgrove vertical-axis turbines. *Wind Engineering* 2006; 30(3): 225-242.
26. Raupach M, Marland G, Ciais P, Canadell J. Global and regional drivers of accelerating CO₂ emissions. *Proceedings of the National Academy of Sciences* 2007; 104(24): 10288-10293.
27. Rijswijk K, Bersee H E N. Reactive processing of textile fiber-reinforced thermoplastic composites – An overview. *Composite Part A: applied science and manufacturing* 2007; 38(3): 666-681.
28. Rudnicki J. Application issues of the semi-markov reliability model, *Polish Maritime Research* 1(85) 2015, 22:55-64, 10.1515/pomr-2015- 000
29. Tomporowski A, Opielak M. Structural features versus multi-hole grinding efficiency. *Eksploatacja i Niezawodność – Maintenance and Reliability* 2012; 14(3): 223-228.
30. Tomporowski A. Stream of efficiency of rice grains multi-disc grinding. *Eksploatacja i Niezawodność – Maintenance and Reliability* 2012; 14(2): 150-153.
31. Ulgiati S, Raugi M, Bargigli S. Overcoming the inadequacy of single-criterion approaches to Life Cycle Assessment. *Ecological Modelling* 2006; 190(3-4): 432-442.
32. Wang D, Bao A, Kunc W, Liss W. Coal power plant flue gas waste heat and water recovery, *Applied Energy* 2012; 91(1): 341-348.
33. Wnuk Z. Ekologia i ochrona środowiska. Wybrane zagadnienia. Rzeszów: Wydawnictwo Uniwersytetu Rzeszowskiego, 2010.
34. Zimmermann T. Parameterized tool for site specific LCAs of wind energy converters. *The International Journal of Life Cycle Assessment* 2013; 18(1): 49-60.

CONTACT WITH THE AUTHORS

Andrzej Tomporowski

e-mail: a.tomporowski1@wp.pl
Uniwersytet Technologiczno-Przyrodniczy
im. J. i J. Śniadeckich w Bydgoszczy
S. Kaliskiego 7,
85-796 Bydgoszcz
POLAND

Józef Flizikowski

e-mail: fliz@utp.edu.pl
Uniwersytet Technologiczno-Przyrodniczy
im. J. i J. Śniadeckich w Bydgoszczy
S. Kaliskiego 7
85-796 Bydgoszcz
POLAND

Marek Opielak

e-mail: m.opielak@pollub.pl
Politechnika Lubelska
Nadbystrzycka 36
20-610 Lublin
POLAND

Robert Kasner

e-mail: robert.kasner@gmail.com
Uniwersytet Technologiczno-Przyrodniczy
im. J. i J. Śniadeckich w Bydgoszczy
S. Kaliskiego 7
85-796 Bydgoszcz
POLAND

Weronika Kruszelnicka

e-mail: weronika.kruszelnicka@gmail.com
Uniwersytet Technologiczno-Przyrodniczy
im. J. i J. Śniadeckich w Bydgoszczy
S. Kaliskiego 7
85-796 Bydgoszcz
POLAND

A METHOD TO ASSESS TRANSVERSE VIBRATION ENERGY OF SHIP PROPELLER SHAFT FOR DIAGNOSTIC PURPOSES

Zbigniew Korczewski

Gdańsk University of Technology, Faculty of Ocean Engineering and Ship Technology, Poland

ABSTRACT

The article discusses a key problem of ship propulsion system vibration diagnostics, which concerns assessing this part of mechanical energy transmitted from the main engine to the ship propeller which is dissipated due to propeller shaft vibration. A simplified calculation model is proposed which allows the total energy of the generated torsional vibration to be assessed from the shaft deflection amplitude measured at the mid-span point between the supports. To verify the developed model, pilot tests were performed on the laboratory rotational mechanical system test rig. In those tests, cyclic bending moment was applied to a unified (cylindrical) material sample, which modelled, at an appropriate scale, structural and functional properties of a real propeller shaft.

Keywords: rotational mechanical system, propeller shaft transverse vibration energy, calculation model

INTRODUCTION

In an ideal propulsion system, the entire energy delivered from the main engine is effectively converted to basic rotational motion of the mechanical system of propeller shafting. Progressive degradation of technical condition of structural elements composing the ship propulsion system leads to worsening of its dynamic characteristics. As a consequence, additional movements are generated, such as longitudinal, transverse and/or torsional vibrations, which accompany the basic rotational motion of the propeller shafting. These additional movements are undesirable from the point of view of the efficiency of energy conversion and transmission in the entire propulsion system. They are the cause of kinetic energy dissipation in the rotational motion and accumulation of internal energy in structural materials. After exceeding critical limits of these energies, a fatigue failure takes place, the course of which is characterised by residual energy processes of vibroacoustic and thermal nature. These processes generate observable diagnostic symptoms of changes of the technical condition of the ship propulsion shafting [Dragantchev, 2000; Szala and Boroński, 2008].

Operational experience concerning various types of ship propulsion systems show that, regardless of the area of use of these systems, primary causes of excessive shafting vibrations are most often related with the below characterised factors [Korczewski, 2017].

TRANSVERSE VIBRATION:

- wear or ageing of structural materials of elements composing the foundation for torque transmission elements. This includes: corrosion of steel washers, and ageing of rubber shock absorbers and washers made of chemically curing plastics, especially in the presence of high temperatures and chemically active products, such as, for instance, lubricating oil or diesel oil;
- wear or ageing of structural materials of flexible couplings and flexible shafting connections with auxiliary installations;
- subsidence of foundation superstructure, as a result of static deformations or impact loads acting on the ship hull (for instance during ship collision, stranding, and hitting a quay or water obstacle);

- permanent deformation of ship hull (due to structural weakening, for instance) inside which the propulsion system was installed;
- static deformation of propulsion shafting, as a consequence of long-term operational downtime;
- fouling, or material loss (loosing), as a consequence of tribological, corrosion or erosion wear of rotating elements, with the resultant nonuniform mass distribution in the rotating system;
- excitations coming from the propulsion engine and the cooperating working machines (for instance, blade system defects, deformations, weakening of connections in turbine engine rotor units and turbo-machines, or mass unbalance in the rotational and back-and-forth motion of engines and piston machines).

These causes usually lead to the following operating inability states of the ship propulsion system:

- propulsion shafting misalignment or bending;
- displacement of centres of gravity of the rotating shafting elements with respect to the rotation axis (statically or dynamically unbalanced centrifugal force).

In both cases, pressure forces increase in bearings, couplings, and gear connections of the propulsion system, all this leading to the development of various forms of tribological wear, and to the increase of assembly clearances. In those cases, the observable diagnostic symptom is the increased amplitude of transverse vibration generated at characteristic structural nodes of the mechanical system, with all above discussed energy and fatigue consequences. When the shafting misalignment or bending is high, axial vibration may also appear.

LONGITUDINAL VIBRATION RESULTING FROM:

- screw propeller damage (Fig.1);
- nonuniform load of propulsion engine cylinders;
- damage of longitudinal vibration damper.



Fig. 1. Damaged blades of ship screw propellers

In those cases, the main sources of excitations are: periodically changing screw propeller thrust, transverse vibration of the hull (vertical hull movements) which provokes longitudinal vibration in thrust bearing, and periodically changing gas and mass forces in the propulsion engine which, acting on the crankpins, deform cranks and make pins move along the shaft axis.

TORSIONAL VIBRATION CAUSED BY:

- nonuniform load of propulsion engine cylinders;
- damage of torsional vibration damper.

As a consequence of excessive amplitudes of transverse, torsional and/or longitudinal vibrations, all elements involved in torque transmission from the engine to the propeller undergo accelerated fatigue wear [Korczewski, 2012 and 2017].

The above considerations show that the key metrological issue in diagnosing the rotational mechanical ship propulsion system is the ability to assess the energy of the vibrating propeller shaft from the measurement of shaft vibration parameters at selected (available) structural nodes. Excessive transverse vibration of the ship propulsion shafting is the most frequent cause of its fatigue damages, at the same time being the basic source of mechanical energy loss in the propulsion system. In this context, the problem of assessing the amount of energy dissipated by the shaft undergoing transverse vibration takes on particular relevance as a basic diagnostic symptom characterising the above discussed operating inability states of ship propulsion shafting.

CALCULATION MODEL OF SHAFT UNDERGOING TRANSVERSE VIBRATION

Even the most precisely balanced propeller shaft deflects statically under its own weight, which results in the displacement of its centre of mass with respect to the axis of rotation [Adams, 2001; Bently and Hatch 2002]. When the ship propulsion system is in operation, the generated centrifugal force is the cause of dynamic shaft deflection, which sums up with its static deflection.

The pulse which excites torsional vibration of the shaft comes from the unbalanced centrifugal force F_r applied to the shaft's centre of mass $s.m.$ and rotating with the shaft at angular speed ω – Fig. 2. The action of the centrifugal force and the shaft weight force, F_G , on the propeller shaft is compensated by the restoring force F_{spr} , defined by the shaft stiffness k , and the damping force F_H in shaft material, bearing supports, and (possibly) oil vibration dampers (this last damping force component is characterised by a generalised damping coefficient b):

$$F_r + F_G = F_{spr} + F_H \quad (1)$$

$$m \cdot y \cdot \omega^2 + m \cdot g = k \cdot y + b \cdot \dot{y} \quad (2)$$

The unbalanced centrifugal force is the cause of considerable dynamic loads of bearings in the analysed mechanical system. To reduce destructive effects of transverse shaft vibration, oil damping is introduced in flexible bearing supports. This solution was also applied in the physical model of rotational propulsion system [Korczewski, 2017] in which the stiffnesses of supports are not the same in all directions in the plane

perpendicular to the geometrical axis of shaft rotation. Hence, an assumption was made that the trajectories of the centre of mass of the deflected shaft and its ends (with supports) have elliptical shapes, with major axes perpendicular to the axis of rotation in vertical direction – Fig.2.

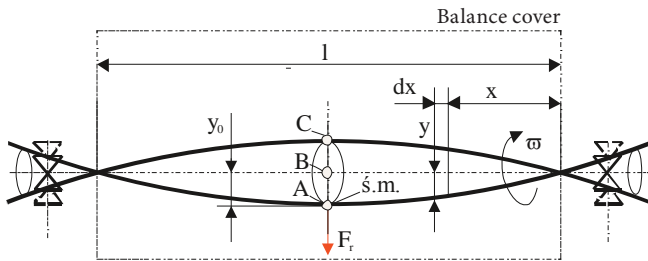


Fig. 2. Scheme of propeller shaft deflection at dynamic load with damping in bearing supports

At the first stage of the analysis, dynamic processes in flexible bearing supports are omitted. To obtain the energy balance for the shaft undergoing transverse vibration, a balance cover was defined which reduces the length of the tested shaft to the distance between two node points. Then, a formula can be worked out for total energy of the shaft mass during one transverse motion cycle, which is the sum of kinetic and potential energy – Fig.3:

$$E_c = E_k + E_p \quad (3)$$

After expanding:

$$E_k = \frac{1}{2} \cdot m \cdot v_y^2 \quad i \quad E_p = \frac{1}{2} \cdot k \cdot y^2 \quad (4)$$

hence

$$E_c = \frac{1}{2} \cdot m \cdot v_y^2 + \frac{1}{2} \cdot k \cdot y^2 \quad (5)$$

where:

- m – shaft mass,
- y – shaft deflection
- v_y – velocity in transverse motion,
- k – shaft stiffness.

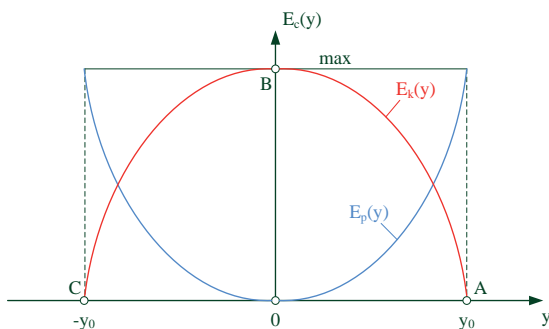


Fig. 3. Changes of potential and kinetic energy in transverse shaft motion as function of shaft deflection

The kinetic energy reaches the maximum for the equilibrium position at point B, as the transverse motion velocity at this point is the highest (and the acceleration equals zero). On the other hand, the maximal values of potential energy occur at points A and C, at which the transverse motion velocity decreases to zero and the acceleration takes the maximum value at the maximal shaft deflection.

Under the static mass load the shaft deflects by the amplitude y_{st} , according to the weight and restoring force balance condition – Fig. 4:

$$F_G = F_{spr} \quad (6)$$

$$m \cdot g = k \cdot y_{st} \quad (7)$$

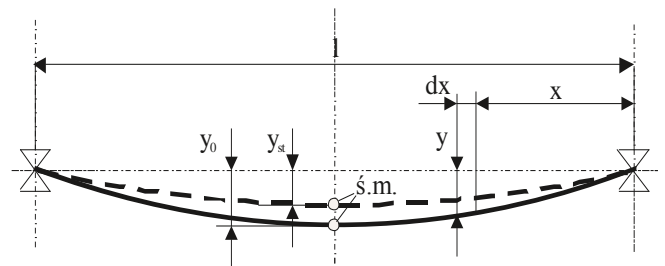


Fig. 4. Scheme of shaft deflections at static load (broken line) and dynamic load (continuous line); damping in bearing supports neglected

In the steady state the shaft stiffness for the concentrated mass positioned at the mid-span point between the supports is given by the relation:

$$k = \frac{m \cdot g}{y_{st}} \quad (8)$$

where: y_{st} – static deflection amplitude (under static mass load of self-aligning bearings).

When the system begins to rotate with angular speed ω , the centrifugal force F_r applied to the centre of mass of the shaft positioned on the principal axis of inertia deflects the shaft by the amplitude y_0 measured at the mid-span point between the supports. For an arbitrary point along the shaft length, an approximate relation can be derived between the average velocity v_y , time τ , and the distance y covered by the material point in the transverse motion:

$$v_y = \frac{y}{\tau} \quad (9)$$

where:

$$\tau = \frac{1}{f} \quad (10)$$

f – frequency of shaft deflections (transverse vibration).

Hence, the average values of material point velocity and acceleration in transverse motion can be determined from the following formulas:

$$v_y = y \cdot f \quad (11)$$

$$a_y = \frac{v_y}{\tau} = v_y \cdot f = y \cdot f^2 \quad (12)$$

Based on this assumption, the shaft stiffness can be calculated from:

$$k = \frac{m \cdot a_y}{y} = m \cdot f^2 \quad (13)$$

Assuming that the shaft deflection line is a sine curve:

$$y = y_0 \cdot \sin \pi \cdot \frac{x}{l} \quad (14)$$

and y_0 is the maximal deflection, and adopting the following boundary conditions with respect to node points:

for $x=0$ and $x=l$, deflection $y=0$,

the elementary kinetic energy of the shaft segment in transverse motion can be determined as:

$$dE_k = \frac{1}{2} \cdot A \cdot \rho \cdot y^2 \cdot f^2 dx \quad (15)$$

where:

A – cross-section area of the analysed shaft segment,
 ρ – density of structural material of the shaft.

Taking into account the adopted boundary conditions and assuming continuous shaft mass distribution, the total kinetic energy of the shaft undergoing transverse vibration is given by the formula:

$$E_k = \frac{1}{2} \cdot A \cdot \rho \cdot f^2 \int_{x=0}^{x=l} y^2 dx \quad (16)$$

or, taking into account the assumption (14):

$$E_k = \frac{1}{2} \cdot A \cdot \rho \cdot f^2 \int_{x=0}^{x=l} y_0^2 \cdot \sin^2 \left(\pi \cdot \frac{x}{l} \right) dx \quad (17)$$

Assuming that the maximal shaft deflection is constant, Equation (17) can be written in the following form:

$$E_k = \frac{1}{2} \cdot A \cdot \rho \cdot f^2 \cdot y_0^2 \int_{x=0}^{x=l} \sin^2 \left(\pi \cdot \frac{x}{l} \right) dx \quad (18)$$

Since the solution of the definite integral in Equation (18) is the expression, hence:

$$E_k = \frac{1}{2} \cdot A \cdot \rho \cdot f^2 \cdot y_0^2 \cdot \frac{1}{2} \cdot l \quad (19)$$

and the final formula for kinetic energy of transverse shaft vibration is:

$$E_k = \frac{1}{4} \cdot m_p \cdot f^2 \cdot y_0^2 \quad (20)$$

where: – total mass of the analysed shaft segment.

The formula for potential energy of shaft mass in transverse motion can be derived in the same way. Taking into account the relation (13), this formula takes the following form:

$$E_p = \frac{1}{4} \cdot m_p \cdot f^2 \cdot y_0^2 \quad (21)$$

As a result, the total energy of the shaft mass undergoing transverse motion is given by the formula¹:

$$E_c = \frac{1}{2} \cdot m_p \cdot f^2 \cdot y_0^2 \quad (22)$$

or

$$E_c = \frac{1}{2} \cdot m_p \cdot v_{y_0}^2 \quad (23)$$

where:– amplitude of the shaft's centre of mass velocity in the transverse motion between two extreme deflections from the steady position.

¹ Assuming that the motion is carried out without any energy loss for overcoming friction resistance.

RESULTS OF MEASUREMENTS AND THEIR ANALYSIS

The adequacy of the developed calculation model of energy dissipation of the propulsion shaft undergoing transverse vibration was experimentally verified on the laboratory rotational mechanical system test rig – Fig. 5 [Korczewski, 2017]. The performed tests consisted in measuring deflections of a unified (cylindrical) material sample loaded with bending-torsional moment. The tested sample modelled, at an appropriate scale, structural and functional properties of a real propeller shaft of a sea-going ship. This propeller shaft composes a dynamic system in which three vibration forms, i.e. transverse, longitudinal, and torsional vibration occur simultaneously. The object of energy analysis was only the transverse vibration of the system. Selected representative measurement results are shown in Fig. 6 in the form of time-histories of cyclic deflection changes of the centre of mass of the tested material sample rotating with angular speed of 1800 rpm and loaded with mass of 30 kg. When analysing the nature of the recorded time-histories, we can conclude that they are not pure harmonic, but are a combination of periodical signals of different amplitudes and frequencies. Therefore, the transverse vibration energy of the material sample was determined according to the relation (23) and using the square of the RMS value of the transverse vibration velocity amplitude, as this parameter takes into account both the history of the recorded signal, and its amplitude (the amplitude value better characterises the intensity of the generated vibration).

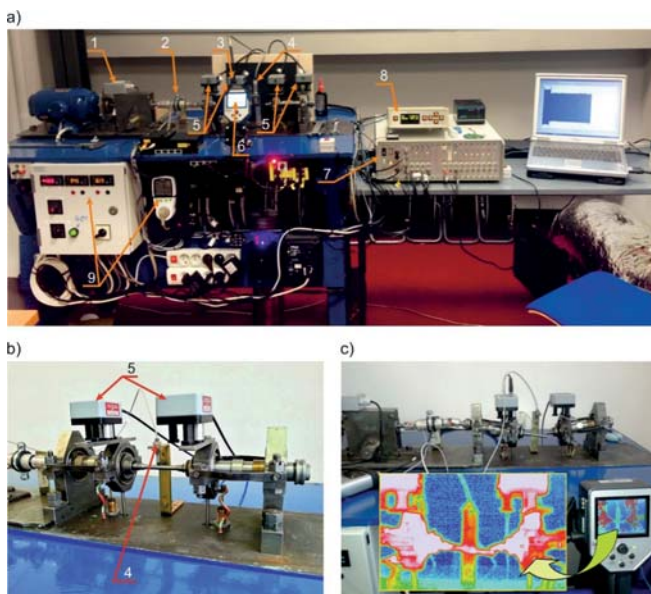


Fig. 5. General view of laboratory rotational propulsion system test rig: a) rig with measuring instrumentation – recorders: thermovision (6), acoustic emission (7), torque and rotational speed (8), electric current parameters (9); converters: rotational speed (1), torque (2), vibration acceleration (3), sample eccentricity (deflection) (4), acoustic emission (5); b) method of fastening of acoustic emission converters (5) and sample eccentricity (deflection) converter (4); c) observation of radiative emission of the sample

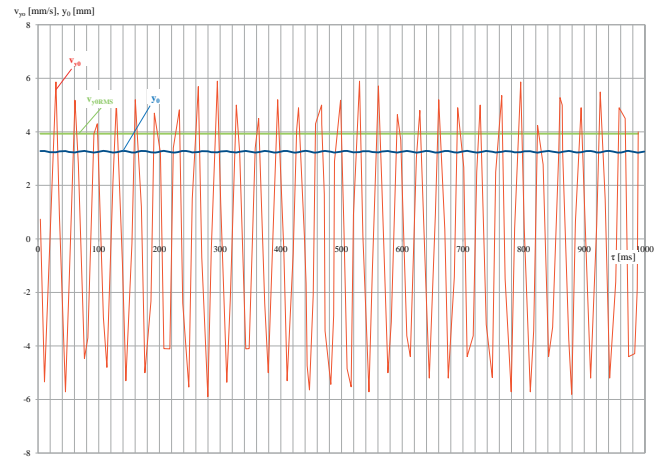


Fig. 6. Time-histories of the centre of mass deflection (y_0), transverse vibration velocity (v_{y0}), and the RMS value of transverse vibration velocity amplitude (v_{y0RMS}) of the tested material sample

The mass m_p of the selected sample segment was 0,028 kg (the mass of the entire sample was 0,108 kg) – Fig. 7. After placing numerical values of physical quantities to Equation (23), the total energy of the selected sample segment undergoing transverse motion was obtained. Its value for one cycle of periodic motion was equal to $0,22 \cdot 10^{-6}$ J. Thirty cycles of this motion are executed during one second, therefore the total amount of energy generated by transverse vibration in one second was $6,6 \cdot 10^{-6}$ J.



Fig. 7. Tested material sample: a) general view, b) selected (tested) sample segment

Taking into account the value of the kinetic energy of the selected sample segment undergoing rotational motion, which in that time (for one second) was approximately equal to 33 J (Fig. 8), the amount of useful energy dissipated in the transverse vibration can be considered negligible. On the other hand, it is of some importance for long-term operation of a real mechanical system, where the masses of propulsion shafting equal several tonnes, as it amounts to several kilojoules per one hour of system operation.

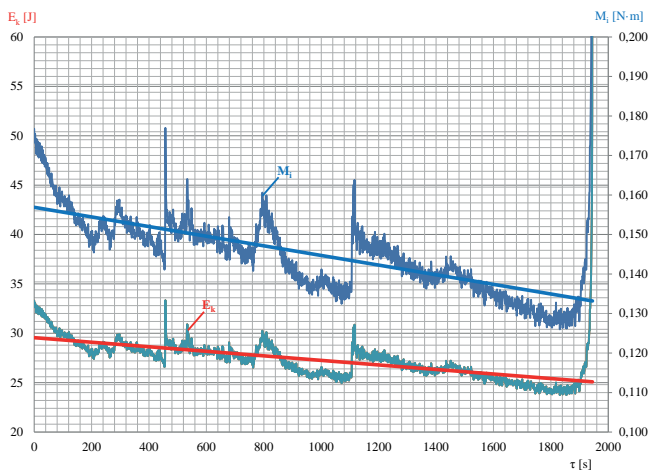


Fig.8. Time-histories of transmitted torque (M_i) and kinetic energy (E_k) in rotational motion of the selected material sample segment, with corresponding trend lines

FINAL REMARKS AND CONCLUSIONS

The performed model tests and experimental research have shown that the centre of mass deflection measurement of a selected propeller shaft segment in the rotational mechanical system can be used for assessing the energy of the generated transverse vibration. The amount of shaft energy relating to its transverse vibration is the measure of kinetic energy dissipation in the rotational motion of the system, and can be used in ship propulsion system diagnostics to identify propulsion shafting misalignment or bending, without the need to shut the ship propulsion system down.

Moreover, estimating the amount of energy generated by the propeller shaft undergoing transverse vibration provides opportunities for evaluating the operation of the ship propulsion system during energy transmission and conversion to work and heat forms. The final result of this activity will be the function describing the fatigue life of ship shafting loaded with bending moment, which can be used in operating diagnostics of ship propulsion systems.

BIBLIOGRAPHY

1. Adams M.L.: Rotating Machinery Vibration: From Analysis to Troubleshooting. Marcel Dekker, New York 2001.
2. Bently D.E., Hatch C.T.: Fundamentals of Rotating Machinery Diagnostics. Bently Pressurized Bearing Press, Minden 2002.
3. Dragantchev H. (2000). Control and diagnostics of ship shafting. Proceedings of the IMAM 2000, Ischia, 2–6 April 2000, Session L, p. 115–122.

4. Korczewski Z.: The conception of energetic investigations of the multisymptom fatigue of the simple mechanical unit. Journal of Polish CIMAC - Vol. 7, No.1/2012, p. 99-108.
5. Korczewski Z.: Operating diagnostics of marine internal combustion engines of piston and turbine type: Selected issues. (in Polish). Wydawnictwo Politechniki Gdanskiej, Gdansk 2017.
6. Szala J., Boroński D.: Material fatigue state assessment in diagnostics of machinery and equipment (in Polish). Wydawnictwo Instytutu Technologii Eksploatacji – PIB, Bydgoszcz 2008.

CONTACT WITH THE AUTHOR

Zbigniew Korczewski

e-mail: z.korczewski@gmail.com
 Gdansk University of Technology
 Gabriela Narutowicza 11/12
 80-233 Gdańsk
POLAND

THE EXPERIMENTAL IDENTIFICATION OF THE DYNAMIC COEFFICIENTS OF TWO HYDRODYNAMIC JOURNAL BEARINGS OPERATING AT CONSTANT ROTATIONAL SPEED AND UNDER NONLINEAR CONDITIONS

Łukasz Breńkacz¹, PhD, Eng.

Grzegorz Żywica¹, PhD, Eng.

Marta Drosińska-Komor², MSc

¹ Department of Turbine Dynamics and Diagnostics, Institute of Fluid Flow Machinery, Polish Academy of Sciences

² Gdańsk University of Technology, Faculty of Ocean Engineering and Ship Technology, Poland

ABSTRACT

Hydrodynamic bearings are commonly used in ship propulsion systems. Typically, they are calculated using numerical or experimental methods. This paper presents an experimental study through which it has been possible to estimate 24 dynamic coefficients of two hydrodynamic slide bearings operating under nonlinear conditions. During the investigation, bearing mass coefficients are identified by means of a newly developed algorithm. An impact hammer was used to excite vibration of the shaft. The approximation by means of the least squares method was applied to determine bearing dynamic coefficients. Based on the performed research, the four (i.e. two main and two cross-coupled) coefficients of stiffness, damping and mass for each bearing were obtained. The mass coefficients add up to the complex shaft weight. These values are not required for modeling dynamics of the machine because the rotor mass is usually known, however, they may serve as a good indicator to validate the correctness of the stiffness and damping coefficients determined.

Additionally, the experimental research procedure was described. The signals of displacements in the bearings and the excitation forces used for determination of the bearing dynamic coefficients were shown. The study discussed in this article is about a rotor supported by two hydrodynamic bearings operating in a nonlinear manner. On the basis of computations, the results of bearing dynamic coefficients were presented for a selected speed.

Keywords: bearing dynamic coefficients, experimental research, nonlinear coefficients, impact excitation, hydrodynamic bearing

INTRODUCTION

Hydrodynamic bearings are integral parts of the vast majority of propulsion systems installed on modern ships. Article [10], provides one example of how complex such a system can be and how its efficiency can be increased using a combination of different devices, i.e. Diesel engine, gas turbine and steam turbine. The contemporary ship power plant is presented in article [14] and operational and economic analysis of some parts of the steam turbine power plant is discussed in article [3]. A summary of losses and energy efficiency of drive motors is presented in paper [18]. Descriptions of hydrodynamic bearings used in shipbuilding industry can be found in papers [16,17]. The analyses

presented in these papers concern various materials used in bearing constructions and load-carrying capacity. Values of stiffness and damping coefficients of hydrodynamic bearings are the most important from the point of view of dynamical performance [12,13]. Because of many difficulties in numerical modelling, many experimental methods for determination of their values have been proposed [9,21]. Experimental investigations were performed with different types of bearings. The paper [8] presents the identification of dynamic coefficients of a hybrid gas bearing that has a sophisticated and robust construction with a complex structure of the foils. The literature study showed that an experimental determination of stiffness and damping bearing characteristics is conducted not just for radial bearings but for thrust bearings as well.

The experimental identification of stiffness and damping characteristics for an axial foil bearing has been dealt with in detail in article [1]. Bearing dynamic coefficients change along with the rotational speed [15,23].

The article presents the continuation of research described in articles [4,5]. The measurement methodology has already been described in detail in these articles. This article focuses on the results from experimental studies. The calculation algorithm for experimental determination of stiffness, damping and mass coefficients of two hydrodynamic bearings using an impulse excitation of the rotating shaft was developed and could be found in article [4]. It is based on conventional linear modelling methods and the least squares method for approximation purposes. When it comes to analyzing systems the operations of which are nonlinear (like in the case of the test rig analyzed in this article), calculations are performed with a certain approximation – as if the response signal would originate from a linearly operating system. The results presented there were calculated using numerically generated signals. The rotor was supported by two hydrodynamic slide bearings. During its operation at constant rotational speed, the shaft was excited by an appropriate force acting between the bearings. The modelled excitation corresponds very closely to the excitation which was applied by an impulse hammer during the experimental research. The displacements of the bearing journals were registered following the application of the excitation to the central part of the shaft. In the next step, the stable operation signal is subtracted from the signal registered after the excitation. As a result, a fading signal which is sinusoidal in shape was obtained. The stiffness, damping and mass coefficients of the rotor – bearings system were determined on its basis and on the basis of excitation force signal.

In numerical simulations dealing with bearings, their stiffness and damping coefficients must be known. The coefficients identification requires either carrying out additional computations or performing experimental research. The computational method discussed herein allows us to obtain not only stiffness and damping coefficients but also mass coefficients — and it does that in one calculation step. The mass coefficients are broadly equivalent to the shaft mass. Calculated values of mass coefficients can be easily verified because the shaft mass is known. The experimental methods for identification of bearing dynamic coefficients are prone to a large amount of measurement errors. Upon verification of mass coefficients, results obtained from an experimental research can be tested for correctness in a swift and straightforward manner. The calculations of added mass coefficients of the skewed marine propellers are shown in publication [22]. The three-dimensional boundary element method (BEM) was developed to predict the propeller added mass and moment of inertia coefficients. The values of the added mass coefficients were predicted based both on geometric and flow parameters of the analyzed propeller.

Paper [6] describes an experimental study which was conducted on a test rig to determine dynamic performance characteristics of a tilting-pad journal bearing. The next

publication [7] shows that by changing operating parameters of the rotating system or the measuring method the authors obtained different values of the bearing dynamic coefficients.

Article [5] concerns the sensitivity analysis of an experimental method for identification of dynamic coefficients of the hydrodynamic bearings. The analyses were conducted on the basis of signals generated by numerical models. The main parameters of concern were as follows: rotor geometry, material properties, position and angle of the measuring sensors as well as location and angle of the vibration excitation applied by an impact hammer made by PCB Piezotronics (model 086C03 with a metal tip). As the numerical model allows all input data to be changed, it is possible to compare the calculated and set dynamic coefficients of the hydrodynamic bearings. It turned out that the theoretical accuracy of the coefficients determination is very high. The sensitivity analysis proved to be very helpful in orienting the attention towards the aspects that are especially relevant in the calculation process. Furthermore, it indicated the need for some adjustments, by the introduction of which the numerical model started to generate correct results.

BASIC TECHNICAL CHARACTERISTICS OF THE TEST RIG AND THE MEASUREMENT RESULTS

The test rig for testing small rotors was built in order to be able to conduct research on rotor – bearings systems and to analyze defects, such as bearing damage, rotor unbalance, shaft misalignment, etc. The photo of the test rig is presented in Fig. 1. Its weight – without the supporting structure – is approximately 60 kg.

The length of the test rig is 1.25 m, and its width and height are 0.36 m and 0.65 m, respectively. The axes of the coordinate system used during the experimental research are shown in the top left-hand corner of Fig. 1. The test rig rests on a 13mm steel plate with two channel bars attached to it that are equipped with rubber feet that allow adjusting the height of the plate and its levelling. The rotor shaft was supported by two bearings. The system was driven by a three-phase motor with a maximum speed of 3450 rpm. The motor speed was adjusted by means of a frequency converter with capacity of 1.5 kW. The motor was connected to a gear that increases the speed with a gear ratio 3.5:1. The presence of the inverter allows varying the motor speed up to 12,000 rpm. The gear is connected to the rotor shaft using a permanent coupling. The coupling diameter is 50 mm and its length is 60 mm. The oil-lubricated bearing system was equipped with a pump. During the experimental tests, the oil pressure was 0.16 MPa. Displacements of the rotor were measured using eddy current displacement transducers (model CWY-DO-501A) having a sensitivity of about 4 mV/ μ m.



Fig. 1. Test rig

The tested rotor has a length of 920 mm. The distance between the coupling and the first bearing support was 170 mm. The rotor was mounted in two bearing supports. The distance between the supports was 580 mm. The rotor disc is equidistant to each bearing supports. The rotor diameter is 19.02 mm and the rotor disc diameter is 152.4 mm. The excitations were applied using an impact hammer at the point that is shifted 30 mm from the rotor disc's midpoint. For safety reasons, the rotor – bearings system was equipped with a lockable casing made of hard transparent plastic.

The rotor was supported by two hydrodynamic bearings (Fig. 2) with the same geometries. The radial bearing clearance is 76 μm and the bearing length is 12.6 mm. Every bearing has two supply ports located on both sides of the shaft. The supply ports have a diameter of 2.54 mm. The oil supply pressure was 0.16 MPa. The viscosity grade of the lubricating oil is consistent with ISO 13 recommendations.



Fig. 2. The hydrodynamic bearing

The vibration trajectories for bearing no. 2 (the one that lies further away from the coupling, respectively) are presented in Fig. 3. The graph represents 12 rotor revolutions at the rotational speed of 4,500 rpm. Signals are filtered using a band-pass filter which rejects frequencies below 1/3X and above 3X (3rd harmonic).

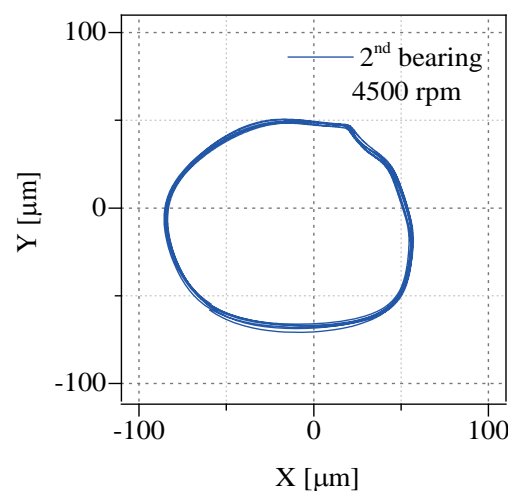


Fig. 3. Vibration trajectories at 4,500 rpm obtained for the bearing situated further away from the coupling

Despite the precise alignment of the shaft ends, the rigid coupling had a big impact on the vibration trajectories of the first bearing. Fig. 4 clearly indicates a phenomenon called „whirl”. [10]. It should be stressed that dynamics of the

rotating system are affected not only by the coupling and bearings but also by the whole supporting structure [2]. There are also other elements (such as twisted blades) that have an impact on vibrations of the entire system since they influence vibration trajectories of the bearing journals [11].

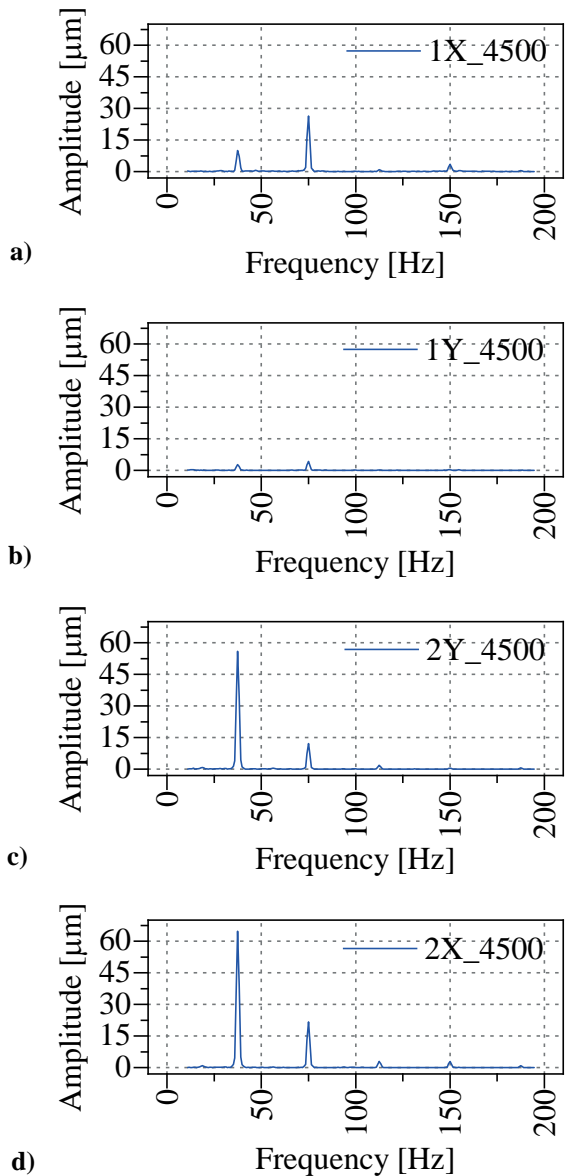


Fig. 4. The FFT spectra presenting the bearing journal displacements for the bearing no. 1 (two top graphs) and no. 2 (two bottom graphs)

Figure 3 presents the FFT spectra showing the bearing journal displacements for both bearings along the X and Y axes. These axes correspond to the axes of the coordinate system already given in Fig. 1. The denotation of “1X” refers to the displacement measurement of bearing no.1 (the one that lies closer to the coupling) in the x-direction (a horizontal direction). Likewise, the denotation of “2Y” indicates the measurement of bearing no. 2 in the y-direction (a vertical direction). The measurements were made at the rotational speed of 4,500 rpm that corresponds to the frequency of 75 Hz. This value can be observed on the graphs as the

second component (counting from the left). Besides the first harmonic (1X), also the 1/2 subharmonic (having the frequency of 37.5 Hz) is present on the graph denoted “1X”. The 1/2 subharmonic dominates the FFT spectra regarding bearing no. 2. This is clearly the indication of the unstable operation of the bearings.

CALCULATION OF DYNAMIC COEFFICIENTS OF THE HYDRODYNAMIC BEARINGS

The calculation diagram of the experimental determination of bearing dynamic coefficients is presented in Fig. 5. In the first step, the necessary experimental research is carried out. The rotor shaft surface (situated at a distance of 30 mm from the disc) is hit in a horizontal direction (X) with an impact hammer when the rotor rotates at constant speed. This action was repeated around a dozen times within 40 seconds. Then, the measurement is performed in the same way with the only difference being that hitting the shaft is performed in a vertical direction (Y). In the second step, the reference signal (corresponding to the stable operation of the rotor) is subtracted from the signal registered after the excitation. This operation was carried out using the computer program called “Signal”, created for this purpose. The third step consists in centering values of the signal corresponding to an excitation force and omitting the values related to the main component. The signals thus obtained are subjected to an FFT (Fast Fourier Transform) analysis [11]. The spectral components received after the centering process are analyzed in a frequency domain. The matrixes A, Z and I are then created. Z matrix contains bearings’ dynamic coefficients that are to be identified, I is an identity matrix and A matrix consists of input signals needed for computations. These input signals relate to excitation forces and measured responses of the mechanical system.

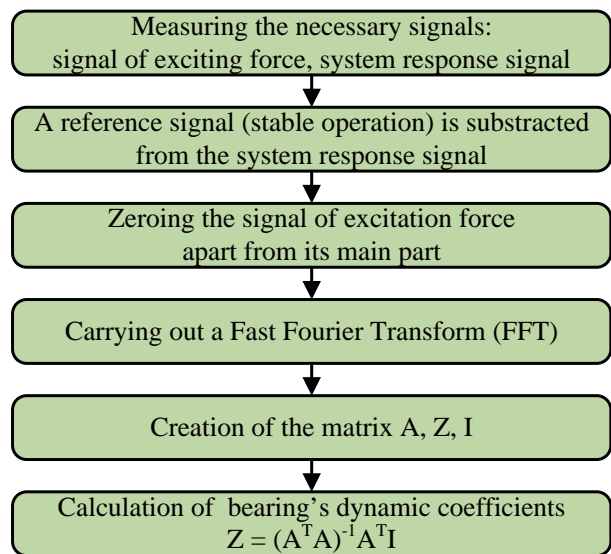


Fig. 5. Calculation procedure for bearing dynamic coefficients

The detailed description of the experimental method for identifying bearing dynamic coefficients is given in paper [4]. Computations are performed with signals represented in a frequency domain. The dynamic coefficients of the bearings are estimated on the basis of the resonance range. The frequencies of the natural vibrations of fluid-flow machinery vary with rotational speed. During the analysis of dynamic coefficients of the bearings, the resonance range of the rotor should be taken into account for each rotational speed. The coefficients are calculated using the least squares method.

If a force applied using the impact hammer is located in the middle part of the rotor, it should be divided by 2 and the obtained value will be the value of the excitation force corresponding to a single bearing. In the event when the excitation is applied at a point that is not equidistant from each of the bearings, the excitation force have to be distributed between the bearings proportionately to the distances between them.

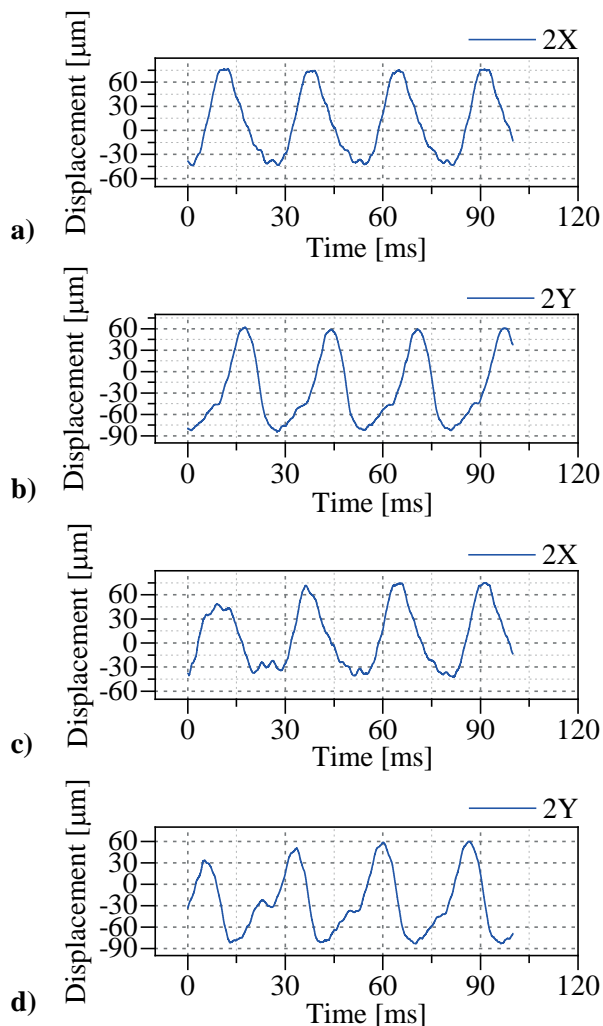


Fig. 6. Stable operation of the bearing no. 2 at 4,500 rpm (the two upper graphs) and the signal obtained after the excitation had been applied (the two lower graphs). The graphs denoted by a) and c) present the signals along the X direction, while the ones denoted by b) and d) the signals along the Y direction

Fig. 6 presents the signals measured during the experimental research. The two upper graphs show the displacements of bearing no. 2 during its stable operation, in the X and Y directions (respectively on the left and right-hand sides). The journal displacements shown on the lower graphs were registered immediately after applying the excitation to the test system using an impact hammer. As we can observe, there is increase or decrease in the vibration amplitude depending on the rotor position. The differences between the lower and upper signals were the basis for carrying out the calculations of dynamic coefficients of the hydrodynamic bearings. The signal resulting from the subtraction of the stable operation signal from the signal registered after the excitation is presented in Fig. 8 as a black curve. This signal relates bearing no. 2 and the X-direction. On its basis, the bearing dynamic coefficients were determined.

CALCULATION RESULTS

The calculations of stiffness, damping and mass coefficients were performed on the basis of the measured displacements of bearing journals and the excitation force signal as well. The calculation process is illustrated in Fig. 5. Table 1 presents the resulting values of stiffness, damping and mass coefficients for the rotor – bearings system. The results were obtained using six data sets. The table lists the average values and their respective standard deviations.

The results obtained for the bearing that lies closer to the coupling are characterized by higher standard deviations. This fact can be explained by the significant impact of the rigid coupling on the bearing operation. This impact could be considerably reduced by replacing the coupling by a more flexible one. During analysis of the results, only the results obtained for the bearing situated at the free end of the rotor's shaft should be considered as reference values.

Notwithstanding the fact that both hydrodynamic bearings have the same geometries, different values of dynamic coefficients have been obtained for the two bearings. Higher standard deviations in the results for bearing no. 1 (in comparison to bearing no. 2) imply that there is a discrepancy between the results obtained for each bearing. Given the highly nonlinear nature of the test system, one could have expected such high standard deviations. The experimental results concerning this type of systems have very little repeatability, which was reflected in the results presented herein. The values of main coefficients (denoted by xx and yy) have lower standard deviations than the cross-coupled coefficients (denoted by xy and yx). Some cross-coupled stiffness, damping and mass coefficients have higher standard deviations than their average values.

The values of errors for dynamic coefficients of hydrodynamic bearings calculated using different experimental methods can be as high as 60 percent – in some cases, even an order of magnitude. A summary of the values of errors obtained for ten or so cases described in the literature was prepared by T.W. Dimond et al. and

presented in paper [9]damping, and mass terms, related to machine vibrations. Detailed numerical values of the bearing dynamic characteristics are necessary for proper design and operation of rotating machinery. The methods of the identification of fluid film journal bearing static and dynamic characteristics, particularly the bearing stiffness, damping, and mass coefficients, from measured data, obtained from different measurement systems, is reviewed. Many bearing tests have been performed to validate a number of different theoretical models, including the classical Reynolds isoviscous model. More advanced bearing models include the thermohydrodynamic (THD). By comparing the obtained standard deviation values with the ones described in the literature, it has been established that our results are satisfactory.

Tab. 1. The values of stiffness, damping and mass coefficients during the operation at 4,500 rpm

dynamic coefficients	bearing that lies further away from the coupling	bearing that lies closer to the coupling
k_{xx} [N/m]	9 733 ± 8 312	43 453 ± 18 308
k_{xy} [N/m]	-11 892 ± 16 333	46 104 ± 48 399
k_{yx} [N/m]	20 724 ± 17 593	24 824 ± 28 357
k_{yy} [N/m]	14 733 ± 14 107	87 802 ± 64 875
c_{xx} [Ns/m]	25 ± 15	25 ± 19
c_{xy} [Ns/m]	-5 ± 22	22 ± 37
c_{yx} [Ns/m]	15 ± 11	-54 ± 36
c_{yy} [Ns/m]	19 ± 17	17 ± 25
m_{xx} [kg]	0.11 ± 0.10	0.52 ± 0.4
m_{xy} [kg]	-0.13 ± 0.23	0.66 ± 0.85
m_{yx} [kg]	0.22 ± 0.40	0.58 ± 0.55
m_{yy} [kg]	0.16 ± 0.13	1.31 ± 1.09

VERIFICATION OF THE RESULTS

For verification of the experimental results, the model of the test system was prepared using Abaqus 6.14-2. The model consisted of a concentrated mass point with one degree of freedom and an elastic-damping element (Fig. 7). The method used for the verification of results is the same as the one proposed by Qiu and Tieu [19]. The force value acting during the experimental research as well as the stiffness and damping characteristics determined on the basis of experimental studies were incorporated into this numerical model. The calculated displacement of the concentrated mass point resulting from a pulse force applied to it was compared with the system response measured during the experimental research.

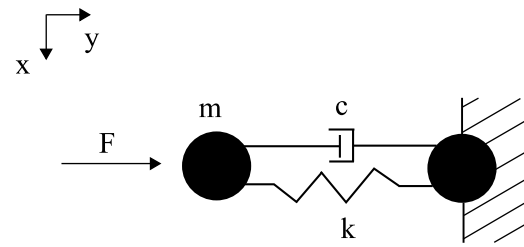


Fig. 7. Simplified schematic diagram of the test system consisting of a concentrated mass and an elastic-damping element

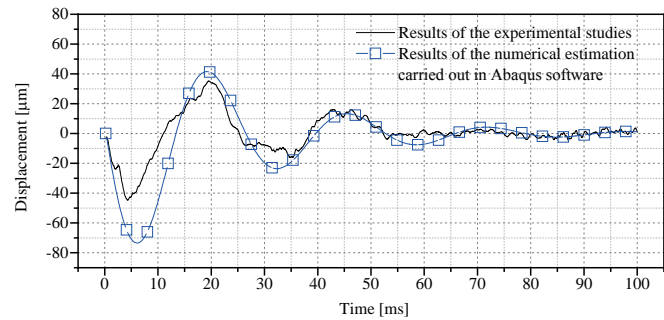


Fig. 8. Dynamic response coming from the real system and the numerical model (this model takes into account the experimentally determined stiffness and damping coefficients)

Both components in the model lie in the same plane. The first component is fully constrained (i.e. all degrees of freedom are removed), while the second component has only one degree of freedom left, namely, motion in the Y direction. The mass attributed to the concentrated mass point was 2.35 kg, representing half of the rotor mass. The two components are connected with one another by an elastic-damping element. The stiffness of this element was 8,700 Nm, and its damping was 51 Nm/s. These are not the average values given in Tab. 1, but the values corresponding to one of the calculation cases carried out at the rotational speed of 4,500 rpm.

The value of the excitation force corresponded to half of the value measured during the experimental research. Its value for the consecutive time steps was $F = [0, 0, 11, 59, 49, 44, 10, 0]$ N. During the analysis, the time step corresponded to the frequency of the measurements. The duration of the excitation force was approximately 0.1 ms and was the same as that in the experimental test.

The calculation results showing the displacements of the concentrated mass point with one degree of freedom are presented in Fig. 8 (blue line with square data markers). Fig. 8 also shows the signal measured during the experimental research (black line). The comparison of the two displacement curves leads to the conclusion that the stiffness and damping coefficients incorporated into the numerical model reflect the essential characteristics of the real object in a reliable manner. In order to ensure that results are reliable, a verification should be performed for each direction. Movement of the bearing journal is described by 4 stiffness coefficients and 4 damping coefficients which have an influence on the system operation at the same time. For verification purposes, they can be considered as separate values.

SUMMARY AND CONCLUSIONS

The object of this study is a rotor supported by two hydrodynamic bearings. This system has a strongly nonlinear nature, e.g. quite a number of large-sized vibration trajectories as well as sub- and super-harmonic vibration components were observed. The research methodology used was developed by the authors of this paper and it is intended for use in analyses of linear systems. The impulse response method (in a simpler version) has been already positively verified for such systems by other researchers. In many experimental studies, test systems are often at the threshold of linear operation and nonlinear algorithms are required to describe them effectively. The article presents the results obtained by the method that uses linear approximation applied to the nonlinear system. Despite a strongly nonlinear nature of the system in question and the fact that the computation results of dynamic bearing coefficients are characterized by large standard deviation values, these results have been positively verified by the authors of this article. A nonlinear nature of the tested system manifests itself when a bearing journal travels along a large-sized trajectory and it leads to changes in properties of a lubricating film. The linearization of dynamic coefficients of hydrodynamic bearings operating in nonlinear conditions can cause that results with large errors may be obtained.

The stiffness, damping and mass coefficients were determined for two bearings in one calculation step. A rigid coupling was used to join the two shafts, namely the rotor shaft and the driving motor shaft. In the experiments, the excitations were generated by an impact hammer near the disc located between the bearing supports. It has been found that the coupling has a big impact on the experimental results. The replacement of the rigid coupling by a coupling that will enable damping of torsional vibration may lead to improved results. Due to that fact, bearing no. 2 (i.e. the one situated further from the coupling) should serve as a reference source of information.

In order to verify the experimental results, the numerical model of the mechanical system in question was created using the Abaqus software. The main component of this system was an elastic-damping element, the stiffness and damping characteristics of which were the same as the ones obtained from the experimental tests. The mass of the concentrated mass point was equal to half of the rotor mass. Following the time-domain analysis, it was found that the response signal generated by the numerical model is very similar to the signal measured during the experimental research, which determined that the dynamic coefficients of the hydrodynamic bearings had been correctly determined.

Motivated by the obtained experimental results, the authors also conducted the theoretical analysis. At the present stage of studies, one can positively state that the experimental method for identification of stiffness, damping and mass coefficients can be used at the support points of rotating machinery equipped with two journal slide bearings. The presented method can also be applied

to machines operating with other types of bearings (e.g. magnetic or foil bearings). However, one should bear in mind that the method has some limitations that need to be overcome to get it fully operational. During the experimental phase of this method, it is of major importance to minimize the impact of the coupling on the dynamics of a rotating system. Another important aspect is to choose an excitation force in such a way as to produce vibration of a test system and, in addition to this, rotor displacements must be linear. What seems to be problematic is the fact that the results obtained from the real object are widely scattered above and below the means (in other words, they have high standard deviations). For bearings with unknown or very complex geometries, values of their basic dynamic parameters can be successfully identified using the methodology presented herein.

ACKNOWLEDGEMENT

The research is being financed by the National Science Centre (NCN) in Poland under the research project no. 2015/17/N/ST8/01825. Calculations were carried out at the Academic Computer Centre in Gdańsk.

BIBLIOGRAPHY

1. Arora, V., Van Der Hoogt, P.J.M., Aarts, R.G.K.M., De Boer, A.: Identification of stiffness and damping characteristics of axial air-foil bearings. *International Journal of Mechanics and Materials in Design*. 2011, 7(3), pp. 231–243.
2. Bagiński, P., Żywica, G.: Analysis of dynamic compliance of the supporting structure for the prototype of organic Rankine cycle micro-turbine with a capacity of 100 kWe. *Journal of Vibroengineering*. 2016, 18(5), pp. 3153–3163.
3. Błaszczuk, A., Głuch, J., Gardzilewicz, A.: Operating and economic conditions of cooling water control for marine steam turbine condensers. *Polish Maritime Research*. 2012, 18(3), pp. 48–54.
4. Breńkacz, Ł.: Identification of stiffness, damping and mass coefficients of rotor-bearing system using impulse response method. *Journal of Vibroengineering*. 2015, 17(5), pp. 2272–2282.
5. Breńkacz, Ł., Żywica, G.: The Sensitivity Analysis of the Method for Identification of Bearing Dynamic Coefficients. In J. Awrejcewicz (Ed.), *Dynamical Systems: Modelling: Łódź Poland, December 7-10, 2015*. Cham: Springer International Publishing 2016, pp. 81–96.
6. Chatterton, S., Pennacchi, P., Dang, P.V., Vania, A.: Identification Dynamic Force Coefficients of a Five-Pad Tilting-Pad Journal Bearing. In *Proceedings of the 9th IFToMM International Conference on Rotor Dynamics*. 2015, pp. 931–941.

7. Dang, P.V., Chatterton, S., Pennacchi, P., Vania, A.: Effect of the load direction on non-nominal five-pad tilting-pad journal bearings. *Tribology International*. 2016, 98, pp. 197–211.
8. Delgado, A.: Experimental identification of dynamic force coefficients for a 110 mm compliantly damped hybrid gas bearing. *Journal of Engineering for Gas Turbines and Power*. 2015, 137(7), pp. 72502-72502–8.
9. Dimond, T.W., Sheth, P.N., Allaire, P.E., He, M.: Identification methods and test results for tilting pad and fixed geometry journal bearing dynamic coefficients – A review. *Shock and Vibration*. 2009, 16(1), pp. 13–43.
10. Dzida, M., Girtler, J., Dzida, S.: On the possible increasing of efficiency of ship power plant with the system combined of marine Diesel engine, gas turbine and steam turbine in case of main engine cooperation with the gas turbine fed in series and the steam turbine. *Polish Maritime Research*. 2009, 16(3), pp. 26–31.
11. Jin, J., Wang, Z., Cao, L.: Numerical analysis on the influence of the twisted blade on the aerodynamic performance of thrbine. 2016, 23, pp. 86–90.
12. Kiciński, J.: *Dynamics of rotors and slide bearings (in Polish)*. Gdańsk: IMP PAN, Maszyny Przepływowe 2005.
13. Kiciński, J., Żywica, G.: *Steam Microturbines in Distributed Cogeneration*. Springer monograph 2014.
14. Kowalczyk, T., Głuch, J., Ziółkowski, P.: Analysis of possible application of high-temperature nuclear reactors to contemporary large-output steam power plants on ships. *Polish Maritime Research*. 2016, 2(90), pp. 32–41.
15. Kozanecki, Z., Kiciński, J., Żywica, G.: Numerical Model of the High Speed Rotors Supported on Variable Geometry Bearings. In *IUTAM Bookseries*. 2011, Vol. 1011, pp. 217–227.
16. Litwin, W.: Influence of local bush wear on water lubricated sliding bearing load carrying capacity. *Tribology International*. 2016, 103, pp. 352–358.
17. Litwin, W., Olszewski, A.: Water-lubricated sintered bronze journal bearings—theoretical and experimental research. *Tribology Transactions*. 2014, 57(1), pp. 114–122.
18. Paszota, Z.: Losses and energy efficiency of drive motors and systems. Replacement of the Sankey diagram of power decrease in the direction of power flow by a diagram of power increase opposite to the direction of power flow opens a new perspective of research of driv. 2013, 20(1), pp. 3–10.
19. Qiu, Z.L., Tieu, A.K.: Identification of sixteen force coefficients of two journal bearings from impulse responses. *Wear*. 1997, 212(2), pp. 206–212.
20. Rao, K.R., Kim, D.N., Hwang, J.J.: *Fast Fourier Transform - Algorithms and Applications*. (Springer, Ed.). Dordrecht 2010.
21. Tiwari, R., Lees, A.W., Friswell, M.I.: Identification of dynamic bearing parameters: a review. *The Shock and Vibration Digest*. 2004, 36(2), pp. 99–124.
22. Yari, E., Ghassemi, H.: Boundary element method applied to added mass coefficient calculation of the skewed marine propellers. 2016, 23(2), pp. 25–31.
23. Zywicka, G., Kicinski, J., Baginski, P.: The static and dynamic numerical analysis of the foil bearing structure. *Journal of Vibrational Engineering and Technologies*. 2016, 4(3), pp. 213–220.

CONTACT WITH THE AUTHORS

Łukasz Breńkacz

Institute of Fluid Flow Machinery
Polish Academy of Sciences
Fiszera 14, 80-231 Gdańsk
POLAND

FINITE ELEMENT ANALYSIS OF VENTILATION SYSTEM FIRE DAMPER DYNAMIC TIME-HISTORY

Dariusz Skibicki

Łukasz Pejkowski

Michał Stopel

UTP University of Science and Technology, Poland

ABSTRACT

The paper presents results of the numerical analysis of the fire damper used in ventilation systems under the earthquake loading. The research was conducted in accordance with the recommendations of the Nuclear Safety Standards Commission. The aim of the analysis was to examine the fire damper with respect to its resistance to service loadings, structural integrity, and capability to stay operative after an earthquake. The analysis was carried out using the Finite Element Method in LS-Dyna software. The earthquake loading was modelled as accelerations, measured in three directions during the earthquake. For modelling of the materials behaviour, material models taking into account the influence of strain rate on hardening were used. The analysis consisted of three stages, which were: loading the construction with the earth gravity, earthquake simulation by loading with accelerations in three directions, and, finally, closing the fire damper. The analysis has shown that some of the construction elements undergo plastic deformations. However, the performed simulation of fire damper closing showed that despite these deformations, the device remains capable to keep its functionality and the damper closes hermetically. The results of the analysis were important design indications for the fire damper prototype.

Keywords: fire barriers, earthquake, finite element method

INTRODUCTION

It is estimated that in the years 2000-2006, the fire was the cause of 5% of ship accidents [1]. Fire dampers are key elements of structural fire protection of buildings, offshore facilities or ships. They play the role of fire barriers, but also protect against toxic hazard. In the initial phase, the air-conditioning system can cause uniform distribution of toxic concentrations [2].

Correct operation of this kind of installation depends on taking into account different general types of loadings at the design stage, such as fatigue loadings for instance [3, 4]. Especially for offshore drilling tower construction types,

the following types of loadings are listed in the NORSOK standard: impact loads caused by explosion or ship collision, and loads caused by extreme weather or earthquake [5].

Like other constructions, the fire barriers are not 100% reliable [6]. For this reason, it is very important to take into account detailed engineering data regarding materials properties and loadings which construction may undergo in the design process. Moreover, an engineer should be equipped with computational methods able to predict the construction's behaviour in extreme conditions. Furthermore, it is desired that using these methods can take into account the postulate of the Damage-Tolerant design strategy, which assumes the possibility of machine usage with an existing damage [7].

According to the idea of this strategy, fire safety elements should keep the ability to reliable task realization even in case of damage or high plastic deformation. Such damages can be the result of explosion or earthquake.

The computational method which can be used to simulate construction's behaviour in real loadings conditions, taking into account degradation of the construction, is the Finite Element Method (FEM) [8–10]. The aim of this work was to test the ventilation channel fire damper prototype in earthquake loading conditions using the FEM method. Using the computer simulation, the strength, stability and suitability of the damper for emergency use in case of earthquake was investigated. The analysis results have made the basis for indicating possible modifications of the fire damper prototype.

ANALYSIS PROGRAMME

The fire damper analysis programme was designed on the basis of "Design of Nuclear Power Plants against Seismic Events; Part 4: Components" [11]. This standard was selected by reason of exceptionally detailed research guidelines and high safety standards. Due to the fact that the present research is a numerical research, the standard guidelines given in point 3.3.1.a and concerning the verification by analysis were taken into account particularly. Based on these guidelines, the following research scheme was assumed:

- 1) determination of excitation in the place of installation,
- 2) modelling and determination of model parameters,
- 3) analysis of mechanical behaviour,
- 4) verification of limit conditions.

As for point 1, the seaside area of Turkey, which is particularly prone to earthquake danger, was selected. With accordance to the option given in Point 4.4.1.1.b of the standard [11], entitled "Time History Method", a real history of accelerations recorded in three directions was selected. The data was acquired from the USGS Earthquake Hazards Program database, available on the website [12]. According to the computational procedure assumed on the basis of [13], the recorded acceleration histories were modified to fit the target design spectra. For this purpose, two design spectra were used. They were prepared using the procedures described in [11, 14] and the data achieved from [15]. The adjustment of the recorded acceleration histories to the design spectra was performed using the Direct Scaling method [13].

As for point 2, the construction of the analysed fire damper was modelled using the FEM method and LS-DYNA software. It is a general-purpose explicit FE code capable of nonlinear dynamic analysis for 3D structures. The choice of the software was made taking into account that LS-DYNA is an ANSI/ASME NQA-1 (nuclear quality assurance) certificated code and is widely used in the nuclear power industry, usually to analyse seismic responses. The numerical model was prepared using the LS-PREPOST software, which was also used for elaboration of results.

As for points 3 and 4, the analysis of mechanical properties and the verification of boundary conditions was divided, in accordance with [11], into 3 areas:

- 1) investigation of resistance to service loadings (results of the gravity and damper closing process) and loadings being the result of the earthquake, that is the strength and stability analysis,
- 2) investigation of structural integrity, that is the analysis of possible occurrence of large deformations and leakage,
- 3) investigation of fire damper capability to stay operative after the earthquake.

Within point 1), the calculated values of maximum equivalent stresses were compared to limit values, such as yield stress and ultimate tensile strength for the applied materials. Within point 2), possible presence of large and irreversible deformations of the fire damper was checked, along with their impact on sealing. Within point 3), the ability of fire damper to close in 20 seconds after the earthquake, which was required by the manufacturer, was checked. The analysis results for points 1) and 2) are presented in Chapter 5.1 and for point 3) in Chapter 5.2.

DETERMINATION OF LOADING AT THE PLACE OF INSTALLATION

The calculations considering the impact of earthquake made use of the acceleration histories for the strongest earthquake in the history, registered on the area of Turkey. The data, given in Tab. 1, was collected from the USGS Earthquake Hazards Program website [12]. The acceleration was recorded in three directions: *N* – north, *E* – east, and *Z* – vertical (Fig. 1).

Tab. 1. Earthquake data recorded for the area of Turkey

Latitude	40.756° N
Longitude	29.955° E
Date	1999-08-17 00:01:38 UTC
Depth	17.0 km
Magnitude	Mw7.4

The time histories were modified using the Direct Scaling method in order to fit them to the target design spectra determined in accordance with the European standard KTA 2201.4 [11]. The spectrum of the time histories was also compared to the target design spectra determined on the basis of the American standard ASCE 7-95 [14]. The target design spectra according to KTA 2201.4 were performed on the basis of parameters determined in the harmonic analysis of the recorded signal and the standard [11] recommendations. The calculated values of parameters required for the spectrum performing are given in Tab. 2.

The target design spectra according to ASCE 7-95 were performed using the data obtained from [15]. The determined parameters used to create the design spectrum are given in Tab. 3.

The target design spectra prepared according to the European KTA 2201.4 standard [11] and the American standard ASCE 7-95 [14], are shown in Fig 2 a and b, respectively. The amplitude-frequency signal characteristics of the selected earthquake, determined using the Fourier transformation, are put on the charts.

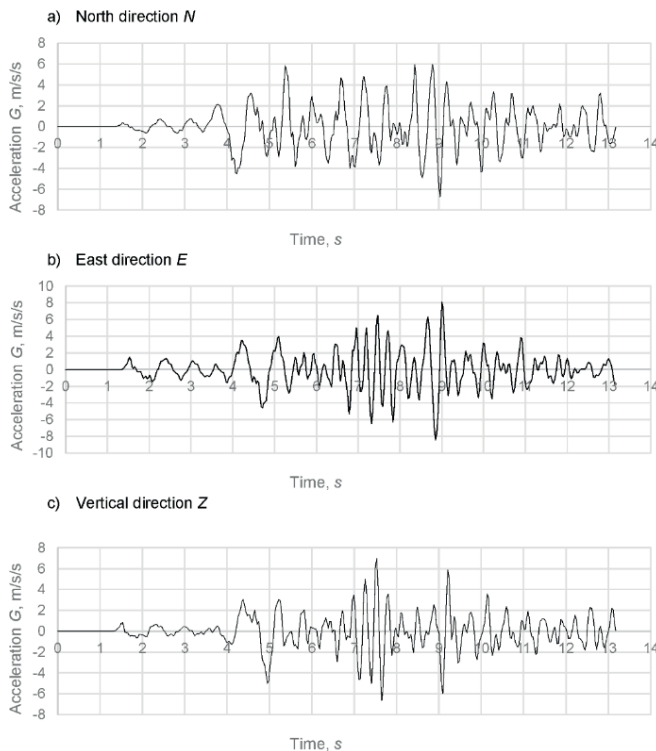


Fig. 1. Time histories of the strongest earthquake recorded on the Turkey territory, accelerations in three directions

Tab. 2. Target design spectrum parameters according to KTA 2201.4

1) Lowest decisive eigenfrequency of the major system at the lower limit value in the variation range of system parameters	$f_1 = 0.5 \text{ Hz}$ $0.8f_1 = 0.4 \text{ Hz}$
2) Highest decisive eigenfrequency of the major system for the upper limit value in the variation range of component parameters	$f_n = 8 \text{ Hz}$ $1.2f_n = 9.6 \text{ Hz}$
3) Upper limit frequency of the response spectrum of the major system	$f_{limit} = 20 \text{ Hz}$
4) Acceleration of the major system (component) at the place of installation of the subsystem,	$a_g = 1.1 \text{ G}$
5) Spectrum amplification factor	$v = 8$

It is almost impossible to achieve response spectra of the recorded accelerograms equal to the design spectra, since the design spectra are based on the medians of numerous different time histories [13]. However, comparing the amplitude-frequency characteristics with the model spectra allows for the conclusion that the character of the selected earthquake does not deviate from typical earthquakes recorded in the selected region.

MODELING AND DETERMINATION OF PARAMETERS

GEOMETRICAL MODEL

The construction model was divided into 24 parts, connected using contacts (Fig. 3). The parts which are immobilized relative to each other were connected using bonding contacts (CONTACT_TIED_SURFACE_TO_SURFACE), while parts which form kinematic pairs were connected using contacts which allow for mutual movement including friction (CONTACT_AUTOMATIC_SURFACE_TO_SURFACE). In total, the model consisted of 2291 elements. Large and flat surfaces were modelled using shell type elements (ELEMENT FORMULATION 2). Parts of the lever system composing the damper opening mechanism were modelled using beam type elements (ELEMENT FORMULATION 1) (Fig. 3.c). Solid type elements (ELEMENT FORMULATION 1) were used to model parts of the rotary node (Fig. 4).

Tab. 3. Target design spectrum parameters according to ASCE 7-95

1) The values of basic parameters: S_s (Short Period Spectral Acceleration) and S_1 (1-sec Period Spectral Acceleration) which are typical for the Turkey region were selected:	$S_s = 1.65 \text{ G}$ $S_1 = 0.75 \text{ G}$
2) The following amplification coefficients were chosen:	
a) Site Amplification Coefficient for $S_s - F_a$ and site Amplification Coefficient for $S_1 - F_v$:	$F_a = 1$ $F_v = 1.5$
b) Spectral response acceleration	$S_{MS} = F_a S_s = 1.65 \text{ G}$ $S_{M1} = F_v S_1 = 1.125 \text{ G}$
c) Designed earthquake spectral response acceleration parameters	$S_{DS} = \frac{2}{3} S_{MS} = 1.1 \text{ G}$ $S_{D1} = \frac{2}{3} S_{M1} = 0.75 \text{ G}$
3) Calculated time parameters	$T_0 = 0.2 \frac{S_{D1}}{S_{DS}} = 0.14 \text{ s}$ $T_s = \frac{S_{D1}}{S_{DS}} = 0.68 \text{ s}$
4) Calculated spectrum parameters	$T = \begin{cases} T < T_0 & S_a = S_{DS} \left(0.4 + 0.6 \frac{T}{T_0} \right) \\ T_0 \leq T < T_s & S_a = S_{DS} \\ T \geq T_s & S_a = \frac{S_{D1}}{T} \end{cases}$

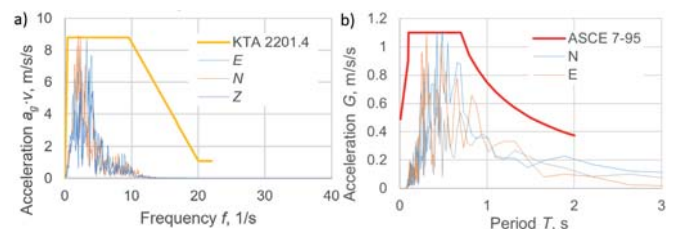


Fig. 2. Loading spectrum

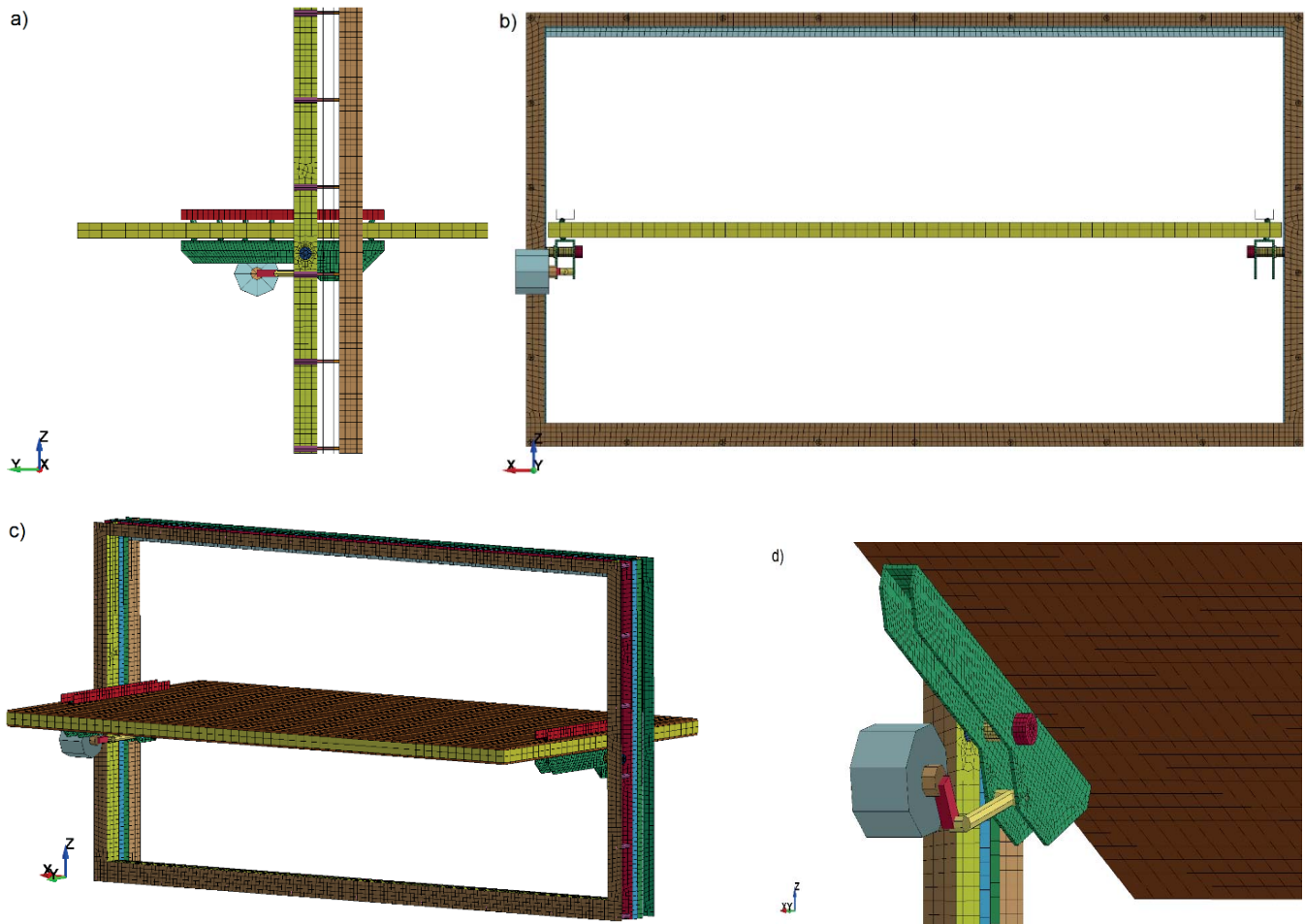


Fig. 3. FEM model of fire damper: a) side view, b) front view, c) isometric view, d) opening lever system

BOUNDARY CONDITIONS

Using the finite elements method, two events were modelled:

- 1) fire damper closing in normal service conditions (without earthquake),
- 2) fire damper closing in case of emergency event, that is after the earthquake episode.

Fire damper closing in normal service conditions consists of two periods:

- 1) gravity application to the whole structure in 2 seconds,
- 2) damper closing in 20 seconds, that is from second 2 to 22 of simulation.

Fire damper closing after the earthquake consist of 3 stages:

- 1) gravity application to the whole structure in 2 seconds,
- 2) an earthquake that lasts for 13 seconds, from second 2 to 15 of simulation,
- 3) damper closing in 20 seconds, from second 15 to 35 of simulation.

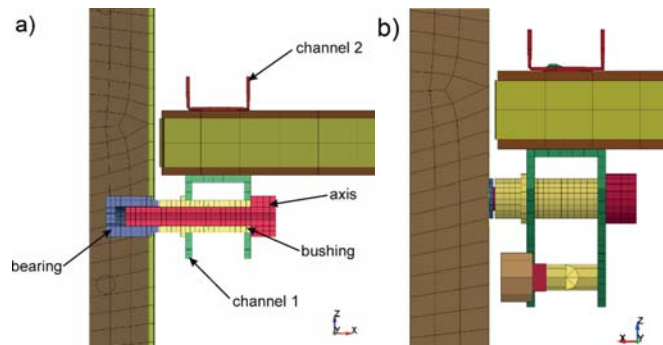


Fig. 4. Model of fire damper bearing

The above described simulation stages are presented in Fig. 5. In the history of vertical component Z , which is in the direction of gravity action, all three stages are visible: (1) the increase of acceleration during the application of earth gravity, (2) the stage of earthquake, and (3), the stage of constant acceleration equal to the gravitational acceleration in the time of fire damper closing. During stages 1 and 2, the rotation of motor arm is blocked. In stage 3, the rotation is being freed and angular acceleration is applied to the arm. Its constant value guarantees damper closing in 20 seconds.

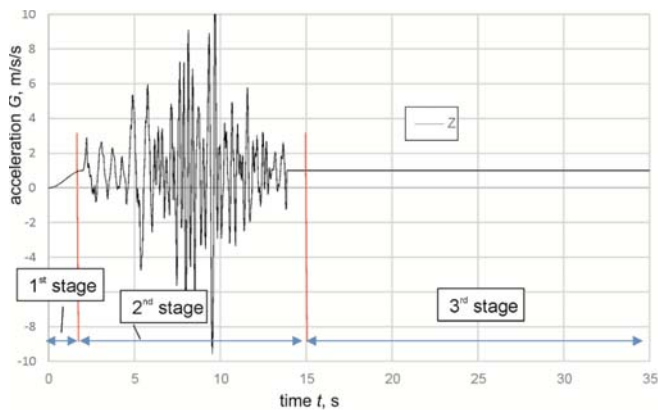


Fig. 5. Three stages of loadings application

MATERIAL MODELS

In order to gather the information on permanent deformations of the construction, material models including plasticity were assumed for metal parts. From among the models including plasticity in LS-DYNA, a commonly used model bearing the name of MAT_PIECEWISE_LINEAR_PLASTICIT was selected. Only for the plate made of fire resistant material characterized by the lack of plastic deformations, the linear elastic model MAT_ELASTIC was selected. The material parameters of the applied models are given in Tab. 4.

Tab. 4. Material models and their parameters

Material grade	Exemplary application	Model type	Young's modulus E [GPa]	Yield stress S_y [MPa]	Ultimate tensile strength S_u [MPa]
S220GD	Sheets	bilinear	190	220	300
S355	Axes, C-sections, pin	bilinear	190	345	470
CuSn8	Bearings bushings	bilinear	190	280	450
PROMATECT®-H	Fire resistant plate	linear	4.2		4.8

The key element of the construction, in view of the fire damper rotation, is the bearing axis made of 1.4306 grade steel. On the basis of preliminary calculations, it was determined that strain rates acting in this element reach values of about 0.09 s^{-1} (Fig. 6). These are the values which can influence plastic deformation of the element [16].

The influence of strain rate on additional hardening was checked using the Johnson-Cook model ([17]):

$$\sigma_y = \left(A + B \cdot \varepsilon_{pl}^n \right) \left(1 + C \cdot \ln \frac{\dot{\varepsilon}}{\dot{\varepsilon}_0} \right) \quad (1)$$

where: A – yield stress, B , n , – hardening parameters, C – strain rate sensitivity parameter, ε_{pl} – effective plastic strain, $\dot{\varepsilon}$ – strain rate, $\dot{\varepsilon}_0$ – strain rate in case of static test.

For the Johnson-Cook model, the material parameters of 1.4306 (304L) grade steel were taken from [18]. They are

equal to: $A = 110 \text{ MPa}$, $B = 1500 \text{ MPa}$, $n = 0.36$, $C = 0.014$. The function that describes the value of additional hardening related to the influence of strain rate is the function in second bracket of (1). After introducing the parameters, we get:

$$\begin{aligned} \left(1 + C \cdot \ln \frac{\dot{\varepsilon}}{\dot{\varepsilon}_0} \right) &= \quad (2) \\ &= \left(1 + 0.014 \cdot \ln \frac{0.09}{0.001} \right) = \\ &= 1.06. \end{aligned}$$

The value of additional hardening resulting from the strain rate of the bearing axis can be estimated as equal to 6%.

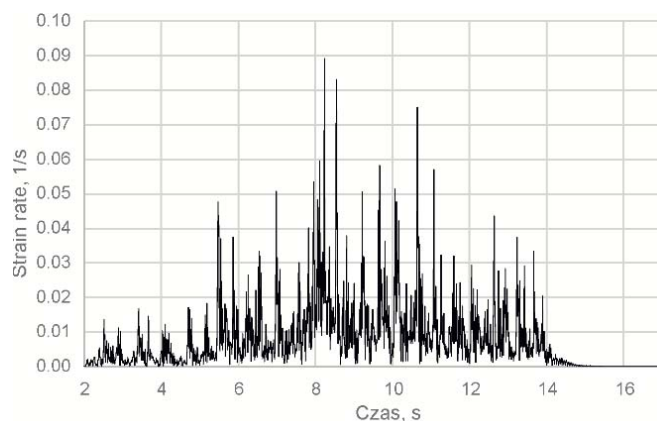


Fig. 6. Equivalent strain rate of bearing axis

This value was assumed significant for the part which decides of proper fire damper closing. Its damage would result in lack of rotation possibility. Thus, the Johnson Cook model was also assumed for the axis in

LS-DYNA software. Its simplified variant neglects the influence of temperature: MAT_SIMPLIFIED_JOHNSON_COOK.

On the basis of KTA standard [11], 4% damping factor for all parts was assumed.

MECHANICAL PROPERTIES ANALYSIS AND BOUNDARY CONDITIONS VERIFICATION

The results of the performed calculations have the form of time-histories of stresses and strains of all elements of the fire damper. The results are presented in two points, regarding to:

- 1) fire damper capability to resist service loadings and structure's integrity,
- 2) fire damper capability to stay operative after the earthquake.

FIRE DAMPER CAPABILITY TO RESIST SERVICE LOADINGS AND STRUCTURE'S INTEGRITY

In the charts below (Fig. 7, Fig. 8, Fig. 9, Fig. 10), the equivalent Huber-von Mises stress history is presented for the most stressed construction elements. In each of the charts, the stress history is presented for elements made of the same material. For better look on the stress level, the values of yield stress and ultimate tensile strength are also shown. Above the charts, the loading history in the form of one acceleration component is also shown.

The chart analysis shows that the yield stress is exceeded in some parts (Fig. 7, Fig. 8). However, none of these elements has been damaged.

Exceeding the yield stress appears in the axis made of 1.4306 steel and in the bearing sleeve made of S355 steel (Fig. 10). In the plastic strain history chart, permanent deformation of these parts, occurring at the most intensive moment of earthquake, is shown. The values of strain are not high, they reach 0.2-0.45%. But there is a question if they affect proper operation of the fire damper. The answer to that question is presented in the next point.

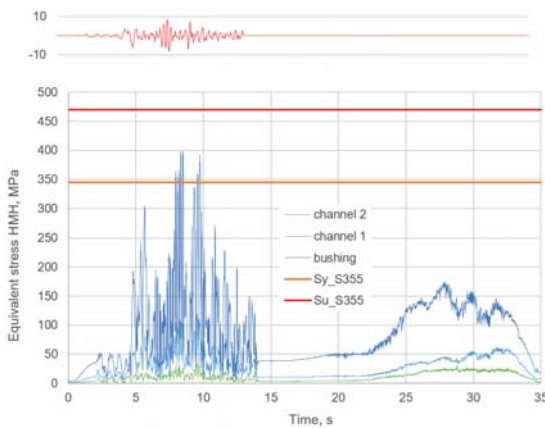


Fig. 7. Equivalent stress history in parts made of S355 steel

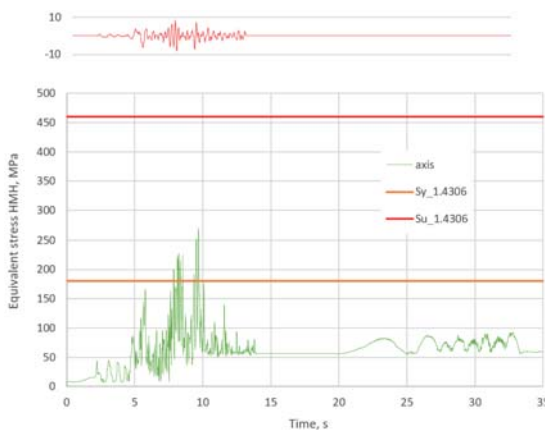


Fig. 8. Equivalent stress history in parts made of 1.4306 steel

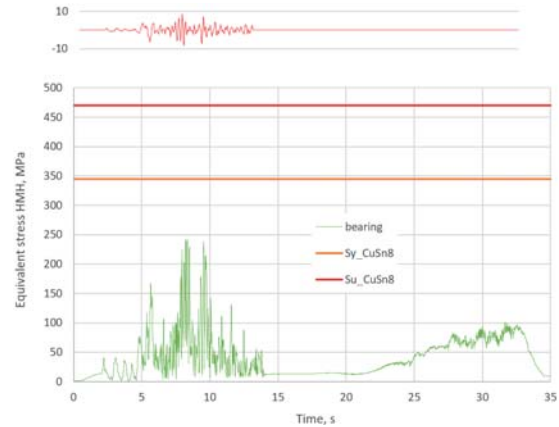


Fig. 9. Equivalent stress history in parts made of CuSn8 bronze

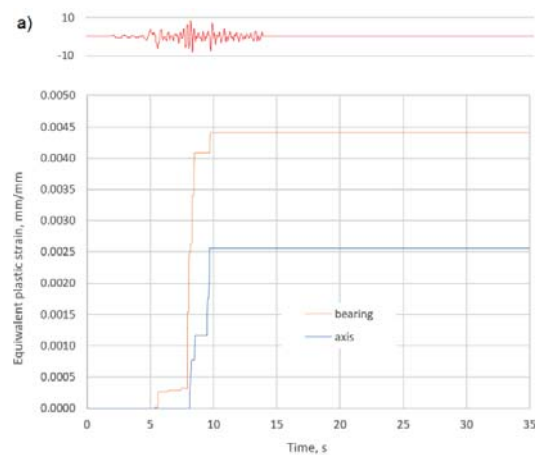


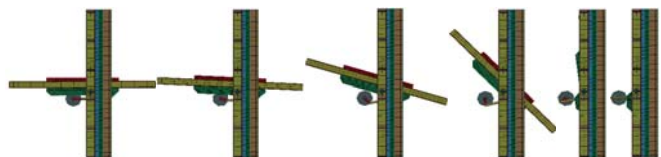
Fig. 10. Equivalent plastic strain history in bearing and axis

FIRE DAMPER FUNCTIONALITY AFTER EARTHQUAKE

The capability to close hermetically decides whether the fire damper is functional. In order to check it, the history of the torque required to close the damper before and after the earthquake was analysed.

Fig. 11 presents the chart of motor torque required to close the fire damper in conditions preceding the earthquake. The achieved results are recommendations for proper selection of the motor.

Fig. 12 a shows the motor torque required to keep the damper open during the application of earth gravity (stage I) and earthquake (stage II), as well as the torque required to close the damper after the earthquake (stage III).



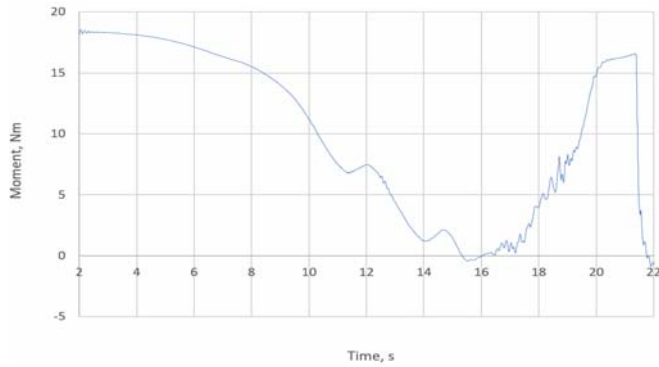


Fig. 11. Motor torque history in the simulation without earthquake

Comparing the period of fire damper closing without earthquake (Fig. 11) and the analogous period of closing after the earthquake (Fig. 12 b), one can notice that in both cases the motor moment reaches similar values. Thus, the presence of plastic deformations does not block damper's ability to close.

Due to the presence of permanent deformations it was checked whether the fire damper has closed hermetically. In Fig. 13, the contact of the fire damper with the frame at second 35 is shown. The change of the distance between the damper and the frame was measured in the middle of the frame's longest side and in its upper and lower part (Fig. 14).

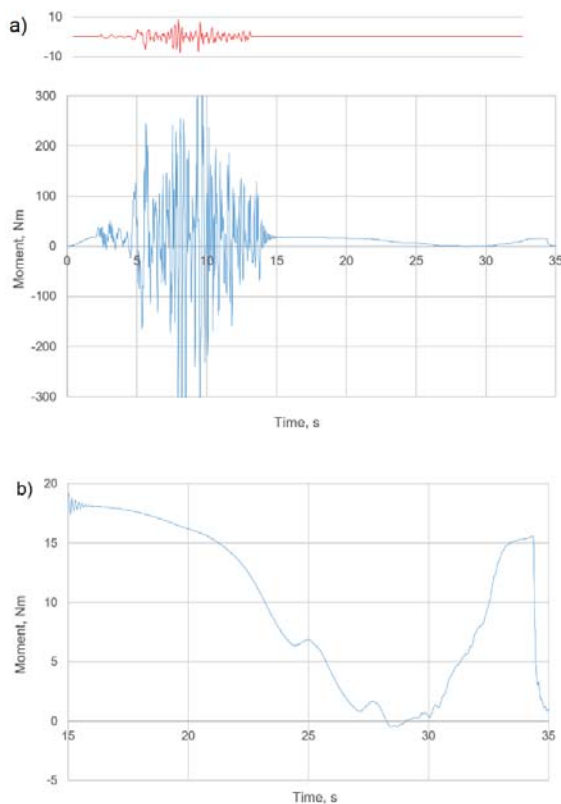


Fig. 12. Motor torque history in the simulation including the earthquake: a) full history, b) torque in stage III, during damper closing

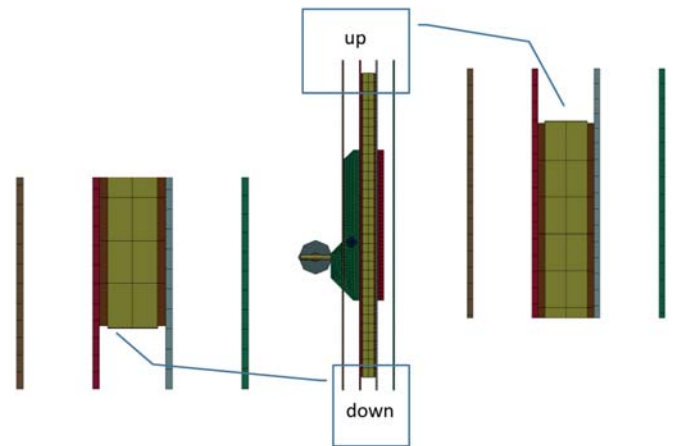


Fig. 13. Illustration of hermetic closing of fire damper

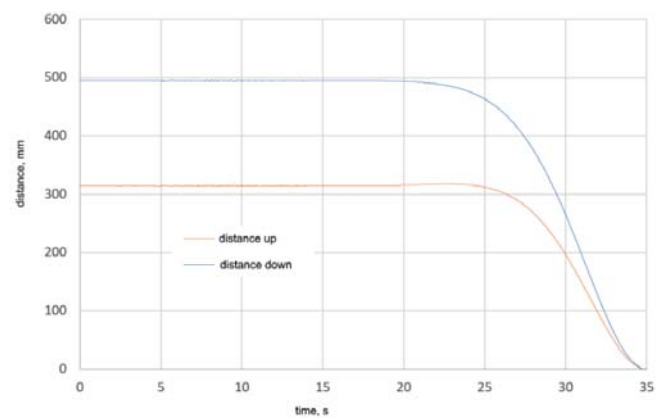


Fig. 14. Distance between fire damper and frame in upper and lower part

CONCLUSIONS

- 1) Modification of recordings to fit into the Design Spectrum by Direct Scaling method allowed to show potentially weak links, due to loading caused by the earthquake.
- 2) LS-DYNA was used to calculate the dynamic time history of a complex construction in earthquake loading conditions. A rich library of material models enabled to capture the strain rate dependent material behaviour. Fire damper operation with the presence of permanent deformation was simulated thanks to effective modelling in the LS-DYNA software.
- 3) From the dynamic gravity and seismic loading time history analysis, performed using the Finite Element Method, the designers received data on stress levels of individual parts of the construction during the fire damper closing process.
- 4) Some of the damper parts exhibit plastic deformations caused by accelerations taking place during the earthquake. However, the equivalent stress does not reach strength limits for the used materials in any of the construction elements.

Despite the presence of plastic strains in some elements, the fire damper loaded with the earthquake remains functional. The dumper closes hermetically within 20 seconds.

ACKNOWLEDGMENTS

The paper refers to the research financed by the National Centre for Research and Development (NCBiR) in the framework of the project POIR.01.01.01-00-1422/15

REFERENCES

1. Kozak, J.: Elastic protection coatings for ship fuel tanks, intended for the increasing of environment protection level. Polish Maritime Research, 15, (2008).
2. Dobrzyńska, R.: Selection of outfitting and decorative materials for ship living accommodations from the point of view of toxic hazard in the initial phase of fire progress. Polish Maritime Research, 16, (2009).
3. Skibicki, D., Sempruch, J., Pejkowski, Ł.: Model of non-proportional fatigue load in the form of block load spectrum. Materwiss. Werksttech. 45, 68–78 (2014).
4. Pejkowski, Ł., Skibicki, D.: Criteria Evaluation for Fatigue Life Estimation under Proportional and Non-Proportional Loadings. Mater. Sci. Forum. 726, 189–192 (2012).
5. Design principles - technical safety. NORSOK S-DP-001.
6. Macgillivray, H.: The Development of Standards for Instrumented Charpy Testing. 1–34 (2008).
7. Stephens, R.I., Fatemi, A., Stephens, R.R., Fuchs, H.O.: Metal Fatigue in Engineering. Wiley (2000).
8. Żyliński, B.: Finite element local analysis of wave slamming on offshore structure. Polish Maritime Research, 1, 8–12 (2009).
9. Augustyniak, M., Porembski, G.: FEM strength analysis of sandwich panels for ship structure applications. Polish Maritime Research, S 1, 24–26 (2006).
10. Bogdaniuk, M., Górecki, Z., Brzóska, M.: FEM analysis of ultimate strength of steel panels. Polish Maritime Research, S 1, 21–23 (2006).
11. Design of Nuclear Power Plants against Seismic Events; Part 4: Components. Nucl. Saf. Stand. Comm. (1996).
12. www.earthquake.usgs.gov; date accessed 2017-10-10.
13. Jia, J.: Modern Earthquake Engineering - Offshore and Land-based Structures. Springer-Verlag GmbH Germany (2017).
14. ASCE 7-95: Minimum design loads for buildings and other structures. Am. Soc. Civ. Eng. ASCE, NY. (1995).
15. Benoit, S.C.: Seismic Design for Buildings. U.S. Army Corps Eng. 829 (2005).
16. Stopel, M., Skibicki, D.: Determination of Johnson-Cook model constants by measurement of strain rate by optical method. AIP Conf. Proc. 1780, (2016).
17. Livermore Software Technology Corporation, LS-Dyna Keyword User's Manual, volume II - Volume II R7.1, Materials & Design, (2014).
18. Xue, Q., Nesterenko, V.F., Meyers, M.A.: Evaluation of the collapsing thick-walled cylinder technique for shear-band spacing. Int. J. Impact Eng. 28, 257–280 (2003).

CONTACT WITH THE AUTHOR

Dariusz Skibicki

e-mail: dariusz.skibicki@utp.edu.pl
UTP University of Science and Technology
Kaliskiego 7
85-796 Bydgoszcz
POLAND

COMPARISON OF SOIL MODELS IN THE THERMODYNAMIC ANALYSIS OF A SUBMARINE PIPELINE BURIED IN SEABED SEDIMENTS

Waldemar Magda

Gdańsk University of Technology, Faculty of Civil and Environmental Engineering,
Department of Geotechnics, Geology and Marine Civil Engineering, Poland

ABSTRACT

This paper deals with mathematical modelling of a seabed layer in the thermodynamic analysis of a submarine pipeline buried in seabed sediments. The existing seabed soil models: a “soil ring” and a semi-infinite soil layer are discussed in a comparative analysis of the shape factor of a surrounding soil layer. The meaning of differences in the heat transfer coefficient of a soil layer is illustrated based on a computational example of the longitudinal temperature profile of a -kilometer long crude oil pipeline buried in seabed sediments.

Keywords: submarine buried pipeline, seabed thermal models, shape coefficient, heat transfer coefficient, longitudinal temperature profile

INTRODUCTION

Heat transfer (based on convection and/or conduction phenomena), from a medium transported by a submarine pipeline (e.g., crude oil or natural gas) to a seabed sediment environment surrounding a buried submarine pipeline, takes place in a pipeline thermodynamic system consisting of several adjacent layers variable in thickness, formed by different materials/substances of different thermodynamic properties.

In general, the following component layers can be distinguished in the thermodynamic system of a partially/fully buried submarine pipeline (Figs. 1 and 2):

- a) inside film (formed by a transported medium),
- b) anti-corrosion inside coating,
- c) steel pipe,
- d) anti-corrosion outside coating,
- e) thermal insulation,
- f) anti-buoyancy (weight) and protective concrete coating,

- g) outside film (formed by seawater flowing around a pipeline – only in the case of an exposed or partially buried submarine pipeline),
- h) seabed soil medium surrounding a partially or fully buried submarine pipeline.



Fig. 1. Thick-walled steel pipe coated with 3M Scotchkote epoxy coating EP2306 HF, and a heavy concrete coating, for 370 km × 48 in. Dolphin (subsea) gas pipeline [10]

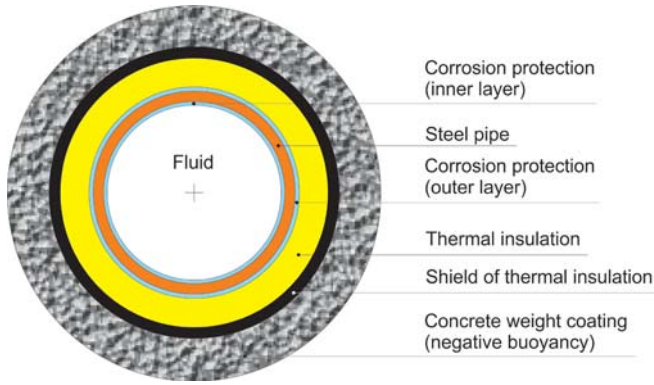


Fig. 2. Cross-section of a typical submarine pipeline structure [8]

The design procedures, established for submarine pipelines either laid on the seabed or buried in seabed sediments, require to take into account the phenomena of heat transfer through a multi-layered thermal barrier of the pipeline structure. In most cases from the list given above (*i.e.*, from (b) to (f), and (h) under certain conditions), the component layers are combined serially and have an annular (in 2D) or a cylindrical (in 3D) shape.

The basic parameters, used in the pipeline thermodynamic analysis and characterizing the component layers, are as follows:

- thermal conductivity λ [W/(m·K)] of the material creating a component layer (a material parameter),
- shape factor S [—] of a component layer (a geometric parameter),
- heat transfer coefficient U [W/(m²·K)] of a component layer (a combined material-geometric parameter).

SINGLE CYLINDRICAL THERMAL BARRIER

Taking into account a single cylindrical layer considered in the thermodynamic analysis, the heat transfer coefficient is given by the following equation

$$U^{(1)} = \frac{\lambda^{(1)}}{r_i^{(1)} \ln\left(\frac{r_o^{(1)}}{r_i^{(1)}}\right)} \quad (1)$$

where:

- $U^{(1)}$ – heat transfer coefficient of a single cylindrical thermal barrier [W/(m²·K)],
- $\lambda^{(1)}$ – thermal conductivity of material forming a single thermal barrier [W/(m·K)],
- $r_i^{(1)}$ – inner radius of a single cylindrical thermal barrier [m],
- $r_o^{(1)}$ – outer radius of a single cylindrical thermal barrier [m].

In order to describe geometrically a cylindrical thermal barrier, the following non-dimensional shape factor can be used

$$S^{(1)} = U^{(1)} \frac{2\pi r_i^{(1)}}{\lambda^{(1)}} \quad (2)$$

Comparing the last two equations, the shape factor of a single cylindrical thermal barrier takes the final practical form

$$S^{(1)} = \frac{2\pi}{\ln\left(\frac{r_o^{(1)}}{r_i^{(1)}}\right)} \quad (3)$$

It is obvious that the shape factor of a single cylindrical thermal barrier depends only on geometric dimensions, *i.e.*: the inner and outer radii of the cylindrical barrier.

A surface conducting heat in a single cylindrical thermal barrier is not constant, it depends on the computational radius, r , where $r_i^{(1)} < r < r_o^{(1)}$. Therefore, for practical purposes, one of the two characteristic surfaces of a single cylindrical thermal barrier, *i.e.*: either the inner or the outer, is usually assumed and defined in derivation of Eq. (1). In the above inquiry the inner surface is assumed, indicated by parameter $r_i^{(1)}$ appearing in the first term of the denominator of Eq. (1) and in Eq. (2).

MULTI-LAYERED CYLINDRICAL THERMAL SYSTEM

In the simplest case, heat transfer through a single thermodynamically homogeneous barrier is considered. However, when a submarine pipeline structure is concerned, it may be necessary to compute the overall heat transfer coefficient, taking into account all meaningful adjacent component layers, thus creating a multi-layered pipeline thermodynamic system.

Adopting the continuity principle for the steady-static heat transfer through the component layers of the buried pipeline thermodynamic system, the overall heat transfer coefficient (also known as the Peclet's coefficient) can be obtained from an electrical resistance analogy between heat transfer and direct current

$$U = \frac{1}{\frac{1}{U_{fi}} + \frac{1}{U_{ai}} + \frac{1}{U_p} + \frac{1}{U_{ao}} + \frac{1}{U_i} + \frac{1}{U_c} + \frac{1}{U_s}} \quad (4)$$

where:

- U – overall heat transfer coefficient of the multi-layered thermodynamic system of the pipeline buried in seabed sediments [W/(m²·K)],
- U_{fi} – heat transfer coefficient of the inside film (boundary-layer between the pipe and the medium transported) [W/(m²·K)],
- U_{ai} – heat transfer coefficient of the inner anti-corrosion coating [W/(m²·K)],
- U_p – heat transfer coefficient of the steel pipe [W/(m²·K)],

- U_{ao} - heat transfer coefficient of the outer anti-corrosion coating [W/(m²·K)],
- U_i - heat transfer coefficient of the thermal insulation coating [W/(m²·K)],
- U_c - heat transfer coefficient of the concrete weight coating [W/(m²·K)],
- U_s - heat transfer coefficient of the seabed soil layer [W/(m²·K)].

The overall heat transfer coefficient (OHTC) of the pipeline is also called the U -value of the pipeline in subsea engineering. From the engineering practice viewpoint it is possible and recommended to simplify Eq. (4) by excluding some components appearing in the main denominator, however, not bringing any meaningful effects to the quality of computational results.

For insulated pipelines, thermal insulation coatings provide an order of magnitude larger thermal resistance than both the inside film (always existing) and the outside film (existing only in the case of totally exposed or partially buried pipelines). Therefore the effects of internal and external film coefficients (U_{fi} and U_{fo}) to the overall U -value of the pipeline can be practically ignored.

The internal and external anti-corrosion coatings are rather thin, made of materials which do not have significant thermal resistances. Therefore the influence of both anti-corrosion coatings can be practically omitted in Eq. (4).

The steel pipe wall-thickness is usually much smaller than the thickness of concrete coating. On the other hand the thermal conductivity of steel is much larger than the conductivity of concrete or seabed soil (see Tables 1 and 2). Consequently, due to a very small temperature drop within the steel pipe wall, the existence of the steel pipe can be also neglected in the thermodynamic analysis of the submarine pipeline.

Tab. 1. Thermal conductivities of selected materials/substances [8]

Material / Substance	Thermal conductivity λ [W/(m·K)]
Air	0.026
Water	0.6
Sand (water saturated)	1.2 ÷ 2.8
Aerogel (@ t=0°)	0.012 ÷ 0.016
Epoxy foam	0.07
Polyurethane foam	0.03 ÷ 0.4
Polypropylene foam	0.12 ÷ 0.2
Syntactic foam	0.08 ÷ 0.15
Phase Change Material (PCM)	0.12 ÷ 0.17
Concrete	0.8 ÷ 1.4
Steel (0.2% C)	50

Tab. 2. Thermal conductivities of typical soil surrounding a pipeline [1]

Type of soil	Thermal conductivity λ [W/(m·K)]
Peat (wet)	0.54
Sand (soaked)	1.90 ÷ 2.42
Clay (wet)	1.04 ÷ 1.56

Thermal conductivities of concrete and seabed soil are comparable ($\lambda_c \approx \lambda_s$, see Tables 1 and 2). Therefore the conditions $\lambda \gg \lambda_c \approx \lambda_s$ means that the multi-layered thermodynamic system of the pipeline buried in seabed sediments can be simplified and approximated by a three-layer system where the thermal insulation, the concrete coating and the seabed surrounding soil are basic regulators of the heat transfer process

$$U = \frac{1}{\frac{1}{U_i} + \frac{1}{U_c} + \frac{1}{U_s}} \quad (5)$$

Insulation manufacturers typically use a U -value based on the outer diameter of an entire pipeline structure, while pipeline designers use a U -value based on the inner diameter [1].

The insulation and concrete coatings have an annular/cylindrical shape, so that computation of the heat transfer coefficients, U_i and U_c , can be performed using Eq. (1). However, as far as seabed soil sediments in the proximity of the submarine buried pipeline is concerned, the question of proper modelling of the soil area/volume arises. For the analysis of heat transfer from the pipeline structure to seabed soil sediments the following two soil models can be adopted:

- “soil ring” model (annular/cylindrical layer of soil adjacent to the pipeline structure),
- soil half-space model (semi-infinite layer of soil surrounding the pipeline structure).

The “soil ring” model is an artificial model, still assuming axisymmetrical heat transfer from the medium transported outwards. The soil half-space model reflects a real situation of the submarine pipeline buried in seabed sediments with an asymmetrical heat transfer from the pipeline structure to seabed soil sediments.

SEABED SOIL MODELS FOR A TOTALLY BURIED PIPELINE

In order to simplify the following considerations leading to a comparison of the above mentioned two seabed soil models, it is assumed that the pipeline structure is only a one-component (one-layer) structure, made of a steel pipe (Fig. 3). Additionally, as recommended in [1], it is assumed that the overall heat transfer coefficient is based on the inner diameter of the entire pipeline structure. It means that computations of all component heat transfer coefficients have to involve the inner diameter of the pipeline structure, represented by the inner diameter of the steel pipe, $r_i^{(p)}$ (see Fig. 3).

“SOIL RING” MODEL

Assuming the “soil ring” model (see Fig. 3), the heat transfer coefficient is given by the following equation (see Eq. (1))

$$U_s \equiv U_{s1} = \frac{\lambda_s}{r_i^{(p)} \ln\left(\frac{r_o^{(s)}}{r_i^{(s)}}\right)} \quad (6)$$

where:

- U_s – heat transfer coefficient of soil [W/(m²·K)],
- U_{s1} – heat transfer coefficient of the “soil ring” model [W/(m²·K)],
- λ_s – thermal conductivity of soil (see Table 2) [W/(m·K)],
- $r_o^{(s)}$ – outer radius of the “soil ring” [m],
- $r_i^{(s)}$ – inner radius of the “soil ring” [m],
- $r_i^{(p)}$ – inner radius of the steel pipe [m].

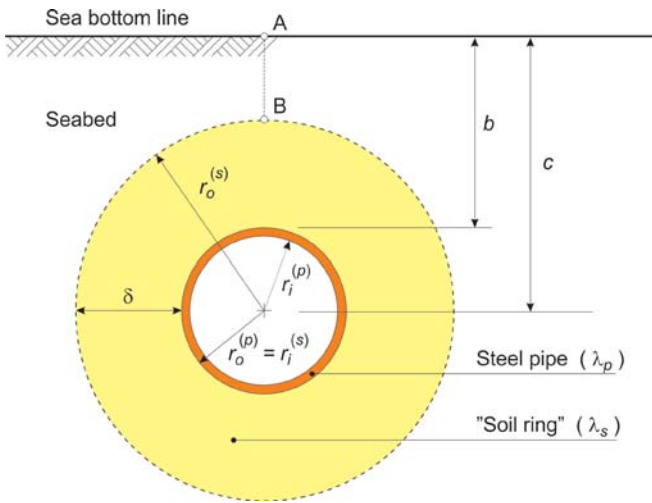


Fig. 3. The “soil ring” model assumed in the thermodynamic analysis of a submarine pipeline buried in seabed sediments [4]

According to Cranmer [4], the outer radius of the “soil ring” must be equal to a threefold value of the inner radius of the “soil ring”

$$r_o^{(s)} = 3r_i^{(s)} \quad (7)$$

It implies the following thickness of the “soil ring”

$$\delta = r_o^{(s)} - r_i^{(s)} = 2r_i^{(s)} \quad (8)$$

It is obvious that Eq. (6) can only be applied when the depth of burial fulfills the following geometric condition (see Fig. 3)

$$b \geq r_o^{(s)} - r_i^{(s)} \quad (9)$$

which, in conjunction with Eq. 7, takes the form

$$b \geq 2r_i^{(s)} \quad (10)$$

where b is the depth of burial of the submarine buried pipeline, measured vertically from the seabed bottom line to the top of the pipeline structure, [m].

After incorporating Eq. (7) into Eq. (6), the heat transfer coefficient of the soil modelled by the “soil ring” can be written as

$$U_s \equiv U_{s1} = 0.91 \frac{\lambda_s}{r_i^{(p)}} \quad (11)$$

whereas the shape factor of the “soil ring” is constant, irrespectively of the geometry of the system considered (see Eq. (3))

$$S_s = U_s \frac{2\pi r_i^{(p)}}{\lambda_s} \equiv S_{s1} = 2\pi \cdot 0.91 = 5.72 = \text{const} \quad (12)$$

where:

- S_s – shape factor of a soil layer [—],
- S_{s1} – shape factor of the soil layer modelled by the “soil ring” [—].

The idea of the “soil ring” was also used by Phetteplace [9]. Recalling the following basic relation

$$U = \frac{1}{R} \quad (13)$$

where:

- U – heat transfer coefficient [W/(m²·K)],
- R – heat transfer resistance [m²·K/W],

the equations presented in [8] can be simply reorganized in order to achieve the following relations:

- for $\frac{c}{r_i^{(s)}} > 1$

$$U_{s2'} = \frac{\lambda_s}{r_i^{(p)} \left[\ln\left(\frac{c}{r_i^{(s)}}\right) + \sqrt{\left(\frac{c}{r_i^{(s)}}\right)^2 - 1} \right]} \quad (14)$$

- for $\frac{c}{r_i^{(s)}} > 4$

$$U_{s2''} = \frac{\lambda_s}{r_i^{(p)} \ln\left(2 \frac{c}{r_i^{(s)}}\right)} \quad (15)$$

Adequate equations for the shape factor of soil are as follows:

- for $\frac{c}{r_i^{(s)}} > 1$

$$S_s \equiv S_{s2'} = \frac{2\pi}{\ln\left(\frac{c}{r_i^{(s)}}\right) + \sqrt{\left(\frac{c}{r_i^{(s)}}\right)^2 - 1}} \quad (16)$$

- for $\frac{c}{r_i^{(s)}} > 4$

$$S \equiv S_{s2''} = \frac{2\pi}{\ln\left(2\frac{c}{r_i^{(s)}}\right)} \quad (17)$$

SOIL HALF-SPACE MODEL

Additionally to the “soil ring” model, the soil half-space model (*i.e.* semi-infinite soil layer) was proposed in the literature [1, 5, 6]. The half-space model is specially dedicated to the case where Eq. (6) cannot be used because of the following condition

$$b < 2r_i^{(s)} \quad (18)$$

For such a case, a more general model was worked out, where the heat transfer coefficient of soil layer was derived assuming the soil area in form of the half-space surrounding the pipeline structure. The soil half-space model yields the following equations [1, 5, 6]:

$$U_s \equiv U_{s3} = \frac{\lambda_s}{r_i^{(p)} \operatorname{ar} \cosh\left(\frac{c}{r_i^{(s)}}\right)} \quad (19)$$

$$S_s \equiv S_{s3} = \frac{2\pi}{\operatorname{ar} \cosh\left(\frac{c}{r_i^{(s)}}\right)} \quad (20)$$

where:

U_{s3} – heat transfer coefficient of the soil half-space [W/(m²·K)],

S_{s3} – shape factor for the soil half-space [—],

c – depth of burial of the submarine buried pipeline, measured vertically from the seabed bottom line to the centre of the pipeline structure cross-section, [m],

$r_i^{(s)}$ – inner radius of the “pipe opening” in the soil half-space [m],

$r_i^{(p)}$ – inner radius of the steel pipe [m].

COMPARISON OF SOIL MODELS

A graphical comparison of the shape factor of the soil layer, S_s , for the range of relative depth of burial $c/r_i^{(s)} = 1\div 6$ and different soil models analysed in the present paper, is shown in Fig. 4.

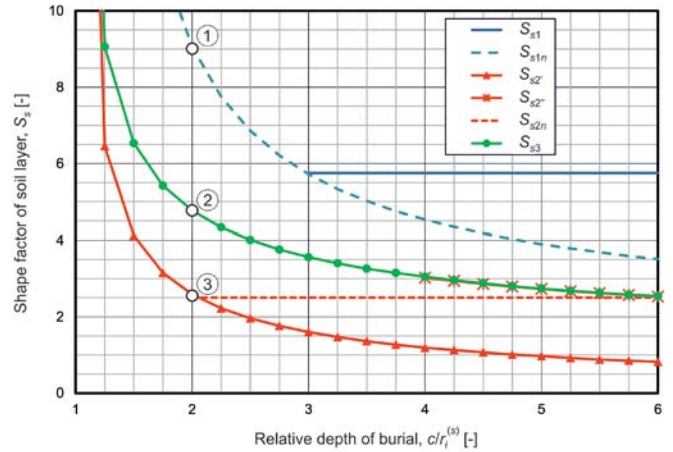


Fig. 4. Comparison of the shape factor of the soil layer surrounding the submarine pipeline structure vs. the relative depth of burial, for different seabed soil models

Based on the comparative analysis, the following findings can be drawn:

- A high convergence of curves S_{s3} and $S_{s2''}$ for $c/r_i^{(s)} = 4\div 6$ can be explained through the following relation

$$\cosh x \approx \ln(2x) \quad \text{for } x \gg 1 \quad (21)$$

that makes Eqs. (17) and (20) equivalent.

- Chronologically the pioneering proposal for the shape factor of the soil layer was introduced in [4]. The assumption of the “soil ring” model makes the shape factor always constant irrespectively of the system geometry, *i.e.*: c and $r_i^{(s)}$ (for the “soil ring” thickness $\delta = 2r_i^{(s)}$ the shape factor was equal to $S_{s1} = 5.72$.

Based on the idea of the “soil ring” model, herewith a certain modification of the model is proposed, assuming the “soil ring” always tangential to the sea bottom line (point A coincides with point B, see Fig. 3), with a variable thickness depending on the depth of burial. It implies that

$$c = b + r_i^{(s)} \quad (22)$$

and

$$S_{s1n} = \frac{2\pi}{\ln\left(\frac{c}{r_i^{(s)}}\right)} \quad (23)$$

Of course, this new solution proposed for the shape factor S_{s1n} has only one common point with the solution S_{s1} , which take place for $c = 3r_i^{(s)}$ (see Fig. 4).

- When the relative depth of burial, $c/r_i^{(s)}$, decreases from 2 to 1, the three functions S_{s1n} , $S_{s3'}$ and S_{s3} show a strong increase of the shape factor, tending asymptotically to infinity for $c/r_i^{(s)} \rightarrow 1$. The increase in the shape factor

S_s for decreasing $c/r_i^{(s)}$ seems to be logical but its high rate is practically abnormal, not to show any practical application. Taking the above into account, and assuming a minimum thickness of soil cover above the pipeline structure fulfilling the condition $b \geq r_i^{(s)}$, a practical range of applicability of the above presented equations for the shape factor of the soil layer can be stated as $c/r_i^{(s)} \geq 2$.

- For the practical range of the relative depth of burial $c/r_i^{(s)} \geq 2$, the range of variation of S_{s2} and $S_{s2'}$ is reasonably small and equal to: $S_{s2'} = 2.59 \div 1.19$ for $c/r_i^{(s)} = 2 \div 4$ and $S_{s2} = 3.02 \div 2.53$ for $c/r_i^{(s)} = 4 \div 6$. Consequently, it seems to be fully justified to assume a practical approximation of the soil model presented in [9], assuming a constant value of the shape factor of the soil layer, *i.e.* $S_{s2n} = 2.5$ (see Fig. 4).
- As far as the curves of S_{s1n} , S_{s2n} and S_{s3} are concerned, one can note that the solution obtained for S_{s3} creates an average solution for both extreme solutions denoted by curves S_{s1n} and S_{s2n} .

LONGITUDINAL TEMPERATURE PROFILE – COMPUTATIONAL ANALYSIS

The meaning of the reported differences in the shape factor values for different seabed soil models will be illustrated based on a computational analysis of a temperature distribution of a medium transported along a submarine buried pipeline. The input data set consists of the following items:

$L = 100$ km	length of the crude oil pipeline
$D_o = 0.8636$ m	outer diameter of the steel pipe (34 in. D)
$D_i = 0.8271$ m	inner diameter of the steel pipe
$s = 0.01825$ m	wall thickness of the steel pipe (0.7185 in. WT)
$Q = 5000$ m ³ /hr	volumetric discharge of crude oil
$S_r = 0.85$	specific density of crude oil
$c_p = 1.8$ kJ/(kg·K)	specific heat of crude oil at constant pressure [2]
$\lambda_s = 2.0$ W/(m·K)	thermal conductivity of soil (sandy seabed sediments; see Table 2)
$t_s = 4^\circ\text{C}$	ambient temperature of seabed pipeline surroundings
$t_1 = 60^\circ\text{C}$	inlet temperature of crude oil
$J_l = 0$ K/m	temperature increment of the crude oil transported along the pipeline due to the Joule-Thompson effect and possible changes in a pipeline route vertical profile

Three different values of the shape factor of the soil layer, *i.e.*: (1) $S = S_{s1n} = 9.06$, (2) $S = S_{s2} = 4.77$, and (3) $S = S_{s3n} = 2.50$, were assumed in the computational analysis. These values were formerly obtained for the seabed soil models discussed previously (see Fig. 4). The highest, practically acceptable, spread in the shape factor values was assumed to happen at the smallest practical relative depth of burial, which is equal to $c/r_i^{(s)} = 2$.

In order to simplify the computational analysis it was additionally assumed that the entire pipeline structure is formed by a steel pipe only. A possible occurrence of additional coatings, *i.e.*: thermal insulation, anti-corrosion, and concrete coatings, are excluded from the present analysis in order to get a better insight into functionality of the above presented pure seabed soil models. This assumption implies the relation $r_i^{(s)} = r_o^{(p)} = D_o/2$. Consequently, the outer diameter of the steel pipe equal to $D_o = 0.8636$ m induces the following values of the heat transfer coefficient: (1) $U_{s1} = 6.5$ W/(m²·K), (2) $U_{s2} = 3.4$ W/(m²·K), (3) $U_{s3} = 1.8$ W/(m²·K), respectively to the above computed values of the shape factor of the soil layer. The computational analysis was based on a computational algorithm presented in [5, 7], and the results obtained are illustrated in Fig. 5.

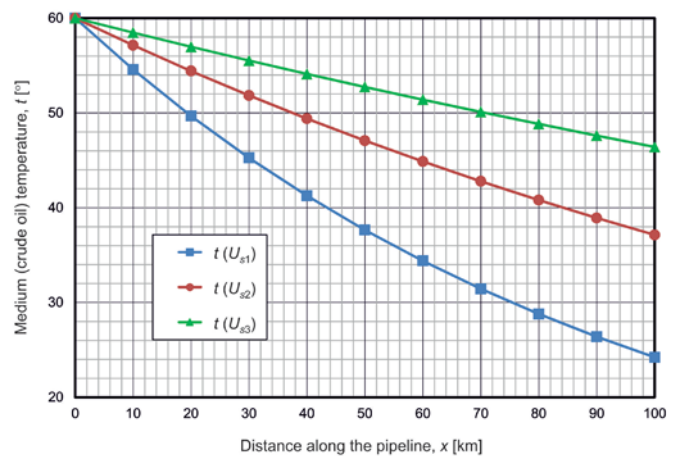


Fig. 5. The crude oil temperature distribution along the submarine buried pipeline for different values of the heat transfer coefficient of the soil layer, representing different seabed soil models

The three computational cases indicate evidently significant monotonic drops in crude oil temperature as the medium travels along the pipeline. Of course, the temperature drop effect was anticipated because the seabed soil layer (wet sandy soil) – the only additional layer considered in the pipeline thermodynamic system – acts, contrary to the steel pipe, as a relatively good thermal insulator. In general, temperature drops at the end of the pipeline depends on the pipeline length. For the 100-km long-distance submarine buried pipeline assumed for the analysis, the computed outlet temperature (*i.e.* at the end-point of the pipeline) of crude oil show the temperature drop equal to: 22.7%, 38.1%, and 59.7% of the inlet temperature set initially to $t = 60^\circ\text{C}$.

Under some special flowing conditions (temperature and pressure), the following issues: wax crystallisation, wax deposition, wax gelation and methane hydrate formation are essential in proper design procedures for submarine pipelines, especially deepwater and ultra-deepwater pipelines. Among others, a crude oil flow in the submarine pipeline can be endangered (or even terminated temporarily or permanently) when the flowing temperature drops beneath a certain critical temperature called the wax crystallisation temperature. This complex situation can be avoided only by preventing the

pipeline thermodynamic system from excessive losses of heat energy convected and/or conducted from the flowing medium to the pipeline ambient environment. The problem becomes acute especially for long-distance submarine pipelines.

For example, assuming the crude oil to have a characteristic similar to waxycrude oils that can be found in the North Sea region (the wax crystallisation temperature ranging from 30 ÷ 40°C), the temperature longitudinal profiles obtained for the last two values of the heat transfer coefficient (U_{s2} and U_{s3}) indicate the “waxy problem” that can appear in the remaining pipeline section after approximately 40 km and 80 km distances, respectively, from the pipeline inlet.

CONCLUSION

Two basic mathematical seabed soil models are discussed in the paper. Comparison of the models led to computation of the shape factor of the soil layer, giving the highest possible range thereof ($S_s = 2.50 \div 9.06$) obtained for the practically smallest relative depth of burial $c/r_i^{(s)} = 2$. Consequently, the heat transfer coefficient of the soil layer was found to cover the range $U_s = 1.80 \div 6.5 \text{ W}/(\text{m}^2 \cdot \text{K})$, respectively. The smallest values of the shape factor and the heat transfer coefficient are related with the “soil ring” model proposed in [8], whereas the largest relate to the modified Cranmer’s “soil ring” solution (see Eq. (23)). The soil half space model creates the solution which averages the above mentioned extreme solutions based on the “soil ring” model of seabed soil sediments.

The meaning of the identified variability of the heat transfer coefficient of the soil layer, U_s , was illustrated performing the computational analysis of the longitudinal temperature profile in the case of the 100-km long crude oil submarine pipeline buried in seabed sediments. The investigated variability range of the heat transfer coefficient covers different situations, e.g. relatively good thermal insulation ensured by the seabed soil layer (case 3 for $U_{s3} = 1.80 \text{ W}/(\text{m}^2 \cdot \text{K})$, and very poor thermal insulation (case 2 for $U_{s2} = 3.40 \text{ W}/(\text{m}^2 \cdot \text{K})$ or case 1 for $U_{s1} = 6.50 \text{ W}/(\text{m}^2 \cdot \text{K})$) which can cause the crude oil transportation process dangerous because of the “waxy problems”.

Due to a lack of suitable literature reports, at the moment it is rather difficult to judge which model of the seabed soil layer gives the best prediction of the real thermal conditions. Probably the only way to get a highly satisfactory answer to this problem is to perform detailed laboratory investigations of a temperature field around a submarine pipeline buried in seabed sediments for steady-state flowing conditions.

REFERENCES

1. Bai Y., Bai Q. (2005): *Subsea Pipelines and Risers*, Elsevier Science 2005.
2. Burger J., Sourieau P., Combarous M. (1985): *Thermal Methods of Oil Recovery*, Éditions Technip, Paris 1985.

3. Carslaw H.S., Jaeger J.C. (1986): *Conduction of Heat in Soils*, Oxford University Press, second Edition, April 10, 1986.
4. Cranmer Jr. J. L. (1984): *BASIC Pipeline Engineering Manual*, PennWell Publishing Company, Tulsa, Oklahoma.
5. Golshan H., Zhou Z.J. (1997): Gas pipeline temperature profile predictions in discontinuous permafrost regions. *Proc. of the Offshore Mechanics and Arctic Engineering (OMAE)*, Vol. V, Pipeline Technology, pp. 177-184.
6. King G. G. (1981): Equation predicts buried pipeline temperatures. *Oil & Gas Journal*, March 16, 1981, PennWell Publishing Company, Tulsa, Oklahoma, pp. 65-72.
7. Magda W. (2005): *Rurociągi podmorskie. Zasady projektowania*, Wydawnictwa Naukowo-Techniczne, Warszawa 2005.
8. [8] Magda W. (2010): Nowoczesne termoizolacje rurociągów podmorskich, *Inżynieria Morska i Geotechnika*, No. 2/2010, pp. 244-256.
9. Phetteplace, G. (2006): What’s Hot and What’s Not: Defending Thermal Damage Claims, *Presentation at the 97th Annual Conference of the International District Energy Association*, 11-14 June 2006, Nashville, TN.
10. <http://www.ofshore-technology.com/contractors/corrosion/3m/3m2.html>.

CONTACT WITH THE AUTHOR

Waldemar Magda

e-mail: waldemar.magda@wilis.pg.gda.pl

Gdańsk University of Technology
 Faculty of Civil and Environmental Engineering
 Department of Geotechnics
 Geology and Marine Civil Engineering
 G. Narutowicza 11/12
 80-233 Gdańsk
POLAND